EVOLUTION OF LAVAS AT MT. SHASTA VOLCANO, N. CALIFORNIA: AN EXPERIMENTAL AND PETROLOGIC STUDY

by

Michael Baldwin Baker

A.B. *Magna Cum Laude*
Harvard College (1979)

SUBMITTED TO THE DEPARTMENT OF
EARTH, ATMOSPHERIC, AND PLANETARY SCIENCES
IN PARTIAL FULFILLMENT OF
THE REQUIREMENTS FOR
THE DEGREE OF

DOCTOR OF PHILOSOPHY

at the

MASSACHUSETTS INSTITUTE OF TECHNOLOGY
FEBRUARY 1988

Signature of Author _____
Department of Earth, Atmospheric, and Planetary Sciences
February 24, 1988

Certified by _____
Timothy L. Grove
Thesis Supervisor

Accepted by _____
William F. Brace
Chairman, Department Committee

EVOLUTION OF LAVAS AT MT. SHASTA VOLCANO, N. CALIFORNIA: AN EXPERIMENTAL AND PETROLOGIC STUDY

by

Michael Baldwin Baker

Submitted to the Department of
Earth, Atmospheric, and Planetary Sciences
in partial fulfillment of
the requirements for
the degree of

Doctor of Philosophy

February 24, 1988

ABSTRACT

Partial melting, fractional crystallization, assimilation and mixing are some of the processes which control the chemical variability observed in tholeiitic and calc-alkaline lavas. This thesis explores how differentiation processes operate at two Cascade volcanos, and investigates the question of primary MORB magmas.

EVOLUTION OF THE GIANT CRATER-CHIMNEY CRATFR LAVA FLOW, MEDICINE LAKE VOLCANO, NORTHERN CALIFORNIA

At Giant Crater-Chimney Crater (GC-CC) a compositionally zoned lava flow of approximately 2 to 6 km^3 was erupted during early Holocene time (10,600 years before present). The earliest erupted lavas were basaltic andesites (51 - 53 wt.% SiO_2), while the later lavas were high alumina basalt (HAB; 47 wt.% SiO_2). Large amounts of crustal assimilation are required to reproduce the elevated incompatible element abundances in the contaminated GC-CC basaltic andesite lavas, with ratios of assimilation to fractionation (R) between 1 and 2. A simple single-stage process of continuous assimilation accompanied by fractionation is not able to generate the compositional variability observed in the erupted lavas. Evidence from major and trace element chemistry and isotopic and mineral compositions from the lavas and their xenoliths indicates that the contaminated basaltic andesite lavas were produced by mixing of primitive HAB with ferrobasalt and melted silicic crust. The ferrobasalt represents the fractionation product of the previous input of HAB into the crustal level reservoir. Crystallization required to produce the evolved basaltic liquid supplied the heat to melt the crust,

however the evolving ferrobasalt did not interact with the melted crustal material. The mixing event that produced the basaltic andesites was triggered by fresh input of primary HAB which incorporated both the fractionation-produced derivative liquids and the granitic crustal melt.

EVOLUTION OF LAVAS AT MT. SHASTA VOLCANO, NORTHERN CALIFORNIA

Major, trace and isotopic analyses of lavas erupted at Mt. Shasta, coupled with detailed mineral chemistry and 1-atmosphere and 2 kbar phase equilibria are used to infer processes of chemical evolution in this magmatic system. The collected samples range from magnesian basaltic andesites (BA) to rhyodacites. The most abundant lavas at the volcano are two pyroxene andesites and dacites (60 to 67 wt.% SiO_2), with ubiquitous disequilibrium phenocryst compositions and textures. A characteristic assemblage is Fe-rich and Mg-rich orthopyroxenes and augites. The evolved phenocryst compositions generally have magnesian rims.

In major element composition space, the andesites and dacites fall along lirear trends between the BAs and the derivative rhyodacites. However, incompatible trace element abundances in these intermediate lavas display a 2 to 3 fold variation. $^{87}/^{87}Sr$ ratios vary from 0.7038 to 0.7027, and are negatively correlated with Sr abundance in a subset of the andesites and dacites.

A minimum of two separate processes are required to explain the observed chemical variation in the andesites and dacites at Mt. Shasta. The major element compositions in the intermediate lavas are the result of mixing between basaltic andesite and rhyodacite lavas, coupled with minor crystal fractionation. Following the mixing event, trace and isotopic compositions of the majority of the andesites and dacites have been affected by mixing with one of at least three separate components: (1) a leucocratic dacitic component with a high Sr abundance but nonradiogenic isotopic ratio and low concentrations of K, Ba, Rb, (2) an intermediate Sr and high Ba and Ce component and (3) continental crust. The leucocratic component is similar, although lower in silica, higher in calcium and much higher in Sr, Ba and La to ophiolitic plagiogranites.

A NUMERICAL ALGORITHM FOR EQUILIBRIUM CRYSTALLIZATION AND MELTING

This chapter presents a temperature-independent method for modeling the compositions of solids and liquid produced by equilibrium crystallization and melting. The technique is based on Fe-Mg and Ca-Na exchange reactions and handles the phases olivine, augite, low-Ca pyroxene and plagioclase. Calculated equilibrium and fractional paths for two mid-ocean ridge basalts show that these two end-member crystal-liquid processes do not begin to produce divergent liquid compositions until after 30 to 40% crystallization. Although magmatic differentiation may lie

between the extremes of perfect equilibrium and fractional crystallization, numerical techniques based on either of these two end-members provide adequate models of the early to middle stages of the natural process. Comparing calculated and observed residual liquid compositions from the Kilauea Iki lava lake demonstrates that the equilibrium model can accurately mimic bulk equilibrium crystallization of olivine coupled with surface equilibrium crystallization of augite and plagioclase. Finally, the algorithm is used to calculate the compositions of low percentage melts from a MORB-depleted mantle. Six percent melting and a harzburgite residue produces a liquid similar in composition to magnesian quartz tholeiites found in many ophiolite assemblages.

MAJOR ELEMENT CONSTRAINTS ON THE COMPOSITIONS AND MELT PERCENTAGES OF PRIMARY MID-OCEAN RIDGE BASALTS.

This chapter presents a technique to calculate the compositions of olivine, orthopyroxene, clinopyroxene and spinel in equilibrium with a mid-ocean ridge basalt (MORB) at ~10 kbars. We also evaluate the uncertainties in each phase composition. Using a variety of potential primary magmas and bulk mantle compositions, we solve the equation: MORB + olivine + orthopyroxene ± clinopyroxene ± spinel = bulk mantle for phase proportions and statistically evaluate each fit. The results show that primitive mid-Atlantic ridge glasses are not primary magmas from a spinel lherzolite mantle. The addition of 5 and 10 wt.% olivine + spinel to the average MORB glass produces two new liquid compositions which may represent primary melts. Thus, these liquids could evolve to the primitive MORB glasses by minor olivine plus spinel fractionation. The wt.% of $CaO+Al_2O_3$ in the bulk mantle proves to be a sensitive guide to the extent of melting required to produce a specific primary basalt composition. Based on 24 successful mass balance solutions and an assumed calcium plus alumina content in the MORB mantle of ~7 wt.%, 6 to 12% partial melting is required to produce primary basalts with 11 to 13% MgO.

Thesis Supervisor: Dr. Timothy L. Grove
Associate Professor of Petrology

TABLE OF CONTENTS

LIST OF FIGURES

LIST OF TABLES

INTRODUCTORY NOTE

This thesis consists of four independent chapters. The first two deal with questions of petrogenesis at calc-alkaline volcanos, while the third and forth chapters describe numerical techniques and calculations concerned with equilibrium crystallization and melting. Chapter 1 presents a mixing model for the development of a compositionally-zoned lava flow at Medicine Lake Highland volcano. The chapter is a collaborative effort with R. J. Kinzler, T. L. Grove, J. M. Donnelly-Nolan, and D. E. Champion. It provides a framework for understanding the more complex chemical variations observed at Mt.Shasta. Chapter 2 integrates major, trace and isotopic data with low and moderate pressure experimental results in order to model the petrogenesis of the lavas at Mt. Shasta. As in the case of other Cascade volcanos which have been studied in great detail (e.g. Medicine Lake and Crater Lake), the processes which produced the andesites and dacites at Mt.Shasta were extremely complex. Geochemical and petrographic information in the andesite and dacite lavas point to mixing between basaltic, derivative silicic and crustal melts. At least two other components are required to model trace and isotopic trends in the andesites and dacites, and these components may be related to the Trinity ophiolite which underlies Mt. Shasta.

Chapter 3 presents a temperature-independent algorithm for calculating the compositions of solids and liquids produced by equilibrium melting and crystallization. The impetus for developing the program was to investigate how quickly

equilibrium versus fractional crystallization of olivine + plagioclase ± augite produced divergent liquid compositions given the same bulk composition. Much to my surprise, a fair amount of crystallization is required (30 to 40%) before the liquids begin to differ appreciably.

Chapter 4 is an outgrowth of the equilibrium melting calculations presented at the end of Chapter 3. Using existing high pressure experimental data, this chapter attempts to answer the questions: Are magnesian mid-ocean ridge glasses primary melts? and, What are the degrees melting required to produce primary basaltic liquids with 11 to 13% MgO?

Each chapter is presented as a self-contained article including references. The abstracts for each chapter have been combined into the thesis abstract.

ACKNOWLEDGEMENTS

First and foremost I would like to thank Tim Grove for his support throughout all stages of my graduate career and for instructing me in the many facets of experimental petrology. He has been a good friend during these six and a half years. I have also enjoyed three field seasons with Tim and his family (including several memorable hikes to the summit of Mt. Shasta). I would also like to thank Fred Frey, Tom Jordan and Dave Walker, the other members of my committee, for reading a long thesis on such short notice.

Bob Christiansen provided unpublished chemical analyses of Mt. Shasta lavas and shared his knowledge of the volcano's geologic history. Dick Price did the XRF analyses of the Mt. Shasta samples. Ro Kinzler ran many of the Sr-isotopes reported in Chapter 2. Fellow students Tom Juster, Ro Kinzler, Larry McKenna, and Vincent Salters read various chapters of this thesis, providing valuable comments and criticism. My office-mate, Larry McKenna, endured with good humor the steady encroachment of reprints and computer printout onto his desk. Steve Recca provided essential instruction in the operation of the new JEOL 733 electron microprobe as well as insight into the world of computers. My thanks to the denziens of the 5th floor for logistical, as well as moral, support.

Many people have contributed to my enjoyment of life at MIT. In paticular, I would like to thank Tom Juster, Allen and Reneau Kennedy, Ro Kinzler, David Lea, Chip Lesher, Larry McKenna, Julie Morris, Mary Reid, Alexana Roshco, Vincent

Salters, Tom Sando, Liz Schermer, Jane Selverstone, Tom Sisson, and Brian Taras for many fond memories. I have enjoyed many close games of squash with Fred Frey over the years.

I would also like to thank my parents for their support and encouragement, not only during this endeavor, but throughout my life. Finally I would like to thank Lind Gee for her assistance in the preparation of this thesis, and for her unfailing friendship.

CHAPTER 1

Development of the Compositionally Zoned Giant Crater - Chimney Crater Lava Flow at Medicine Lake Volcano, Northern California: Assimilation in a Calc-alkaline Magmatic System

INTRODUCTION

The entire compositional spectrum of lavas that constitute the calc-alkaline series is represented at Medicine Lake Volcano. High alumina basalt (HAB) is the dominant lava type, with basaltic andesite (BA), andesite, dacite and rhyolite present in order of decreasing volumetric abundance (Donnelly-Nolan, 1988). Among the variety of magmatic lineages present at the volcano (Barsky, 1975; Condie and Hayslip, 1975; Mertzman, 1977a,b; Grove and Donnelly-Nolan, 1986) are basaltic andesites which have been produced by an open system process involving the incorporation of a granitic crustal component. The operation of an open system process which involved the mixing of a melted granitic crustal component with basaltic magma was first proposed by Anderson (1941), based on petrographic observation of phenocryst/xenocryst associations in Holocene basaltic andesite lavas. Later, Eichelberger (1975) expanded on the Anderson model. Grove et al. (1982) and Gerlach and Grove (1982) proposed that fractional crystallization of primary HAB accompanied by assimilation of a granitic crustal component played a role in the development of these contaminated basaltic andesite lavas. Grove et al. (1982) showed that variation in isotopic characteristics was consistent with such a process, and Grove et al. (1988) identified shallow level (6 to 10 km depth) granitic rocks, probably plutonic equivalents of erupted silicic magmas, as the material most likely to have been that assimilated by

basalt. Donnelly-Nolan (1988) summarizes these models for the development of Medicine Lake volcano.

In this paper, we describe a single lava flow whose age and chemical relations provide some insight on the mechanisms by which assimilation of granitic material by basalt may have occurred. We conclude that the process of assimilation is one in which basaltic liquid is the dominant magma type, overwhelming the volume of silicic melt produced by the melting of granitic crust. In some instances, the melted granitic crust is produced by heat supplied through large amounts of fractionation of basaltic material. The melted crust and highly fractionated basalt are mixed with variable amounts of primitive basalt, and these interactions are well preserved in the compositionally zoned eruption of the Giant Crater-Chimney Crater system.

GEOLOGIC SETTING

In this paper the name Giant Crater - Chimney Crater (GC-CC) is used to describe the lava flows erupted from Giant, Chimney and Double Hole Craters. These flows are located on the south flank of Medicine Lake Volcano, N. California (Fig. 1-1). The lavas erupted from these craters have similar paleomagnetic orientations, and two radiocarbon dates on charcoal preserved beneath the Giant Crater lavas give an early Holocene age (10,600 years before present (y.b.p.)). We also present chemical data on the Horse Caves - Water Caves (HC-WC) lavas which have a different

paleomagnetic orientation and precede the GC-CC event by a few hundred years. Previous descriptions of the GC-CC lavas include Baer (1970), Greeley and Baer (1971) and Donnelly-Nolan (1987). A detailed map of the lavas and a discussion of the field, paleomagnetic and radiocarbon evidence which constrain the age relations may be found in Champion and Donnelly-Nolan (in prep).

The lava flow is 40 km in length, and the total area covered by GC-CC and Double Hole lavas is 210 km^2. The HC-WC lavas cover 9.3 km^2. Flow thicknesses in the GC-CC lava system range from 50m near the vents to 30m in the lava tube to 10 to 20m in the southern portion of the flow. Assuming average thicknesses of 10 and 30m, the volume of erupted material from Chimney, Giant and Double Hole craters is between 2.1 and 6.3 km^3, respectively. On the basis of initial detailed mapping in the vicinity of Giant and Chimney Craters, five eruptive units were defined and designated 1 (oldest) to 5 (youngest). Subsequently, mineralogy, texture and chemical composition were found to correlate systematically with eruptive age. This correlation between chemical composition and eruptive age is consistent over the area of the entire flow. The areal extent of the age and chemical groups is summarized in Fig. 1-1 for the entire flow, and in Fig. 1-2 for the northern part of the flow. Groups 1 and 2 overlap in chemistry, and will be referred to as Group 1,2 for purposes of this discussion.

CHEMISTRY, PETROGRAPHY AND AGE-COMPOSITIONAL CORRELATIONS

The chemical variability of the age groups is summarized in Fig. 1-3 for major elements, and incompatible and compatible trace elements. Whole rock chemistry, mineral chemistry and isotopic compositions of lavas and inclusions are found in Tables 1-1 through 1-5. Sample locations and analytical methods are described in Appendices 1-A and 1-B, respectively. The earliest basaltic andesite lavas (Groups 1,2 and 3) have high SiO_2 and incompatible trace element abundances, and low MgO and compatible trace element abundances. These lavas were more viscous upon eruption and built up thick flows around the vents. The latest lavas (Groups 4 and 5) are high alumina basalt with low SiO_2 and high MgO. Incompatible and compatible trace element abundances are low and high, respectively, relative to Groups 1-3.

Group 4 lavas occur over a large areal extent. The entire Double Hole eruption consisted of Group 4 lava and most of the southern part of the GC-CC flow is Group 4 (Figs. 1-1 and 1-2). These lavas form a tight grouping on all element - element diagrams (Fig.1-3), and we propose that magma mixing was responsible for producing this homogeneous magma type.

Group 5 lavas are the next most abundant lava type, are the last erupted and are geochemically the most primitive of all the GC-CC lavas. The Group 5 HAB lavas are present in Giant Crater (Fig. 1-2) and were transported by a lava tube

system as far as the end of the lava flow (40 km). The lava tube at Giant Crater is a prominent feature that can be traced for at least 22 km, making it one of the longest known terrestrial lava tubes (Greeley and Baer, 1971). In subsequent discussions, we assume that a magma geochemically similar to the most mafic of the Group 5 lavas was parental to the more evolved GC-CC lavas.

Petrography and Mineral Chemistry

The textures of mineral assemblages associated with each chemical group are shown in Fig. 1-5 and mineral chemistry is summarized in Fig. 1-6. Group 1, 2 and 3 lavas are sparsely porphyritic, containing no more than 4 vol.% phenocrysts. The phenocryst assemblage is dominantly plagioclase, with olivine, quartz, augite and orthopyroxene present in lesser proportions. Andesine plagioclase xenocrysts (Figs. 1-5b and 1-6, Table 1-4) are reacted, resorbed and overgrown by An-rich rims. Quartz xenocrysts have embayed margins and are surrounded by an SiO_2-rich melt zone (Fig. 1-5c). Orthopyroxene phenocrysts have Fe-rich cores and Mg-rich overgrowth rims. Fe-rich olivine (Fo_{60-70}) and Fe-rich augite ($Wo_{41}En_{46}$) are present as glomerocrystic intergrowths with plagioclase (An_{70-72}) and are reverse-zoned to Mg-rich rims (Fig. 1-5e, Table 1-4). Mg-rich olivine (Fo_{88-80}) and An-rich plagioclase (An_{84-80}) are also present as glomerocrystic intergrowths (Figs. 1-5d and 1-6). The phenocryst assemblages are not in equilibrium with the

lavas in which they have been preserved. As recognized by Anderson (1941), Gerlach and Grove (1982) and Grove et al. (1988), these minerals assemblages are characteristic of granitic (An_{35-45} plagioclase, Fe-rich orthopyroxene and quartz), ferrobasaltic (Fe-rich olivine and augite and An_{70} plagioclase) and Mg-rich HAB (Fo_{88} olivine and An_{84} plagioclase) components. Inclusions found in the Group 1 lavas further support the involvement of these magma components in producing the Group 1, 2 and 3 lavas, as discussed in the next section.

The Group 4 samples, which form a tightly clustered, geochemically distinct group on element - element variation diagrams (Fig. 1-3), are aphanitic and characterized by a pilotaxitic groundmass of plagioclase, olivine, with less abundant spherulitic augite, Fe-Ti oxides and glass. Rarely, cm-sized An_{84-80} plagioclase xenocrysts are found in these lavas. These xenocrysts contain sieve-textured interiors and cuspate outer margins indicative of dissolution by the enclosing magma.

The youngest lavas (Group 5) are aphanitic to fine-grained, equigranular, and distinctively non-porphyritic. Glassy chill margins contain <1 vol.% microphenocrysts (Fig. 1-5a). Olivine microphenocrysts are normally zoned from Fo_{88} cores to Fo_{80} rims, and plagioclase microphenocrysts are also normally zoned from An_{86} cores to An_{76} rims (Fig. 1-6). The Group 5 HABs exhibit a broad range in groundmass textures from glassy to spherulitic near chill margins to

intersertal, intergranular and subophitic in phyric samples. Augite is the most abundant groundmass mineral with Fe-Ti oxides present in lesser proportion.

Inclusions

Inclusions have been found only in Group 1 lavas, and consist of two types: highly melted granitic inclusions and magmatic cumulate mafic inclusions. The granitic inclusions are amoeboidal to flattened in shape with external margins that are covered by a rind of basaltic andesite. The melted granitic inclusions are highly vesicular and consist largely of glass (50 to 70 vol.%) with rounded to irregular quartz and rounded plagioclase in nearly equal proportion (25 to 15 vol.% each; Fig. 1-5h). These inclusions are similar to highly melted granitic inclusions found in Burnt Lava at Medicine Lake Volcano (Grove et al., 1988).

Two cumulate mafic magmatic inclusions have also been found in the Group 1 lavas. Both are ovoid, vesicular and 3 to 5 cm in longest dimension. One is a troctolite (Figs. 1-5f and 1-6), containing plagioclase laths normally zoned from An_{80} cores to An_{63} rims. Olivine is compositionally uniform at Fo_{85} and contains a thin Fe-rich rim of Fo_{77}. The second inclusion is a ferrogabbro, which has been invaded and permeated by basaltic andesite magma. As a consequence, all the Fe-Mg silicates contain Mg-rich reaction overgrowth rims (Fig. 1-5g). The primary mineral phases are olivine Fo_{74}, which is overgrown by a Fo_{82} reaction rim, and augite

$Wo_{42}En_{45}Fs_{13}$, overgrown by a $Wo_{42}En_{49}Fs_{7}$ reaction rim. Plagioclase is zoned from An_{76} cores to An_{66} rims.

The granitic and mafic inclusions found in the Group 1 lavas support the hypothesis based on phenocryst assemblages that several components have been involved in producing Group 1, 2 and 3 lavas. The highly melted granitic inclusions are remnants of a granitic component that has been added to Group 1 lavas, while the cumulate mafic inclusions are residues of fractional crystallization. The troctolite contains Mg-rich olivine and An-rich plagioclase cumulate from an early stage of HAB differentiation. As we show in the next section, extensive fractionation of HAB magma is required to produce a magma that would crystallize the ferrogabbro cumulate.

Isotopic Compositional Variation

The variation in isotope composition among the Group 1 to 5 lavas (Table 1-5) is generally consistent with a process of progressive contamination of mantle-derived HAB (Group 5) by a radiogenic crustal component. The HAB lavas, represented by Groups 4 and 5, have the lowest $^{87/86}Sr$, highest Sr abundance, highest $^{143/144}Nd$ and lowest Nd abundance. The Group 1 BAs have the highest $^{87/86}Sr$, lower Sr abundance, lower $^{143/144}Nd$ and higher Nd abundance. The highly melted silicic inclusions found in the Group 1 BA lavas have $^{87/86}Sr$ and $^{143/144}Nd$ close to that of their enclosing hosts. Although these inclusions have radiogenic

isotope signatures that are slightly more crust-like than the BA lavas, their geochemical characteristics are not suggestive of assimilant material. Similar inclusions have been found in the Burnt Lava flow (Grove et al., 1988), and it has been proposed that inclusion and host have nearly achieved isotopic equilibrium. Based on the similarity in texture, mineralogy, Nd and Sr abundances between these two suites of highly melted inclusions, we propose that the highly melted inclusions in Giant Crater have also undergone extensive reequilibration with their enclosing BA host.

DISCUSSION

Models and Assumptions

The presence of mineral assemblages indicative of a granitic component and inclusions of highly melted granitic xenoliths, combined with the isotope signature of a radiogenic component provides evidence for the assimilation of granitic crustal material in the most evolved GC-CC lavas. Consequently, the GC-CC flow should be an ideal setting for a study of the process by which parental HAB evolved to contaminated BA.

We assume that the mafic Group 5 HAB lavas are representative of the parental magma which evolved to contaminated BA. HAB is the dominant magma type at Medicine Lake, appearing repeatedly throughout the eruptive history of the volcano. The latest eruptive episode at Giant Crater, which was a primitive HAB, is assumed to represent

replenishment of the magma reservoir(s) by an undifferentiated magma batch that was similar to that which underwent a fractionation and assimilation process. The lavas were produced during a single eruptive episode and presumably sample a compositionally zoned magmatic system that was tapped during its evolution.

No "simple" model of fractionation combined with assimilation reproduces the full compositional spectrum exhibited in the zoned eruption. We assume that only three components are responsible for producing the observed compositional spectrum at GC-CC: Group 5 HAB, derivative ferrobasalt and melted shallow level granitic crust. There is substantial evidence that this assumption is correct. Any successful model must provide a mechanism which allows for the large amount of assimilation that is required to produce the extreme incompatible element enrichments observed in contaminated BAs. Such large amounts of assimilation require substantial amounts of heat to melt granitic crust, which must be supplied by large amounts of fractional crystallization of HAB and/or lesser amounts of fractionation of large volumes of HAB parent magma which is not erupted.

Low Pressure Fractional Crystallization

As a basis for comparison, a low pressure fractional crystallization path has been calculated using the most primitive Group 5 HAB composition. This fractionation path

was constrained using the experimental results of Grove et al. (1982) and follows the procedure outlined in Grove and Donnelly-Nolan (1986) and Grove et al. (1988). The model is tabulated in Table 1-6 and plotted in the Oliv-Cpx-Qtz and Oliv-Plag-Qtz pseudoternaries in Fig. 1-7. The early oliv + plag part of the fractionation model is also shown on selected element-element variation diagrams in Fig. 1-8. The HAB has olivine and plagioclase as liquidus phases, and crystallizes these two phases alone for a substantial interval (F=1.0 to 0.52, where F = fraction of liquid remaining). In the pseudoternary plots, this crystallization path parallels the Oliv-Cpx and Oliv-Plag bases. Thus, the compositional variation of the GC-CC Group 5 lavas appears to be produced by fractional crystallization of olivine + plagioclase at or near 1 atm, and an iron-rich segregation vein in a Group 5 lava (82-72a) provides an example of extensive 1-atm crystallization, which has reached oliv-plag-augite multiple saturation (Fig. 1-7). In contrast to the low pressure fractionation path, the compositional trend of Groups 1,2 through 4 is one of Qtz enrichment, nearly orthogonal to low pressure crystallization path.

Further evidence for low pressure fractional crystallization is preserved in the cumulate xenoliths found in Group 1 lavas. The cumulate gabbro (1160M) contains oliv-plag-cpx associations which would be in equilibrium with a highly evolved oliv-plag-cpx saturated liquid, much more Fe-rich than the most evolved Group 1 sample (83-1). The end

point of the fractional crystallization model represents a liquid that could be in equilibrium with this cumulate sample.

The overall trend of lavas from Groups 1,2 through 4 is not consistent with low pressure fractional crystallization. Any crystallization process involving the anhydrous phases found in the GC-CC lavas is incapable of producing the observed trend away from the Oliv-Plag-Cpx base of the Oliv-Plag-Cpx-Qtz quaternary. Simultaneous crystallization of the assemblage oliv-plag-cpx at elevated pressure (5 to 10 kbar) will not move residual liquids in the required direction. Such crystallization results in very little enrichment in normative quartz, because both the liquid and the crystallizing phases lie nearly in the Oliv-Plag-Cpx plane of composition space. Using the reported compositions of experimentally produced clinopyroxenes from 8 to 10 kbar experiments, oliv-plag-cpx crystallization would produce nepheline-normative residual liquids.

The projected positions of the granitic inclusions found in Holocene and Pleistocene lavas at Medicine Lake volcano (Grove et al., 1988) are also shown in the pseudoternaries (Fig. 1-7). Contamination of HAB by melted granitic crust could produce the trend of silica enrichment shown by the GC-CC series. Moreover, xenocrysts of quartz, Na-rich plagioclase and highly melted granitic xenoliths are found in abundance in the high-SiO_2 (Group 1) lavas, and are absent in the low-SiO_2 (Group 4 and 5) lavas. Our initial

attempts to model compositional variation by crustal contamination assumed assimilation combined with fractional crystallization (AFC) was the process which produced the GC-CC trend. However, none of the AFC models could produce the variations observed in the lavas. For example, a model that attempted to generate the most SiO2-rich Group 1 lava from the Group 5 parent is shown in Table 1-6. This AFC model crystallized olivine and plagioclase in proportions consistent with 1-atm phase equilibrium constraints, and required large amounts of assimilation (R=2.0) to match the major element abundances and the high incompatible element abundances of the Group 1 lavas. However, the model does not provide a good fit, and several key major and minor elements are fit very poorly (e.g. Ti, Fe, Na, P). No AFC model which begins with the Group 5 parent, crystallizes olivine and plagioclase and assimilates granitic crust describes the compositional variations displayed by the Group 4,3,2 and 1 lavas. For example, models which fit the incompatible element enrichments miss the parabolic trends described by FeO vs MgO and TiO_2 vs MgO (Fig. 1-3). In all AFC models, the compatible trace elements Ni, Sc, Cr are higher in the Group 1 lavas than the model predicts.

A further problem is the difficulty of mixing hot, low viscosity basalt melt with large amounts of cooler, high viscosity silicic crustal melt. Using the model of Sparks and Marshall (1986) as a guide, only the R = 1.0 model (Table 1-6) would be mechanically feasible for AFC. Models

with R>1 exceed the limit beyond which the mixing of a mafic and silicic liquid produces nearly complete crystallization of the mafic member.

Multi-component Mixing Model

The evolved gabbro cumulates in the Group 1 lavas suggest that ferrobasalt was an important third component in the process which generated the GC-CC lavas. This ferrobasalt was produced by extensive fractionation of an HAB parent at shallow crustal levels.

Several multicomponent mixing models have been constructed for the GC-CC lavas. Major element models are reported in Table 1-6 and trace element and isotope mixing models are reported in Table 1-7. We used the average granitic inclusion composition reported in Grove et al. (1988) as the crustal assimilant. For the highly fractionated basalt component, we chose two candidates. The first is the end point of the calculated 1-atm fractional crystallization path (Table 1-6). This fractionation calculation was carried to the point where the residual liquid would be in equilibrium with the Fe-rich olivine and clinopyroxene found as xenocrysts and in cumulate gabbro 1160M. The second is represented by the late-stage Fe-rich segregation vein (82-72a, Table 1-1), which formed at the surface during cooling of a Group 5 lava flow. The 1-atm dynamic crystallization experiments of Baker and Grove (1985) show that crystallization paths followed during

cooling in HAB lava flows depart significantly from equilibrium. As expected, the residual liquid from the low-pressure fractional crystallization path and the segregation veins differ significantly.

The first set of models were calculated to produce the Group 4 lavas, the least evolved (Group 3) lavas and the most evolved (Group 1) lavas by mixing parent HAB, ferrobasalt and granitic assimilant. In every case, the best fits are those which used the low pressure fractionation ferrobasalt as the Fe-rich component. A second model assumed that Group 4 lavas were produced by mixing HAB parent, ferrobasalt and Group 3 lavas, and a final model tested the possibility that the continuous Group 3 to Group 1 trend could be produced by mixing Group 3 lava with granitic assimilant. The trace element models used element abundances measured in the appropriate Group 5, 4, and 3 lavas, the trace element abundances of the average granitic inclusion of Grove et al. (1988) and calculated trace element abundances for the model ferrobasalt liquid. The predicted abundances, methods and assumptions are found in Table 1-7.

A Model for the Compositionally Zoned Eruption

Bowen (1922) showed that the heat necessary to cause assimilation of crust must come from the latent heat of crystallization of the basaltic magma. This heat must both raise the temperature of the crust as well as melt it, limiting the amount of assimilation which may occur. Recent

geochemical models of the process couple the assimilation and fractional crystallization process (Taylor, 1980; DePaolo, 1981), by assuming that the crustal material is assimilated continuously as crystallization proceeds. In our past discussions of the Medicine Lake magmatic system, we have used similar assumptions in developing geochemical models. However, as we have shown, simple AFC models (Table 1-6) do not produce acceptable fits to the GC-CC data.

However, separating crustal melting from the contamination process solves the heat budget problem, and removes the difficulty of trying to mix a large volume of crustal melt into a small volume of basalt. Extensive fractionation of a large volume of parent HAB at shallow crustal levels produces ferrobasalt residual liquid and produces heat to melt silicic crust. These two components are present in the same magma reservoir. Since the rate of heat diffusion is 3 to 4 orders of magnitude faster than that for chemical diffusion, the heat released by basalt crystallization melts surrounding wall rock, but chemical interaction between the melted crust and ferrobasalt is minimal. Further, a compositionally layered magma reservoir is produced, since the granitic crustal melt will rise to the top of the magma reservoir and pond above the denser ferrobasalt (Table 1-8). Crystallization of the parental basalt will produce first troctolitic, then gabbroic cumulates. Both cumulus assemblages will be denser than the HAB liquid. Buoyant liquid residual from fractionation

segregates from cumulate residue and a magma chamber stratigraphy evolves in which denser cumulates are overlain by less dense ferrobasalt, which is overlain by light silicic crust. This process is illustrated in cartoon form (Fig. 1-9).

One test of the multicomponent mixing model is to see if the component volumes involved in the mixing process can provide the heat necessary to melt the crustal material that is present in the mixture. The generation of the Group 1 and 3 lavas may be used as an example. The relative volume of each lava group is calculated in Table 1-8 and the mixing models (Table 1-6) can be used to estimate the amount of magma involved to produce each component. The combined volume of Groups 1, 2 and 3 is 0.7 km^3, and the estimated mass would be 1.83×10^{15} gm. Of this mass 15% or 2.75×10^{14} gm is assimilated granitic crust. The heat required for melting this crust depends on the temperature difference between the crust and its melting point, and the latent heats of melting and solidification of crust and basalt, respectively. We assume a crustal melting temperature of 950°C, a specific heat of 0.33 cal gm^{-1} $^oC^{-1}$ and latent heats of 50 and 100 cal gm^{-1} for granite and basalt, respectively. At shallow levels, (6 km, T=200°C), 8.2×10^{16} cal are required to melt the amount of crust that is present in the Group 1, 2 and 3 magmas. This heat could be supplied by the crystallization of 1.32×10^{15} gm of primitive high alumina basalt. The calculated proportion of ferrobasalt in

the Groups 1-3 lavas could be produced by the crystallization of 1.06×10^{15} gm of HAB. Thus, the heat liberated by fractionation of the mass of ferrobasalt in the Group 1, 2 and 3 magmas is only 20% lower than that required to melt the crust present in these magmas. There was probably more than enough magma in the reservoir to supply the heat needed to melt crust (see below), and the calculation above represents only a minimum estimate.

Origin of Groups 3 and 4 by Multiple Intrusion Followed by Mixing

If the magma reservoir illustrated in Fig. 1-9 is replenished with HAB magma, this light hot liquid will rise through the cumulate pile and denser ferrobasalt and pond beneath the melted silicic crust (Fig. 1-9c). This input of hot magma produces turbulent convection and entrainment of the overlying and underlying layers (Huppert and Sparks, 1980; Huppert et al., 1986; Freund and Tait, 1985), and forms the Group 1, 2 and 3 mixed magmas (Fig. 1-9d). The density of the ferrobasalt liquid and the GC-CC lavas is shown in Fig. 1-10. Group 1, the first erupted lava has the lowest density, and density increases continuously to a maximum at Group 5, the last erupted lava. The eruption may have tapped a compositionally zoned, density stratified magma chamber. The process which produced the zoning would be repeated injection of parental HAB, followed by extensive fractionation, reinjection of parental HAB and mixing.

Fig. 1-9e illustrates a renewed injection of HAB after the Group 1, 2 and 3 mixing event. The HAB rises through the denser cumulate pile and ferrobasalt which was not incorporated into the first HAB mixture. In this case the HAB mixes with denser ferrobasalt below and lighter Group 3 magma above to produce Group 4. Recall the extreme compositional uniformity and aphanitic nature of the Group 4 magmas, as well as their widespread abundance. The mixing proportions required for Group 4 would produce a melt that is close to its liquidus. A temperature estimate (Table 1-8) which assumes no excess heat of mixing, gives 1202 ^{o}C, which is only 28 ^{o}C below the 1 atm liquidus. A minimum water content for the melted granitic crust is 2 wt.%, which would raise the water content of the mixed magma to 0.5 wt.%. Such volatile contents at shallow crustal levels would lower the liquidus by 15 to 20 ^{o}C. Therefore, the Group 4 magma was probably very close to its liquidus after mixing.

A final event, input of parental HAB into the magma reservoir, triggered an eruption in which the compositional zoning was preserved. Spera (1984) has considered the conditions under which the withdrawal of magma from a reservoir would preserve compositional zoning. His analysis considers conduit width (100 to 140m at Chimney and Giant Craters), conduit width/chamber width and chamber width/chamber depth. For a magma with physical properties of basalt, Spera's numerical models predict a withdrawal process in which layering is preserved for a magma reservoir

2 km wide and 1 km deep. The volume of such a chamber is close to the lower limit of our volume estimate for GC-CC. Thus, the preservation of layering during the eruption of the GC-CC system is consistent with the constraints of Spera's numerical model.

CONCLUSIONS

In this discussion we have outlined a process by which assimilation of granitic crust by basaltic magma has led to the development of highly contaminated basaltic andesite magmas. In the case of the GC-CC lavas, assimilation and fractional crystallization did not occur as concurrent processes. The process which produced the contaminated lavas was one in which heat provided by extensive basalt fractionation melts crust, but with little chemical exchange between the fractionating magma and melted crustal material. The existence of xenocrysts in the contaminated lavas which record extensive crystallization to ferrobasalt residual liquid provide strong evidence of the operation of this process.

Recent discussions of the mechanisms of compositional zoning in magma chambers have concluded that melted crust would rise to the top of the chamber and develop as a stable layer chemically isolated from the underlying basalt (McBirney et al., 1985; Campbell and Turner, 1987). The challenge posed in these discussions is how to get these chemically isolated layers to mix. As Campbell and Turner

(1987) suggest, the input of a hot parental HAB magma which is lighter than the ferrobasalt, but denser than the granitic melt causes mixing and entrainment of the chemically isolated layers above and below. Models of this process for the GC-CC lavas show that this process may be multistage and complex.

REFERENCES

Abbey S (1978) Studies in "standard samples" for use in the general analysis of silicate rocks and minerals Part 5 - 1977 edition of "usable" values: X-ray spectrometry 7 99-121

Albee AL Ray L (1970) Correction factors for electron probe microanalysis of silicates oxides carbonates phosphates and sulfates. Anal Chem 42. 1408-1414

Allegre CJ, Minster JF (1978) Quantitative models of trace element behavior in magmatic processes Earth Planet Sci Lett 38.1-25

Anderson CA (1941) Volcanoes of the Medicine Lake Highland California. University of California Department of Geological Sciences Bulletin 25: 347-442

Baer RL (1970) Petrology of Quaternary lavas and geomorphology of lava tubes, south flank of Medicine Lake Highland, California. M.S. thesis, Univ. of New Mexico, 120 p

Baker MB and Grove TL (1985) Kinetic controls on pyroxene nucleation and metastable liquid lines of descent in a basaltic andesite. Amer Mineral 70:279-287

Barsky CK (1975) Geochemistry of basalts and andesites from the Medicine Lake Highland, California. Ph.D. Dissertation, Washington University, 373 p

Bence AE, Albee AL (1968) Empirical correction factors for the electron microanalysis of silicates and oxides. J Geol 76:382-403

Bougault H, Hekinian R (1974) Rift valley in the Atlantic Ocean near 36°50'N: Petrology and geochemistry of basaltic rocks. Earth Planet Sci Lett 24:249-261

Bowen NL (1922) The behavior of inclusions in igneous magma. J. Geol. 30:513-570

Bryan WB Finger LW Chayes F (1969) Estimating proportions in petrographic mixing equations by least squared approximation. Science 163:926-927

Campbell IH, Turner JS (1987) A laboratory investigation of assimilation at the top of a basaltic magma chamber. J Geol 95:155-172

Condie KC, Hayslip DL (1975) Young bimodal volcanism at Medicine Lake volcanic center, northern California. Geochim. Cosmochim. Acta 39: 1165-1178

DePaolo DJ (1981) Trace element and isotopic effects of combined wallrock assimilation and fractional crystallization. Earth Planet Sci Lett 53: 189-202

Donnelly-Nolan JM (1987) Medicine Lake Volcano and Lava Beds National Monument, California. Geol. Soc. Amer. Centennial Field Guide Cordilleran Section pp. 289-294

Donnelly-Nolan JM (1988) A magmatic model of Medicine Lake volcano, California. J Geophys Res (submitted)

Eichelberger JC (1975) Origin of andesite and dacite: evidence of mixing at Glass Mountain in California and at other circum-Pacific Volcanoes. Geol Soc Amer Bull 86:1381-1391

Freund A, Tait SR (1986) The entrainment of high-viscosity magma into low-viscosity magma in eruption conduits. Bull Volcanol 48:325-339

Fujimaki H, Tatsumoto M, Aoki K (1984) Partition coefficients of Hf, Zr and REE between phenocrysts and groundmasses. J Geophys Res 89:B662-B672

Gerlach DC, Grove TL (1982) Petrology of Medicine Lake Highland volcanics: characterization of the end members of magma mixing. Contrib Mineral Petrol 80:147-159

Gill J (1981) Orogenic andesites and plate tectonics. New York. Springer Verlag. 390 pp

Greeley R, Baer R (1971) Hambone, California and its magnificent lava tubes - Preliminary Report (abstract). Geol Soc Amer Abst w. Prog, 3, 128

Grove TL, Baker MB (1984) Phase equilibrium controls on the tholeiitic vs. calc-alkaline differentiation trends. J Geophys Res 89: 3253-3274

Grove TL, Donnelly-Nolan JM (1986) The evolution of young silicic lavas at Medicine Lake volcano, California. Implications for the origin of compositional gaps in calc-alkaline series lavas. Contrib Mineral Petrol 92:281-302

Grove TL, Gerlach DC, Sando TW (1982) Origin of calc-alkaline series lavas at Medicine Lake volcano by fractionation, assimilation and mixing. Contrib Mineral Petrol 80:160-182

Grove TL, Kinzler RJ, Baker MB, Donnelly-Nolan JM, Lesher CE (1988) Assimilation of granitic crust by basaltic magma at Burnt Lava flow, Medicine Lake volcano, Northern California: Decoupling of heat and mass transfer. Contrib Mineral Petrol (in press)

Hart SR, Brooks C (1977) The geochemistry and evolution of early Precambrian mantle. Contrib Mineral Petrol 61:109-128

Hart SR and Davis KE (1978) Nickel partitioning between olivine and silicate melt. Earth Planet Sci Lett 40:203-219

Huppert HE, Sparks RSJ (1980) The fluid dynamics of a basaltic magma chamber replenished by influx of hot, dense ultrabasic magma. Contrib Mineral Petrol 75:279-289

Huppert HE, Turner JS (1981) Double-diffusive convection. J Fluid Mech 106: 299-329

Huppert HE, Sparks RSJ, Whitehead JA, Hallworth MA (1986) Replenishment of magma chambers by light inputs. J Geophys Res 91:6113-6122

Irving AJ (1978) A review of experimental studies of crystal/liquid trace element partitioning. Geochimica Cosmochimica Acta 42.743-770

McBirney AR, Baker BH, Nilson RH (1985) Liquid fractionation, part I: basic principles and experimental simulations. J Volcanol Geotherm Res 24:1-24

Mertzman SA (1977a) Recent volcanism at Schonchin and Cinder Buttes, Northern California. Contrib Mineral Petrol 61:231-243

Mertzman SA (1977b) The petrology and geochemistry of Medicine Lake volcano. Contrib Mineral Petrol 62:221-247

Mo X, Carmichael ISE, Rivers M, Stebbins J (1982) The partial molar volume of Fe_2O_3 in multicomponent silicate liquids and the pressure dependence of oxygen fugacity in magmas. Mineral Mag 45:237-245

Naney MT (1983) Phase equilibria of rock-forming ferromagnesian silicates in granitic systems. Amer J Sci 283:993-1033

Nelson SA, Carmichael ISE (1979) Partial molar volumes of oxide components in silicate liquids. Contrib Mineral Petrol 71:117-124

O'Hara MJ, Mathews RE (1981) Geochemical evolution in an advancing, periodically replenished, periodically tapped, continuously fractionated magma chamber. J Geol Soc London 138:237-277

Philpotts JA, Schnetzler CC (1970) Phenocryst-matrix partition coefficients for K, Rb, Sr and Ba, with applications to anorthosite and basalt genesis. Geochim Cosmochim Acta 34:307-322

Richard P, Allegre CJ (1980) Neodymium and strontium isotope study of ophiolite and orogenic lherzolite petrogenesis. Earth Planet Sci Lett 47:65-74

Sparks RSJ, Marshall LA (1986) Thermal and mechanical constraints on mixing between mafic and silicic magmas. J Volcanol Geotherm Res 29:99-124

Spera FJ (1984) Some numerical experiments on the withdrawal of magma from crustal reservoirs J Geophys Res 89:8222-8236

Spera FJ, Yuen DA, Clark S, Hong HJ (1986) Double-diffusive convection in magma chambers: single or multiple layers? Geophys Res Lett 13:153-156

Spera FJ, Yuen DA, Kemp DV (1984) Mass transfer rates along vertical walls in magma chambers and marginal upwellings. Nature 310:764-767

Steele IM, Lindstrom DJ (1981) Ni partitioning between diopside and silicate melt: A redetermination by ion microprobe and recognition of an experimental problem. Geochim Cosmichim Acta 45:2177-2183

Taggart JE, JR, Lichte, FE and Wahlberg JS (1981) Methods of analysis of samples using X-ray fluorescence and induction-coupled plasma spectroscopy. U.S. Geol. Survey Prof. Paper 1250, 683-687

Taylor HP (1980) The effects of assimilating country rock by magmas on $^{18}O/^{16}O$ and $^{87}Sr/^{86}Sr$ systematics of igneous rocks. Earth Planet Sci Lett 47: 243-254

Yoder HS, Jr. (1973) Contemporaneous basaltic and rhyolitic magmas. Amer Mineral 58:153-171

Zindler A (1980) Geochemical processes in the earth's mantle and the nature of crust-mantle interactions: evidence from studies of Nd and Sr isotope ratios in mantle-derived igneous rocks and lherzolite nodules. Ph.D. dissertation, Mass. Inst. of Tech. 263 p.

Figure 1-1. Map of Giant Crater-Chimney Crater, Double Hole and Horse Cave-Water Cave lava flows. Inset shows location of flows relative to Tulelake, CA and the Oregon-California border. Dots show sample locations. Numbers identify age-chemical groups.

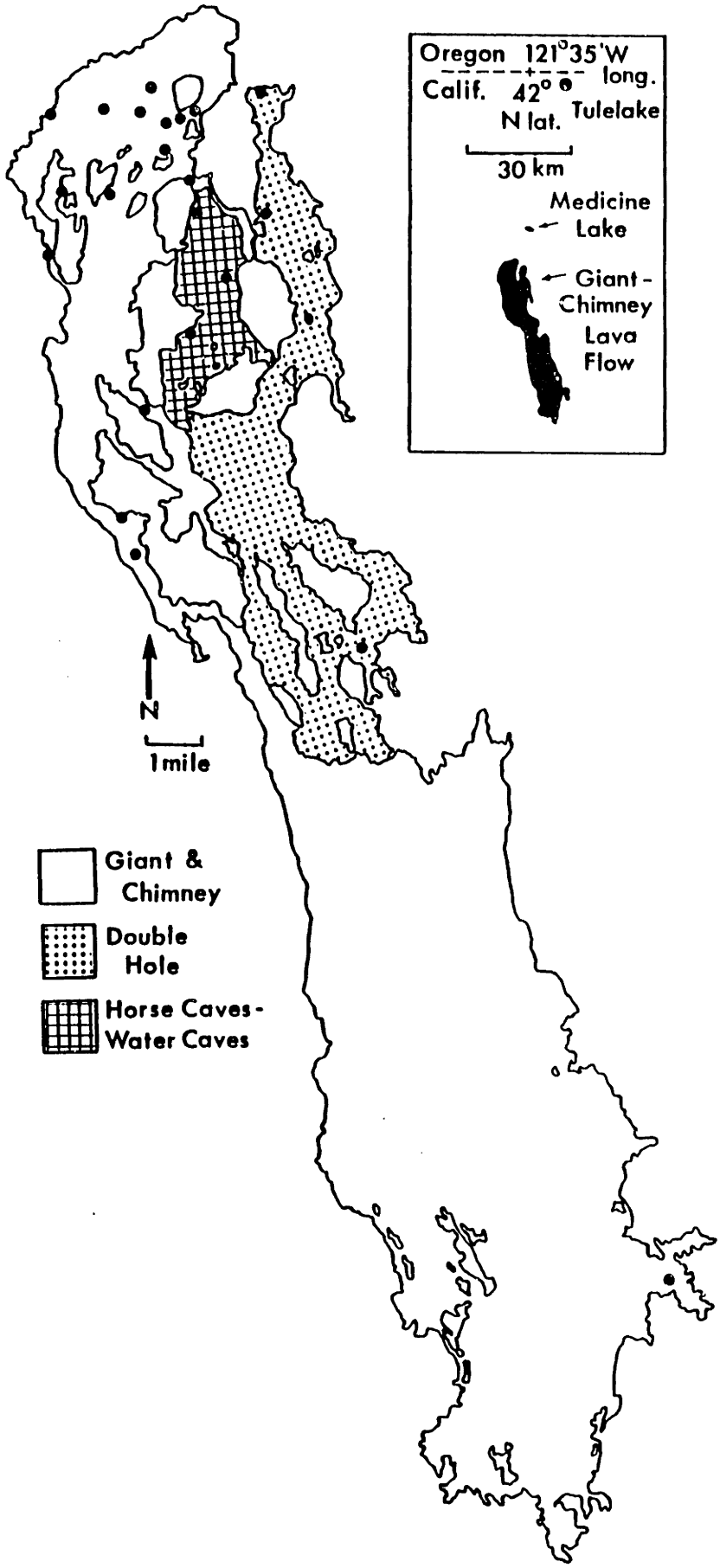
Oregon 121°35'W long.
Calif. 42° N lat.
Tulelake
30 km
Medicine Lake
Giant - Chimney Lava Flow
N
1 mile
Giant & Chimney
Double Hole
Horse Caves - Water Caves

Figure 1-2. Map of Giant Crater-Chimney Crater area. Flow units are numbered according to stratigraphic age. Squares show sample locations. Giant Crater is located directly south of the arrow in the circular patch of Group 5 lava. Chimney Crater is located directly west of the arrow in Group 1 lava.

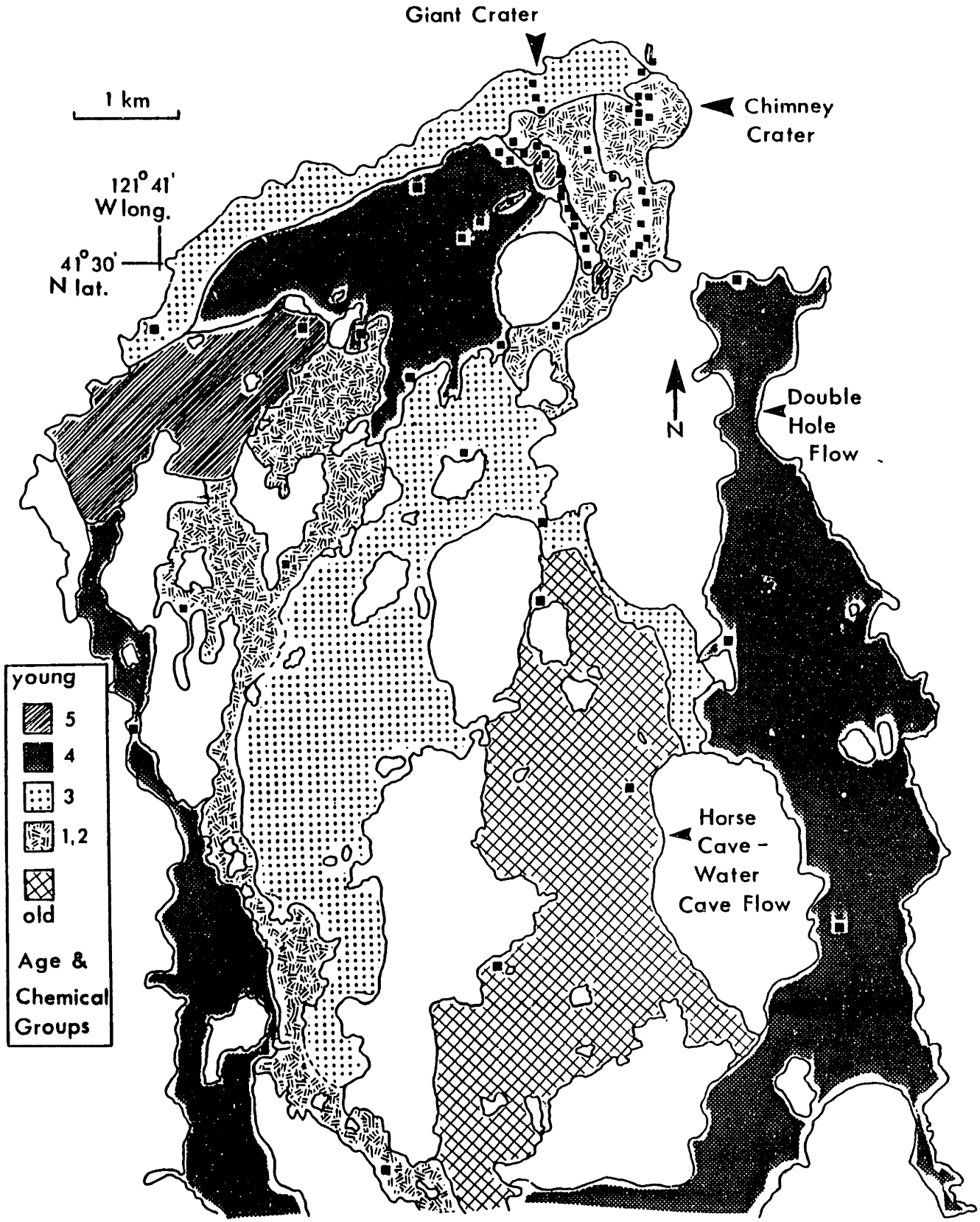
Giant Crater
1 km
Chimney Crater
121°41' W long.
41°30' N lat.
N
Double Hole Flow
Horse Cave - Water Cave Flow
young
5
4
3
1,2
old
Age & Chemical Groups

Figure 1-3. Variation diagrams (wt.%) of major elements vs. MgO for the Giant Crater-Chimney Crater lava flow. Numbers 1 through 5 in the SiO_2-MgO diagram refer to the stratigraphic units in Figs. 1-1 and 1-2.

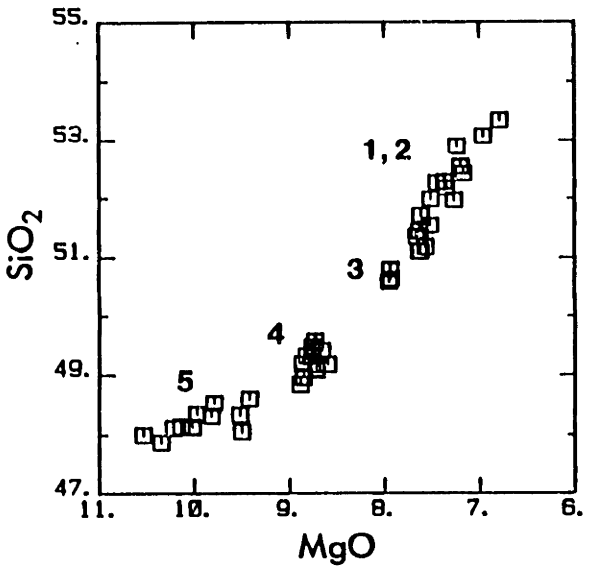
55.
53.
51.
49.
47.
SiO2
1, 2
3
4
5
11.
10.
9.
8.
7.
6.
MgO

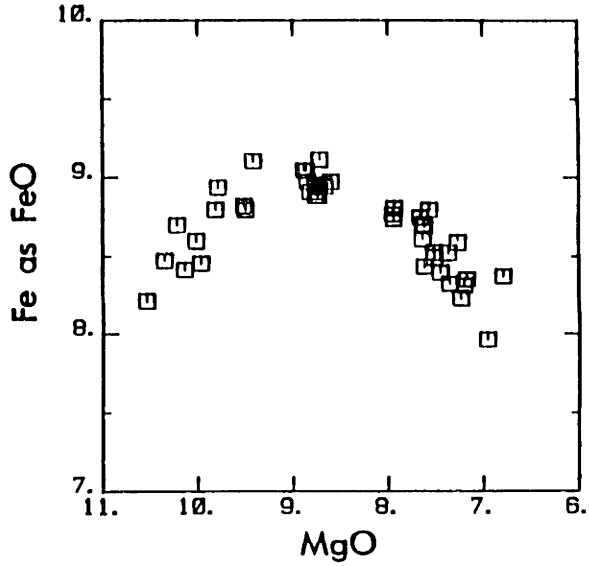
10.
9.
8.
7.
Fe as FeO
11.
10.
9.
8.
7.
6.
MgO

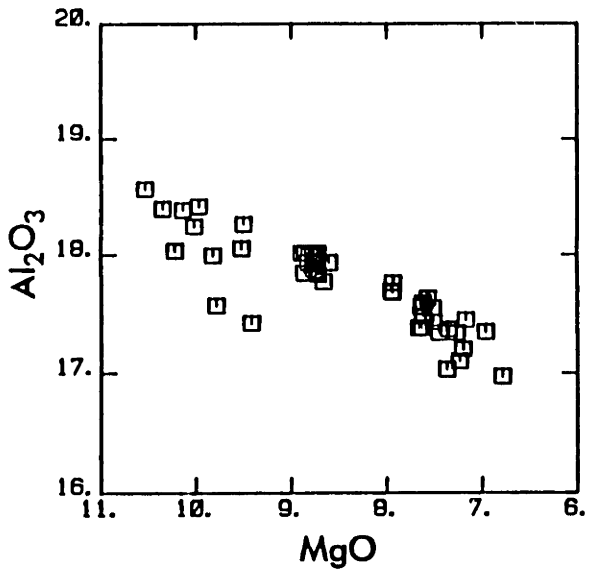
20.
19.
18.
17.
16.
Al2O3
11.
10.
9.
8.
7.
6.
MgO

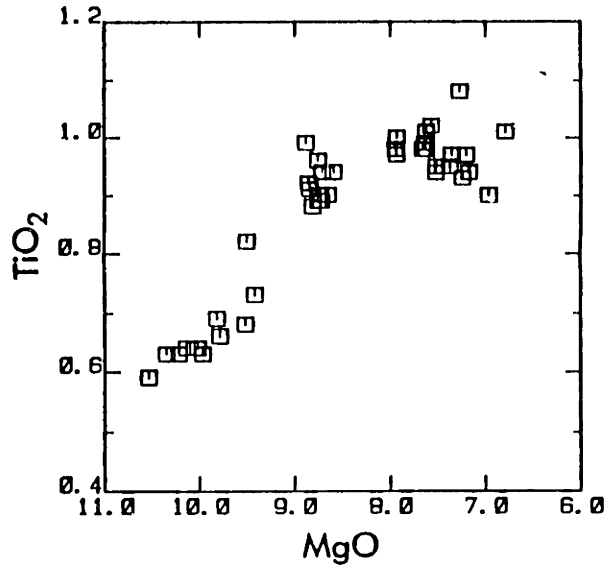
1.2
1.0
0.8
0.6
0.4
TiO2
11.0
10.0
9.0
8.0
7.0
6.0
MgO

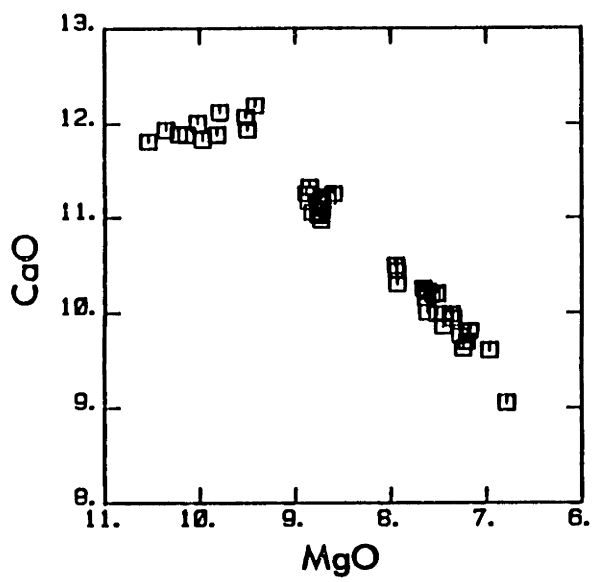
13.
12.
11.
10.
9.
8.
CaO
11.
10.
9.
8.
7.
6.
MgO

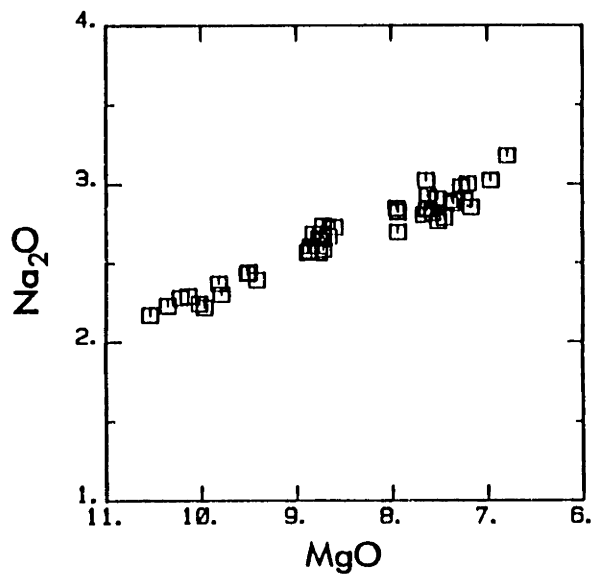
4.
3.
2.
1.
Na2O
11.
10.
9.
8.
7.
6.
MgO

Figure 1-4. Variation diagrams of minor and trace elements vs. MgO (wt.%). Numbers 1 through 5 in the K_2O-MgO diagram refer to the stratigraphic units in Figs. 1-1 and 1-2. K_2O is in units of wt.%. Reported analytic uncertainties are based on replicate analyses of BHVO-1 for the U. Mass. data; where 2σ values are not plotted, the uncertainties are smaller than the symbol size.

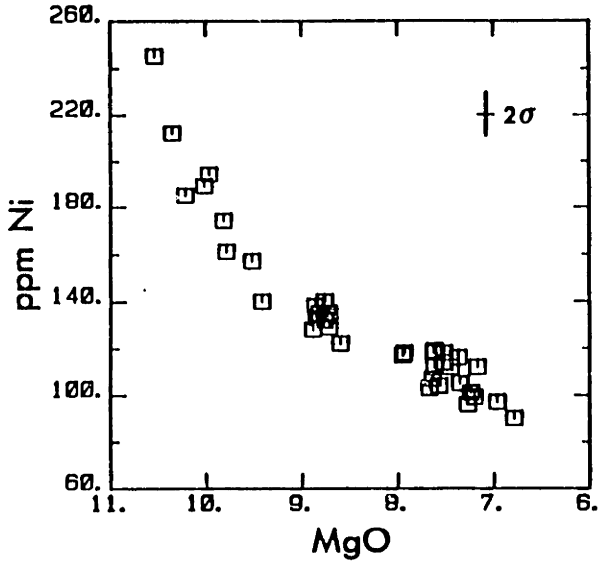
260.
220.
180.
140.
100.
60.
ppm Ni
2σ
11.
10.
9.
8.
7.
6.
MgO

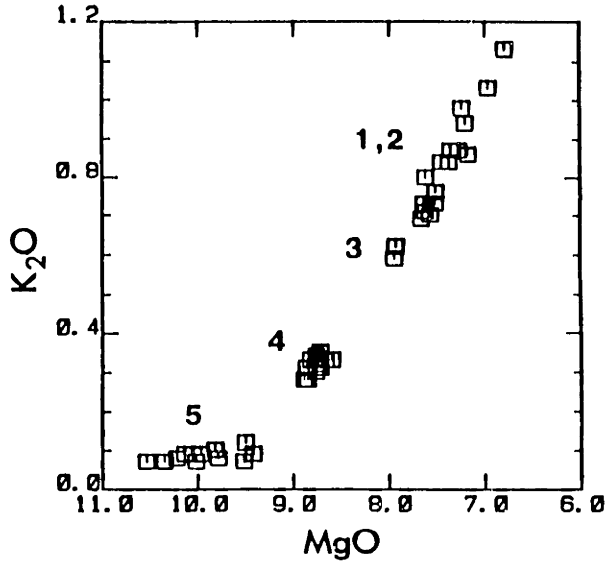
1.2
0.8
0.4
0.0
K2O
1,2
3
4
5
11.0
10.0
9.0
8.0
7.0
6.0
MgO

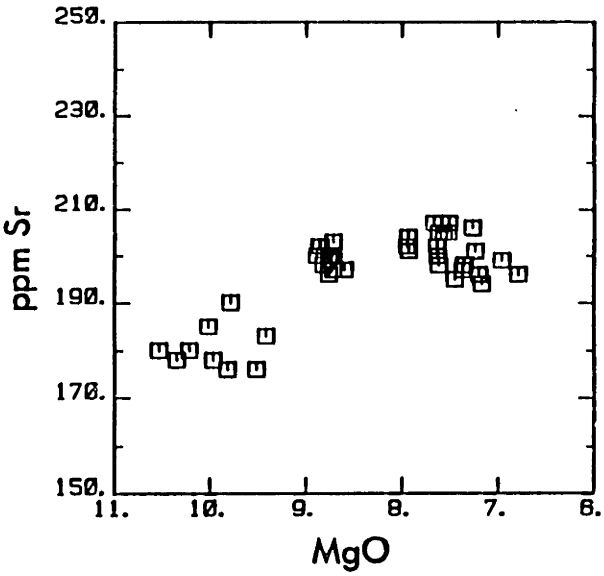
250.
230.
210.
190.
170.
150.
ppm Sr
11.
10.
9.
8.
7.
6.
MgO

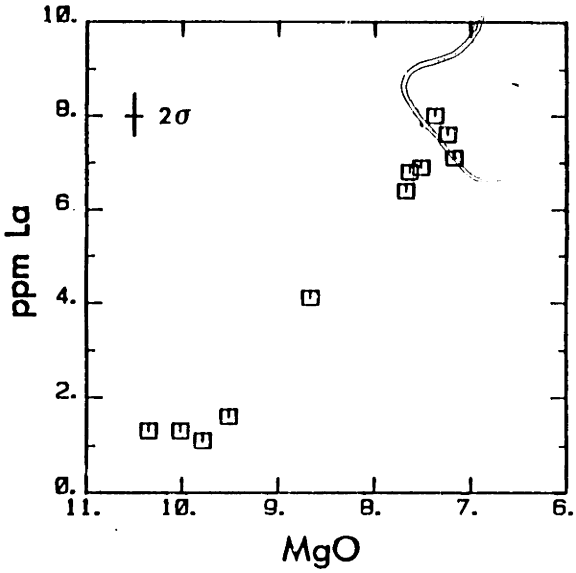
10.
8.
6.
4.
2.
0.
ppm La
2σ
11.
10.
9.
8.
7.
6.
MgO

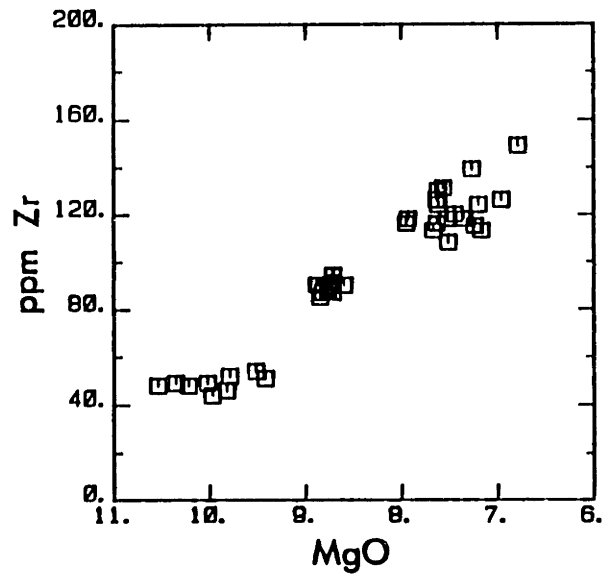
200.
160.
120.
80.
40.
0.
ppm Zr
11.
10.
9.
8.
7.
6.
MgO

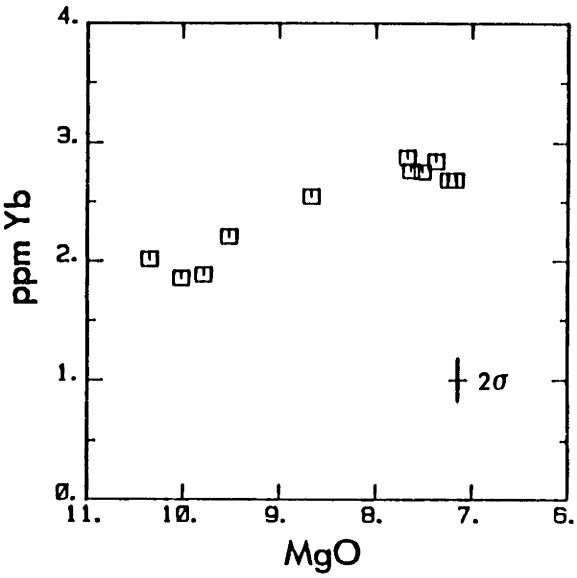
4.
3.
2.
1.
0.
ppm Yb
2σ
11.
10.
9.
8.
7.
6.
MgO

Figure 1-5. Petrographic characteristics of Giant Crater-Chimney Crater lavas and inclusions. (a) Back-scattered electron image (BEI) of olivine-plagioclase microphenocrysts in glassy chill margin of 85-16a.(b) BEI image of resorbed reacted Na-rich xenocryst core surrounded by reaction rim of pyroxene + plagioclase and Ca-rich overgrowth rim (83-5). (c) BEI image of resorbed quartz xenocryst surrounded by SiO_2-rich glass (83-5). (d) BEI image of Mg-rich olivine and Ca-rich plagioclase glomercryst in 83-5. (e) BEI image of resorbed and reacted Fe-rich olivine with Mg-rich overgrowth rim.

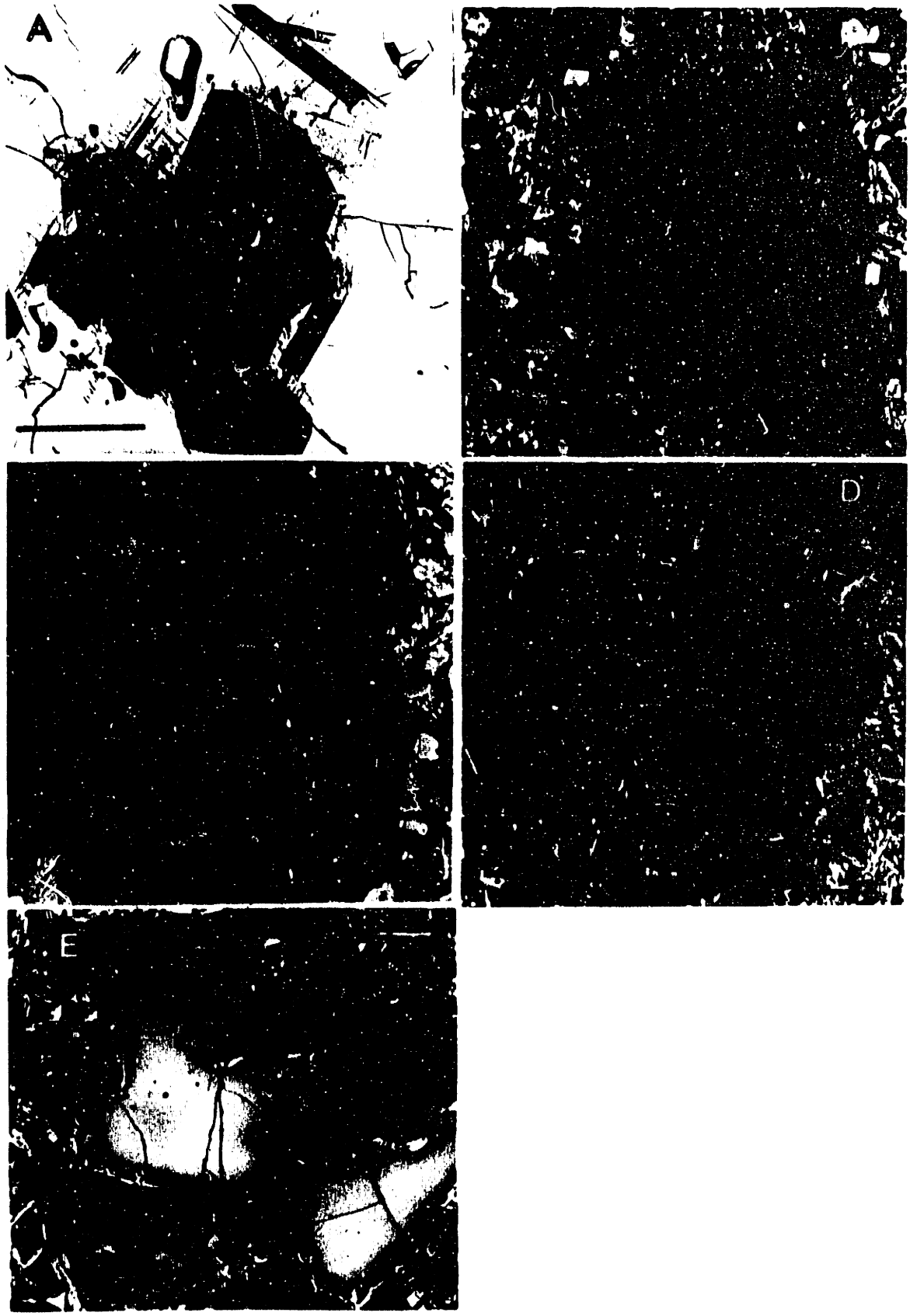
A
D
E

Figure 1-5. (f) BEI image of cumulate tractolite 1159M. (g) BEI image of olivine, plagioclase and clinopyroxene in 1160M gabbro. (h) BEI image of highly melted granitic inclusion showing relict plagioclase and quartz (85-32). Scale bars in all images are 100 microns

Figure 1-6. Plagioclase, olivine and clinopyroxene compositions from selected Giant Crater-Chimney Crater samples.

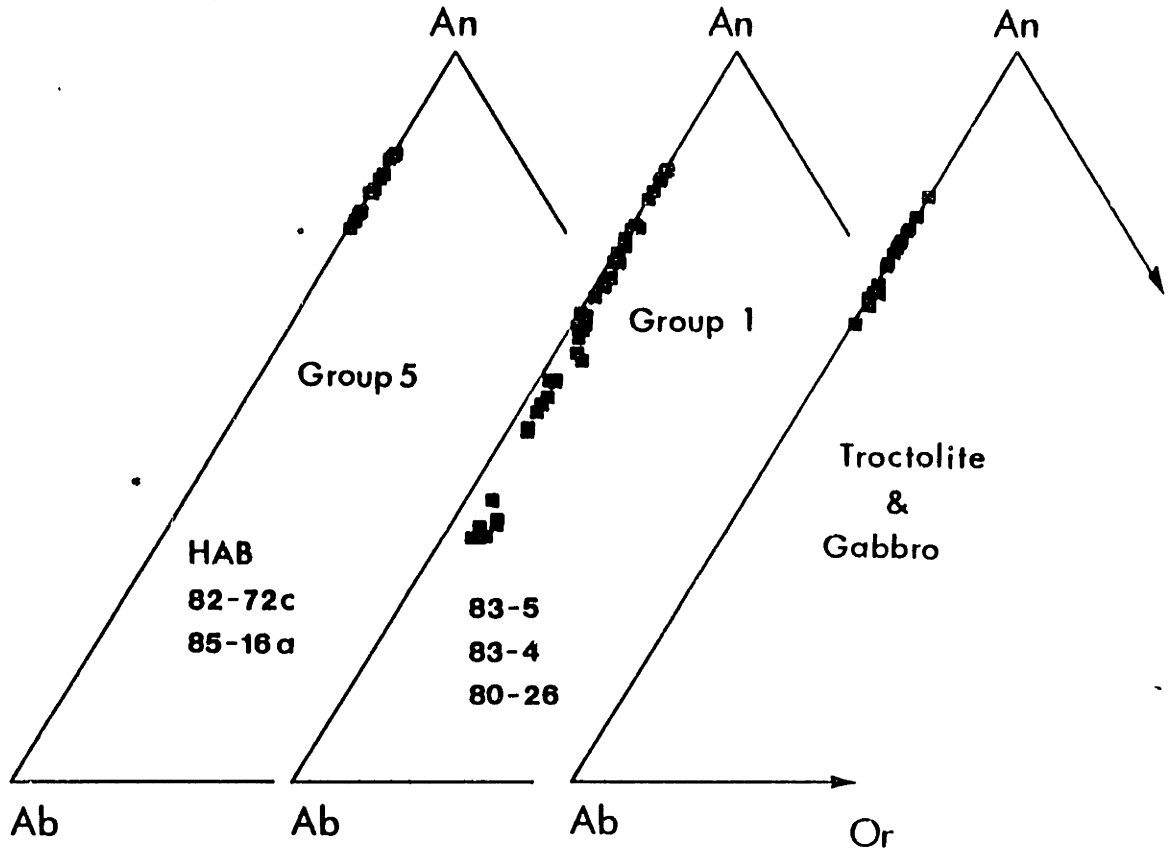
An
An
An
Group 5
Group 1
Troctolite
&
Gabbro
HAB
82-72c
85-16a
83-5
83-4
80-26
Ab
Ab
Ab
Or

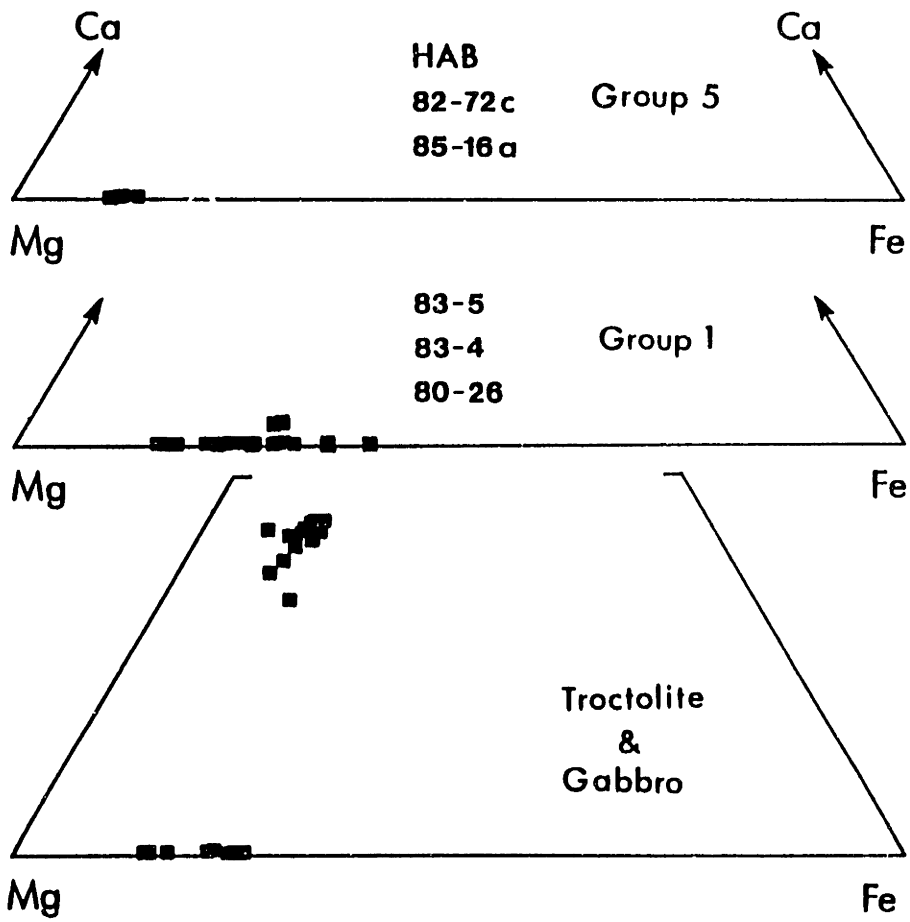
Ca
Ca
HAB
82-72c
85-16a
Group 5
Mg
Fe
83-5
83-4
80-26
Group 1
Mg
Fe
Troctolite
&
Gabbro
Mg
Fe

Figure 1-7. Compositions of the Giant Crater-Chimney Crater lavas projected onto the olivine-clinopyroxene-quartz and olivine-plagioclase-quartz pseudoternaries. Projected compositions of granitic inclusions collected from Medicine Lake Holocene rhyolites define the granitic inclusion field (Grove et al., 1988). The segregation vein marks the plotted position of 82-72a dikelet (Table 1-1). Solid line shows low pressure fractionation model to HAB residual liquids = ferrobasalt (Table 1-6). The plagioclase-saturated boundaries are from Walker et al. (1979) and Grove et al. (1982).

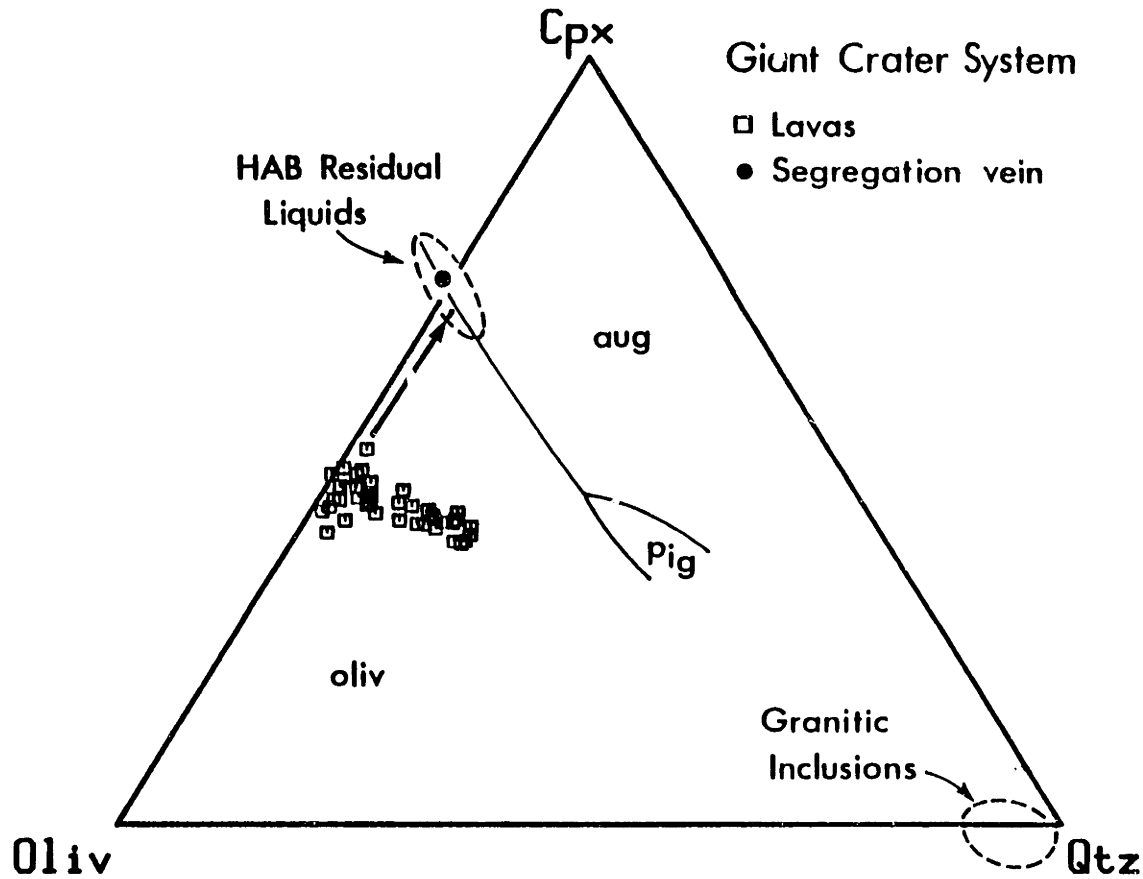
Cpx
Giant Crater System
Lavas
Segregation vein
HAB Residual Liquids
aug
pig
oliv
Granitic Inclusions
Oliv
Qtz

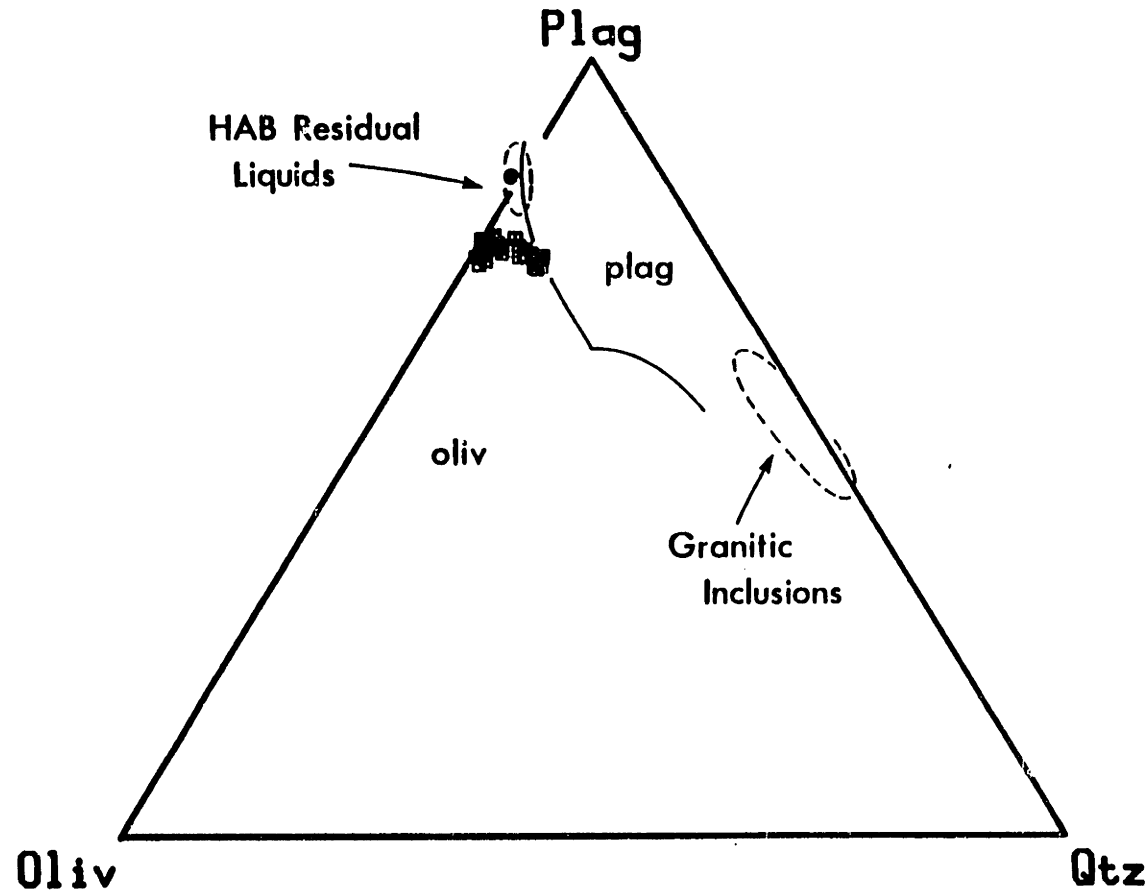
Plag
HAB Residual Liquids
plag
oliv
Granitic Inclusions
Oliv
Qtz

Figure 1-8.. A portion of the fractional crystallization calculation to ferrobasalt (Table 1-6) projected onto the Al_2O_3, FeO, K_2O and Ni vs. MgO variation diarams. Each plus sign represents one step in the fractionation model. Field outlines are age-chemical groups.

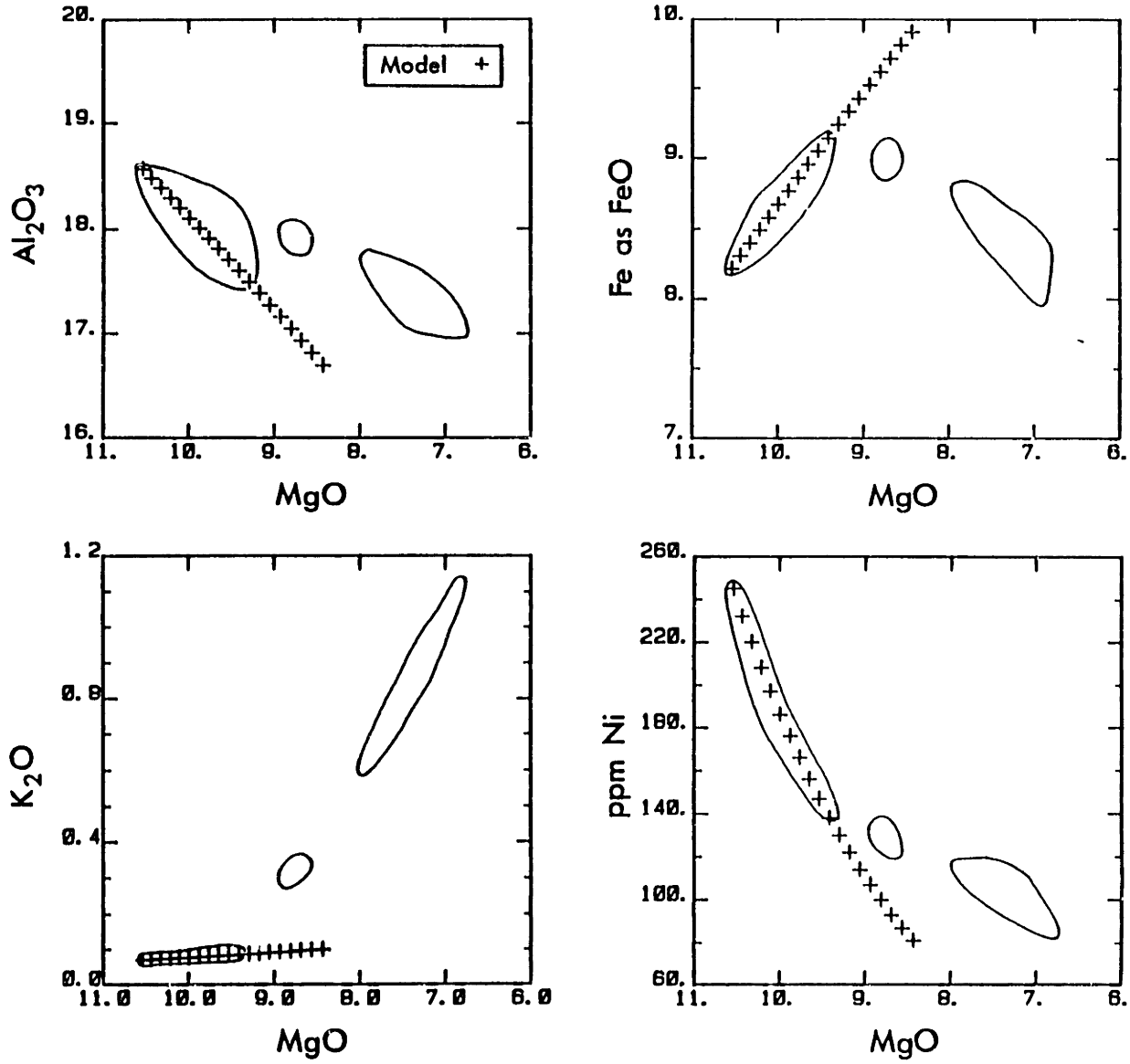
Model +
Al_2O_3
Fe as FeO
K_2O
ppm Ni
MgO
20.
19.
18.
17.
16.
10.
9.
8.
7.
1.2
0.8
0.4
0.0
260.
220.
180.
140.
100.
60.
11.
10.
9.
8.
7.
6.
11.0
10.0
9.0
8.0
7.0
6.0

Figure 1-9. Cartoon of a magma chamber showing a proposed sequence of magma replenishment, fractionation, replenishment and mixing that could produce compositional zoning observed in the Giant Crater-Chimney Crater lavas.

Magma chamber processes

A

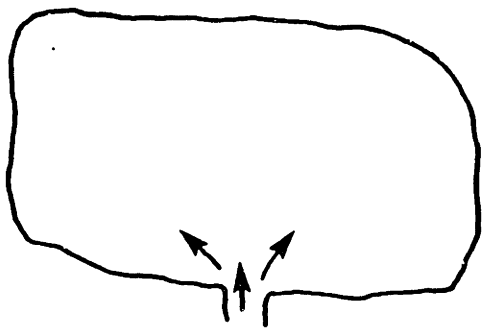

HAB intrudes

Crustal melting

B

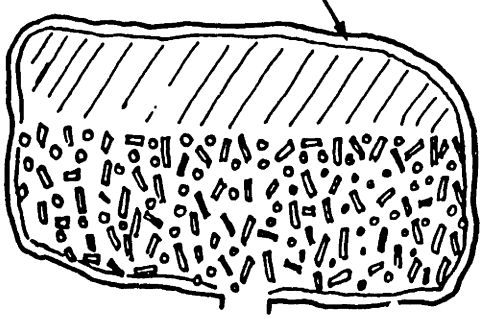

Cumulate formation

Differentiation to Ferrobasalt

C

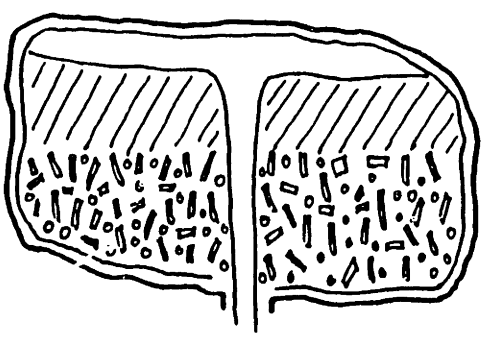

HAB reintrudes

Mixing to form Groups 1, 2 & 3

D

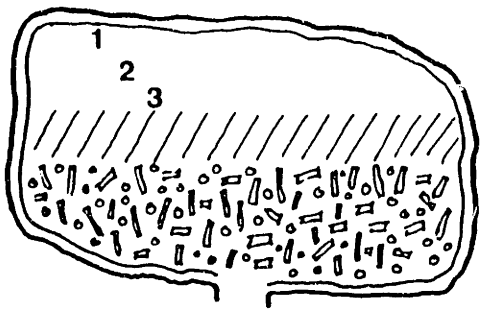

E

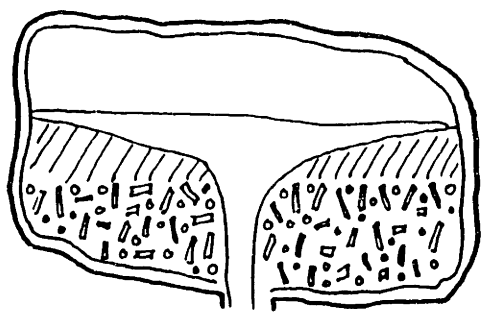

HAB reintrudes

Mixing to form Group 4

F

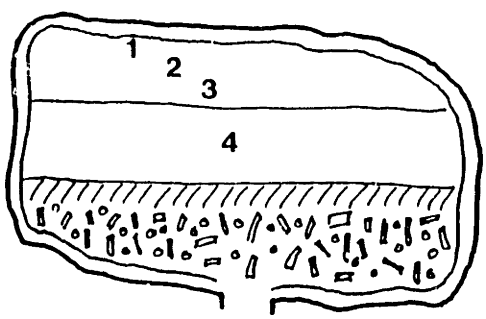

Figure 1-10. Calculated liquid densities for the Giant Crater-Chimney Crater lavas (squares) and the low pressure fractionation calculation to ferrobasalt (pluses) plotted against MgO. Calculation used Nelson and Carmichael (1979) and Mo et al. (1982) molar volumes for Fe_2O_3, and assumes anhydrous magma.

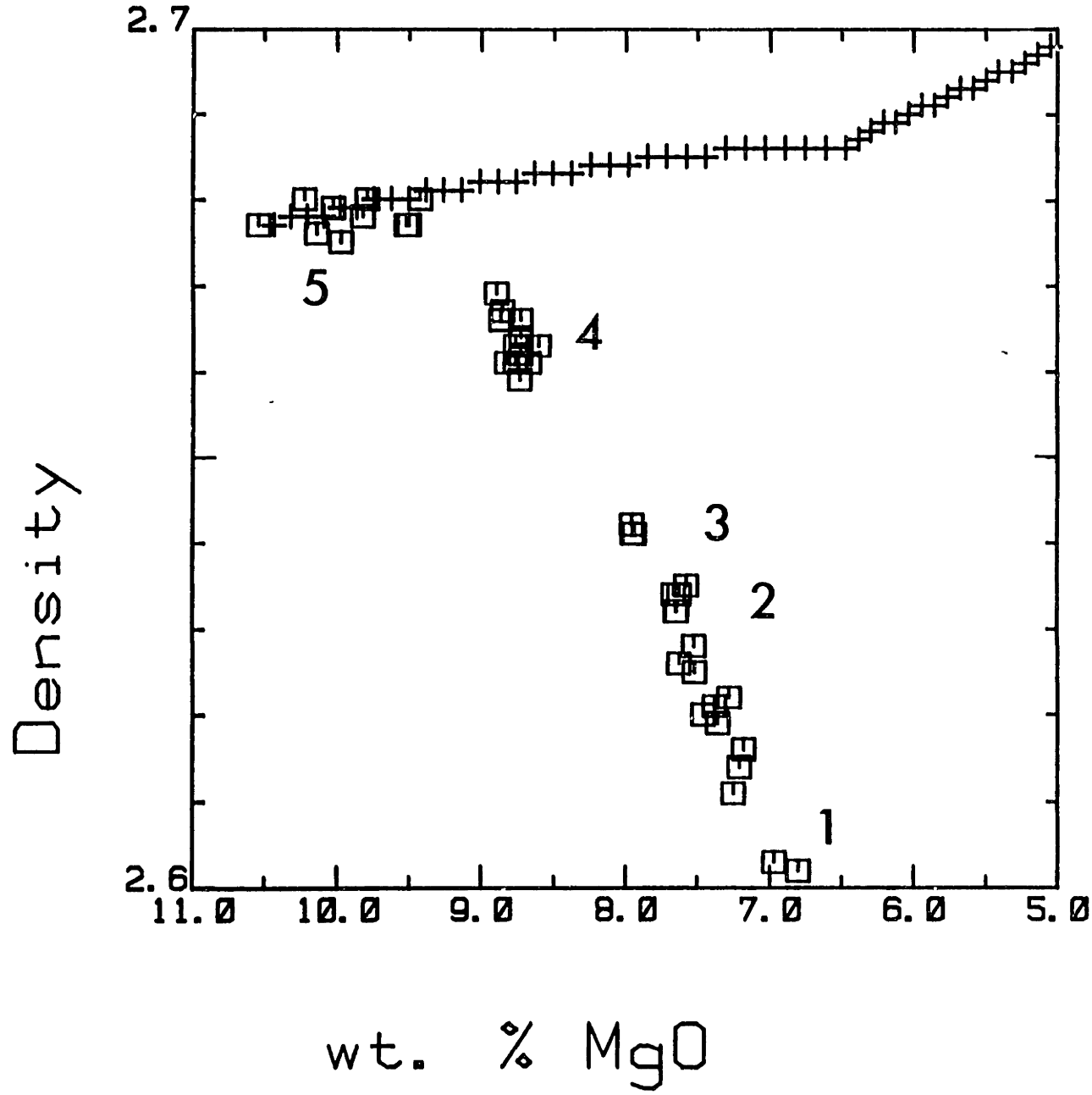
2.7
2.6
Density
11.0
10.0
9.0
8.0
7.0
6.0
5.0
wt. % MgO
1
2
3
4
5

Table 1-1. Major element analyses of lavas and inclusions from Giant Crater-Chimney Crater lava flow

Age[1]	Field #	Lab[2]	SiO_2	TiO_2	Al_2O_3	Fe_2O_3	MnO	MgO	CaO	Na_2O	K_2O	P_2O_5
1-1	83-1	(2)	52.62	0.89	16.92	8.73	0.15	6.75	9.50	3.18	1.02	0.14
1-2	83-2	(2)	52.98	1.03	16.70	9.20	0.16	6.54	9.06	3.16	1.07	0.16
1-3	83-3	(2)	50.66	1.01	17.17	9.63	0.16	7.32	10.07	2.95	0.69	0.14
1-4	83-4	(2)	52.03	0.96	16.75	9.10	0.16	6.96	9.57	3.15	0.93	0.17
1-5	83-5	(2)	51.15	0.93	17.14	9.36	0.16	7.30	10.10	3.06	0.72	0.12
1-6	1008M	(1)	51.0	0.99	17.3	9.63	0.16	7.60	10.3	2.82	0.71	0.16
1-7	83-7	(2)	51.72	0.96	16.94	9.13	0.17	7.12	9.83	3.02	0.86	0.16
1-8	83-9	(2)	51.91	0.94	16.95	9.22	0.15	7.23	9.77	2.93	0.83	0.15
1-9	879M	(1)	51.7	0.94	16.9	9.40	0.15	7.32	10.1	2.87	0.83	0.14
1-10	1002M	(1)	51.5	0.93	17.2	9.15	0.15	7.07	9.85	2.81	0.85	0.15
1-11	1006M	(1)	51.4	0.94	17.3	9.36	0.16	7.45	10.1	2.74	0.75	0.15
1-12	1007M	(1)	50.9	0.98	17.3	9.67	0.17	7.62	10.4	2.79	0.69	0.15
1-13	1009M	(1)	52.4	0.92	17.0	9.10	0.15	7.20	9.75	2.88	0.97	0.13
1-HC[4]	887M	(1)	49.50	0.98	17.90	9.21	0.15	8.62	10.30	2.89	0.62	0.16
1-HC	1017M	(1)	53.60	0.95	17.00	8.37	0.13	7.24	8.91	3.03	1.26	0.16
1-HC	1144M	(1)	52.70	0.59	17.00	8.48	0.14	7.53	9.18	3.00	1.14	0.15
1-2-GC	1249M	(1)	51.10	0.96	17.00	9.38	0.15	7.25	10.00	2.70	0.75	0.14
1-2-GC	1264M	(1)	51.60	0.92	16.70	9.23	0.15	7.02	9.81	2.62	0.85	0.12
1-2-GC	1276M	(1)	51.50	0.81	17.20	9.38	0.15	6.79	9.87	2.71	0.81	0.16
2-1	82-37	(2)	51.40	1.06	16.87	9.38	0.16	7.03	9.62	3.13	0.86	0.19
2-2	83-24	(2)	50.82	0.97	17.18	9.46	0.17	7.43	10.14	3.19	0.72	0.17
2-3	83-8	(2)	51.20	0.97	17.02	9.23	0.16	7.38	9.88	2.98	0.79	0.17
3-1	82-66	(2)	50.93	1.00	17.25	9.57	0.16	7.43	10.16	3.09	0.70	0.16
3-2	82-65	(2)	50.17	0.97	17.26	9.61	0.16	7.71	10.38	2.99	0.58	0.15
3-3	82-64	(2)	50.29	0.96	17.22	9.56	0.16	7.68	10.31	2.83	0.61	0.16
3-4	82-71	(2)	50.39	0.99	17.39	9.69	0.16	7.71	10.23	2.98	0.61	0.17
3-GC	328-M	(1)	51.10	0.99	17.40	9.71	0.16	7.56	10.20	2.87	0.74	0.14
3-GC	1278M	(1)	50.40	1.00	17.20	9.70	0.16	7.37	10.20	2.60	0.64	0.15
3-GC	1266M	(1)	50.20	0.97	17.20	9.61	0.13	7.58	10.40	2.64	0.59	0.13
3-GC	1256M	(1)	50.30	0.95	17.40	9.59	0.16	7.55	10.20	2.68	0.63	0.13
4-1	82-38	(2)	49.25	0.92	17.68	9.84	0.17	8.46	11.06	2.55	0.33	0.11
4-2	82-39	(2)	48.87	0.93	17.63	9.84	0.15	8.48	11.02	2.88	0.35	0.13
4-3	82-60	(2)	49.14	0.91	17.73	9.78	0.17	8.45	11.08	2.64	0.29	0.10
4-4	82-36	(2)	49.17	0.91	17.54	9.74	0.17	8.40	10.97	2.66	0.32	0.11
4-5	881M	(1)	49.0	0.90	17.7	9.90	0.16	8.63	11.4	2.65	0.33	0.11
4-6	82-54	(2)	48.62	0.93	17.53	9.81	0.19	8.45	11.09	2.79	0.32	0.15
4-7	82-55	(2)	48.93	0.90	17.63	9.77	0.17	8.49	11.05	2.66	0.32	0.10
4-8	82-56	(2)	48.30	0.98	17.52	9.89	0.19	8.59	11.10	2.69	0.28	0.15
4-9	82-59	(2)	48.93	0.95	17.45	9.77	0.18	8.50	11.05	2.74	0.33	0.15
4-10	82-58	(2)	48.62	0.92	17.44	9.81	0.16	8.31	11.09	2.85	0.33	0.10
4-11	82-57	(2)	48.43	0.90	17.52	9.81	0.15	8.56	11.17	2.73	0.28	0.11
4-12	82-61	(2)	48.60	0.93	17.33	9.96	0.17	8.43	11.06	2.71	0.31	0.14
4-13	82-62	(2)	48.89	0.94	17.57	9.94	0.17	8.54	11.18	2.56	0.30	0.11
4-DH	1010M	(1)	49.10	0.96	17.70	10.30	0.17	8.79	11.50	2.72	0.30	0.11
4-DH	1016M	(1)	49.20	0.94	17.60	10.10	0.16	8.50	11.30	2.69	0.34	0.11
4-DH	1232M	(1)	49.30	0.96	17.50	9.87	0.16	8.00	10.80	2.54	0.40	0.12
4-DH	1233M	(1)	49.00	0.93	17.50	9.97	0.16	8.29	11.10	2.53	0.32	0.11

4-GC	1018M	(1)	49.20	0.93	17.60	10.00	0.16	8.49	11.30	2.65	0.34	0.11
4-GC	1277M	(1)	48.50	0.91	17.70	9.90	0.16	8.29	11.30	2.58	0.27	0.11
4-GC	1257M	(1)	48.20	0.91	17.40	10.20	0.17	8.87	11.20	2.44	0.20	0.10
4-GC	1253M	(1)	48.10	0.99	17.50	10.10	0.16	8.76	11.20	2.42	0.24	0.10
4-GC	1259M	(1)	48.30	0.89	17.60	10.10	0.16	8.83	11.10	2.43	0.24	0.11
4-GC	1252M	(1)	48.60	0.90	17.80	9.84	0.16	8.26	11.10	2.47	0.29	0.12
5-1	883M	(1)	47.7	0.67	17.9	9.71	0.16	9.44	12.2	2.41	0.07	0.06
5-2	904M	(1)	48.1	0.66	17.5	9.89	0.16	9.75	12.3	2.29	0.08	0.03
5-3	1004M	(1)	47.8	0.64	18.2	9.53	0.16	10.0	12.2	2.24	0.07	0.06
5-4	79-35g	(1)	47.8	0.65	18.7	9.51	0.15	9.95	12.1	2.26	0.07	0.03
5-5	79-35g	(2)	47.77	0.65	18.07	9.23	0.16	9.76	11.89	2.27	0.09	0.05
5-6	82-72a 1-2	(2)	47.96	0.70	17.69	9.66	0.17	9.46	11.89	2.35	0.10	0.05
5-7	82-72a 1	(1)	47.8	0.63	18.0	9.64	0.16	10.2	12.1	2.28	0.08	0.06
5-8	82-72a 2-3	(1)	48.3	0.73	17.4	10.1	0.17	9.41	12.4	2.39	0.09	0.06
5-9	82-72a dikelet	(1)	49.9	2.24	13.6	14.5	0.26	5.13	10.1	3.97	0.32	0.20
5-10	82-72c	(2)	47.91	0.64	18.08	9.27	0.16	9.58	11.82	2.20	0.09	0.05
5-10	82-72c	(1)	48.0	0.66	17.9	9.64	0.16	10.0	12.1	2.36	0.08	0.06
5-11	82-72f	(1)	47.6	0.59	18.5	9.09	0.15	10.5	12.0	2.16	0.07	0.06
5-12	880M	(1)	47.4	0.63	18.3	9.36	0.15	10.3	12.1	2.22	0.07	0.05
5-GC	1020M	(1)	47.9	0.82	18.2	9.73	0.16	9.47	11.9	2.43	0.12	0.08
5-GC	1261M	(1)	47.50	0.62	18.30	9.24	0.15	9.36	11.6	2.09	0.07	0.05
Inclusions												
	1159M-a	(1)	46.10	0.18	21.90	5.95	0.08	12.00	11.4	1.73	0.09	-
	1160M	(1)	49.30	0.46	19.30	7.74	0.12	9.43	10.5	2.36	0.53	0.08
BCR-1[3]		(2)	54.40	2.24	13.46	13.31	0.19	3.39	6.94	3.49	1.69	0.41
BHVO-1		(2)	50.04	2.76	13.76	12.21	0.17	7.11	11.45	2.30	0.52	0.27

[1]Location of sample on Fig. 1 and relative age. Oldest = 1 and youngest = 5.

[2]Analyses were obtained by X-ray fluorescence. Those denoted by (1) are from the U.S. Geological Survey at Lakewood, Colorado. Analysts: J. Taggart, Ardith J. Bartel, K. Stewart. Those denoted by (2) are from University of Massachusetts, Amherst, MA. Analysts: M.B. Baker, D. Termey.

[3]Averages of 23 replicate analyses.

[4]See Appendix A for description and location of samples.

Dashes in element columns indicate that element was below detectability limit or was not analyzed.

Table 1-2. Trace element analyses of lavas from Giant Crater-Chimney Crater lava flow

Age	Field #	Y	Sr	Rb	Pb	Ga	Nb	Zr	Ni	Cr	V	Ce	Ba
1-1	83-1	25.9	199	31.5	7	17.8	4.5	126	97	133	174	23	234
1-2	83-2	28.6	196	30.7	4	15.9	6.1	149	85	120	201	27	251
1-3	83-3	27.2	205	18.6	6	16.4	3.9	131	104	137	182	19	178
1-4	83-4	25.9	196	28.0	6	16.1	4.1	124	99	136	181	20	215
1-5	83-5	25.1	205	20.2	5	17.3	4.4	118	112	150	194	18	192
1-7	83-7	25.3	198	24.9	4	15.9	4.0	118	105	141	182	21	192
1-8	83-9	25.3	195	24.4	5	15.9	3.9	120	107	142	188	19	205
2-1	82-37	28.3	206	24.3	8	16.9	5.5	139	96	132	193	16	211
2-2	83-24	26.4	202	19.2	5	15.2	4.4	126	107	144	184	19	170
2-3	83-8	26.4	198	22.3	6	15.6	4.7	124	114	148	190	22	186
3-1	82-66	26.7	205	19.4	5	16.0	4.6	130	106	145	192	19	179
3-2	82-65	26.2	202	15.3	5	16.8	4.0	116	117	153	194	18	148
3-3	82-64	26.5	204	16.6	6	16.5	-	-	-	-	-	-	-
3-4	82-71	26.2	201	16.6	5	17.1	4.1	118	118	153	188	22	152
4-1	82-38	22.7	196	7.6	5	16.0	2.7	88	134	175	197	9	83
4-2	82-39	23.7	200	8.5	-	15.0	3.4	94	130	173	200	11	99
4-3	82-60	23.3	200	6.9	3	15.7	2.7	89	126	180	201	10	79
4-4	82-36	22.9	200	8.0	4	16.4	3.0	90	129	180	204	11	98
4-6	82-54	-	197	-	-	-	2.9	87	135	172	189	12	81
4-7	82-55	-	198	-	-	-	2.4	87	135	169	187	6	99
4-8	82-56	-	200	-	-	-	2.7	90	128	170	184	6	88
4-9	82-59	-	199	-	-	-	3.2	88	132	172	189	9	85
4-10	82-58	-	197	-	-	-	3.1	90	122	166	188	12	77
4-11	82-57	23.5	202	6.1	3	16.5	2.6	85	133	173	189	11	78
4-12	82-61	23.9	203	6.9	4	16.8	2.8	91	129	170	195	11	81
4-13	82-62	24.2	202	6.4	5	15.7	3.1	90	132	175	201	11	86
5-4	79-35d	-	182	-	-	-	1.3	48	157	179	185	6	43
5-6	82-72a 1-2	-	176	-	-	-	1.8	46	168	198	191	7	31
5-10	82-72c	-	178	-	-	-	1.3	44	187	205	184	6	24

Trace elements obtained by X-ray fluorescence at Univ. of Massachusetts, Amherst, Ma. Analysts: M.B. Baker, D. Tormey.
See Table 1 for description of abbreviations.

Table 1-3. Trace and rare earth element analyses of lavas from Giant Crater-Chimney lava flow

Age	Field #	Co	Cr	Cs	Hf	Th	Sc	La	Ce	Nd	Sm	Eu	Gd	Yb	Lu	Ba	Rb	Sr	Zr	Y	Ni
1-6	1008M	36.8	133	1.15	2.78	2.39	35.0	6.8	19.2	12.3	2.97	1.03	3.75	2.77	0.41	188	14	200	116	24	118
1-9	879M	40.3	142	1.52	2.81	3.25	34.5	8.0	16.2	10.9	3.21	0.94	4.1	2.85	0.46	-	21	197	118	25	116
1-10	1002M	33.3	130	1.35	2.69	2.86	31.9	7.1	18.0	9.8	2.68	0.96	3.47	2.69	-	204	19	194	113	25	112
1-11	1006M	36.4	130	1.31	2.63	2.49	33.7	6.9	17.8	10.9	2.80	1.00	3.73	2.76	-	161	16	207	108	23	114
1-12	1007M	36.5	135	1.09	2.71	2.25	34.7	6.4	18.0	10.7	2.95	1.04	3.75	2.88	0.41	175	16	207	113	26	103
1-13	1009M	34.0	120	1.73	2.67	3.26	32.1	7.6	20.0	11.5	2.85	0.97	3.50	2.69	0.41	219	25	201	115	24	101
4-5	881M	45.5	170	0.53	1.96	0.85	36.8	4.1	9.8	7.0	2.60	0.85	2.80	2.55	0.39	-	-	-	-	-	-
5-1	883M	50.6	209	-	1.07	-	38.7	1.6	4.4	6.0	1.68	0.66	-	2.21	0.35	-	2	176	54	19	157
5-2	904M	44.7	200	0.17	1.02	0.16	40.0	1.1	4.1	4.0	1.45	0.66	2.04	1.89	-	28	-	190	52	21	161
5-3	1004M	44.4	190	0.45	0.95	0.16	36.2	1.3	4.9	4.2	1.42	0.61	2.08	1.86	-	38	-	185	49	17	189
5-8	82-72a 1	-	-	-	-	-	-	-	-	-	-	-	-	-	-	29	1	180	48	17	185
5-9	82-72a 2-3	-	-	-	-	-	-	-	-	-	-	-	-	-	-	55	-	183	51	18	140
5-1	82-72f	-	-	-	-	-	-	-	-	-	-	-	-	-	-	29	-	180	48	17	245
5-2	880M	49.9	199	0	1.04	0	34.6	1.3	4.2	4.4	1.52	0.58	1.2	2.02	0.33	-	2	178	49	16	212

Co, Cr, Cs, Hf, Th, Sc and REE elements analyzed by instrumental neutron activation analysis at the U.S. Geological Survey, Reston, VA. Ba, Rb, Sr, Zr, Y and Ni analyzed by energy dispersive X-ray fluorescence at the U.S. Geological Survey, Menlo Park, CA. Analysts: J. Budahan, R. Knight, D. Viti, P. Bruggman, J. Lindsay, T. Frost, D. McKown. See Table 1 for discussion of abbreviations.

Table 1-4. Representative analyses of minerals and glasses in Giant Crater-Chimney Crater lavas and inclusions

	Group 1 lavas								Group 4 lavas			Group 5 lavas			
	olivine				plagioclase			augite	oliv	plag		olivine		plagioclase	
	1	2	3	4	5	6	7	8	9	10	11	12	13	14	15
SiO_2	36.3	38.6	40.1	37.1	47.5	50.9	54.8	51.3	39.6	49.3	47.2	40.6	41.0	47.0	47.0
TiO_2	0.07	0.04	0.04	0.09	-	-	-	0.82	0.02	-	-	0.0	0.02	-	-
Al_2O_3	0.04	0.05	0.06	0.09	33.4	30.6	27.0	3.38	0.07	31.9	32.9	0.09	0.09	33.0	32.7
FeO	33.8	19.5	13.3	29.8	0.60	0.88	0.56	7.84	13.5	0.30	0.20	11.5	10.8	0.46	0.48
MgO	29.6	41.3	46.2	32.4	0.13	0.08	0.08	16.3	46.4	0.23	0.19	47.4	49.0	0.21	0.33
MnO	0.53	0.32	0.20	0.45	-	-	-	0.19	0.14	-	-	0.14	0.19	-	-
CaO	0.30	0.31	0.27	0.32	16.6	13.7	9.91	20.0	0.30	15.5	16.8	0.29	0.33	16.1	17.4
K_2O	-	-	-	-	0.03	0.21	0.40	-	-	0.04	0.02	-	-	0.02	0.03
Na_2O	-	-	-	-	1.85	3.36	5.60	0.17	-	2.71	1.96	-	-	1.54	1.59
sum	100.64	100.11	100.17	100.25	100.11	99.73	98.35	100.00	100.03	99.98	99.27	100.02	101.43	98.33	99.53

Inclusions								
olivine				plagioclase		augite	
16	17	18	19	20	21	22	23
40.4	39.2	38.3	40.2	48.4	49.8	50.6	52.2
0.04	0.05	0.0	0.0	-	-	0.81	0.28
0.0	0.04	0.0	0.0	32.5	30.9	3.74	3.21
14.2	20.7	23.1	14.7	0.46	0.46	7.04	4.63
46.0	40.1	38.0	44.5	0.17	0.20	15.6	17.6
0.19	0.35	0.44	0.25	-	-	0.23	0.12
0.28	0.49	0.24	0.38	16.2	14.8	20.6	21.0
-	-	-	-	0.01	0.07	-	-
-	-	-	-	2.22	3.08	0.33	0.18
101.11	100.93	100.08	100.03	99.96	99.31	98.95	99.22

1, core iron-rich, reverse-zoned olivine, 83-4
2, groundmass olivine, 83-4
3, olivine microphenocryst 83-5
4, olivine intergrown with plagioclase (#6) and augite (#8), 83-1.
5, plagioclase phenocryst, 83-5
6, plagioclase intergrown with olivine (#4) and augite (#8) in glomerocryst, 83-1
7, sodic plagioclase xenocryst core, 83-4
8, augite intergrown with olivine (#4) and plagioclase (#6), 83-1
9, olivine microphenocryst, 82-39
10, plagioclase microphenocryst, 82-39
11, plagioclase xenocryst, 82-59
12, olivine microphenocryst in glassy chill margin, 85-16a (Fig. 3a)
13, olivine microphenocryst in chilled margin, 82-72c
14, plagioclase microphenocryst in glassy chill margin, 85-16a (Fig. 3a)
15, plagioclase microphenocryst in chilled margin, 82-72c
16, core of olivine in cumulate troctolite 1159M (Fig. 3f)
17, rim of olivine in cumulate 1159M
18, core of reverse-zoned olivine in 1160M cumulate gabbro (Fig. 3g)
19, rim of reverse-zoned olivine in 1160M
20, core of plagioclase in 1159M cumulate troctolite
21, core of plagioclase in 1160M cumulate gabbro (Fig. 3g)
22, core of augite in 1160M cumulate gabbro
23, reaction overgrowth rim on augite, 1160M

Table 1-5. Isotopic data for selected samples from Giant Crater-Chimney Crater lava flow.

Isotopic Compositions

Age[1]	Field #	87/86 Sr	143/144 Nd	ppm Sr	ppm Nd
1-4	83-4	0.70345(3)	0.512904(25)	198	11.2
3-3	82-64	0.70335(3)	0.512872(16)	203	10.6
4-6	82-55	0.70343(3)	0.512982(18)	203	7.8
5-4	79-35d	0.70340(3)		179	
5-7	82-72a	0.70334(3)		175	
1	85-17[2]	0.70341(3)		94	
1	85-32	0.70376(3)	0.512857(15)	115	

[1]Sample designation from Table 1 and relative age. Oldest = 1 and youngest - 5. See Appendix A for sample location and description of samples.

[2]85-17 and 85-32 are highly melted granitic inclusions collected from the talus deposit in Chimney Crater.

Table 1-6. Fractionation AFC and mixing models for Giant-Crater-Chimney Crater Lavas

1. Fractionation Model. HAB to ferrobasalt

	SiO2	TiO_2	Al_2O_3	FeO	MgO	CaO	Na_2O	K_2O	P_2O_5	oliv/Fo	plag/An	aug/En	F
HAB parent	47.99	0.59	18.56	8.21	10.54	11.81	2.17	0.07	0.05	0.33/89	0.67/80		1.0
	50.16	1.13	15.25	11.33	6.47	12.77	2.68	0.13	0.10	0.33/78	0.67/78		0.52
	50.17	1.14	15.21	11.46	6.38	12.70	2.70	0.14	0.10	0.09/78	0.49/77	0.41/48	0.51
MFB	50.44	1.43	14.51	13.55	5.04	11.59	3.12	0.18	0.13	0.09/70	0.49/73	0.41/44	0.38

2. Combined assimilation and fractionation models.
Assimilant is average granitic inclusion composition of Grove et al. (1988)

HAB parent (as above)

R = 1.0	54.65	0.65	16.72	7.62	6.91	9.66	2.67	1.05	0.07	0.33/85	0.67/73	0.78
R = 1.5	54.22	0.60	17.05	7.36	7.43	9.64	2.62	1.00	0.07	0.33/86	0.67/73	0.85
R = 2.0	54.93	0.58	17.01	7.07	7.26	9.32	2.66	1.12	0.06	0.33/87	0.67/73	0.87
Group 1	53.06	0.90	17.35	7.96	6.96	9.60	3.02	1.03	0.12			

3. Multicomponent magma mixing models estimated from materials balance calculations

mixed magma = component 1+ component 2+ component 3+									ΣR^2	wt. % components in model		
Group 4= HAB+AGI+MFB	49.57	0.91	17.45	9.00	9.09	11.09	2.60	0.28	0.33	0.76	0.04	-0.20
Group 3= HAB+AGI+MFB	51.58	0.95	16.94	8.74	8.13	10.26	2.80	0.59	0.47	0.65	0.11	0.24
Group 1= HAB+AGI+MFB	53.43	0.86	16.81	8.02	7.58	9.55	2.86	0.88	0.84	0.61	0.19	0.20
Group 1= HAB+AGI+FSV	54.00	0.51	17.59	6.66	8.17	9.33	2.61	1.12	4.37	0.76	0.15	0.08
Group 4=HAB +Group3+MFB	49.58	0.91	17.63	8.97	8.90	11.07	2.60	0.33	0.12	0.52	0.38	0.10
Group 1= Group 3+AGI	52.88	0.93	17.21	8.29	7.20	9.70	2.87	0.91	0.29	0.94	0.06	

4. Compositions used for magma mixing models

HAB parent	48.02	0.59	18.57	8.21	10.55	11.82	2.17	0.07
MFB	50.51	1.43	14.53	13.57	5.05	10.61	3.13	0.18
FSV	50.57	2.27	13.78	13.59	5.20	10.24	4.02	0.32
Group 4	49.46	0.90	17.79	8.95	8.67	11.23	2.66	0.33
Group 3	51.42	0.98	17.41	8.75	7.67	10.27	2.80	0.69
Group 1	53.12	0.90	17.37	7.97	6.97	9.61	3.02	1.03
AGI	73.88	0.26	14.25	1.65	0.45	1.48	3.87	4.07

1 Forward modelling fractionation calculation for HAB to Fe-rich ferrobasalt. The model ferrobasalt (MFB) is calculated assuming fractional crystallization and uses 1-atm phase equilibria as constraints. Oliv, plag and aug columns show starting and end point compositions of minerals removed, and phase proportions (weight fractions). Fo = forsterite content in oliv, An = anorthite content in plag, and En = enstatite content in augite. See Grove and Donnelly-Nolan (1986) for details of computational procedure. K_D^{Ca-Na} = 1.3 for plagioclase, K_D^{Fe-Mg} = 0.29 for olivine and K_D^{Fe-Mg} = 0.23 for augite.

2 Results of forward modelling AFC calculation. Starting composition is HAB parent. Each row shows the closest approach to the Group 1 basaltic andesite at the indicated R value, and should be compared with Group 1 representative analysis.

3 Materials balance calculation was used to solve the expression: mixed magma = component 1+component 2 + component 3 for different choices of mixed magma and components. The modeled value of the mixed magma is shown for each regression example. The modeled mixed magma is calculated by multiplying the weight proportion of each component estimated by the regression by the oxide abundance for each oxide in each component. Mass balance calculations were carried out using unweighted multiple linear regression (Bryan et al., 1969). Weight % of estimated components corresponds to the components in the left-hand column. Only one example using FSV is shown. Other materials balance calculations using FSV gave significantly poorer fits.

4 Whole-rock compositions used in the regression models are corrected (see Table 1 and Appendix B) then renormalized to 100% after MnO and P_2O_5 were excluded. HAB parent = 82-72f, MFB = model ferrobasalt (see above), FSV = Fe-rich segregation vein, 82-72a. Group 4 = 881M, Group 3 = 1007M, Group 1 = 83-1, AGI = average Medicine Lake granitic inclusion from Grove et al. (1988).

Table 1-7. Trace element rare earth element and isotope models for fractionation and mixing

Element	Fractionation model: HAB to ferrobasalt[a]								Inclusions and lavas[b]				Mixing Models[c]				
	Partition coefficients				Bulk partition coefficient		Parent HAB	Model Ferrobasalt	Granitic Inclusions	Group 4	Group 3	Group 1	Group 4= HAB+AGI +MFB	Group 3+ HAB+AGI +MFB	Group 1= HAB+AGI +MFB	Group 4= HAB+ Group 3+ MFB	Group 1= Group 3+ AGI
	data source	oliv	plag	aug	F=1.0 to 0.52	F=0.52 to 0.38											
La	1	0.008	0.03	0.10	0.02	0.06	1.3	3.3	18.4-26.8	4.1	6.4	7.1-7.6	2.4-2.7	3.7-4.6	5.0-6.5	3.4	7.1-7.6
Ce	1	0.008	0.03	0.13	0.02	0.07	4.2-4.9	10.7-12.4	33.9-57.5	9.8	18.0	18-20	6.7-8.5	9-12.5	11.1-16.4	10.1-10.6	19.0-20.4
Nd	1	0.006	0.02	0.29	0.02	0.13	4.2-4.4	10.5-11.0	14.2-26.6	7.0	10.7	9.8-11.5	5.9-6.6	6.8-8.4	7.4-9.9	7.3-7.5	10.9-11.7
Sm	1	0.005	0.01	0.48	0.01	0.2	1.42-1.54	3.5-3.7	2.97-5.49	2.6	2.95	2.68-2.85	1.9-2.1	2.1-2.5	2.1-2.7	2.2-2.3	2.9-3.1
Eu	1	0.005	0.02	0.56	0.01	0.24	0.58-0.61	1.41-1.48	0.34-0.96	0.85	1.04	0.96-0.97	0.74-0.80	0.75-0.86	0.70-0.85	0.84-0.86	1.0-1.04
Yb	1	0.009	0.02	0.60	0.02	0.26	1.86-2.02	4.45-4.84	0.81-3.97	2.55	2.88	2.69	2.34-2.66	2.37-2.91	2.18-2.95	2.51-2.63	2.7e-2.95
Lu	1	0.009	0.01	0.56	0.01	0.24	0.33	0.80	0.09-0.61	0.39	0.41	0.41	0.41-0.44	0.42-0.47	0.38-0.48	0.41	0.39-0.42
Sc	2	0.27-0.37	0.02-0.07	4.95	0.10-0.17	2.06-2.10	34.6-36.2	42.2-46.8	1-9	36.8	34.7	31.9-32.1	34.8-37.2	32.8-35.8	29.8-33.2	35.4-36.7	32.7-33.2
V	4	0.09	0.1	0.74	0.10	0.36	191	420.5	1	195-204	190	174-201	229	225	201	214	179
Cr	4	1.1	0.02	13.0	0.38	5.44	190-199	70.8-74.2	0-7	170	135	120-130	159-166	140-147	130-138	157-162	127
Ni	4,6,7	23-111	0.06	4.4-1.9	4.84	2.5-3.54	245-189	6.9-12.3	0	126-135	103	101-112	145-189	125-162	117-152	138-168	97
Co	4	3.0	0.1	1.32	1.06	0.86	44.4-50	44.6-50.2	0-4	45.5	36.5	33.3-34	42.7-48.2	39.7-45.0	36.2-41.3	41.4-44.9	34.4-34.6
Rb	3	0.01	0.03-0.19	0.01-0.14	0.02-0.13	0.02-0.15	1-2	4.6-5.2	92-196	6-8	16	19-25	5.4-10.4	11.9-24.1	19.0-39.5	7.1-7.6	20.6-26.8
Zr	1	0.005	0.009	0.13	0.01	0.06	48-49	123-126	85-293	85-95	113	113-115	66-70	75-84	79-92	109-110	186-190
Ba	3	0.01	0.05-0.59	0.01-0.05	0.04-0.40	0.03-0.31	38	70-97	671-959	80-99	175	204-219	70-87	115-153	164-224	93-96	204-222
Sr	2,3,5	0.01	1.28-2.84	0.06-0.15	0.86-1.91	0.65-1.41	176-185	85-226	131-196	196-202	196-205	194-201	156-193	145-195	141-193	180-197	199-206
87/86							.70337		.70404-.70483	.70343		.70345	.70340-.70343		.70346-.70364		

a Fractionation calculation performed using the multisequence fractional crystallization expression of Allegre and Minster (1978). Mineral proportions are taken from Table 6 HAB to ferrobasalt model. Bulk partition coefficients calculated using tabulated partition coefficients. Data source shows literature sources for partition coefficients. 1. Fujimaki et al. (1984). 2. Irving (1978). 3. Philpotts and Schnetzler (1970). 4. Bougault and Hekinian (1974). 5. Gill (1981). 6. Hart and Davis (1978). 7. Steele and Lindstrom (1981). Trace element abundances for parent HAB are from analyses of 82-72f, 880M and 1004M.

b Trace element abundances in lavas and inclusions. Granitic inclusion abundances are a 2 standard deviation range around the average granitic inclusions in Grove et al. (1988). Group 4 is represented by analysis of 881M Group 3 represented by analysis of 1007M Group 1 range represented by analyses of 1002M and 1009M.

c Trace element abundances in Groups 4, 3 and 1 lavas calculated using mixing models from Table 6.

d Isotope mixing models calculated using element abundances from Table 5 and mixing proportions from Table 6. $^{87/86}Sr$ for granitic inclusions represent the range of values from Grove et al. (1988).

Table 1-8. Liquidus temperatures of lavas, densities of lavas and volume relations

Liquidus temperatures of GC-CC lavas*

Lava type, sample	Data source	Liquidus at 1 atm (°C)
Group 5 (79-35g)	Grove et al. (1982)	1231
Group 4 (82-54)	Baker (1988)	>1230
Group 1 (83-1)	unpub. exp. data	>1190
ferrobasalt	Grove et al. (1982)	1145
granitic melt	Naney (1983)	>950

Estimated temperatures of mixed magmas[b]

Lava type	Mixture	Estimated Temperature
Group 4	HAB+AGI+MFB	1202
Group 4	HAB+MFB+Group 3	1203
Group 3	HAB+AGI+MFB	1179
Group 1	HAB+AGI+MFB	1160

Estimated volumes of age-composition groups[c]

Group	Area (km^2)	Volume (km^3)
5	70.9	2.13
4	116	3.48
3	12.6	0.38
1+2	10.2	0.31
total	210	6.3

a Temperature of ferrobasalt estimated from first appearance of clinopyroxene in the Grove et al. (1982) 1 atm experiments. Granite melt temperature is a minimum estimate for a liquid saturated with plagioclase and orthopyroxene, the two phases present in the melted granitic inclusions. Such a liquid would contain between 2 and 6 wt. % H_2O.

b Mixtures are those calculated by materials balance in Table 6. See Table 6 for abbreviations. Estimated temperatures assume no excess heat of mixing.

c Area estimates from Figs. 1 and 2. Volume estimate assumes average flow thickness of 30 m.

APPENDIX 1-A: SAMPLE LOCATIONS

Samples listed in Tables 1-5. Most are located in Medicine Lake, California 15' quadrangle. The exceptions are noted below.

Group 1 lavas

The following samples were collected from the rim or the interior of Chimney Crater, 121°37.70'W long., 41°30.83'N lat.

83-1 Interior of crater on N side, massive glassy tholoid flow.

83-2 Vesicular spatter from NW rim of crater.

83-3 From horizontal bench on SW side of crater interior.

83-4 Interior of crater on E side, massive tholoid flow.

83-5 From flow surface 30 meters S of crater rim.

1008M 121°37.94' W long., 41°30.54'N lat., flow between Cousin Cone and Chimney Crater.

83-7 121°37.78'W long., 41°30.39'N lat., pahoehoe flow N of Cousin Cone.

83-9 121°37.76'W long., 41°30.30'N lat., aa flow from Cousin Cone.

879M 121°37.70'W long., 41°30.17'N lat., aa flow from Cousin Cone.

1002M 121°37.81'W long., 41°30.12'N lat., Cousin Cone pahoehoe from channel.

1006M 121°37.81'W long., 41°30.39'N lat., Chimney Crater pahoehoe, just N of Cousin Cone.

1007M 121°37.76'W long., 41°30.42'N lat., aa from Chimney Crater, just N of Cousin Cone.

1009M 121°37.67'W long., 41°31.08'N lat., from Shastine Crater.

887M 121°38.31'W long., 41°28.22'N lat., lava from Horse Caves flow, Hambone, Calif., 15' quadrangle.

1017M 121°38.61'W long., 41°26.49' N. lat., Water Caves flow, Hambone, Calif., 15' quadrangle.

1144M 121°37.76'W long., 41°27.19'N lat., lava flow from Water Caves sampled at tube, Hambone, Calif., 15' quadrangle.

1249M 121°38.36'W long., 41°29.68'N lat., Giant Crater lava SE of Papoose Hill. Hambone, Calif., 15' quadrangle.

1264M 121°40'W long., 41°28.35'N lat., Giant Crater lava, 1 mile W of Snag Hill, Hambone, Calif., 15' quadrangle.

1276M 121°40.90'W long., 41°28.44°N lat., Giant Crater lava, east of big island, Hambone, Calif., 15' quadrangle.

Group 2 lavas

82-37 121°38.54'W long, 41°30.58'N lat., pahoehoe overflow from lava channel between Giant and Chimney Craters.

83-24 121°38'W long., 41°30.66'N lat., pahoehoe overflow from lava channel between Giant and Chimney Craters.

83-8 121°37.73'W long., 41°30.54'N lat., pahoehoe flow.

Group 3 lavas

82-66 121°38.70'W long., 41°30.95'N lat., aa flow from Chimney Crater.

82-65 121°38.67'W long., 41°30.86'N lat., aa flow from Chimney Crater.

82-64 121°38.67'W long., 41°30.78'N lat., aa flow from Chimney Crater.

82-71 121°37.74'W long., 41°30.04'N lat., pahoehoe flow from Chimney Crater.

328M 121°39.38'W long., 41°25.22'N lat., Giant Crater basalt from quarry, Hambone, Calif., 15' quadrangle.

1278M 121°41.03'W long., 41°29.68'N lat., Giant Crater basalt, west edge of flow, Hambone, Calif., 15' quadrangle.

1266M 121°38.36'W long., 41°29.69'N lat., Giant Crater basalt, just NE of Snag Hill, Hambone, Calif., 15' quadrangle.

1256M 121°38.85'W long., 41°29'N lat., Giant Crater basalt 0.5 mile N of Snag Hill, Hambone, Calif., 15' quadrangle.

Group 4 lavas

82-38 121°38.54'W long., 41°30.51'N lat., lava flow from Giant Crater.

82-39 121°38.63'W long., 41°30.51'N lat., massive flow lobe from Giant Crater.

82-36 121°38.38'W long., 41°30.57'N lat., lava from Giant Crater.

The following samples, 881M and 82-54 to 82-60 were collected from a prominent aa flow from Giant Crater, which trends SE from the Crater rim.

82-60 121°38.29'W long., 41°30.37'N lat.

881M 121°38.04'W long., 41°29.97'N lat., Hambone, Calif., 15' quadrangle.

82-54 121°38.25'W long., 41°30.30'N lat.

82-55 121°38.21'W long., 41°30.24'N lat.

82-56 121°38.14'W long., 41°30.17'N lat.

82-59 121°38.09'W long., 41°30.14'N lat.

82-58 121°38.04'W long., 41°30.08'N lat.

82-57 121°38.04'W long., 41°30.03'N lat.

82-61 121°38.63'W long., 41°30.25'N lat. pahoehoe from vent S of Giant Crater.

82-62 121°39.18'W long., 41°30.46'N lat., aa flow from Giant Crater.

1010M 121°37.13'W long., 41°29.90'N lat., lava from Double Hole Crater, Hambone, Calif., 15' quadrangle.

1016M 121°37.11'W long., 41°28.03'N lat., lava from Double Hole flow, SE of Powder Hill, Hambone, Calif., 15' quadrangle.

1232M 121°36.27'W long., 41°26.49' N lat., lava from Double Hole, N of Porcupine Butte, Hambone, Calif. 15' quadrangle.

1233M 121°36.61'W long., 41°21.56'N lat., lava from Double Hole Crater, near S end of flow, Hambone, Calif., 15' quadrangle.

1018M 121°40'W long., 41°23.49'N lat., Giant Crater lava tube at Powder Hill Road. Hambone, Calif., 15' quadrangle.

1277M 121°41.18'W long., 41°27.54'N lat., lava from Giant Crater, W of big island, Hambone, Calif., 15' quadrangle.

1257M 121°39.25'W long., 41°29.35'N lat., lava from Giant Crater, 1 mile NW of Snag Hill, Hambone, Calif., 15' quadrangle.

1253M 121°38.67'W long., 41°29.61' N lat., Giant Crater lava S of Papoose Hill, Hambone, Calif., 15' quadrangle.

1259M 121°39.61'W long., 41°29.63'N lat., lava from Giant Crater, 1.5 mile NW of Snag Hill, Hambone, Calif., 15' quadrangle.

1252M 121°38.92'W long., 41°30.15'N lat., lava from vent 3 S of Giant Crater.

Group 5 lavas

883M 121°38.40'W long., 41°30.51'N lat., upper floor of Giant Crater, SW side.

904M 121°38.56'W long., 41°30.34'N lat., drainback in hole SW of Giant Crater.

1004M 121°38.31'W long., 41°30.52'N lat., base of E wall in Giant Crater.

79-35 same location as 1004M.

82-72 same location as 904M.

85-16 same location as 904M.

880M 121°37.94'W long., 41°29.97'N lat., rootless vent SW of Cousin Cone, Hambone, Calif., 15' quadrangle.

1020M 121°29.66'W long., 41°12.34'N lat., Giant Crater lava, 2 miles N of Timbered Crater.

1261M 121°40'W long., 41°29.66'N lat., Giant Crater lava from vent 4, Hambone, Calif., 15' quadrangle.

Inclusions

The following inclusions were collected from the talus in Chimney Crater, on the N and E sides. Sample location is given above for Group 1.

85-17

85-32

1159M

1160M

APPENDIX 1-B: ANALYTICAL METHODS

Major element whole-rock compositions were obtained by XRF at the USGS analytical laboratories in Lakewood, Colorado, and at the University of Massachusetts at Amherst, MA. Analyses are reported in Table 1 and are coded to each analytical facility. The accuracy of the USGS data was estimated from Taggart et al. (1981) who report replicate XRF analyses of igneous rock standards. The accuracy of the U. Mass XRF data was estimated using 23 replicate analyses of BCR-1 and BHVO-1 collected at the U. Mass facility. The averages of these analyses and standard errors are reported in Table 1. Several samples have been analyzed at both facilities and these duplicate analyses are also reported in Table 1.

We have applied a series of normalizing procedures to the data in Table 1 in an effort to remove inter-laboratory biases. Analytical procedures at the U. Mass. facility involved measurement of a working standard (either BCR-1 or BHVO-1) along with a set of unknowns. Thus, the measured value for each element in each unknown was divided by a correction factor, which is the ratio of the measured oxide concentration in either BCR-1 or BHVO-1 divided by the accepted value for that standard. Accepted oxide values for BCR-1 and BHVO-1 are from Abbey (1978). For the USGS data set it was necessary to only correct CaO to a reference standard. The CaO normalization factor was calculated from the standard rock analyses reported by Taggart et al. (1981). Following these corrections, Fe_2O_3 in both data sets was converted to FeO and all analyses were renormalized to 100%. The renormalized analyses are plotted in Figs. 3 and 4 and are used in all of the modelling presented in this paper. USGS major element data from the Lakewood, CO analytical facility only are plotted in Figs. 3 and 4. Several analyses reported in Table 1 (all 1200M series) were carried out at the USGS Menlo Park analytical lab. These analyses appear

to differ from the Lakewood and U. Mass data and at present we do not have the comparative data necessary to develop a correction procedure.

Whole rock trace element abundances were determined by XRF at USGS, Menlo Park, CA and at U. Mass, Amherst, MA, and by INAA at the USGS facility in Reston, VA. Data are reported in Tables 2 and 3.

Compositions of mineral phases in selected GC-CC lavas and inclusions were obtained at M.I.T. with either the 3-spectrometer MAC-5 or 4-spectrometer JEOL-733 electron microprobes. Both instruments made use of the on-line data reduction and matrix correction procedures of Bence and Albee (1968) with modifications of Albee and Ray (1970). The same set of mineral and glass standards was used with both machines. Selected analyses are reported in Table 4.

Isotopic compositions of Sr and elemental abundances of Sr and Nd (by isotope dilution) were determined on selected samples. The methods described in Hart and Brooks (1977) were used to determine Sr isotopic composition and concentration, and the methods described in Zindler (1980) and Richard and Allegre (1980) were used to determine the isotopic composition and abundance of Nd. Data are reported in Table 5. Isotopic analyses were performed on the nine-inch mass spectrometer (NIMA-B) at M.I.T. Sr 87/86 ratios were normalized to 86/88 = 0.1194 and are reported relative to Eimer and Amend $SrCO_3$ = 0.70800. In-run precision for the 87/86 Sr ratio as represented by 2σ is typically <0.005%. Analytical uncertainty on the isotope dilution measurements for Sr is estimated to 0.5%. Nd isotopic compositions were normalized to 146/144 = 0.7219. All reported analyses had in-run 2σs of <0.004%.

CHAPTER 2

Evolution of Lavas at Mt. Shasta Volcano, N. California: An Experimental and Petrologic Study

INTRODUCTION

This Chapter discusses the petrogenesis of lavas from Mt. Shasta, a massive stratovolcano located near the southern end of the Cascade volcanic chain. Mt. Shasta is a long-lived volcanic edifice which has evolved over a period of more than 600,000 years (Crandell et al., 1984). Detailed field mapping has delineated four major episodes of cone building within the last 100,000 years (Christiansen et al., 1977). This study presents major element, trace element and isotopic data on the lavas from each of these volcanic episodes. The dominant rock types at Mt. Shasta are pyroxene andesite and dacite. A distinctive high magnesian basaltic andesite, found on the flanks of the volcano, is less abundant. Rare rhyodacite lavas are also present. The andesites and dacites at Mt. Shasta span a limited compositional range, but contain phenocryst compositions which cover the entire spectrum of magma compositions at the volcano. For example, a single sample may contain An_{30} to An_{80} plagioclase cores, and extremely magnesian (Mg#=85) and Fe-rich (Mg#=65) orthopyroxenes and augites (Mg#=100xMg/(Mg+Fe*), where Fe* equals total iron as FeO). Disequilibrium phenocryst assemblages are ubiquitous in Mt. Shasta andesites, suggesting that mixing between basaltic and silicic liquids was involved in the petrogenesis of the andesites and dacites.

Petrogenetic models for the evolution of calc-alkaline lavas generally stress the role of fractional crystallization of parent basalts in the production of andesites and dacites (Gill, 1981). Assimilation of a crustal component by basaltic magma

and/or mixing of basalt and silicic melts are also processes which appear to operate at many volcanoes (Gill, 1981; Grove and Kinzler, 1986). The geochemistry of the Mt. Shasta andesites and dacites and their phenocryst assemblages point to complex processes of fractional crystallization, mixing of magmas and assimilation of the chemically diverse crust which lies beneath the volcano. We suggest that the development of the major and trace element signatures of the intermediate lavas at Mt. Shasta did not develop synchronously. Major element trends indicate mixing between basaltic andesites and rhyodacite derivative liquids, while trace element signatures reflect interaction between the mixed andesites and either silicic crust, a high Sr, low Rb, Ba component, or an intermediate Sr, Ba component. Petrographic and geochemical data combined with one-atmosphere and moderate pressure phase equilibria provide constraints for modeling the magmatic differentiation at this volcano.

GEOLOGIC SETTING AND SAMPLING

Mt. Shasta lies near the southern end of the Cascade chain (Fig. 2-1a) and is flanked on the south and west by pre-Tertiary rocks of the Klamath Mountain province and to the northeast and east by Tertiary volcanics of the High Cascades. The geology of Mt. Shasta was first studied comprehensively by Williams (1932a,1934); areas to the north and south along the Cascade chain have been mapped by Williams (1932b, 1942, 1949) and Macdonald (1963, 1964, 1965). Macdonald (1966) summarized the regional geology of the Cascade Range and Modoc Plateau in

northern California. This review will draw heavily on these sources as well as the preliminary work of Christiansen et al. (1977), and recent seismic, magnetic and gravity studies on the southern Cascades (Fuis et al., 1987; Zucca et al., 1987; Grisom, 1980; Blakely et al., 1985).

Paleozoic and Mesozoic low grade meta-sedimentary sequences and intrusive plutonic rocks of the Klamath Mountain province outcrop approximately 30 km west and 16 km south of Mt. Shasta. Quartzites and coarse-grained quartz monzonites are exposed 16 km NNW of Shasta at Haystack Butte, an inlier of the Klamath Mountain province (Macdonald, 1966). The eastern boundary of the Trinity ophiolite, also part of the Klamath province, lies approximately 20 km southwest of the volcano. Seismic, magnetic and gravity data indicate that rocks of the Klamath province, including the Trinity ultramafic sheet, are present at depth beneath Mt. Shasta (Grisom, 1980; Blakely et al., 1985; Fuis et al., 1987).

Cretaceous and early Tertiary sedimentary rocks of the Chico and Hornbrook Formations are exposed to the west and northwest of Mt. Shasta and are inferred to lie atop the Eastern Klamath belt sequence beneath the volcano. These two formations consist of massive arkosic sandstones units with interbedded shales, sandstones and conglomerates (Peck et al., 1956).

Also present beneath the Mt. Shasta edifice are rocks of the Tertiary Western Cascade volcanic series (WCVS). The WCVS forms a nearly continuous belt of andesitic flows and fragmental deposits throughout the Cascades (McBirney and White, 1982).

Northwest of Mt. Shasta, the WCVS rests unconformably on the Hornbrook formation or overlaps it to rest on rocks of the Klamath Mountain province (Macdonald, 1966). The WCVS outcrops at Sheep Rock, approximately 17 km north of Shasta, and consists of beds of andesitic tuff breccias with thicknesses of up 500 meters. Although the WCVS rocks are discontinuous in outcrop to the west of the volcano, they are probably present beneath Mt. Shasta as a result of north-south faulting in the Miocene (Williams, 1949). The western and southern base of the volcano rests directly on older (late Pliocene ?) andesites of the High Cascades. To the east, Shasta lava flows are covered by Quaternary volcanics (Macdonald, 1966).

Christiansen et al. (1977) have delineated four major episodes of andesite cone building at Mt. Shasta. The earliest lavas were erupted 80,000-120,000 y.b.p., and formed the Sargents Ridge cone, which comprises the southern flank of the volcano. The next eruptive episode occurred between 80,000 and 10,000 y.b.p. from a vent near the present summit. This second cone is preserved as part of the old summit dome, and is named Misery Hill. Shastina, the third major cone, formed approximately 10,000 y.b.p. and is offset to the west of the other three eruptive centers. The fourth episode of major volcanism (2,000 to 3,000 y.b.p.) formed Hotlum cone, which comprises the present summit and much of the northeast flank of Mt. Shasta (Christiansen et al., 1977; personal communication). The general lack of erosional horizons between andesite flows suggests that each cone-building episode involved nearly

continuous eruption of lavas over periods lasting less than a few thousand years. Two-pyroxene andesites were the dominant lava types during each major cone building stage. Towards the end of most of the episodes, hornblende andesites were erupted along with pyroxene andesites. Each of the four eruptive stages ended with the generation of dacite domes and pyroclastic flows (Christiansen et al., 1977). Basaltic andesite flows and cinder cones of Sargents Ridge and Misery Hill age occur below approximately 2,100 m on the flanks of the volcano.

As a part of this chapter, andesites and dacites were collected from all four eruptive groups and an effort was made to sample the compositional spectrum within each episode of cone building. Basaltic andesites were collected from lavas and cinder cones of Sargents Ridge and Misery Hill age. Basaltic andesites were also collected from a cinder cone of uncertain age north of Haystack Butte. Rhyodacite was sampled at McKenzie Butte, which lies on the southern extension of a north-south alignment of vents that includes the summit of Mt. Shasta.

High alumina basalts (HAB) from north and east of the volcano were collected in order to test for possible petrologic links between the HABs and the basaltic andesites. All samples are located on Fig. 2-1b; Appendix 2-A gives detailed sample locations.

ANALYTICAL AND EXPERIMENTAL METHODS

Major element whole-rock compositions were obtained by XRF at La Trobe University, Bundoora, Australia, following the

techniques present in Norrish and Hutton (1969). FeO was determined by wet chemistry. Gravimetric methods were used to determine H_2O. Whole-rock trace element concentrations were obtained by XRF following the methods described in Norrish and Chappel (1967). Analyses are reported in Tables 2-1 through 2-9, Average BCP-1 analyses are listed in Table 2-1.

Based on four pairs of replicate analyses, percent error ((1σ/concentration)x100) for major elements is generally less than 0.5%; exceptions are TiO_2, MgO and K_2O, 1-2%; and P_2O_5, ~6%. Trace element precision is generally better than 5%. Percent errors for major and trace elements are reported in Table 2-1. Samples were analyzed over the time period 1982 to 1987, and changes in instrumentation between 1985 and 1986 introduced a systematic bias in the Al_2O_3 values for the 1985 samples. After reanalyzing four 1983 samples, Al_2O_3 concentrations in the 1985 data set were lowered by 2.4% relative. The duplicate analyses are reported in Table 2-2. The tables contain the uncorrected 1985 analyses. After corrections, all analyses were renormalized to 100% on an anhydrous basis with all Fe as FeO. The renormalized data are shown in the figures and are used in the modeling calculations.

Isotopic compositions of Sr were determined on selected samples following the methods described in Hart and Brooks (1977) and are summarized in Table 2-10. Isotopic analyses were performed on the nine-inch mass spectrometer (NIMA-B) at M.I.T. $Sr^{87/86}$ ratios were normalized to 86/88 = 0.1194 and are reported relative to Eimer and Amend $SrCO_3$ = 0.70800. In-run precision

for the $^{87/86}Sr$ ratio as represented by 2σ is typically <0.005%.

Compositions of mineral phases in the Mt. Shasta lavas and inclusions were obtained at M.I.T. with either the 3-spectrometer MAC-5 or the 4-spectrometer JEOL-733 electron microprobe, using the same set of mineral and glass standards. Both instruments used the on-line data reduction and matrix correction procedures of Bence and Albee (1968), with the modifications of Albee and Ray (1970). Selected analyses are reported in Table 2-11. Modal data collected on the Mt. Shasta lavas is reported in Tables 2-12 and 2-13. Each mode represents between 1000 and 1100 points on a given thin section.

One-Atmosphere Experiments

One-atmosphere (atm) phase relations for selected Mt. Shasta compositions were determined under controlled fO_2 conditions using a Deltech DT31VT vertical quenching furnace. Liquidus temperatures were determined for a larger set of lavas from Mt. Shasta as well as from Medicine Lake volcano, northern California. In each experiment, 70 to 100 mg of powdered sample was sintered onto 0.8 mm diameter FePt wire loops fabricated to minimize Fe-exchange with the silicate charge (Grove, 1981). All experiments were run at the quartz-fayalite-magnetite buffer (QFM) using constant mixing proportions of CO_2 and H_2, and total flow rates of approximately 0.1 ml/sec. Oxygen fugacity was monitored using a CSIRO ZrO_2-CaO electrolyte cell (Arculus and Delano, 1981) calibrated at the Fe-FeO buffer. Temperature was monitored with Pt-Pt^{90}/Rh^{10} thermocouples calibrated against the

melting points of NaCl, Au and Pd on the IPTS 1968 temperature scale (Biggar, 1972). Results of the melting experiments are presented in Tables 2-14 through 2-16.

Two-kilobar Experiments

Two kilobar (kbar) melting experiments were run in TZM pressure vessels with $pH_2O = P_{total}$ at temperatures of 980 to 900°C. Starting material was a finely powdered sample of 85-3, one of the more magnesian andesites found at Mt. Shasta. Five to ten mg of material were enclosed in 1.5 mm diameter (OD) FePt alloy capsules (~4 wt.% Fe), synthesized to be in equilibrium with the activity of iron in the bulk composition. Several capsules, and a mixture of nickel and nickel oxide were packed into a 6.3 mm diameter (OD) AuPt capsule. Seventy-five ml of water were added prior to sealing the outer capsule. The entire assemblage was then weighed, heated to 110°C and then re-weighed to test the weld. Experimental runs lasted from 45 to 87 hours; results are reported in Table 2-14b.

PETROGRAPHY AND PETROLOGY OF LAVAS AND INCLUSIONS FROM MT SHASTA

The following sections summarize the petrography and mineral chemistry of lavas and inclusions found in the vicinity of Mt. Shasta. Earlier petrologic and geochemical studies of Mt. Shasta include Williams (1932b, 1934), Smith and Carmichael (1968), Condie and Swenson (1973), Peterman et al. (1970), Anderson (1974; 1976) and Newman et al. (1986). Williams (1934) noted the preponderance of two-pyroxene andesites at Mt. Shasta,

and the presence of mafic inclusions consisting of calcic plagioclase, hornblende and minor orthopyroxene and Fe-Ti oxides in many of the lavas. The magnesian character of the lavas and the low K_2O and Rb contents compared to andesites from Medicine Lake and Mt. Lassen are discussed by Smith and Carmichael (1968) and Condie and Swenson (1973). Smith and Carmichael (1968) also describe the broad variations in phenocryst composition, and the magnesian character of some of the pyroxene phenocrysts. Based on the chemistry of melt inclusions in Mg-rich olivine phenocrysts, Anderson (1974) concluded that the parental Mt. Shasta magmas were hydrous and picritic in composition. Trace element and U-Th disequilibrium data indicate that three component mixing is required to model the trace element characteristics of the andesites. These three components are basaltic liquids, silicic liquids and cumulates related to the mafic and andesitic liquids (Newman et al., 1986)

The Mt. Shasta lavas and surrounding high-alumina basalts span a compositional range from ~48 to ~71 wt.% SiO_2. In the classification scheme of Peccerillo and Taylor (1976) (Fig. 2-2), most of the rocks are divided into low-K tholeiites, low-K basaltic andesites, andesites, dacites and rhyolites. The low-potassium tholeiites will be designated as high alumina basalts in this work. Although three of the Sargents Ridge lavas fall just within the low-K tholeiite field, they are clearly affiliated with the larger group of basaltic andesites. The three Misery Hill basaltic andesites plot above the main group of Sargents Ridge and Haystack basaltic andesites, consistent

with the different phenocryst assemblages observed in these two sets of lavas.

The samples will be described in the following groups: high alumina basalt (HAB), basaltic andesite (BA), andesite and dacite and the rhyodacite of McKenzie Butte. The HABs are not clearly linked to any cone building episode at the volcano. We have included them in this study in order to test for possible genetic links between the high-Al basalts and the basaltic andesites. Although the BAs samples represent two different stages of volcanism, we consider them together because they form a chemically coherent group. We describe the andesite and dacite lavas by age, with the exception of the unique, compositionally-zoned Panther Creek flow. The most silicic lavas found in the vicinity of the volcano are the rhyodacites of McKenzie Butte, which were erupted contemporaneously with the Sargents Ridge lavas. Throughout the following sections, specific samples will be referred to by field number. Samples are located on Fig. 2-1b and locations are described in Appendix 2-A.

High Alumina Basalts

HAB's collected from north and east of Mt. Shasta are generally aphyric lavas containing rare phenocrysts of olivine and plagioclase. The groundmass consists of laths of plagioclase, granular olivine and coarsely spherulitic pyroxene and displays textures ranging from intergranular/intersertal to hyalophitic. Large spheroidal to sinuous vesicles are present in most thin sections.

Olivine phenocrysts are normally zoned with core compositions in the range Fo_{84-86}. Rim compositions cover a broad spectrum from Fo_{80} to Fo_{38}. The olivine phenocrysts contain only rare glass inclusions. Plagioclase phenocrysts are normally zoned from An_{81-70} (cores) to An_{71-40} (rims). Selected olivine and plagioclase analyses are listed in Table 2-11.

Basaltic Andesites

Basaltic andesites were collected from two of the four major cones which comprise Mt. Shasta, Sargents Ridge and Misery Hill. Basaltic andesites were also found at a cinder cone of uncertain age north of Haystack Butte (Fig. 2-1b). All of the lavas are moderately porphyritic and contain between 10 and 20 vol.% phenocrysts. Olivine, augite and rare plagioclase phenocrysts are present in the Misery Hill samples. The Sargents Ridge and cinder cone lavas with >7.50 wt.% MgO contain olivine ± rare plagioclase phenocrysts; less magnesian samples generally contain augite in addition to olivine and plagioclase. Groundmass textures in all lavas range from pilotaxitic/intergranular to hyalophitic. The groundmass mineral assemblage consists of plagioclase, olivine and pyroxene. Olivine phenocrysts in the more evolved samples exhibit thin discontinuous pyroxene overgrowths. Cr-Al spinel inclusions in olivine are ubiquitous in the basaltic andesites. Modal data for selected samples are presented in Table 2-12.

Compositions of olivine, plagioclase and augite phenocrysts are summarized in histogram form in Figs. 2-3, and

representative analyses are reported in Table 2-11. Olivine phenocrysts are normally zoned and have core compositions in the range Fo_{88-91} in the most magnesian lavas. Olivine phenocrysts are more variable in composition (Fo_{77-88}) in the evolved lavas. Rim compositions fall between Fo_{60} and Fo_{80}. One reverse-zoned olivine phenocryst was found in sample 85-36, with Fo_{73} (core) $\rightarrow$ Fo_{89} $\rightarrow$ Fo_{68} (rim). Plagioclase is normally zoned with most core compositions between An_{81} and An_{86} (Fig. 2-3b). Rim and groundmass compositions fall in the range An_{76-51}. Fig. 2-3c shows that augite phenocryst Mg#s lie within the range 83-88. Wo contents in these pyroxenes are between 40 and 46. The augite phenocrysts are commonly sector-zoned, with the sector parallel to the c-axis depleted in Ti, Al, Cr and Ca relative to the adjacent sectors. Pigeonite and subcalcic augite are present in the groundmass, and pigeonite is common as thin overgrowths on groundmass and phenocryst olivines. The compositions of spinel inclusions in olivine phenocrysts are plotted in Fig. 2-4, along with the spinel fields from mid-ocean ridge basalts (Dick and Bullen, 1984) and the Trinity ophiolite (Quick, 1981). The BA spinels exhibit Mg* values (where $Mg^*=Mg/(Mg+Fe^{2+})$) between 0.38 and 0.66 and Cr/(Cr+Al) values in the range 0.44 to 0.70. Spinels with Cr/(Cr+Al) ratios of ~0.70 are from the Misery Hill basaltic andesite 82-94a and lie above the MORB and Trinity fields. Spinel inclusions from the remaining BAs overlap the spinel field from the Trinity ophiolite.

Andesites and Dacites : Sargents Ridge

Andesites and dacites from the Sargents Ridge cone are porphyritic lavas which contain 21 to 42 vol.% phenocrysts of plagioclase, orthopyroxene, clinopyroxene ± Fe-Ti oxides ± amphibole ± olivine. The fine-grained pilotaxitic to hyalopilitic groundmass consists of plagioclase, pyroxene, Fe-Ti oxides and glass. Plagioclase constitutes between 61 and 83 vol.% of the total phenocryst assemblage (Table 2-13). Plagioclase phenocrysts are subhedral, tabular to rectangular in outline and up to 4.2 mm in longest dimension. Non-rim phenocryst anorthite contents are summarized in Fig. 2-5, and representative analyses are given in Table 2-11. Core compositions range from An_{80} to An_{34}, with a majority of the analyses falling in the range An_{40-60}. Sieve-textured plagioclase grains are present in most thin sections, and in general have core compositions between An_{35} and An_{45}. The sieve-textured region may constitute the entire core of a grain or may form a concentric band between a clear rim and an unreacted core (Fig. 2-6). Plagioclase phenocrysts contain apatite inclusions as well as inclusions of orthopyroxene, augite and Fe-Ti oxides.

Orthopyroxene phenocrysts are equant to rectangular in morphology and are rarely greater than 1.5 mm in length. Modal proportions range from 2 to 6 vol.%. Core compositions (Mg#s) of the orthopyroxene phenocrysts are plotted in histogram form in Fig. 2-7a. The compositional spectrum is bimodal with a majority of orthopyroxene cores exhibiting Mg#s in the range 62 to 66. These Fe-rich grains display both normal and reverse zoning, and

often contain inclusions of ilmenite and/or magnetite. The reverse zoning takes the form of a distinct overgrowth rim of more magnesian orthopyroxene (Fig. 2-6). In rare cases, Fe-rich orthopyroxenes are partially rimmed by magnesian augite. Many of the Sargents Ridge samples contain a small subset of Mg-rich orthopyroxene phenocrysts ($Wo_{1-2}En_{80-90}$) which could have crystallized from the andesites and dacites. Orthpyroxene Mg#s calculated using the FeO*/MgO molar ratios in these lavas and an Fe-Mg $K_D^{opx/liq}$ of 0.21 (Grove, unpublished data) cover the range from 85 to 88.

Augite phenocrysts (1 to 4 vol.%) are subhedral and rectangular in outline and < 1.0 mm in longest dimension. Fig. 2-7b shows a histogram of Mg#s in augite phenocryst cores. The compositions show a bimodal distribution with the two peaks centered on values of 74-76 and 86-88. Wo-contents for both populations fall in the range 38 to 46. In contrast to the orthopyroxene distribution (Fig. 2-7a), the majority of augite phenocrysts have Mg#s > 80, and many of these magnesian augites exhibit hour-glass sector zoning similar to that observed in the basaltic andesites (Fig. 2-6). Calculated augite Mg#s for these bulk rock compositions are 84 to 87 (Fe-Mg $K_D^{aug/liq}$ = 0.23; Grove, unpublished data). Fe-Ti oxides are sometimes present as inclusions in the Fe-rich population of augite phenocrysts. Representative augite compositions are listed in Table 2-11.

Amphibole phenocrysts are present in several Sargents Ridge samples. The phenocrysts are equant to acicular in morphology with elongate grains generally having hollow cores. Inclusions

in the amphiboles include Fe-Ti oxides, plagioclase and orthopyroxene. Normalized Ca - Mg - Fe contents are plotted in Fig. 2-8; Mg#s range from 64 to 80. Representative analyses are reported in Table 2-11. The more magnesian compositions are generally from amphiboles that partially or completely rim Mg-rich olivines or pyroxenes. A subset of the amphibole phenocryst population in 82-88b is reversed-zoned. Strongly pleochroic cores are Fe-rich (Mg#s ~64) and are surrounded by less pleochroic rims with Mg#s in the range 68 to 74. Amphiboles in 82-85 are rimmed by granular Fe-Ti oxides. In some cases, the dehydration reaction has produced amphibole pseudomorphs of finely-intergrown plagioclase + pyroxene + ilmenite/magnetite.

Olivine phenocrysts/xenocrysts are present in seven of the Sargents Ridge andesites and dacites and are either rimmed by orthopyroxene or display scalloped grain boundaries. With the exception of sample 82-86, olivine core compositions fall in the range Fo_{82-90}. Olivines in 82-86 are more Fe-rich, with Fo-contents between 68 and 77. The composition of the orthopyroxene overgrowth rim is directly correlated with the composition of the enclosed olivine, e.g. Fo_{69} rimmed by $Wo_{2.4}$ $En_{65.7}$ and Fo_{84} rimmed by $Wo_{2.3}$ $En_{82.5}$.

Ilmenite and magnetite phenocrysts are subhedral (< 0.3 mm in diameter), locally display faint cuspate grain boundaries and constitute < 1 vol.% of the Sargents Ridge samples. They occur both as composite intergrowths (Haggerty, 1976; Fig. Hg-2) or as two discrete grains sharing a common interface. Only in the more silicic dacites do the oxide phenocrysts display extensive

oxidation-exsolution lamellae.

Circular to ellipsoidal quartz xenocrysts are present in three of the more silicic lavas (SiO_2 > 61 wt.%). These quartz grains are invariably highly fractured and have irregular boundaries. Samples 82-87, 82-95 and 82-102 contain both olivine and quartz.

Andesites and Dacites: Misery Hill

Intermediate lavas from the Misery Hill cone contain 24 to 44 vol.% phenocrysts of plagioclase, orthopyroxene and clinopyroxene, ± amphibole, oxides and olivine set in a fine-grained hyalopilitic to pilotaxitic groundmass. Plagioclase, the most abundant phenocryst phase, constitutes between 69 to 79% of the total phenocryst volume. The groundmass consists of plagioclase laths, granular to microlitic pyroxene, granular oxides and glass. Samples 82-99 and 82-100 are from pyroclastic deposits called the Red Banks and consist of a matrix of compacted glass shards.

Plagioclase phenocrysts are subhedral, tabular/rectangular in outline and up to 2.5 mm in longest dimension. Fig. 2-9 summarizes the range of phenocryst core compositions; the overall variation is from An_{28} to An_{88}, with two major populations, An_{41-52} and An_{55-68}. All of the phenocrysts show complex oscillatory zoning (Fig. 2-6c,d) and many display a fine sieve-textured interior or a region of coarse wormy melt inclusions. Compositions of sieve-textured grains generally fall in the range An_{40-50}, while the coarser reaction texture is

usually associated with a more calcic plagioclase, e.g. An>70. A given thin section will also contain plagioclase phenocrysts that appear unreacted but which have the same compositions as adjacent reacted grains. Mineral inclusions in the plagioclase phenocrysts include apatite, orthopyroxene and Fe-Ti oxides.

Normally and reverse-zoned orthopyroxene phenocrysts comprise between 1.7 and 6.6 vol.% of the Misery Hill lavas. The subhedral grains (≤1.4 mm in longest dimension) show a three-peaked distribution with respect to Mg# (Fig. 2-10a), with maxima at 56-59, 66-68 and 82-84. Based on the range of bulk Fec*/MgO molar ratios in these lavas, equilibrium orthopyroxenes would have Mg#s of 82-88. In contrast to the orthopyroxenes in the Sargents Ridge lavas, orthopyroxenes with magnesian cores (Mg#>74) comprise ~50 wt.% of the Misery Hill population. The Fe-rich orthopyroxenes often contain inclusions of ilmenite, magnetite and apatite. The reverse-zoning displayed by some of the orthopyroxene phenocrysts takes the form of optically distinct magnesian overgrowth rims (Fig. 2-6j). Orthopyroxenes with Mg#s in the range 80-84 are sometimes partially rimmed by magnesian clinopyroxene with Mg#s ranging from 83-88.

Augite phenocrysts ($Wo_{45-39}En_{52-40}$) are subhedral, ≤1.8 mm in longest dimension and comprise between 1.4 and 2.7 vol.% of a given thin section. 82% of the analyses of augite cores have Mg#s in the range 80 to 92 (Fig. 2-10b); based on an Fe-Mg K_D of 0.23, the bulk composition should crystallize augites with Mg#s between 80 and 87. The more Fe-rich augites are reverse-zoned, and in rare cases, the Fe-Mg zoning is oscillatory. For example,

the following series of Mg#s marks the progression from core to rim in one grain, 78→87→78→82. Many of the magnesian augite phenocrysts display hour-glass sector zoning, with the sector growing parallel to the c-axis depleted relative to the adjacent sector in Ti, Al, Cr and Ca.

Amphibole phenocrysts are present in four of the Misery Hill samples and their compositions are plotted in Fig. 2-11. The phenocrysts are equant to acicular in morphology with elongate grains having hollow cores. Fe-Ti oxides, plagioclase and orthopyroxene are often present as inclusions. Amphibole Mg#s range from 83 to 58 with most grains either unzoned or normally zoned. Amphiboles in Misery Hill lavas display a range of dehydration-reaction textures, from thin oxide rims to pseudomorphs of finely-intergrown plagioclase + pyroxene + Fe-Ti oxide (Fig. 2-6n).

Olivine phenocrysts/xenocrysts are present in three of the Misery Hill samples and are normally zoned and rimmed by orthopyroxene. Core compositions range from Fo_{90} to Fo_{69}. Mg#s of the orthopyroxene overgrowths are directly correlated with the olivine composition, e.g. Wo_1En_{79} orthopyroxene rimming Fo_{81-82} olivine, and Wo_3En_{66} orthopyroxene rimming Fo_{71} olivine (Fig. 2-6p).

Ilmenite and magnetite occur as inclusions in Fe-rich pyroxene, as individual phenocrysts and, more rarely, as coexisting oxide pairs. The textures of the coexisting pairs are similar to those described in the Sargents Ridge lavas. Most oxide grains do not show oxidation-exsolution lamellae.

Magnetite and ilmenite comprise <1 vol.% of a given thin section.

Quartz xenocrysts are present in several thin sections. They are circular to cuspate in outline, up to 0.8 mm in longest dimension. These xenocrysts are sometimes partially rimmed by granular pyroxene.

Andesites: Panther Creek Flow

This compositionally zoned flow is located on the southeast flank of the volcano; silica content varies from 55 to 59 wt.%. Although the flow is of Misery Hill age (Christiansen et al., 1977) the bulk chemistry of the lavas set them apart from the majority of cone-building andesites. The Panther Creek lavas are the most MgO-rich and silica-poor andesites sampled at the volcano. The lavas are porphyritic, containing ~15 to 20 vol.% phenocrysts of plagioclase, olivine, augite, and orthopyroxene. Unlike the other intermediate lavas, plagioclase phenocrysts comprise < 6 vol.% of the rocks, and mafic phenocrysts are more than twice as abundant as plagioclase. Plagioclase core compositions in the Panther Creek samples display a nearly flat distribution from An_{37} to An_{85} (Fig. 2-12). Many of the phenocrysts exhibit sieve-textured cores and clear rims. Apatite inclusions are present in the plagioclase phenocrysts from all of the Panther Creek lavas.

Olivine phenocrysts make up 1 to 2 vol.% of the Panther Creek lavas; core compositions are shown in Fig. 2-14a. More than 50% of the analyses are in the range Fo_{87-90}, which overlaps

with the distribution of forsterite contents found in the more magnesian basaltic andesites. A small number of core compositions are as iron-rich as Fo_{77}. Many of the magnesian olivine phenocrysts contain chrome spinel inclusions (Fig. 2-6o). These spinels are similar in composition to the spinels from the basaltic andesites.

Augite (6-8 vol.%) is the most abundant phenocryst phase in the Panther Creek samples. Grains are subhedral and ≤ 1.5mm in longest direction. Like the olivine phenocrysts, the majority of the augites are magnesian with Mg#s greater than 85 (Fig. 2-13b). The MgO-rich phenocrysts are often sector-zoned (Fig. 2-6e). Orthopyroxene phenocrysts, on the other hand, are bimodally distributed with respect to Mg# (Fig. 2-13c), with peaks centered at 66 and 79. The Fe-rich orthopyroxene grains contain ilmenite and magnetite inclusions and both iron and magnesian-rich varieties are often rimmed by augite (Fig. 2-6k).

Amphibole (?) pseudomorphs consisting of finely-intergrown plagioclase, pyroxene and oxides, although rare, are present in all of the Panther Creek lavas (Fig. 2-6m). Quartz xenocrysts were not observed in any of the samples. While oxides are abundant as inclusions in orthopyroxene and plagioclase, ilmenite and magnetite phenocrysts were not observed in the groundmass.

Andesites and Dacites: Shastina

Andesites and dacites were the only rock types sampled from the Shastina cone. Modal phenocryst abundances range from ~2 to ~20 vol.% and the phenocryst assemblage consists of plagioclase, orthopyroxene, clinopyroxene and rare amphibole. With the exception of two samples, plagioclase is the most abundant phenocryst phase, constituting more than 50% of the phenocryst assemblage (Table 2-13). These two lavas (82-82; 83-58) contain augite and orthopyroxene phenocrysts (~2 vol.%) but few plagioclase microphenocrysts, setting them apart petrographically from the other silicic lavas at the volcano.

Plagioclase phenocrysts lack the resorption textures displayed by plagioclase phenocrysts from Sargents Ridge and Misery Hill. Phenocryst core compositions are summarized in Fig. 2-14 and representative analyses are reported in Table 2-11. The distribution of An-contents in the phenocryst cores differs from the Sargents Ridge and Misery Hill distributions, and in general is much more calcic with the vast majority of analyses falling in the range An_{50-70}. Individual phenocrysts are normally zoned, although complex oscillatory zoning is present. Plagioclase groundmass compositions range from An_{50} to An_{60}.

Orthopyroxene phenocrysts are subhedral, tabular grains, and are quite magnesian with Mg#s between 79 and 87 (Fig. 2-15a). The first orthopyroxenes which crystallize from the Shastina lavas should have Mg#s between 85 and 89 (calculated using a Fe-Mg K_D of 0.21; Grove, unpublished data). Zoning is normal with rim compositions in the range $Wo_{3-4}En_{61-80}$, although

unusual multiply reverse-zoned orthopyroxenes are present in some of the lavas; e.g. core Mg# = 70, rim Mg# = 81. Inclusions in the orthopyroxene phenocrysts include Cr-Al spinels and magnesian augites. The spinels are chrome and iron rich; Cr/(Cr+Al) = 0.60-0.73 and Mg* = 0.19-0.54. Magnesian augite sometimes occurs as an overgrowth rim on both Mg-rich and more Fe-rich orthopyroxenes.

Clinopyroxene phenocryst core compositions are summarized in histogram form in Fig. 2-15b; representative analyses are given in Table 2-11. Augite phenocrysts are Mg-rich, with most analyses lying between Mg#s of 80 and 90; calculated range based on bulk rock compositions is 84 to 88. Wo-contents for the phenocrysts fall in the range 40 to 44. Many of the phenocrysts display sector-zoning similar to that observed in augites from the basaltic andesites. Small orthopyroxenes are sometimes present as inclusions in the Mg-rich augite phenocrysts. Reverse-zoned augites are present in all thin sections probed; cores are in the range $Wo_{42-45}En_{39-43}$, interiors $Wo_{44-45}En_{47-49}$ and rims $Wo_{44-45}En_{45-48}$. Normally zoned grains have rim compositions with Mg#s between 70 and 80.

Andesites and Dacites: Hotlum

The Hotlum andesites and dacites contain ~30 vol.% phenocrysts of plagioclase, orthopyroxene, augite and Fe-Ti oxides ± amphibole, with plagioclase comprising ~65% of the total phenocryst assemblage. The pilotaxitic groundmass consists of plagioclase, pyroxene, Fe-Ti oxides and glass.

Plagioclase phenocrysts (≤2.6 mm in longest dimension) display the same textural characteristics observed in the Sargents Ridge and Misery Hill samples: either sieve-textured cores or cores with coarse wormy melt inclusions. The distribution of An-contents in the phenocryst cores varies from An_{32} to An_{79} (Fig. 2-16). While there is abundant structure in the histogram, the majority of analyses fall between the bounds An_{40} and An_{50}. There is also a small population of calcic phenocrysts with anorthite contents between 70 and 80. Most grains exhibit oscillatory zoning, with rim compositions in the range An_{50-60}. Compositions of the sieve-textured cores are quite variable (An_{35-62}). Apatite, orthopyroxene and Fe-Ti oxides are present as inclusions in the plagioclase phenocrysts.

Orthopyroxenes are the second most abundant phase in the Hotlum lavas (1.1 to 5.2 vol.%). Orthopyroxene phenocrysts are subhedral, equant to rectangular in outline, and generally ≤1.2 mm in longest dimension. Fig. 2-17a shows a histogram of Mg#s from orthopyroxene phenocryst cores. The majority of analyses are in the range 64 to 69; the most magnesian grains have Mg#s of 85 to 89 and are normally zoned to 70-80. Calculated equilibrium compositions have Mg#s of 84 to 89 (Fe-Mg K_D = 0.21). The Fe-rich orthopyroxenes are reverse-zoned with discrete, more magnesian rims (Mg# = 75-85). Mg-rich augite overgrowths are present on some of the orthopyroxene phenocrysts. Magnetite, ilmenite and apatite are present in the Fe-rich orthopyroxene cores while Cr-Al spinels are found in the magnesian orthopyroxenes (Table 2-11).

Clinopyroxene phenocrysts (~1 to 3 vol.%) are subhedral, ≤1.0 mm and in the compositional range Wo_{39-45} En_{38-51}. Clinopyroxene phenocryst core compositions form two distinct populations with respect to Mg# (Fig. 2-17b), with one population ranging between 67 and 77 and the other between 84 and 90. The latter range covers the spectrum of calculated equilibrium compositions (Mg# = 83-88). Members of the magnesian group are often sector-zoned, while the more Fe-rich augite phenocrysts are generally reverse-zoned with magnesian rims (Mg# ~80). Augite phenocrysts of varying compositions are sometimes partially rimmed by orthopyroxene with a similar Mg#.

Amphibole is a phenocryst phase in four of the Hotlum samples. Within a given thin section, amphiboles show a wide range of dehydration textures ranging from thin oxide rims to finely intergrown plagioclase, pyroxene and Fe-Ti oxides pseudomorphed after amphibole. These amphibole pseudomorphs are more abundant than unreacted grains in the Hotlum lavas. Both magnetite and ilmenite occur as phenocrysts in Hotlum lavas (<1 vol.%), and display textures similar to those described from the Sargents Ridge andesites and dacites.

Rhyodacite: McKenzie Butte

The rhyodacite lavas collected at McKenzie Butte (Fig. 2-1b) contain phenocrysts of plagioclase, orthopyroxene, Fe-Ti oxides and amphibole. The hyalopilitic groundmass consists of microlitic plagioclase, granular pyroxene, oxides and glass. Euhedral plagioclase phenocrysts comprise between 12 and 17

vol.% of the lavas, ranging up to ~4 mm in longest dimension. Phenocryst compositions are plotted in Fig. 2-18a. Overall chemical zoning trends are normal, with core compositions between An_{30-50} and rim compositions in the range An_{20-36}. The plagioclase phenocrysts are free of the reaction textures, but contain inclusions of amphibole, Fe-Ti oxides and orthopyroxene.

Orthopyroxene phenocrysts comprise ~1 vol.% of the McKenzie Butte rhyodacite and are normally zoned from Wo_2En_{63-50} to Wo_2En_{55-49}. Compositions are plotted in Fig. 2-18b. Elongate amphibole phenocrysts are not abundant (<1 vol.%), and have Mg#s in the range 61 to 50. Both titano-magnetite and ilmenite are present as phenocrysts and as inclusions in orthopyroxene and plagioclase. Together, they comprise <1 vol.% with magnetite present in greater relative abundance.

Inclusions

A variety of silicic to ultramafic inclusions are present in the Mt. Shasta lavas. Xenolithic material in the basaltic andesites is restricted to the lavas from Haystack Butte, and consists of graywacke (Hornbrook formation ?), granitic material, rhyolite tuffs, granoblastic quartz aggregates and andesites. Xenoliths range from a few cm to tens of cm in size and show little evidence of mechanical/chemical interaction with the basaltic andesites. Xenolith/basalt contacts are very sharp both in hand sample and in thin section. We infer that most of these inclusions represent a sampling of the near surface

stratigraphy beneath the volcano, e.g. Western Casacade Volcanic Series lavas.

A granitic xenolith was found in a Haystack Butte basaltic andesite. The inclusion shows no evidence of partial melting and consists of medium-grained feldspars, anhedral quartz and interstitial biotite. The contact with the basaltic andesite is quite sharp and weak microcline twins are present in some of the alkali feldspars.

Eight mafic and two ultramafic cm-sized inclusions were found in the Mt. Shasta lavas. Mineral assemblages and compositions in the mafic inclusions suggest that they are cumulates derived from evolved basaltic to andesitic liquids, similar to those inclusions described by Williams (1932b; 1934). The lherzolite and orthopyroxene xenoliths may represent pieces of the Trinity ophiolite.

Mafic inclusions: Plagioclase, augite, orthopyroxene, Fe-Ti oxides ± olivine ± amphibole are present in the mafic inclusions, with textures ranging from gabbroic to granoblastic. Olivine occurs in two of the five inclusions and is always rimmed by orthopyroxene. Forsterite contents range from 86 to 78. The majority of plagioclase grains in the inclusions are normally zoned between An_{90} and An_{67}. More albitic and compositionally variable grains (An_{68-10}) are present in veins or interstices between pyroxenes. In sample 83-53-1, plagioclase shows evidence of internal dissolution (e.g. Tsuchiyama and Takahashi, 1983) with adjacent micron-sized regions of An_{80} and

An_{40}. Sample 85-48e-9 contains 50 to 100 mm sized regions of granoblastic plagioclase with well-developed 120° triple junctions.

Augite and orthopyroxene are present in all inclusions, covering the compositional range $Wo_{1-3}En_{84-65}$ and $Wo_{40-47}En_{48-42}$. Magnesian pyroxenes (Mg#>75) are either unzoned or show slight normal zoning. The more Fe-rich pyroxenes are reverse-zoned. For example, core and rim Mg#'s of 65 and 72 are common in orthopyroxenes in sample 85-53-1.

Amphibole is present in sample 85-48e-5 and has Mg#s of 83 to 79. Normalized Ca-Mg-Fe abundances are 25-26:61-59:12-15. Millimeter sized patches of finely-intergrown plagioclase, orthopyroxene, augite and Fe-Ti oxides are present in several of the inclusions and these assemblages may represent amphibole that has undergone subsolidus dehydration reactions (Mazzone et al., 1987). Sample 85-48e-9 contains these amphiboles (?) pseudomorphs and coexisting ilmenite and magnetite, which yielded a temperature of 720°C.

Ultramafic inclusions: An unusual meshed-textured inclusion is present in sample 85-2a. The interior consists of stacked plates of orthopyroxene with very low Ca-contents ($Wo_{0.2}En_{90}$), often separated by a thin band of silica-rich glass. The plates are arranged in a crude herringbone pattern. Granular orthopyroxene and augite and, to a lesser extent, olivine are present near the contact with the andesite. These phases are also quite magnesian; augite ($Wo_{44}En_{51}$), orthopyroxene (Wo_2En_{90}) and olivine

(Fo_{89}). The olivine is completely encased in orthopyroxene. At the edge of the inclusion, Mg#s in the pyroxenes drop to between 73 and 84. The composition of the interstitial glass in the interior of the inclusion is variable, with silica ranging from 66 to 79 wt.%. The other major oxides in the glass are Al_2O_3 (23.2-13.6 wt.%), Na_2O (8.6-2.3 wt.%) and K_2O (0.9-5.4 wt.%). The morphology and chemistry of the orthopyroxene grains suggest that the inclusion was originally serpentinite from the Trinity ophiolite which has been metamorphosed by the enclosing andesitic magma.

A cm-sized peridotite inclusion was found at sample locality 85-48. This inclusion contains granoblastic zones of olivine, orthopyroxene and clinopyroxene. Chrome spinel and magnesian amphibole (Mg#s ~87) are present in trace abundance. Olivine and pyroxene cores are homogeneous with Mg#s in the range 90-88 and 92-89, respectively. The orthopyroxenes have thin gradational Fe-rich rims (Mg#~85). The phase assemblage and mineral compositions in this inclusion suggests that it is derived from the Trinity ophiolite. The Al_2O_3 (2.0-3.3 wt.%) and Cr_2O_3 (0.7 to 1.2 wt.%) values in the clinopyroxenes are similar to the abundances of these elements in clinopyroxenes from the Trinity ophiolite(Quick, 1981). Among Shasta lavas, only the augite phenocrysts from the basaltic andesites have similar minor element contents. However the Mg#s of these phenocrysts are < 88.

Summary of petrography and mineral chemistry

The andesite and dacite lavas at Mt. Shasta (58-67 wt.% SiO_2) are phenocryst-rich, containing ~15-34 vol.% plagioclase, 1-7 vol.% orthopyroxene and 1-8 vol.% augite. A broad range of phenocryst compositions, often forming bimodal distributions, are characteristic of the intermediate lavas. The magnesian augites and olivines found in the andesites and dacites have similar compositions and types of sector zoning to augites found in the basaltic andesites. The Fe-rich orthopyroxene phenocrysts in the andesites and dacites are rimmed by more magnesian orthopyroxene, indicating that they were not in equilibrium with this coexisting liquid. The rarer evolved augite and olivine phenocrysts found in the intermediate lavas are similar in composition to those phases found in the coarse-grained (cumulate ?) inclusions. Amphibole phenocrysts are distributed sporadically throughout the andesite and dacite lavas. Quartz xenocrysts occur more commonly in the dacites.

MAJOR ELEMENT CHEMISTRY

Major element variations in all of the Shasta lavas are plotted as a function of MgO content in Fig. 2-19. Each major eruptive group is discussed below.

High Alumina Basalts

Major element compositions of the HABs are summarized in Table 2-1. These lavas show limited compositional variabilty, with MgO contents between ~8.8 and 9.8 wt.%, and, with the

exception of a single sample, SiO_2 contents between 48 and 49 wt.% (Fig. 2-19a). The HABs have higher concentrations of TiO_2, Al_2O_3, FeO* and CaO, lower Na_2O and K_2O abundances, and similar P_2O_5 contents compared to the BAs at the MgO values. The lavas are similar in composition to the more evolved HABs from Medicine Lake volcano (Chapter 1; Donnelly-Nolan, unpublished data), and have Mg#s of 66.5 to 63.6.

Basaltic Andesites

Major element compositions of basaltic andesites from the Sargents Ridge and Misery Hill cones, and from the cone north of Haystack Butte are given in Table 2-2. These lavas have high MgO contents (~11 to 7 wt.%), high Mg#s (63.5 to 72.1), and SiO_2 values between 51.6 and 54.4 wt.%. SiO_2, Al_2O_3, FeO*, CaO and K_2O correlate strongly with MgO content. SiO_2, Al_2O_3, K_2O and P_2O_5 increase, while FeO* and CaO decrease with decreasing MgO. While showing considerable scatter, TiO_2 and Na_2O increase with decreasing MgO (Figs. 2-19b and 2-19f). The three basaltic andesites from Misery Hill are compositionally distinct from the larger group of Sargents Ridge and Haystack Butte BAs. At the same MgO content, the Misery Hill lavas have higher SiO_2, TiO_2, K_2O and P_2O_5 contents, and lower wt.% Al_2O_3 and FeO* relative to the other BAs.

Andesites, Dacites and Rhyodacites

Compositions of the intermediate to silicic lavas are plotted in Fig. 2-19 and reported in Tables 2-4, 2-6 and 2-8. MgO contents vary from ~5.5 to 0.5 and SiO_2 contents vary from 57 to 71 wt.%. TiO_2, FeO*, CaO and P_2O_5 decrease monotonically with decreasing MgO content (Fig. 2-19), with total variations on the order of 0.77 to 0.45, 5.6 to 3.0, 8.3 to 4.2, and 0.34 to 0.11 wt.%, respectively. Sodium and potassium increase with decreasing MgO and range from 3.7 to 6.4 and 0.8 to 2.8 wt.%, respectively. Al_2O_3 contents in the andesites and dacites form a nearly vertical cluster when plotted against wt.% MgO content (Fig. 2-19c). The lavas from Sargents Ridge and Misery Hill display the largest variation in Al_2O_3 at nearly constant MgO values, 16.2 to 18.0 and 16.0 to 17.9 wt.% respectively. Two of the three rhyodacite samples have similar compositions, while the third sample is depleted in silica and enriched in alumina. This sample has experienced extensive deuteric alteration and the low SiO_2 value may reflect leaching of silica.

Alumina in the andesite and dacite lavas is the only oxide not correlated with MgO. Since fractional crystallization or mixing of basaltic and silicic liquids will produce linear, nonvertical trends in Fig. 2-19c, the scatter in this figure may reflect the redistribution of plagioclase. Fig. 2-20 shows modal plagioclase plotted against ΔAl_2O_3 in the Sargents, Misery and Hotlum samples, where ΔAl_2O_3 for each of the samples in an eruptive unit is defined as the alumina content in the rock minus the average Al_2O_3 content in the lavas from that unit.

Fig. 2-20a shows that the modal proportion of large plagioclase phenocrysts (>0.5 mm) is not correlated with ΔAl_2O_3. The Spearman rank-order correlation coefficient (r_s) for these two parameters is 0.23, and the probability that they are uncorrelated is 31%. Rank correlations are preferable to linear correlations, since testing the "strength" of the correlation does not depend on knowing the data's probability distribution (Dixon and Massey, 1957; p.208). Total plagioclase mode is plotted against ΔAl_2O_3 in Fig. 2-20b. The two parameters show a significant positive correlation, with $r_s = 0.52$. Although Fig. 2-20 suggests that lavas with high alumina have accumulated plagioclase, the process is apparently not a simple redistribution of the large phenocrysts which are present in the rocks. Although redistribution of the modal plagioclase present in these lavas can produce the dispersion in Al_2O_3 (see below), our size classification apparently does not identify the mobil plagioclase fraction for every sample.

In order to understand how the addition or subtraction of plagioclase would move a sample in the MgO-oxide composition space, the average plagioclase composition in 82-86 was added to and subtracted from 82-86 in 5, 10 and 15 wt.% proportions (Fig. 2-21). Fig. 2-21b shows that ±10 wt.% plagioclase redistribution reproduces much of the variability in alumina contents observed in the Shasta andesite and dacite samples. Note that 10 wt.% represents approximately half of the average modal plagioclase present in the lavas. Figs. 2-21a and c show that plagioclase redistribution would tend to blur, but not destroy, the

correlations between SiO_2 and MgO and between CaO and MgO. Plagioclase accumulation does not explain the variation in Na_2O at constant MgO content (Fig. 1-21d).

A striking feature of the Mt. Shasta lavas is their low FeO*/MgO ratios compared to average andesite and dacite compositions from other calc-alkaline volcanic centers. Fig. 2-22 shows FeO*/MgO vs. wt.% SiO_2 for the Mt. Shasta samples, with the fields for Medicine Lake volcano (Donnelly-Nolan, unpublished data) and Crater Lake (Bacon and Druitt, 1988). The tholeiitic-calc-alkaline line from Miyashiro (1974) is shown for reference. FeO*/MgO ratios lie between 0.5 to 1.0 for the BAs and between 1.0 and 1.5 for the andesites and the majority of dacites. The two rhyodacites have ratios of ~5. Fractional crystallization plus varying amounts of crustal assimilation have been the dominant processes operating at Medicine Lake and Crater Lake volcanos (Grove et al., 1982; Grove and Donnelly-Nolan, 1986; Bacon and Druitt, 1988). The heavy dashed line in Fig. 2-22 is part of the andesite to rhyolite fractionation trend for Medicine Lake lavas (Grove and Donnelly-Nolan, 1986). The crystallizing assemblage in the example is plagioclase, orthopyroxene, amphibole, and magnetite. The fact that the Mt. Shasta samples define a shallower trend than either the Medicine Lake or Crater Lake lavas or calculated fractional crystallization paths suggests that the Shasta trend was not produced solely by fractional crystallization. Mixing between a basaltic liquid and a silicic melt (low wt.% MgO) or assimilation of a low FeO*/MgO component (with abundant MgO)

during fractional crystallization are two processes which can produce nearly constant FeO*/MgO ratios with increasing SiO_2

TRACE ELEMENT CHEMISTRY

Ferro-magnesian trace elements in the Mt. Shasta lavas are plotted against MgO content in Fig. 2-23, while Sr and incompatible element abundances vs. MgO are shown in Fig. 2-24. Fields defined by lavas from Medicine Lake volcano (Donnelly-Nolan, unpublished data) and Crater Lake volcano (Bacon and Druitt, 1988) are shown in each figure. Trace element variations in each of the different compositional groups are discussed below.

High Alumina Basalts and Basaltic Andesites

Fig. 2-23a shows Ni abundances in the HABs and BAs, as well as the fields for Medicine Lake (Donnelly-Nolan, unpublished data) and Crater Lake (Bacon and Druitt, 1988) lavas. The HABs contain between 25 and 50 ppm Ni, and are low relative to the basaltic andesites (~150 to 200 ppm at 9 wt.% MgO) and HABs from Medicine Lake volcano (~100 to 155 ppm at 9 wt.% MgO; Chapter 1; Donnelly-Nolan, unpublished data). Ni concentrations in the BAs show a strong positive correlation with MgO content, and range from 240 ppm in the most magnesian lavas to ~90 ppm at 7 wt.% MgO. The BAs plot well within the Medicine Lake field, although the three Misery Hill samples are offset to lower Ni abundances relative to the rest of the BAs.

Chromium in the Shasta HABs ranges from 413 to 521 ppm, is

strongly correlated with decreasing MgO and overlaps the BA trend (Fig. 2-23b). For comparison, HABs from Medicine Lake rarely have more than 275 ppm Cr at 10 wt.% MgO. The overall variation in chromium content within the BAs is from ~700 to ~200 ppm, and as before the Misery Hill lavas plot below the trend defined by the Sargents Ridge and Haystack Butte samples.

Fig. 2-24 shows Sr and incompatible trace element abundances vs wt.% MgO for Mt. Shasta, Medicine Lake and Crater Lake lavas. With the exception of Sr and Y, the Shasta HAB and BA fields overlap. Sr is fairly constant (216 ± 14 ppm) in the HABs and is approximately 100 ppm lower than in the majority of BAs. Sr increases from ~300 ppm to ~400 ppm with decreasing MgO in the Sargents Ridge and Haystack lavas. These values are equivalent to Medicine Lake lavas at the same MgO content. Among the BAs, the three Misery Hill samples have the highest Sr concentrations (~600 ppm).

Variations in Rb, Ba, La and Y in the HABs are small, with averages of 7, 153, 5 and 25 ppm, respectively. The HAB fields for Rb, Ba, and La overlap those for the BAs, while Y abundances are elevated relative to the BAs (Figs. 2-24b,c,d and f). Similarly, Rb, Ba and La concentrations in the HABs and BAs lie within the Medicine Lake field, while Y concentrations are lower. Rb concentrations increase slightly with decreasing MgO contents in the Sargents Ridge and Haystack BAs; absolute abundances range from 4 to 9 ppm. Ba, La and Y show negative linear trends in the Sargents and Haystack BAs as a function of decreasing MgO content. Total variations are Ba: 114 to 231; La:

3 to 8; Y: 14 to 18 ppm. The Misery Hill lavas have elevated Ba (~250 ppm) and La (~11 ppm) values. Ba/La ratios in the basaltic andesites lie in the range 25 to 45 (Fig. 2-26)

Zr (Fig. 2-24e) in the HABs and the BAs correlates negatively with MgO, increasing from 52 to 83 ppm (HABs) and 38 to 63 (Sargents and Haystack BAs), and is low relative to Medicine Lake lavas at the same MgO content.

Andesites, Dacites and Rhyodacites

With the exception of the Panther Creek Lavas, Ni contents in the most MgO-rich andesites may vary by a factor of 5, e.g. four Sargents Ridge lavas with 4.1 to 4.2 wt.% MgO have from ~15 to ~75 ppm Ni. This is approximately twice the range exhibited by the Crater Lake and Medicine Lake andesites (Fig. 2-23a). The variability disappears with decreasing MgO content; for example, the three Misery Hill dacites with ~3 wt.% MgO have 18 ± 6 ppm Ni. The Panther Creek lavas show a strong positive correlation between Ni and MgO abundances; Ni concentrations decrease from 51 ppm at 5.6 wt.% MgO to 37 ppm at 4.2 wt.% MgO. The two McKenzie Butte rhyodacites have <5 ppm Ni.

The intermediate to silicic lavas form a well-defined trend of decreasing Cr with decreasing MgO (Fig. 2-23b). The most magnesian Panther Creek lavas have ~130 ppm Cr, while the two rhyodacites have < 5 ppm Cr. Analyses of andesites and dacites from Crater Lake and Medicine Lake volcanos show similar trends.

Rb shows a 9-fold variation in the lavas with 3 to 4 wt.% MgO. With the exception of the Panther Creek samples, the

andesites and dacites from the different cones display near-vertical trends in Rb vs MgO (Fig. 2-24a) and a total variation in Rb content from 16 to 70 ppm. The five Panther Creek samples define a smooth trend of increasing Rb with decreasing MgO; from 20 ppm at ~5.6 wt.% MgO to 33 ppm Rb at ~4.2 wt.% MgO. Andesites and dacites at Mt. Shasta and Crater Lake have approximately equivalent Rb contents. With the exception of three lavas, samples from Mt. Shasta plot in the lower half of the Medicine Lake trend

The Sargents Ridge and Misery Hill andesites and dacites show 2 to 4 fold variations in Sr and incompatible element abundances over a limited range of MgO contents (4.5 to 3.0 wt.%). Total variations are Sr: 487 to 1478 ppm; Ba: 211 to 693 ppm; La: 11 to 30 ppm; Y: 7 to 20 ppm; Zr 91-190 ppm. Fig. 2-24c shows that a large fraction of the andesites and dacites lie below the Medicine Lake and Crater Lake Ba values in the range of 4 to 2 wt.% MgO. However, both Mt. Shasta and Crater Lake andesites are enriched relative to Medicine Lake intermediate lavas in Sr (Fig. 2-24a). La and Zr values in the Mt. Shasta andesites and dacites plot either in, or slightly below, the Medicine Lake and Crater Lake fields. The Panther Creek lavas form trends that are distinct from the other andesites and dacites. Ba, La and Sr all decrease with decreasing MgO. Total variations are Ba: 591-490; La: 26-22; Sr: 976-703 (all values in ppm).

The two rhyodacite samples cover a substantial range in incompatible element abundances (in ppm): Ba, 639 to 808; Sr,

249-381; Rb, 42-65; Y, 22-44; Zr, 191-239; La, 25-115. Some of this variation may reflect the influx of incompatible elements during deuteric alteration, as 85-43, the more enriched of the two samples (except in Rb), is extensively altered. Fig. 2-25 shows ppm Rb vs wt.% K_2O variations in the Mt. Shasta lavas. The BAs have an average K/Rb ratio of 600±100. With increasing K_2O content, K/Rb ratios drop to 300 to 400. The andesites and dacites from Mt. Shasta generally lie within the Medicine Lake field, and both sets of lavas have much higher ratios than the Crater Lake samples (K/Rb $\leq$ 100).

Ba vs La variations in the three sets of lavas are shown in Fig. 2-26. Like the Medicine Lake and Crater Lake samples, the majority of Shasta andesites and dacites have Ba/La ratios between 20 and 40. The lowest Shasta lavas plot in the enriched MORB field defined by Wood et al. (1979a,b).

Correlations Among Trace and Major Elements and Modal Proportions

Table 2-18 contains the matrix of trace element and selected major element Spearman rank-order correlation coefficients for Sargents, Misery, Shastina and Hotlum andesites and dacites. In Table 2-18, zeros indicate those pairs of elements where the probability (prob.) that the data are not correlated is >10%. As expected, many of the incompatible trace elements are positively correlated with one another, e.g. Ba, Rb, La and Zr. Sr concentrations increase with decreasing Ba, Rb and Nb, and increasing La and Ce. Sr is also positively

correlated with Ni, Cr and Cu. Surprisingly, La and Ce also show positive correlations with Ni and Cr.

Correlation coefficients for Sr and the major element oxides are also given in Table 2-18. Significant negative correlations exist between Sr and SiO_2 and K_2O; while MgO, CaO and P_2O_5 are positively correlated with Sr. Sr concentrations in the andesites and dacites are also anti-correlated with the modal proportion of plagioclase phenocrysts that are greater than 0.5mm in longest dimension (r_s = -0.40). When compared with total plagioclase phenocryst content (all grains ≥ 0.05mm), the negative correlation is not significant (r_s = -0.30; prob. ~0.19). Sr content is not correlated with vol.% orthopyroxene but does show a significant correlation with modal augite (r_s = 0.46)

Sr ISOTOPIC VARIATIONS

Strontium isotopic compositions of selected Mt. Shasta lavas are reported in Table 2-10. $^{87}Sr/^{86}Sr$ ratios vary from 0.70377 to 0.70272. This striking range of isotopic compositions at the volcano has been described by Peterman et al. (1970) and Mertzman (1986). Fig. 2-27a shows $^{87/86}Sr$ ratios as a function of MgO content with the field defined by calc-alkaline lavas (HAB to andesite) at Medicine Lake volcano (Grove et al., 1982; Grove et al., 1988; Chapter 1; Kinzler, unpublished data). There are two trends in the Mt. Shasta data. One approximately horizontal trend stretches from BA to andesite and dacite and has $^{87/86}Sr$ ratios of ~0.7036. The other group consists of andesites and

dacites with non-radiogenic ratios of 0.7031 to 0.7028. The Medicine Lake trend shown in Fig. 2-27a is indicative of fractional crystallization accompanied by assimilation of continental crust (Grove et al., 1982). A subset of the andesitic lavas at Mt. Shasta show as an inverse correlation between $^{87/86}Sr$ and Sr abundance (Fig. 2-27b). The most Sr-rich sample, 85-48b (1446 ppm) has the lowest 87/86 ratio (0.70272). For comparison, Sr isotopic compositions of clean whole rock and mineral separates from the Trinity ophiolite range from 0.7033 to 0.7025, although Sr abundances are 2 to 3 orders of magnitude lower (Jacobsen et al., 1984). The lowest $^{87/86}Sr$ ratios at Mt. Shasta plot well within the normal MORB field (0.7022-0.7030; Allegre et al., 1983). Basaltic andesites and intermediate lavas at Mt Lassen, south of Shasta also have low $^{87/86}Sr$ ratios ($\geq$ 0.7029) and low incompatible element to Sr ratios (Bullen and Clynne, 1987).

EXPERIMENTAL PHASE RELATIONS

One-Atmosphere

The results of one-atm melting experiments on basaltic andesite samples 82-94a, 75SH-70, and andesite samples 85-55 and 83-58 are reported in Table 2-14a. Phenocryst abundances in the first three compositions are < 15 vol.%; sample 83-58 contains < 2 vol.% phenocrysts. Phase compositions are given in Table 2-15. Phase appearance temperatures are summarized in Fig. 2-28, and glass compositions are displayed on the Oliv-Cpx-Qtz pseudoternary subprojection in Fig. 2-33. Some of the shorter

andesite experiments (24-48 hrs) did not produce well-developed "equilibrium" overgrowth rims on the plagioclase and pyroxene grains, and crystalline phase compositions are not reported for these experiments. Nevertheless, we have included these runs in mass balance calculations using average core compositions. Calculated phase proportions were the same within uncertainty using either average rim or average core+rim compositions in some of the longer duration experiments.

Olivine is the liquidus phase for 82-94a, appearing at ~1270°C, followed by plagioclase at ~1204°C and augite at ~1180°C (Fig. 2-28). Orthopyroxene is present in the lowest temperature run at 1140°C and is often found as a reaction rim around olivine. Average Fe-Mg K_Ds for olivine and augite are 0.29 ± 0.01 and 0.25 ± 0.01 (where $K_D=(Fe/Mg)^{xtl}/(Fe/Mg)^{liq}$, with all Fe as Fe^{2+}). These values are consistent with olivine and high-Ca pyroxene K_Ds determined from high alumina and mid-ocean ridge basalts (see Chapter 3). The plagioclase-liquid Ca-Na K_D (where $K_D=(Ca/Na)^{xtl}/(Ca/Na)^{liq}$) is ~1.3, an appropriate 1-atm value for this bulk composition (see Fig. 3-2b, Chapter 3). The Fe-Mg K_D for orthopyroxene-liquid in the lowest temperature run is 0.24. Along the low pressure cotectic, 82-94a crystallizes olivine, plagioclase and augite in the proportions 10:60:30.

In 75SH-70, one of the intermediate MgO basaltic andesites, plagioclase is the first phase to crystallize. Olivine joins plagioclase within 10-15°C of the liquidus, and oliv + plag co-crystallize in the proportions ~0.75 plag to 0.25 oliv. Augite was not observed in the lowest temperature experiment (~46°C

below the liquidus). The average olivine K_D is 0.29; Ca-Na exchange coefficients between plagioclase and liquid fall in the range 1.4 to 1.7.

85-55 is the most magnesian andesite collected at the volcano. Its near liquidus phase relations are summarized in Fig. 2-28 (the liquidus was not determined for this composition). Plagioclase is the first phase to crystallize, and is joined by orthopyroxene at ~1170°C. Augite is present in the 1147°C run.

The 1-atm relations for andesite 83-58 are marked by a high liquidus temperature (~1212°C) and a large primary plagioclase phase volume. Plagioclase crystallizes for ~45°C before orthopyroxene appears. Between ~1150 and 1102°C, cotectic proportions of plag and opx are ~0.75 and 0.25. Over this temperature interval, silica content increases from 66 to 70 wt.%. The lowest temperature run (1055°C) contained plagioclase, orthopyroxene and augite. The co-existing glass has 74 wt.% silica and less than 1 wt.% MgO. In the 1102 and 1055°C runs, the Ca-Na K_D for plagioclase is 2.3 and 4.4, respectively. The orthopyroxene K_D decreases from 0.22 at ~1100°C to 0.16 at 1055°C. The Fe-Mg K_D for augite in the lowest temperature run is 0.08. Juster and Grove (1988) also found that pyroxene Fe-Mg K_Ds decreased markedly as the coexisting glass approached rhyolite compositions.

Fig. 2-29 shows the glass compositions projected onto the Oliv-Cpx-Qtz pseudoternary diagram. The phase boundaries are based on the co-existing crystalline assemblages in each

experimental run, and are topologically similar to those constructed by Walker et al. (1979) and Grove and Bryan (1983). The major difference is in the apparent absence of a pigeonite phase volume in Fig. 2-29. The oliv-plag-aug cotectic for the Shasta lavas terminates at a reaction point involving orthopyroxene as opposed to pigeonite. The same relationship (opx replacing pigeonite) was found by Baker and Eggler (1983) in a series of 1-atm experiments on Aleutian HAB and andesites. Pigeonite is the first low-Ca pyroxene to crystallize from high-Al basalt and MORB liquids (Grove et al., 1982; Grove and Bryan, 1983; Tormey et al., 1987; Juster and Grove, 1988). Grove and Juster (1987) have shown that the type of low-Ca pyroxene that crystallizes first from basaltic to andesitic compositions is a linear function of temperature and the Mg* ratio of the liquid. With increasing Mg* at constant temperature and bulk composition, orthopyroxene replaces pigeonite as the first low-Ca pyroxene. For example, calc-alkaline magmas that crystallize orthopyroxene at QFM will crystallize opx above the Nickel-Nickel-Oxide (NNO) buffer. As discussed in the major element section, the Shasta lavas have uniformly high Mg#s. The basaltic andesite liquid that is saturated with opx at 1140°C has an Mg# of 52. MORB and HAB liquids that are saturated with pigeonite at 1140±5°C have Mg#s between 46 and 43 (Grove et al., 1982; Grove and Bryan, 1983; Juster and Grove, 1988). This relationship explains why pigeonite is observed in the groundmass in the BA lavas, when, based on Fig. 2-29, the first low Ca-pyroxene should be opx. Fractional crystallization during cooling

produces a sufficient decrease in Mg* relative to the equilibrium value at the same temperature that pigeonite crystallizes instead of orthopyroxene.

Moderate Pressure

The results of an initial set of 2 kbar water saturated melting experiments at NNO on a Shasta andesite are summarized in Table 1-14b. Over the temperature interval 980 to 930°C, the runs contain plagioclase, orthopyroxene and augite. Amphibole replaces augite in the lowest temperature experiment (900°C). Water content in the glasses vary from ~5 wt.% at 980 to ~9 wt.% at 900°C (values determined by difference). Sodium counts were constant during glass analyses indicating that Na was not being volatilized. On an anhydrous basis, SiO_2 increased from 66 wt.% at 980° to 70 wt.% at 900°C. Although the experiments were run in Fe-Pt capsules, mass balance calculations show that the glasses have lost between 50 and 75% of the bulk FeO. Apparently the capsule alloy capsule contained too little iron. The pyroxenes and amphiboles in these experiments are very magnesian, indicating that the solid phases have at least partially re-equilibrated with the changing liquid compositions. Mg/(Mg+Fe) ratios in the pyroxenes vary from 0.94 to 0.82. The plagioclase Ca-Na K_D in these runs is 4.9±0.6; 1 to 2 kbar water saturated and undersaturated experiments on a Mt. Saint Helens dacite (Rutherford et al., 1985) yield K_D values in the range 3.5 to 4.3. "FeO" was included as a separate phase during mass balance calculations in order to compensate for iron loss.

Weight fraction of liquid varies from ~0.76 at 980° to 0.51 at 900°C (these proportions normalized to 1 on an "FeO" free basis). Calculated mean cotectic proportions over the temperature interval 980 to 930°C are approximately 0.55 plag, 0.28 opx and 0.17 cpx. These results demonstrate the extent to which water destabilizes plagioclase; at one-atm, the proportions of plagioclase to pyroxene are ~75:25. The 2-kbar phase proportions and plagioclase K_Ds will be used as a starting point for modeling fractional crystallization in the andesites at Mt. Shasta.

INTENSIVE PARAMETERS

Basaltic Andesites

In 82-94a, augite joins olivine and plagioclase after ~40% crystallization at 1-atm. The Mg* ratio in the liquid at the point of augite appearance is between 0.66 and 0.62 (Tables 2-14a and 2-15; Fe^{2+} calculated using eqn (1) from Kilinc et al., (1983)). The phenocryst assemblage in 82-94a suggests that augite preceded plagioclase and joined olivine after an interval of olivine crystallization that is shorter than that observed in the 1-atm experiments. Calculated Mg* ratios of liquids in equilibrium with the most magnesian olivine and augite phenocrysts in sample 82-94a are shown in Fig. 2-30. Also plotted are the Mg* ratio in the glasses which bracket the appearance of augite in the 1-atm experiments. The Mg* ratio at the 1-atm liquidus was calculated at the QFM buffer using the bulk composition and a temperature of 1270°C. Note that augite

appearance based on phenocryst compositions occurred at a higher liquid Mg* ratio than expected based on the 1-atm phase relations. K_D values used to calculate model liquid Mg*s from the olivine and augite phenocryst compositions are 0.31±0.03 (Irvine, 1979) and 0.23±0.02. The augite K_D was calculated from the experimental data in Table 2-15 and from pyroxene and glass compositions reported by Tormey et al. (1987). The abundance of Fe^{2+} in each pyroxene was calculated using charge balance constraints.

Gust and Perfit (1987) report high pressure phase relations on a magnesian lava (MK-15) similar in composition to 82-94a. Above 5 kbars, augite replaces plagioclase as the second crystallizing phase, and between 5 and 10 kbar the oliv+aug field approaches the liquidus. A shrinking olivine primary phase volume is consistent with the Mg* relationships shown in Fig. 2-30. If the high pressure anhydrous phase relations of MK-15 can be applied to the evolution of sample 82-94a, then the phenocryst assemblage in sample 82-94a crystallized at pressures between 6 and 10 kbars.

Andesites, Dacites and Rhyodacites

We have estimated the pre-eruption temperatures and oxygen fugacities in the Mt. Shasta andesites and dacites from co-existing magnetite-ilmenite pairs. The thermodynamic formulation of Spencer and Lindsley (1981) with updated Margules parameters from Anderson and Lindsley (1985) was used to estimate T and fO_2. The mole fractions of ulvospinel and ilmenite in coexisting

oxides were computed using the mineral recalculation schemes of Lindsley and Spencer (1982). Average temperatures for selected Sargents Ridge, Misery Hill and Hotlum lavas range from ~775 to 910°C, with most samples between 850 and 900°C. Oxygen fugacities for the Sargents and Hotlum lavas lie ~1/2 to 2 orders of magnitude above NNO, while fO_2s for the Misery data cluster around the NNO buffer curve. Average temperatures do not correlate with MgO content or phenocryst assemblage, and temperature estimates for amphibole bearing rocks overlap with those from non-amphibole bearing samples. However, the Sargents Ridge lavas containing amphibole are more oxidizing than those rocks that are amphibole-free. Both amphibole and non-amphibole bearing Misery Hill samples plot along the NNO buffer curve. Calculated temperature and log fO_2 for the McKenzie Butte rhyodacite are 830°C and -13.2 (~NNO), respectively.

The occurrence of amphibole in the andesitic to dacitic lavas at Mt. Shasta places some constraints on pH_2O for a given depth of the magma chamber. The amphibole appearance temperature in andesitic liquids lies between 900 and 1000°C over the pressure range of 4 and 10 kbars, and at a specific pressure, does not begin the decrease until the mole fraction of H_2O is less than 0.5 (Eggler, 1972a,b; Eggler and Burnham, 1973; Allen and Boettcher, 1978; Ritchey and Eggler, 1978; Rutherford et al, 1985). This range of amphibole appearance temperatures is above the calculated two-oxide temperatures for the andesites and dacites for these samples. Thus, if the intermediate lavas at Mt. Shasta evolved at depths of greater than 8 km, pH_2O must

have been less than $0.5(P_{total})$. We would expect amphibole to be present in all of the andesites and dacites if pH_2O had been > $0.5(P_{total})$. At pressures between 1 and 2 kbars, andesitic magmas must be close to water saturated in order to stabilize amphibole at temperatures of 850 to 900°C. Following the same reasoning, if the intermediate lavas evolved at depths < 6 km, then pH_2O must have been close to P_{total}. However, if pH_2O had been << P_{total}, we would not expect to find any amphibole preserved in the andesites and dacites.

The presence of amphibole pseudomorphs in lavas that contain apparently stable amphibole suggests that temperature and/or volatile content has varied during the evolution of these lavas. Repeated mixing between hot, dry mafic magmas and more evolved, water-rich silicic liquids is consistent with this observation, as well as the complex, oscillatory zoning observed in some orthopyroxene phenocrysts (Figs. 2-6g, h, i, j, and l).

Summary

The compositions of augite phenocrysts in 82-94a coupled with pressure-temperature phase relations determined on a similar bulk composition (Gust and Perfit, 1987) suggest that the phenocrysts in this sample, if anhydrous, formed at pressures greater than 5 kbars.

The sporadic occurrence of amphibole and the temperatures calculated from coexisting oxides in the andesite and dacite lavas indicate that either (1) P_{total} > 4 kbar and pH_2O < $0.5(P_{total})$ or (2) P_{total} < 4 kbar and pH_2O was between 0.5 and

1.0 times P_{total}. If the basaltic andesites and andesites evolved at approximately the same depth, then the andesites and dacites must have been water understaturated.

DO THE MT. SHASTA LAVAS REPRESENT LIQUIDS?

Porphyritic lavas may or may not represent liquid compositions. If phenocrysts in a phyric lava are present in cotectic proportions, then the bulk composition will still lie along the cotectic. However, selective accumulation or phenocryst redistribution will modify the liquid composition, blur the liquid line of descent and complicate the interpretation of forward and mass balance models. The correlation between modal plagioclase and bulk alumina, discussed earlier, suggests that some of the andesite and dacite lavas at Shasta may have experienced plagioclase accumulation. Before attempting to model the geochemical evolution of the Mt. Shasta lavas, we consider the question of whether the basaltic andesite and andesite samples represent liquid or near-liquid compositions.

Basaltic Andesites

As summarized in Table 2-12, phenocryst contents range from 9 to 17 vol.% in the basaltic andesites. In the MgO-rich samples, olivine is major phenocryst phase and the magnesian character of these lavas may result from olivine accumulation. We test the hypothesis of olivine accumulation by adding olivine to the average of the three samples that mark the first

appearance of augite in the Sargents Ridge and Haystack Butte lavas (Fig. 2-31). The composition of this olivine was calculated using K_D of 0.29 (all Fe as FeO; Chapter 3) and the average FeO/MgO ratio in the three samples. The tick marks in Fig. 2-31 represent the weight fractions of olivine added. Although olivine accumulation successfully matches the Al_2O_3 vs MgO variation, the addition line does not reproduce the CaO content in the most MgO-rich lavas. The curvature of the basaltic andesite trend on the Ni vs MgO plot (Fig. 2-23a) is also not consistent with simple olivine accumulation, which would tend to form a straight line in Ni-MgO space. The curvature of the basaltic andesite compositions on the Ni-MgO plot is consistent with olivine fractionation and the experimentally determined Ni partition coefficient for olivine-liquid (Hart and Davis, 1978; Elthon, 1987).

Comparing calculated liquidus olivine compositions to the most forsteritic olivines in the magnesian basaltic andesites provides an additional test for olivine accumulation. If these lavas accumulated olivine, then the calculated liquidus olivine compositions will have higher Mg/(Mg+ΣFe) ratios than the observed phenocrysts. Fig. 2-32 shows that this is not the case and we may reject the hypothesis of olivine accumulation. The forsterite brackets were calculated at QFM and NNO and include uncertainties in the Fe^{2+}-Mg K_D (0.31±0.03; Irvine, 1979) and the MgO and FeO contents in the bulk rocks. The open circles represent the average of the four or five most magnesian olivine core compositions in each sample; in every case, these averages

lie within the brackets. Based on the above criteria, it is likely that the basaltic andesites represent liquid or near-liquid compositions.

Andesites and Dacites

The modal proportions of plagioclase in the vast majority of Shasta andesites and dacites vary from 15 to 38 vol.% (Table 2-13). These values are typical of Cascade-Alaska-Aleutian lavas with between 60 and 64 wt.% silica, based on the compilations of Ewart (1979, 1982). The abundant presence of plagioclase phenocrysts is a ubiquitious feature of andesites and dacites and poses problems for determining if any given sample represents a liquid composition.

The mixed character of the intermediate lavas at Mt. Shasta and the fact that $K_D^{pl/liq}$ is poorly known as a function of bulk composition, pressure and pH_2O precludes matching calculated and observed plagioclase compositions as a test for phenocryst accumulation. However, 1-atm liquidus temperature-bulk compositional relationships may provide a useful test for plagioclase accumulation in andesite and dacite magmas. Thompson (1973) observed that liquidus temperatures (T_L) for terrestrial lavas vary smoothly as a function of MgO content. Crawford et al (1987) have used this observation to distinguish high alumina basalts that may have accumulated plagioclase from those lavas that represented liquids. Since most plagioclase compositions melt at much higher temperatures than common basalts and andesites, adding plagioclase to a melt should raise the

liquidus temperature of the new bulk composition above a trend defined by aphyric lavas. We have calibrated T_L determined at one-atm as a function of bulk composition using 12 aphyric basalts and andesites and a linear expression of the form,

$$T_L\ (°C) = a + b(Mg^*) + c_iX_i + c_2X_2 \qquad (1)$$

where X_1 and X_2 are the mole <u>percents</u> of Fe_2O_3 and K_2O and a, b, c_1 and c_2 are the fitted parameters. Ferrous iron was calculated using the expression from Kilinc et al. (1983) and the reported temperature and log fO_2 of the superliquidus run. Bulk compositions and one-atm liquidus temperatures used to calibrate eqn (1) are reported in Tables 2-16 and 2-17. The initial inputs to the model were the midpoints of the liquidus temperature brackets given in Table 2-16. These initial attempts resulted in large model residuals for some compositions. To reduce these residuals, the temperatures were adjusted within the experimental brackets. Often varying T_L for one composition reduced the residuals for all other bulk compositions. Adjusting the liquidus temperature within the experimental brackets is permissible, since properly determined brackets only require that the actual value lie somewhere inside. The final set of calculated coefficients and their uncertainties are:

$a = 1195.9 \pm 11.2$ (°C)

$b = 145.8 \pm 12.8$ (°C)

$c_1 = -112.1 \pm 5.2$ (°C/mole%)

$c_2 = -51.05 \pm 3.20$ (°C/mole%)

Eqn (1) reproduces the adjusted liquidus temperatures with a mean error of 0.07%; the largest residual is ~3°C.

Liquidus temperatures determined at QFM for 5 Shasta andesites and dacites with varying modal proportions of plagioclase are given in Table 2-17. Fig. 2-33 compares the difference between the measured and calculated liquidus temperatures (ΔT_L) for each sample with the rock's vol.% plagioclase. The uncertainty on ΔT_L is ~20°C. All five of the Shasta lavas plot within 25°C of the zero line in Fig. 2-33, suggesting that these lavas have not experienced plagioclase accumulation. This conclusion is consistent with the relationship between ΔAl_2O_3 and modal plagioclase (Fig. 2-20), which suggests that "cotectic" plagioclase content in the Shasta lavas are on the order of 20 vol.%. The HAB AT-1 from Baker and Eggler (1983) is also plotted on Fig. 2-30. ΔT_L and modal plagioclase for this sample are 120°C and 29 vol.%, respectively, indicating that this sample does not represent a liquid. Crawford et al. (1987) also concluded that AT-1 did not represent a liquid composition.

PETROGENESIS OF LAVAS AT MT. SHASTA

The 1-atm phase diagram developed above provides a convenient starting point for discussing the evolution of the lavas at Mt. Shasta. All samples are projected onto the Oliv-Cpx-Qtz pseudoternary in Fig. 2-34, along with the 1-atm phase boundaries from Fig. 2-29. The heavy arrows outline the expected low-pressure fractionation path for one of the magnesian basaltic andesites. At 1-atm, the first phase to crystallize is olivine, followed by plagioclase, and the projected residual liquids move away from the olivine corner until they reach the oliv-plag-aug boundary curve. Cotectic crystallization of these three phases continues until the residual liquid reaches the opx-in reaction point. Under conditions of fractional crystallization, the liquid will move through the reaction point and continue down temperature along the aug-plag-opx cotectic. This low pressure path does not pass through the projected positions of the evolved basaltic andesites or the larger group of andesites and dacites. In the sections below we use mass balance and forward modeling techniques to test whether major element variations within and between groups of lavas can be produce by crystal fractionation. The mass balance problems were solved using the non-linear least squares algorithm of Albarede and Provost (1977), which includes the compositional uncertainties on each phase. The compositions of olivine and plagioclase in equilibrium with a specific residual liquid were calculated using Fe-Mg, or Ca-Na K_Ds and stoichiometric constraints (see Chapter 4 for a discussion of the method).

Errors on these two phase compositions were determined by propogating the errors on the K_Ds and liquid compositions through the calculation. The compositions and uncertainties for the remaining phases are discussed in each section. For a given model, the probability function Q (Bevington, 1969) provided an unbiased estimation of the "goodness-of-fit". We accepted models with Q-values ≥ 0.05, which is equivalent to a 95% confidence level. The forward modeling was based on the fractional crystallization algorithm described by Grove and Baker (1984).

Basaltic Andesite Fractionation Models

As discussed earlier, the 1-atm phase relations in BA sample 82-94a differ substantially from the crystallization sequence inferred from the phenocryst assemblage. The relative proportions of olivine and augite (3:2) suggests that sample 82-94a was close to multiple saturation with respect to olivine and augite. The trace modal abundance of plagioclase in sample 82-94a indicates that plagioclase appearance was suppressed relative to augite at the P and T conditions of crystallization.

Based on its phenocryst assemblage, sample 75SH-70 was multiply saturated with olivine, plagioclase and augite. The 1-atm phase relations of sample 75SH-70 preclude relating it to 82-94a by low pressure fractional crystallization. Furthermore, low pressure crystallization of 75% plagioclase and 25% olivine (1-atm proportions from sample 75SH-70) is not consistent with the negative correlation between Al_2O_3 and MgO observed in the basaltic andesites (Fig. 2-19c). Like 82-94a, the 1-atm

experiments and the phenocryst assemblage for 75SH-70 suggest that at the P, T and pH_2O conditions of crystallization, plagioclase was suppressed while the appearance of augite was enhanced relative to olivine.

In an effort to smooth out minor chemical fluctuations in the basaltic andesites prior to modeling, the major element oxides have been described by linear or 2nd order polynomial functions of MgO. We place no petrologic significance on our fits but use them simply to calculate mean starting and end point compositions for modeling. Uncertainties on the liquid compositions were calculated from the 2σ fraction errors reported in Table 2-1. The change in phenocryst assemblage from olivine + spinel in the more magnesian lavas to olivine + spinel + plagioclase + augite in the more evolved members of the suite suggest a two stage fractionation process. Accordingly, three liquids have been calculated at MgO values of 10.82, 8.5 and 7.0 wt.%. The intermediate value was selected to produce a liquid just prior to augite saturation.

Mass balance calculations: Olivine, plagioclase, augite and spinel compositions used in the mass balance equation,

7.0% MgO liq + oliv + plag + aug + sp = 8.5% MgO liq

are summarized in Table 2-19. Olivine and plagioclase compositions were calculated using Fe-Mg and Ca-Na K_D values of 0.30 ± 0.03 and 3.0 ± 0.1, respectively, and the 7.0 wt.% MgO

liquid. The plagioclase K_D was determined from the most calcic plagioclase core compositions and bulk CaO and Na_2O contents in four BA samples. The Fe-Mg content in the augite has been recalculated using a K_D of 0.25 ± 0.03 and the FeO and MgO contents in the calculated liquid. The remaining oxides in the model augite represent average values from phenocryst core compositions. Similarly, the spinel composition used in the model is the average of spinel analyses collected from all of the basaltic andesites. Although the uncertainties in the phase compositions are not reported in Table 2-19, they were included in the non-linear least-squares algorithm. The solution to the mass balance expression is also given in Table 2-19. Normalized phase proportions are 34.7 ± 4.8 oliv; 31.4 ± 9.3 plag; 33.2 ± 7.3 aug; 0.3 ± 0.2 sp and 89.0 ± 0.9 percent liquid remaining. The calculated proportions of augite are higher than the normalized modal abundance (wt.%) of augite observed in the BAs (≤25).

We were not able to model the path from 10.8 MgO to 8.5 wt.% MgO successfully. No combination of oliv ± plag ± aug ± sp produced an acceptable fit. Q-values ranged from 10^{-15}, for oliv + sp to 10^{-5} for oliv + plag + aug + sp. Either these more MgO lavas do not represent a liquid line of descent or another phase was involved in their evolution. Note that there is no petrographic evidence for assimilation in the Sargents Ridge basaltic andesites and no strong evidence for crustal assimilation in the Haystack Butte lavas. Nonetheless, the presence of the Trinity ultramafic sheet underneath the volcano

suggests two potential criptic assimilants: orthopyroxene and free silica. At pressures corresponding to the depth of the peridotite mass, orthopyroxene will not be a liquidus phase for the basaltic andesites and the magmas may dissolve orthopyroxene while moving through the massif. Experiments of Fisk (1986; 1987) suggest that this dissolution process may be quite complicated. We have modeled this process as a simple mass balance problem. The second possible assimilant is free silica released by dehydration reactions of the type

$$\text{serpentine} \rightarrow \text{olivine} + H_2O + SiO_2$$

The orthopyroxene used in the mass balance expression is the mean of 17 analyses reported by Quick (1981). The second assimilant composition was calculated by subtracting olivine from average serpentine and talc compositions from the Trinity Peridotite (Peacock, 1987) and renormalizing the remaining mass. These two assimilant compositions were included in the expression,

8.5% MgO liq + phase 1 + phase 2 + ... + assim. = 10.8% MgO liq.

As before, no model produced an acceptable Q-value, although the assemblage oliv, plag, aug, sp and opx resulted in the lowest χ^2 value (Q=0.009). The ratio of mass assimilated to mass crystallized (R) for this model is 0.4. Note that the model is not consistent with the phenocryst assemblage of olivine, spinel

± rare plagioclase. Since we were unable to constrain the major element variations, we have not attempted to model the trace element trends between 10.9 and 8.5 wt.% MgO. Nevertheless, the decrease in Ni and Cr over this MgO interval indicates that olivine and spinel must be important fractionating phases.

Forward modeling: Using the fractional crystallization algorithm described by Grove and Baker (1984), we have computed a fractionation path starting with the 8.5% MgO liquid (Table 2-21). The phase proportions from the mass balance calculations were used as starting solutions. By trial-and-error modeling, the phase assemblage that produced the closest match to the major element data is 38.2% oliv, 20.4% plag, 41.0% aug and 0.4% sp. These proportions are within the 2σ uncertainties on the proportions calculated from the mass balance regression. With the exception of K_2O, FeO proved to be the most difficult element to fit. In the current model, iron remains essentially constant. We were not able to reproduce the slight drop in FeO content observed between 8.5% and 7.0% MgO. Fig. 2-35a compares the liquid composition from the fractionation path at F = .918 to oxide values calculated with the regression equations at MgO = 7.0 wt.%. With the exception of K_2O, the fits are all within 3%. Potassium from the fractionation model differs by ~11% from the expected composition.

Following the approach used for the major elements, linear and exponential equations have been fit to Ni, Zr, Sr, Rb, Ba and La, and elemental abundances have been calculated at MgO

values of 8.5 and 7.0 wt.%. The former values were used as inputs to the fractionation calculation and the calculated values are compared with the regression values in Fig. 2-35b. The partition coefficient for Ni was calculated from the expression of Elthon (1987), the remaining partition coefficients are from Henderson (1982) and were held constant during fractionation. Ni, Cr, Sr and Zr are within 94% of the expected values, while Rb, Ba and La are within 90 to 95% of the predicted values.

Origin of the Basaltic Andesites

The magnesian basaltic andesites at Mt. Shasta appear to be unique among lavas from the high Cascades. A survey of rocks from Medicine Lake (Chapter 1; Donnelly-Nolan, unpublished data), Crater Lake (Bacon and Druitt, 1988), Newberry (Higgins, 1973) and the High Cascades between Crater Lake and Mt. Hood (Conrey, unpublished data) failed to produce examples of lavas with >52 wt.% SiO_2 and > 8 wt.% MgO. We conclude that a set of processes unique to the Mt. Shasta area produced the Sargents Ridge, Misery Hill and Haystack Butte basaltic andesites. HAB is ubiquitous in the Cascades and appears to be involved in the generation of andesites at many of the Cascade volcanos (McBirney and White, 1982; Grove et al., 1982; Bacon and Druitt, 1988). In the following discussion we will explore whether interaction between HAB and harzburgite is capable of producing the Mt. Shasta basaltic andesites. Fig. 2-36 shows the fields for Medicine Lake and Mt. Shasta high-Al basalts and the Shasta

basaltic andesites projected onto the Oliv-Cpx-Qtz pseudoternary, along with the 1-atm phase boundaries. At moderate to low pressures, the HABs lie in the olivine ± plagioclase phase volume, and if placed in contact with a harzburgite assemblage, should dissolve orthopyroxene and crystallize olivine. The vectors in Fig. 2-36 show the direction that the high alumina basalt liquids would move subject to olivine crystallization and orthopyroxene dissolution. The sum of these two vectors encompasses the basaltic andesite field on the pseudoternary. The Trinity peridotite is predominately harzburgite (Quick, 1981) and we suggest that HAB magmas traversing this ultramafic body may have interacted with the orthopyroxene to produce the magnesian basaltic andesites erupted at Mt. Shasta.

A number of recent papers have investigated how silicic and basaltic magmas interact with ultramafic material and how the liquid compositions would change as a result of such a process (Fisk, 1986; 1987; Kelemen and Ghiorso, 1986; Kelemen, 1986). Interaction between a mid-ocean ridge basalt and oliv + opx at 1-atm produces a boundary layer liquid which is enriched in silica, calcium and alkalies relative to the starting glass (Fisk, 1986; 1987). The increase in K_2O and Na_2O in the boundary layer over that expected from crystallization of the observed olivine is a result of the diffusion of the alkalies from the basalt into the silica-rich liquid (Watson, 1982, Fisk, 1986). Given this complicated behavior of the alkalies, we have set the uncertainties on Na_2O and K_2O to 1.0 in the mass balance

expression HAB - oliv + opx = BA, effectively minimizing the leverage that these two oxides exert on the fit. The phase compositions used in the mass balance problem are reported in Table 2-22. The relatively low Mg#s in the Shasta high-Al basalts suggest that these lavas have undergone low pressure olivine fractionation and are not suitable primary basalt compositions for the mass balance calculation. Instead, we used one of the more magnesian Medicine Lake HABs (Mg#=70). The basaltic andesite mean composition is taken at 10.82 wt.% MgO (see Table 2-20). The "best-fit" solution (Q = 0.0004) is 83% HAB - 19% oliv + 36% opx = BA; the ratio of mass assimilated to mass crystallized is 1.9. The sodium and potassium values calculated from the regression are ~32 and 84% lower than those observed in the basaltic andesite. These differences can be reconciled by diffusive exchange of K_2O and Na_2O between the basaltic andesite and the high-Al basalt or by minor assimilation of the more silicic rocks that lie above and below the Trinity ophiolite (Fuis et al., 1987).

Starting with Cr values of ~200 ppm, the assimilation of orthopyroxene can easily produce the high Cr values observed in the primitive basaltic andesites. The model is less successful in reproducing the > 200 ppm Ni values in the basaltic andesites. Starting with 245 ppm Ni in the HAB, the phase proportions from the model (Table 2-22) yield a predicted Ni value of ~175 ppm in the BA. The expected value is ~240 ppm. Olivine and augite partition coefficients for Ni were 9.2 and 2.6 (Elthon, 1987; Henderson, 1982) and were held constant since

MgO remains relatively constant during this assimilation, fractional crystallization (AFC) process. Nickel concentration in the orthopyroxene was calculated from the average olivine value (Quick, 1981) and an average $(D_{Ni})^{opx/oliv}$ determined from the data of Stosch (1981), Hervig and Smith (1982) and Brearley et al. (1984). Fe-Ni sulfide blebs (≤ 20μm in size) were found in one of the ultramafic inclusions collected as sample locality 85-48. Although present in trace abundance in the inclusion, the blebs contain > 160,000 ppm Ni. Assimilation of ~0.05% of this material would greatly improve the fit between the model and the observed Ni content. With the exception of Sr and Y, trace element contents in the Medicine Lake HABs and the Shasta BAs are similar, and thus consistent with such an AFC process.

An R of ~2 violates simple heat budget constraints, which assume that basalt undergoes fractional crystallization to supply both the heat required to raise the solid to the temperature of the basalt and the latent heat necessary for melting (Bowen, 1928; Grove and Baker, 1984). This heat budget problem can be reconciled if the mass of HAB in the magmatic system was 2 to 3 times the mass of basaltic andesite. The crystallization of this larger volume of HAB provides the heat to drive the process. The evolved high-Al basalts around the flanks of the volcano may represent the products of fractional crystallization that drove the assimilation process.

Andesite, Dacites and Rhyodacites

In a long-lived volcanic system like Mt. Shasta, fractional crystallization, mixing, episodic injection of basaltic magma and assimilation may all occur and leave their chemical signatures on the erupted lavas. Petrographic and geochemical evidence point to the importance of open system processes in the evolution of the intermediate volcanics at Mt. Shasta. Quartz xenocrysts and ultramafic to mafic xenoliths are fairly common in the andesite and dacite lavas. The extremely large variations in certain trace elements at nearly constant MgO-values are almost impossible to reconcile with any simple fractional crystallization model. Moreover, the differences in $^{87/86}Sr$ ratios between the parental basaltic andesites and many of the andesites suggests that either, (1) some of the andesites are not related to the sampled basalts or are related to basalts with much higher Sr concentrations and lower 87/86 ratios which were not sampled at the volcano, or (2) the trace element and isotopic compositions of the intermediate lavas reflect the addition/assimilation of one or more components with a high Sr and low 87/86 signature. The reminder of this Chapter will explore this second possibility.

Fractional crystallization - basaltic andesite to andesite: In this section, we explore whether the more magnesian andesite liquids may be related to the basaltic andesite compositions by fractional crystallization. Starting and end-point compositions for the group of andesite and dacite lavas are based on linear

fits to the oxides using MgO as the independent variable (excluding Panther Creek). Alumina is uncorrelated with MgO and was determined by difference after calculating all other oxides. The slope and y-intercept for each equation is given in Table 2-23. This exercise confirms what is visually apparent in Fig. 2-19: the major oxides, with the exception of Al_2O_3, vary linearly with MgO in the andesite and dacite lavas.

The most magnesian of the large group of andesites at Mt. Shasta have MgO contents of ~4.5%. The average andesite calculated from the regression equations at 4.5% MgO is given in Table 2-24. Plagioclase, augite and orthopyroxene compositions calculated to be in equilibrium with this liquid are also given in the Table. Three plagioclase compositions were calculated using K_Ds of 2, 3 and 4. The minor element abundances in the pyroxenes represent averages of rim compositions from samples 85-57, 82-102 and 85-59. The FeO and MgO contents in the pyroxenes were calculated from the Fe/Mg ratio in the model liquid and K_Ds of 0.21 for opx and 0.23 for augite (Table 2-15; Grove, unpublished data). Using different combinations of these phases we have test the following mass balance equations,

andesite + plag + oliv + aug + mag/ilm = BA at 7% MgO

andesite + plag + opx + aug + mag/ilm = BA at 7% MgO

As before, statistical criteria were used to accept or reject a particular model based on the χ-squared value and the degrees of

freedom in the problem. The acceptable solution for the first equation is 26.1% plag (An_{65}), 6.6% oliv, 8.4 aug, 3.0% mag, 0.6% ilm and 55.3% liquid. All three plagioclase compositions produced good fits in the second mass balance expression. The calculated proportions of magnetite and ilmenite lie in the range 3.9 to 4.2 wt.%. The lack of Fe-Ti oxide phenocrysts in both the basaltic andesites and primitive andesites suggests that both of these models are not petrologically reasonable. We will return to the question of the origin of the magnesian andesites below.

Fractional crystallization - andesite to dacite: The 2 kbar plagioclase, augite and orthopyroxene proportions were used as a starting point in the andesite to dacite fractionation models. The starting composition is the regression-based liquid calculated at 4.5% MgO using the linear coefficients from Table 2-23. The plagioclase Ca-Na K_D was 4.9 and Fe-Mg K_Ds for opx and augite were 0.21 and 0.23. Calculated liquids are given in Table 2-25. The major discrepancy between the calculated path and the observed andesite-dacite chemical variations is in TiO_2 and FeO. Both of these oxides increase during the calculation, while the observed values decrease with decreasing MgO. Based on the TiO_2-MgO and FeO-MgO trends (Fig. 2-19), mag/ilm must be important crystallizing phases if the dacites are related to the andesites by fractional crystallization.

The results of mass balance calculations which attempt to derive the average dacite at 2 wt.% MgO from the average

andesite at 4.5 wt.% MgO using either plag + opx + aug + ilm + mag or plag + opx + amph + ilm + mag are reported in Table 2-26. Plagioclase compositions were calculated using K_Ds of 2 (An_{53}), 3 (An_{63}) and 4 (An_{70}). The assemblage plag, opx, aug and Fe-Ti oxides did not produce an acceptable solution. An_{70} produced the best-fitting (although unacceptable) model and the calculated phase proportions are given in Table 2-26. The normalized proportions of plag, opx, aug and oxides for this model are 60:24:10:6; the calculated silicate wt.% are similar to the phase proportions determined under water-saturated conditions at 2 kbars. The calculated proportions of the assemblage plag (An_{70}), opx, amph, mag and ilm are 38:0:59:2:1. Although this model did result in an acceptable fit, the calculated proportion of orthopyroxene is zero, and is inconsistent with the petrographic observations on these lavas.

The results of the mass balance calculations suggest that the evolution from andesite to dacite lavas has not been controlled by crystal fractionation. The plag + pyx + oxide model produces a poor fit to the data and requires an An-rich plagioclase composition that is not abundant in the andesites and dacites (see Figs. 2-5 and 2-9). More than half of the plagioclase core compositions in the intermediate lavas are less sodic than An_{50} and most rim compositions lie in the range An_{35-55}. In addition, a fractionation model does not account for the Fe-rich orthopyroxenes which are ubiquitous in the andesites and dacites. The amphibole model also requires a calcic plagioclase. The high amphibole content and the absence of orthopyroxene in

the calculated assemblage is not consistent with the phenocryst populations observed in the lavas.

Mixing processes: major and trace elements : The linear MgO-oxide trends for the andesites and dacites (Figs. 2-19) could be produced by mixing basaltic andesite and rhyodacite liquids. The scatter in the MgO-Na_2O and MgO-K_2O trends require at least one more component that is depleted in sodium and enriched in potassium relative to linear combinations of evolved BA and rhyodacite liquids. Average continental crust (Taylor and McLennan, 1986) represents a possible third component.

Petrographic evidence for mixing of basaltic and silicic liquids include the sporadic distribution of amphibole, olivine and quartz phenocrysts/xenocrysts throughout the andesites and dacites (Fig. 2-37), and the bimodal distribution of phenocryst compositions in these lavas. The magnesian overgrowth rims on the Fe-rich orthopyroxene phenocrysts are particularly distinctive. The magnesian augites in the andesites and dacites have Mg# distributions that are similar to the distribution observed in the BAs (compare Figs. 2-17b, 2-15b, 2-13b, 2-10b and 2-7b with 2-3c), and both sets of augite phenocrysts exhibit sector zoning. Fe-rich orthopyroxenes in the intermediate lavas overlap with the orthopyroxene compositions found in the McKenzie Butte rhyodacite. The extreme range in plagioclase An-contents observed in a given andesite or dacite sample is also consistent with mixing between basaltic and silicic magmas.

The rare Fe-augite, olivine and extremely calcic

plagioclase phenocrysts are similar to the phase compositions found in the mafic inclusions and may reflect disagregated cumulate material. In Chapter 1, we found that, in addition to primitive HAB and melted silicic crust, evolved basaltic liquids and their associated cumulate assemblages represented an important mixing component in the Giant Crater-Chimney Crater lavas. While it was possible to calculate the composition of the ferrobasalt at Giant Crater-Chimney Crater, our imperfect understanding of moderate pressure phase relations make it difficult to calculate liquid compositions in equilibrium with the rare Fe-rich augites and olivines in the Shasta andesites and dacites. On the basis of Th/U variations, Newman et al. (1986) also suggested that cumulate material represents an important mixing component in the Shasta system.

However, on closer inspection, the mixing lines for different oxides-MgO pairs do not intersect the basaltic andesite trend at the same MgO content or miss the rhyodacite field (Fig. 2-38). More importantly, mixing lines between the evolved basaltic andesites and the one rhyodacite sample do not pass through the andesite-dacite field in MgO-Sr and MgO-Y space, and do not pass through the densest cluster of lavas on the MgO-Ba and MgO-Rb plots. Based on the MgO-Sr relations in the Mt. Shasta lavas, a mixed andesite with ~4.5 wt.% MgO would have ~350 ppm Sr. Note that we have only a single unaltered rhyodacite sample, which may not be representative of the silicic end-member.

This inconsistency in mixing lines may be resolved by

inferring that the chemical characteristics of the andesites and dacites reflect the signatures of two separate processes. The first process consisted of one or more mixing events between the evolved BA and derivative rhyodacite liquids. Based on the thermal-mechanical mixing model of Sparks and Marshall (1986), the resulting mixed andesite would have MgO contents ≥ 3.8 wt.% (BA must have comprised ≥ 50% of the mixture). Furthermore, the more evolved andesites and dacites would be produced by andesite + rhyodacite ± BA mixing coupled with minor crystal fractionation. The second process produced the observed Sr enrichments in the andesites and dacites, and altered certain element abundances. Recall that certain major and trace elements are correlated with Sr (Table 2-18) and, in general, it is these elements that do not lie along the BA-rhyodacite mixing lines. Using Sr as an indicator of the unspecified enrichment process, we have determined three dimensional planes for selected major and trace elements in MgO-Sr-oxide/element compositional space and calculated new oxide and trace element values at 4.5 wt.% MgO and 350 ppm Sr. The data set consisted of those andesites and dacites with <40 ppm Rb. This removes samples with quartz xenocrysts (a crustal component). The new SiO_2, TiO_2, FeO and K_2O values are plotted in Fig. 2-38 and lie on or very near the dashed BA-rhyodacite mixing line. The "corrected" TiO_2 value still falls substantially off the dashed mixing line. The largest relative change is in K_2O, which has increased (at 4.5 wt.% MgO) from 1.08 to 1.43. Ba and Rb calculated from the MgO-Sr regression are plotted as solid circles in Fig. 2-39 along

with the BA, andesite-dacite and rhyodacite fields and the BA-rhyodacite mixing line. Again, both calculated points lie on or near the respective mixing line.

A large fraction of the andesite-dacite population at Mt. Shasta lie below the BA-rhyodacite mixing lines in MgO-La, MgO-Y, and MgO-Zr composition space (Fig. 2-24). Neither crystal fractionation (bulk Ds < 1 for plag + opx ± aug ± amph + oxides + apatite) nor projection along a Sr enrichment line can explain the trace element abundances. The tremendous trace element differences between the unaltered and altered McKenzie Butte samples suggests that some of the variability observed in the Shasta andesites and dacites may reflect near or subsolidus fluid/vapor transport.

The Sr components

In the following section we will attempt to characterize the components that were involved in the Sr enrichment processes at the volcano. The characteristics of these different components are most clearly displayed when selected trace elements are plotted against Sr.

Sr vs K_2O,Rb: Fig. 2-40 show three distinct groups and/or trends. The basaltic andesites form a linear array of positive slope in the lower left hand corner. The majority of silicic samples from all four cones form curved trends that stretch from ~500 ppm Sr and 1.5% K_2O or 70 ppm Rb to ~1450 ppm Sr and 0.8% K_2O or 15 ppm Rb. Three Sargents Ridge lavas plot above the curved arrays at Sr of 900 to 1000 ppm. The two McKenzie Butte

rhyodacite lavas lie to the left of the andesite-dacite arrays. Also plotted are the values for the average upper crust from Taylor and McLennan (1985). Lavas that contain quartz xenocrysts are shown by solid symbols. Trends toward two mixing components are immediately apparent in Fig. 2-40; one with the Sr and Rb characteristics of continental crust and the other, a high Sr (>1500 ppm) and low K_2O and Rb component which is labelled Sr-I in the figure. The lavas with low Sr and high Rb are the same compositions that have high Na_2O and SiO_2 contents. These chemical characteristic coupled with the presence of quartz inclusions suggests that this small subset of lavas has interacted with continental crust. Based on our limited Sr isotopic data, the trend of increasing Sr concentration is also a trend of decreasing 87/86 Sr. The two high Sr lavas labelled in Fig. 2-40 are the two samples which contain peridotite inclusions. Sample 85-48b has the lowest 87/86 ratio yet determined at the volcano, 0.70272.

Sr vs Ba and La : Fig. 2-41 shows some of the same features as the previous plot. The average crustal values are plotted as circled stars and the presence of quartz and the two samples containing peridotite inclusions are noted as in Fig. 2-40. The BAs form a coherent group and display positive correlations between Ba and Sr and La and Sr. The andesite and dacite lavas also shows trends toward a crustal component and the SR-I component, which must have <250 ppm Ba and > 15 ppm La. The Panther Creek lavas, which were coherent with the larger group of andesites and dacites in Fig. 2-40 form an independent trend

in Sr-Ba and Sr-La composition space. Together with the three Sargents Ridge samples which plotted above the main trend in Fig. 2-40, these eight lavas have elevated Ba and La contents compared to other samples with > 700 ppm Sr. We interpret this trend as pointing to a third mixing component, with Sr > 1000 ppm, Ba > 700 ppm and La > 30 ppm. This component is labelled Sr-II in the figure.

A number of lines of evidence indicate that the Sr enrichment observed in many of the Shasta andesites and dacites is not the result of fractionation processes. (1) Sr abundance is not correlated with the vol.% of plagioclase, the one major constituent in the lavas that has a Sr partition coefficient > 1. Neither is Sr correlated with wt.% Al_2O_3. Among the phenocryst phases, only modal augite is both positively correlated with Sr, and $(D_{Sr})^{aug/liq}$ ~0.1 (Gill, 1981). (2) The vertical Sr-MgO trend (Fig. 2-24a) is not consistent with any reasonable liquid line of descent. (3) Sr abundance is negatively correlated with Sr isotopic composition.

If the Sr-I and Sr-II in Figs. 2-40 and 2-41 reflect mixing processes, then these two subsets of lavas should define straight lines on element/Sr vs 1/Sr plots. These diagrams can be used to calculate the composition of the high-Sr end-member. Using the samples which define the Sr-I trend, ratios of major and trace elements to Sr form coherent linear mixing lines when plotted against 1/Sr. For most elements, least squares fits of the data have linear correlations > 0.95. The maximum Sr abundance in Sr-I is constrained by Rb/Sr vs 1/Sr; Rb/Sr = 0

when Sr = 1880. Using this upper limit on the Sr concentration in Sr-I, we have calculated the remaining oxide and trace element abundances from each regression equation. The resulting composition is given in Table 2-27. In terms of silica content, Sr-I is a dacite with 64 wt.% SiO_2. However, the CaO content is high, ~6 wt.%, and Na_2O/K_2O is ~5. The Mg# is also high, ~61. Ba and La are 230 and 21 ppm respectively. The calculated 87/86 Sr ratio is 0.7026. Sr-I is similar to some leucratic lavas found in ophiolites, although keratophyres and plagiogranites have lower Mg#s and much lower (by a factor of 10) Sr and Ba concentrations (Coleman, 1977). Nevertheless, the presence of the Trinity ophiolite beneath Mt. Shasta and the occurrence of ultramafic xenoliths in the samples which define the Sr-I trend suggest that this component is linked to the ophiolite. Further work is needed to define this link, as well as to constrain the chemical character of Sr-II.

CONCLUSIONS

In this chapter, we have used mineral chemistry, major, trace and isotopic compositions of the basaltic andesites, andesites, dacites and rhyodacites at Mt. Shasta as well as phase equilibria to understand the evolution of this volcano. The dominant feature of the mineral assemblages in the intermediate lavas is the diversity of the phenocryst assemblages. We infer that the dynamic processes in the Shasta magmatic system must be much more complex than those of the Giant Crater-Chimney Crater system (Chapter 1) and that at least

six components are required to explain the major and trace element compositions of the andesites and dacites. These components are: evolved basaltic andesite, derivative rhyodacite, cumulates and accompanying liquid from the BA → rhyodacite fractionation path, continental crust and two high Sr components.

Two major conclusions of this study are: (1) mixing between basaltic andesite and derivative rhyodacite liquids has played a fundamental role in the evolution of the andesites at Mt. Shasta. The oscillatory zoning exhibited by the augite and orthopyroxene phenocrysts suggest that mixing has occurred repeatedly throughout the volcano's history. (2) Geochemical data and peridotite inclusions found in the intermediate lavas suggest that the andesites and dacites have interacted chemically with the Trinity ophiolite which underlies the volcano. The extreme Sr-enrichment observed in some of the intermediate lavas reflects mixing between the "mixed" andesitic magmas and a "dacitic" liquid with ~1800 ppm Sr and an 87/86 Sr ratio of ~0.7026. This component may be related to the Trinity ophiolite.

We have also constructed a phase diagram appropriate for high Mg# lavas which may be used to show low pressure fractionation paths. And finally, our experimentally calibrated expression for 1-atm liquidus temperatures holds promise as a test for plagioclase accumulation in andesite and dacite rocks.

REFERENCES

Albarede, F. and Provost, A. (1977) Petrologic and geochemical mass-balance equations: An algorithm for least-squares fitting and general error analysis. Computers and Geoscience 3, 309-326.

Albee, A.L. and Ray, L. (1970) Correction factors for electron probe microanalysis of silicates, oxides, carbonates, phosphates and sulfates. Anal. Chem. 42, 1408-1414.

Allegre, C.J., Hart, S.R. and Minster, J.-F. (1983) Chemical structure and evolution of the mantle and continents determined by inversion of Nd and Sr isotopic data, II. Numerical experiments and discussion. Earth Planet. Sci. Lett. 66, 191-213.

Allen, J.C. and Boettcher, A. (1978) Amphiboles in andesites and basalts II. Stability as a function of P-T-fH_2O-fO_2. Amer. Mineral. 63, 1074-1087.

Anderson, A.T. (1976) Magma mixing: petrological process and volcanological tool. J. Volcan. Geotherm. Res. 1, 3-33.

Anderson, A.T., (1974) Evidence for a picritic, volatile-rich magma beneath Mt. Shasta, California. J. Petrol. 15, 243-267.

Anderson, D.J. and Lindsley, D.H. (1985) New (and final!) models for the Ti-magnetite/ilmenite geothermometer and oxygen barometer. EOS, Trans. Am. Geophy. Union 66, 416.

Arculus, R.J. and Delano, J.W. (1981) Intrinsic oxygen fugacity measurements: Techniques and results for spinels from upper

mantle peridotites and megacryst assemblages. Geochim. Cosmochim. Acta 45, 899-914.

Bacon, C.R. and Druitt, T.H. (1988) Compositional evolution of the zoned calcalkaline magma chamber of Mount Mazama, Crater Lake, Oregon. Contrib. Mineral. Petrol. (in press).

Baker, D.R., and Eggler, D.H. (1983) Fractionation paths of Atka (Aleutians) high-alumina basalts; constraints from phase relations. J. Volcan. Geotherm. Res. 18, 387-404.

Baker, D.R. and Eggler, D.H. (1987) Composition of anhydrous and hydrous melts coexisting with plagioclase, augite and low-Ca pyroxene from 1-atm to 8 kbar: Application to the Aleutian volcanic center of Atka. Amer. Mineral. 72, 12-28.

Bence, A.E. and Albee, A.L. (1968) Empirical correction factors for the electron microanalysis of silicates and oxides. Jour. Geol. 76, 382-403.

Bevington, P.R. (1969) "Data reduction and error analysis for the physical sciences". McGraw-Hill, 336pp.

Biggar, G.M. (1972) Diopside, lithium metasilicat, and the 1968 temperature scale. Mineral. Mag. 38, 768-770.

Blakely, R.J., Jachens, R.C., Simpson, R.W. and Couch, R.W. (1985) Tectonic setting of the southern Cascade Range as interpreted from its magnetic and gravity fields. Geol. Soc. Amer. Bull. 96, 43-48.

Bowen, N.L. (1928) "The evolution of igenous rocks" Princeton University Press, ??pp.

Bullen, T.D. and Clynne, M.A. (1987) Isotopic diversity at Lassen volcanic center, southern Cascade Range, California. EOS, Trans. Amer. Geophys. Union 68, 1526.

Christiansen, R.L., Kleinhampl, F.J., Blakely, R.J., Tuchek, E.T., Johnson, F.L. and Conyac, M.D. (1977) Resource appraisal of the Mt. Shasta wilderness study area, Siskiyou County, California. Open-file Report 77-250, U.S. Geol. Survey, 53 pp.

Church, S.E. and Tilton, G.R. (1973) Lead and strontium isotopic studies in the Cascade Mountains: bearing on andesite genesis. Geol. Soc. Am. Bull. 84, 431-454.

Condie, K.C. and Swenson, D.H. (1973) Compositional variation in three Cascade stratovolcanoes: Jefferson, Rainier and Shasta. Bull. Volcan. 37, 205-230.

Crandell, D.R, Miller, C.D., Glicken, H.X., Christiansen, R.L. and Newhall, C.G. (1984) Catastrophic debris avalanche from ancestral Mcunt Shasta volcano, California. Geology 12, 143-146.

Crawford, A.J, Falloon, T.J. and Eggins, S. (1987) The origin of island arc high alumina basalts. Contrib. Mineral. Petrol. 97, 417-430.

Dick, H.J.B. and Bullen, T. (1984) Chromian spinel as a petrogenetic indicator in abyssal and alpine-type peridotites and spatially associated lavas. Contrib. Mineral. Petrol. 86, 54-76.

Dixon, W.J. and Massey, F.J. (1957) "Introduction to Statistical Analysis". McGraw-Hill, Inc., 488 pp.

Eggler, D.H. (1972a) Water-saturated and undersaturated melting relations in a Paricutin andesite and an estimate of water content in natural magma. Contrib. Mineral. Petrol. 34, 261-271.

Eggler, D.H. (1972b) Amphibole stability in H_2O-understatured calk-alkaline melts.'Earth Planet. Sci. Lett. 15, 28-34.

Eggler, D.H. and Burnham, C.W. (1973) Crystallization and fractionation trends in the system andesite-H_2O-CO_2-O_2 at pressures to 10 kb. Geol. Soc. Am. Bull. 84, 2517-2532.

Eichelberger, J.C. (1975) Banded andesitic bombs of Mt. Shasta, California. Geol. Soc. America, Abs. with Programs 7, 1065-1066.

Elthon, D. (1987) Partitioning of Ni between olivine and high-MgO basaltic liquids. Lunar Planet. Sci. Conf. XVIII, 258-259.

Ewart, A. (1976) Mineralogy and chemistry of modern orogenic lavas - some statistics and implications. Earth Planet. Sci. Lett. 31, 417-432.

Ewart, A. (1979) A review of the mineralogy and chemistry of Tertiary-Recent dacitic, latitic, rhyolitic and related salic volcanic rocks. In, Trondhjemites, Dacites and Related Rocks. ed. Barker, F., Elsevier, 659 pp.

Ewart, A. (1982) The mineralogy and petrology of Tertiary-Recent orogenic volcanic rocks: with special reference to the andesitic-basaltic compositional range. In, Andesites, Orogenic Andesites and Related Rocks. ed. Thorpe, R.S., Wiley, 724 pp.

Fisk, M.R. (1986) Basalt magma interaction with harzburgite and the formation of high-magnesian andesites. Geophy. Res. Lett. 13, 467-470.

Fisk, M.R. (1987) The chemical effects of contamination of basalt with mafic minerals during migration through the mantle. Hawaii Symposium on How Volcanoes Work, 76.

Foutain, J.C. (1979) Geochemistry of Brokeoff volcano, California. Geol. Soc. Amer. Bull. 90, 294-300.

Fuis, G.S., Zucca, J.J., Mooney, W.D. and Milkereit, B. (1987) A geologic interpretation of seismic-reflection results in northern California. Geol. Soc. Amer. Bull. 98, 53-65.

Gill, J.B. (1981) "Orogenic Andesites and Plate Tectonics". Springer-Verlag, 390 pp.

Griscom, A. (1980) Klamath Mountains province. In, Intepretation of the gravity map of California and its continental margin. ed. Oliver, H. Calif. Div. Mines. Bull. 205, 34-36.

Grove, T.L. (1981) Use of FePt alloys to eliminate the iron loss problem in 1-atmosphere gas mixing experiments: Theoretical and practical considerations. Contrib. Mineral. Petrol. 78, 298-304.

Grove, T.L. and Baker, M.B. (1984) Phase equilibrium controls on the tholeiitic versus calc-alkaline differentiation trends. J. Geophys. Res. 89, 3253-3274.

Grove, T.L. and Bryan, W.B. (1983) Fractionation of pyroxene-phyric MORB at low pressure: An experimental study. Contrib. Mineral. Petrol. 84, 293-309.

Grove, T.L. and Kinzler, R. J. (1986) Petrogensis of andesites, Ann. Rev. Earth Planet. Sci. 14, 417-454.

Grove, T.L., and Donnelly-Nolan, J.M. (1986) The evolution of young silicic lavas at Medicine Lake volcano, California: Implications for the origin of compositional gaps in the calc-alkaline series lavas. Contrib. Mineral. Petrol. 92, 281-302.

Grove, T.L., and Juster, T. (1987) Orthopyroxene and pigeonite stability relations at 1-atm in natural andesite and basalt liquids. Geol. Soc. Amer. Abstr. with Prgms 19, 685.

Grove, T.L., Kinzler, R.J., Baker, M.B., Donnelly-Nolan, J.M., Lesher, C.E. (1988) Assimilation of granitic crust by basaltic magma at Burnt Lava flow, Medicine Lake volcano, Northern California: Decoupling of heat and mass transfer. Contrib. Mineral. Petrol. (in press)

Grove, T.L., Gerlach, D.C. and Sando, T.W. (1982) Origin of calc-alkaline series lavas at Medivine Lake volcano by fractionation, assimilation and mixing. Contrib. MIneral. Petrol. 80, 160-182.

Grove, T.L., Gerlach, D.C., Sando, T.W. and Baker, M.B. (1983) Origin of calc-alkaline series lavas at Medicine Lake volcano by fractionation, assimilation and mixing: corrections and clarifications. Contrib. Mineral. Petrol. 82, 407-408.

Gust, D.A and Perfit, M.R. (1987) Phase relations of a high-Mg basalt from the Aleutian island arc: implications for

primary island arc basalts and high Al-basalts. Contrib. Mineral. Petrol. 97, 7-18.

Hart, S.R. and Brooks, C. (1977) The geochemistry and evolution of early Precambrian mantle. Contrib. Mineral. Petrol. 61, 109-128.

Hart, S.R. and Davis, K.E. (1978) Nickel partitioning between olivine and silicate melt. Earth Planet. Sci. Lett. 40, 203-209.

Henderson, P. (1982) "Inorganic Geochemistry." Pergomon Press, 353 pp.

Higgins, M.W. (1973) Petrology of Newberry volcano, central Oregon. Geol. Soc. Amer. Bull. 84,455-488.

Irvine, T.N. (1979) Rocks whose composition is determined by crystal accumulation and sorting. In "The Evolution of the Igneous Rocks: Fiftieth Anniversary Perspectives" ed. Yoder, H.S., Princeton University Press, 588 pp.

Jacobsen, S.B., Quick, J.E. and Wasserburg, G.J. (1984) A Nd and Sr isotopic study of the Trinity peridotite; implications for mantle evolution. Earth Planet. Sci. Lett. 68,361-378.

Juster, T., and Grove, T.L. (1988) Experimental constraints on the generation of Fe-Ti basalts, andesites and rhyodacites at the Galapagos Spreading Center, 85°W and 95°N. Jour. Geophys. Res., submitted.

Kelemen, P.B. (1986) Assimilation of ultramafic rock in subduction-related magmatic arcs. Jour. Geol. 94, 829-843.

Kelemen, P.B. and Ghiorso, M.S. (1986) Assimilation of peridotite in calc-alkaline plutonic complexes: evidence

from the Big Jim complex, Washington Cascades. Contrib. Mineral. Petrol. 12-28.

Kilinc, A., Carmichael, I.S.E., Rivers, M.L., and Sack, R.O. (1983) The ferric-ferrous ratio of natural silicate liquids equilibrated in air. Contrib. Mineral. Petrol. 83, 136-140.

Lindsley, D.H. and Spencer, K.J. (1982) Fe-Ti oxide geothermometry: reducing analyses of coexisting Ti-magnetite (Mt) and ilmenite (Ilm). EOS, Trans. Amer. Geophys. Union 62, 471.

Macdonald, G.A. (1963) Geology of the Manzanita Lake quadrangle, California. U.S. Geol. Survey Geol. Quad. Map GQ-248, scale 1:62500.

Macdonald, G.A. (1964) Geology of the Prospect Peak quadrangle, California. U.S. Geol. Survey Geol. Quad. Map GQ-345, scale 1:62500.

Macdonald, G.A. (1965) Geology of the Harvey Mountain quadrangle, California. U.S. Geol. Survey Geol. Quad. Map GQ-443, scale 1:62500.

Macdonald, G.A. (1966) Geology of the Cascade Range and Modoc Plateau. In, Geology of Northern California. ed. Bailey, E.H. Calif. Div. Mines Bull. 190, 65-95.

Mahood, G.A. and Baker, D.R. (1986) Experimental constraints on the depths of fractionation of mildly alkalic basalts and associated felsic rocks: Pantelleria, Strait of Sicily. Contrib. Mineral. Petrol. 93, 251-264.

Mazzone, P., Stewart, D.C. and Hughes, J.M. (1987) Sub-solidus dehydration of amphiboles in an andesitic magma. Contrib. Mineral. Petrol. 97, 292-296.

McBirney, A.R. and White, C.M. (1982) The Cascade province. In Andesites, Orogenic Andesites and Related Rocks. ed. Thorpe, R.S., Wiley, 724 pp.

Mertzman, S.A. (1986) A west to east geochemical tranverse of the Cascade arc: Mount Shasta to Medicine Lake, northern California, U.S.A. (abstr) in International Volcanological Congress, 185.

Miyashiro, A. (1974) Volcanic rock series in island arc and active continental margins. Am. J. Sci. 274, 321-355.

Newman, S., Macdougall, J.D. and Finkel, R.C. (1986) Petrogenesis and ^{230}Th- ^{238}U disequilibrium at Mt. Shasta, California, and in the Cascades. Contrib. Mineral. Petrol. 93, 195-206.

Norrish, K. and Chappel, B.W. (1967) X-ray fluorescence spectrography. In, Physical Methods in Determinative Mineralogy, ed. Zussman, J. Academic Press, 514 pp.

Norrish, K. and Hutton, J.T. (1969) An accurate x-ray spectrographic method for the analysis of geologic samples. Geochim. Cosmochim. Acta 33, 431-454.

Peacock, S.M. (1987) Serpentinization and infiltration metasomatism in the Trinity peridotite, Klamath province, northern California: implications for subduction zones. Concrib. Mineral. Petrol. 95, 55-70.

Peccerillo, A., and Taylor, S.R. (1976) Geochemistry of Eocene calc-alkaline volcanic rocks from the Kastamonu area, northern Turkey. Contrib. Mineral. Petrol. 58, 63-81.

Peck, D.L., Imlay, R.M. and Popenoe, W.P. (1956) Upper Cretaceous rocks parts of southwestern Oregon and northern California. Bull. Amer. Ass. Petrol. Geol. 40, 1968-1984.

Peterman, Z.E., Carmichael, I.S.E. and Smith, A.L. (1970) Sr87/Sr86 ratios of Quaternary lavas of the Cascade Range, northern California. Geol. Soc. Am. Bull. 81, 311-317.

Quick, J.E. (1981) Petrology and petrogenesis of the Trinity peridotite, an upper mantle diapir in the eastern Klamath mountains, northern California. J. Geophys. Res. 86, 11837-11863.

Ritchey, J.L. and Eggler, D.H. (1978) Amphibole stability in a differentiated calk-alkaline magma chamber. An experimental investigation. Carnegie Inst. Wash, Yearb. 77, 790-793.

Roeder, P.L. and Emslie, R.F. (1970) Olivine-liquid equilibria. Contrib. Mineral. Petrol. 29, 275-289.

Rutherford, M.J., Sigurdsson, H., Carey, S. and Davis, A. (1985) The May 18, 1980, eruption of Mount St. Helens 1. Melt composition and experimental phase equilibria. J. Geophys. Res. 90, 2929-2947.

Sack, R.O., Carmichael, I.S.E., Rivers, M. and Ghiorso, M.S. (1980) Ferric-ferrous equilibria in natural silicate liquids at 1 bar. Contrib. Mineral. Petrol. 75,369-376.

Smith, A.L. and Carmichael, I.S.E. (1968) Quaternary lavas from the southern Cascades, western U.S.A. Contrib. Mineral. Petrol. 19, 212-238.

Spark, R.S.J. and Marshall, L.A. (1986) Thermal and mechanical constraints on mixing between mafic and silicic magmas. J. Volc. Geotherm. Res. 29, 99-124.

Spencer, K.J. and Lindsley, D.H. (1981) A solution model for coexisting iron-titanium oxides. Amer. Mineral. 66, 1189-1201.

Taylor, S.R. and McLennan, S.M. (1985) "The Continental Crust: Its Composition and Evolution". Blackwell Scvientific Pub. 312 pp.

Thompson, R.N. (1973) One-atmosphere melting behavior and nomenclature of terrestrial lavas. Contrib. Mineral. Petrol. 41, 197-204.

Tormey, D.R., Grove, T.L. and Bryan, W.B. (1987) Experimental petrology of normal MORB near the Kane Fracture Zone: 22°-25° N, mid-Atlantic ridge. Contrib. Mineral. Petrol. 96, 121-139.

Tsuchiyama, A. (1985) Dissolution kinetics of plagioclase in the melt of the system diopside-albite-anorthite, and origin of dusty plagioclase in andesites. Contrib. Mineral. Petrol. 89, 1-16.

Tsuchiyama, A. and Takahashi, E. (1983) Melting kinetics of a plagioclase feldspar. Contrib. Mineral. Petrol. 84, 345-354.

Walker, D., Shibata, T. and DeLong, S.E. (1979) Abyssal tholeiites from the Oceanographer Fracture Zone II. Phase equilibria and mixing. Contrib. Mineral. Petrol. 70, 111-125.

Watson, E.B. (1982) Basalt contamination by continental crust: some experiments and models. Contrib. Mineral. Petrol. 80, 73-87.

Watson, E.B. and Jurewicz, S.R. (1984) Behavior of alkalies during diffusive interaction of granitic xenoliths with basaltic magma. Jour. Geol. 92, 121-131.

Williams, H. (1932a) Geology of the Lassen Volcanic National Park, California. Calif. Univ. Dept. Geol. Sci. Bull. 21, 195-385.

Williams, H. (1932b) Mount Shasta, a Cascade volcano. Jour. Geol. 45, 417-429.

Williams, H. (1934) Mount Shasta, California. Zeitschr. Vulkan. 15, 225-253.

Williams, H. (1942) The geology of Crater Lake National Park, Oregon, with a reconnaissance of the Cascade range southward to Mount Shasta, Carnegie Inst. Washington Pub 540, 160pp.

Williams, H. (1949) Geology of Macdoel quadrangle (California). Calif. Div. Mines Bull. 151, 7-60.

Wood, D.A., Joron, J.-L., and Treuil, M. (1979b) A re-appraisal of the use of trace elements to classify and discriminate between magma series erupted in different tectonic settings. Earth Planet. Sci. Lett. 45, 326-336.

Wood, D.A., Joron, J.-L., Treuil, M., Norry, M., and Tarney, J. (1979a) Elemental and Sr isotope variations in basic lavas from Iceland and the surrounding ocean floor. Contrib Mineral. Petrol. 319-339.

Zucca, J.J., Fuis, G.S., Milkereit, B., Mooney, W.D. and Catchings, R.D. (1986) Crustal structure of northeastern California. J. Geophys. Res. 91, 7359-7382.

Figure 2-1. (a) Map of nothern California and Nevada and southern Oregon showing the location of Mt. Shasta relative to other major Cascade volcanos.

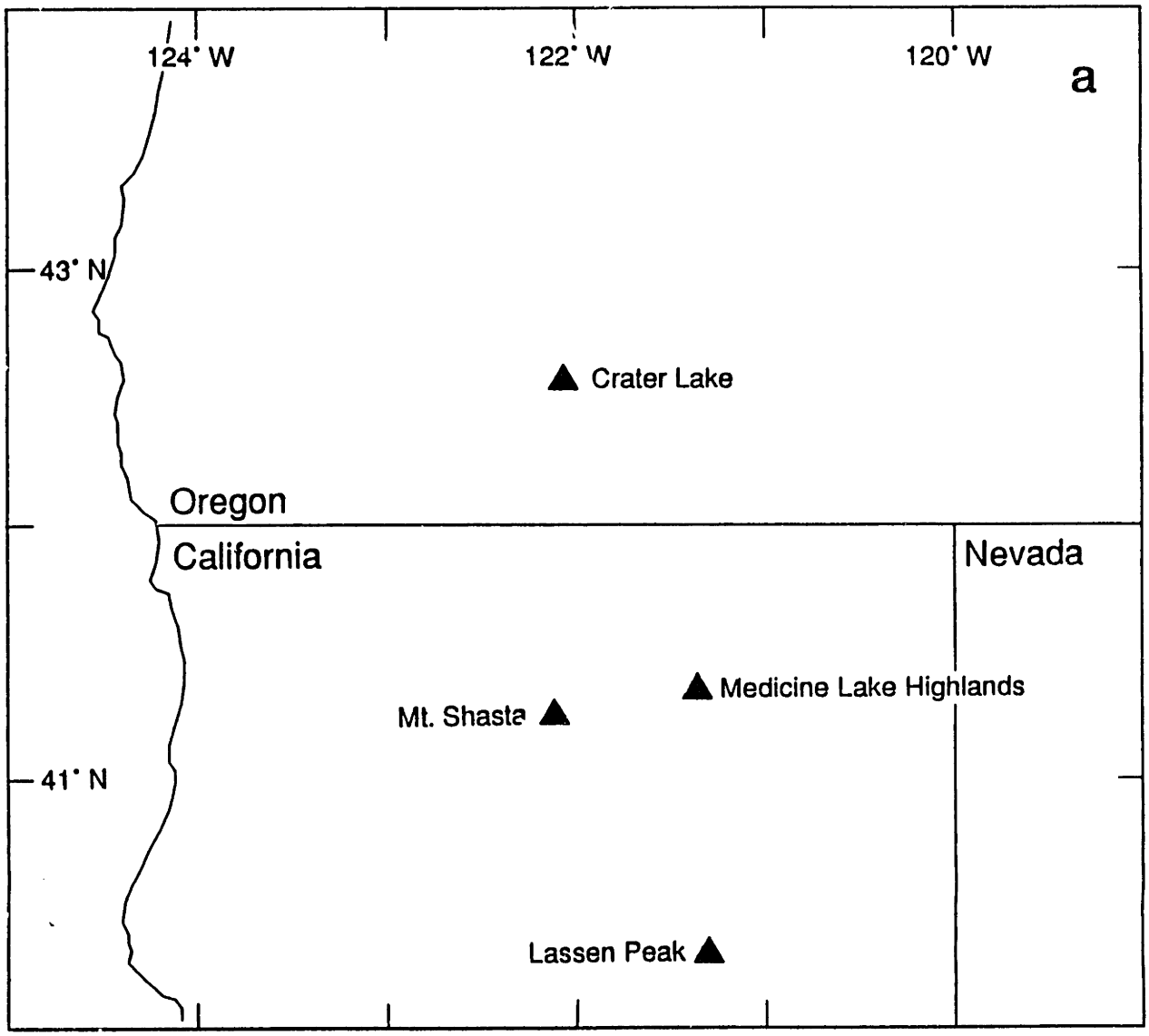
124° W
122° W
120° W
a
43° N
Crater Lake
Oregon
California
Nevada
Medicine Lake Highlands
Mt. Shasta
41° N
Lassen Peak

Figure 2-1. (b) Sample location map for Mt. Shasta and vicinity. Contour elevations are given in feet, detailed location descriptions are given in Appendix 2-A.

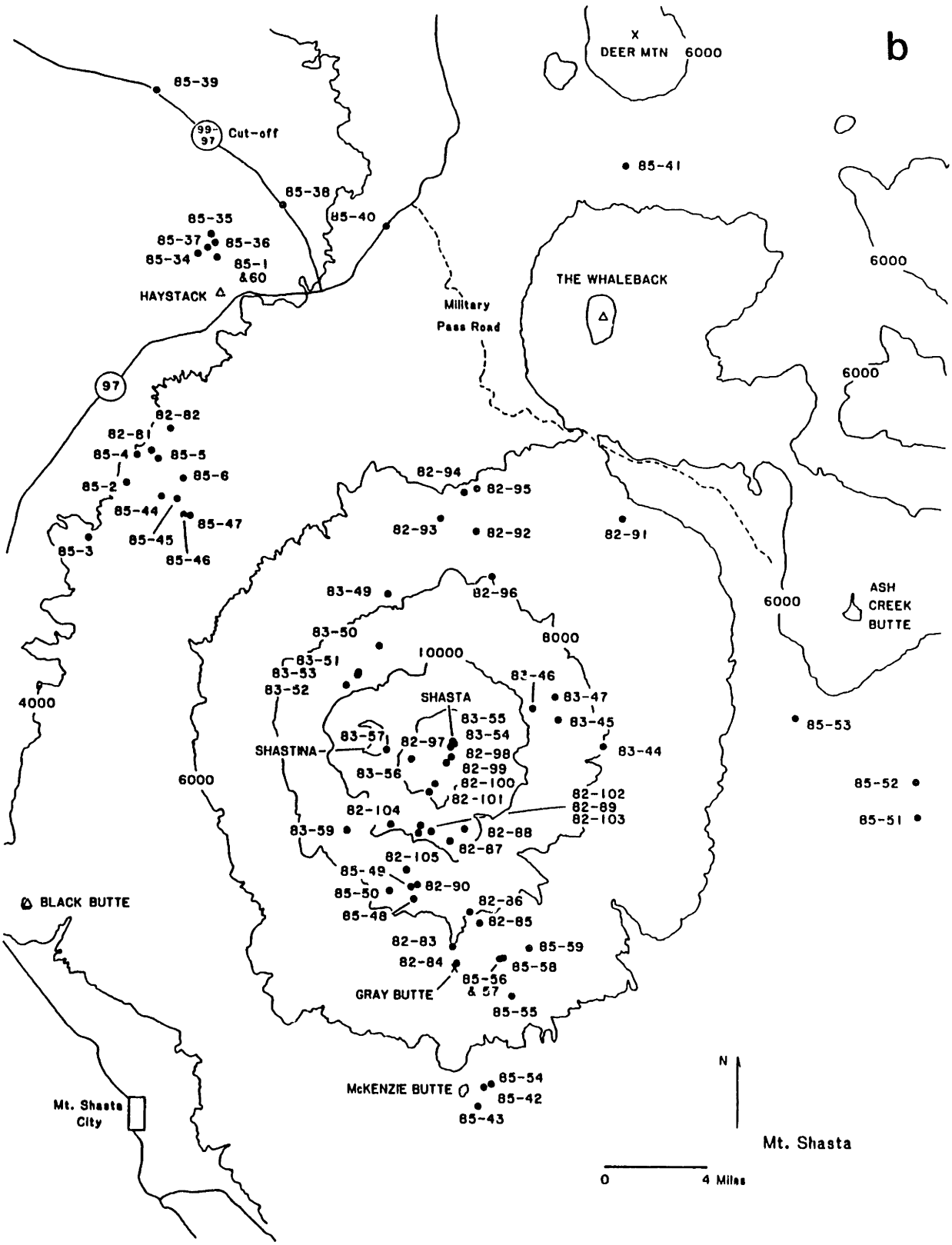
b
DEER MTN 6000
85-39
99-97 Cut-off
85-38
85-40
85-41
85-35
85-37
85-36
85-34
85-1 &60
HAYSTACK
Military Pass Road
THE WHALEBACK
6000
97
82-82
82-81
85-4
85-5
85-2
85-6
85-44
85-47
85-45
85-46
85-3
82-94
82-95
82-93
82-92
82-91
83-49
82-96
83-50
8000
83-51
10000
83-53
83-52
4000
83-46
83-47
SHASTA
83-55
83-45
83-54
83-57
SHASTINA
82-97
82-98
83-44
82-99
83-56
82-100
6000
82-101
82-102
82-89
82-103
82-104
83-59
82-88
82-87
82-105
85-49
82-90
85-50
82-86
85-48
82-85
82-83
85-59
82-84
85-58
85-56 & 57
GRAY BUTTE
85-55
ASH CREEK BUTTE
6000
85-53
85-52
85-51
BLACK BUTTE
McKENZIE BUTTE
85-54
85-42
85-43
Mt. Shasta City
N
Mt. Shasta
0
4 Miles

Figure 2-2. SiO_2 - K_2O variation diagram for the Mt. Shasta lavas. Classification scheme from Peccerillo and Taylor (1976).

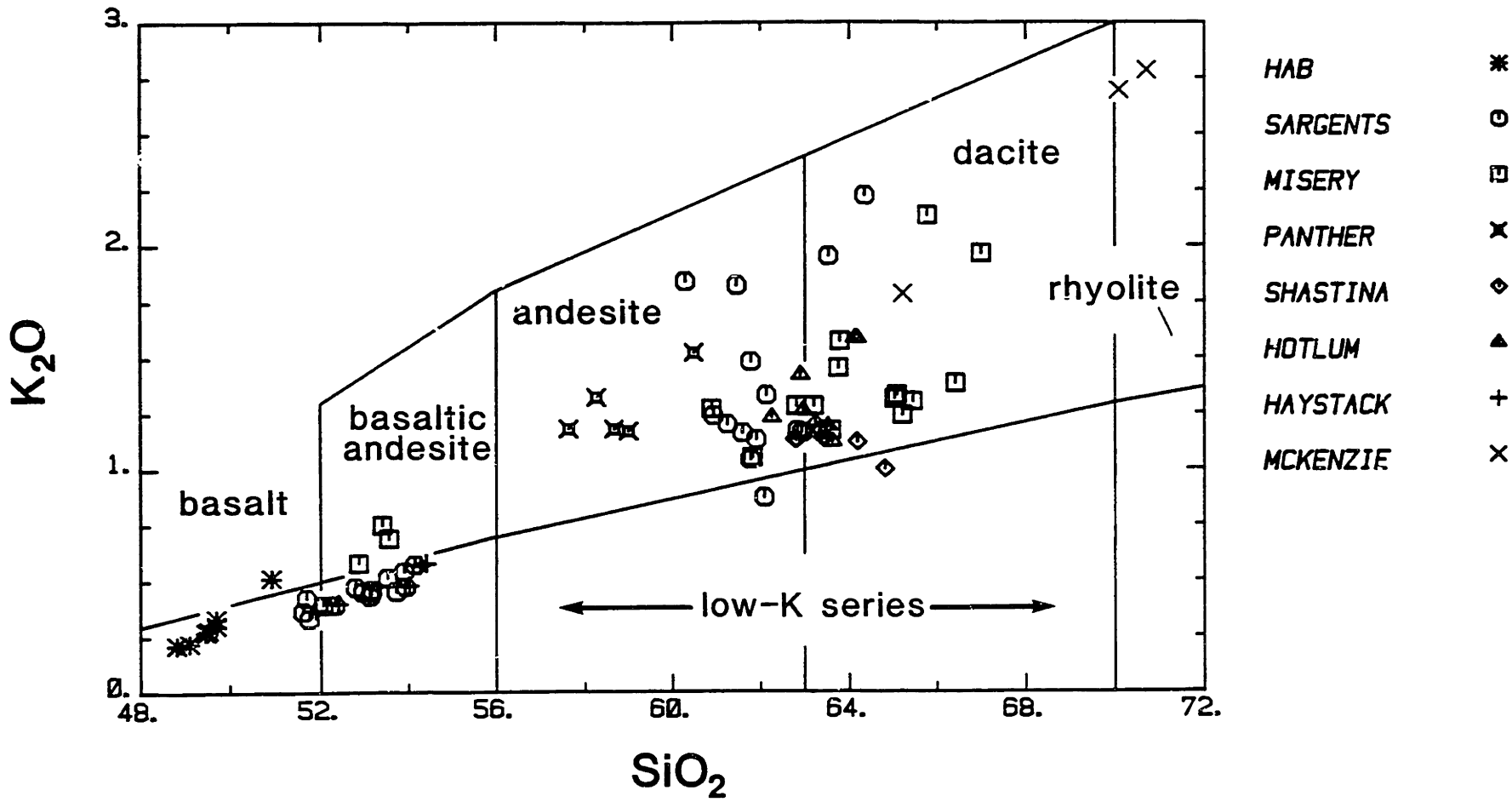
3.
2.
1.
0.
48.
52.
56.
60.
64.
68.
72.
K_2O
SiO_2
basalt
basaltic andesite
andesite
dacite
rhyolite
low-K series
HAB
SARGENTS
MISERY
PANTHER
SHASTINA
HOTLUM
HAYSTACK
MCKENZIE

Figure 2-3. Compositional variations in phenocrysts from the basaltic andesites (a) olivine, (b) plagioclase, (c) augite. Only analyses of cores are included in each histogram ,total number of analyses given in parentheses. Fo = forsterite content, An = anorthite content, Ca/(Ca+Na), molar and Mg# = Mg/(Mg+Fe*), where Fe* equals total iron as FeO.

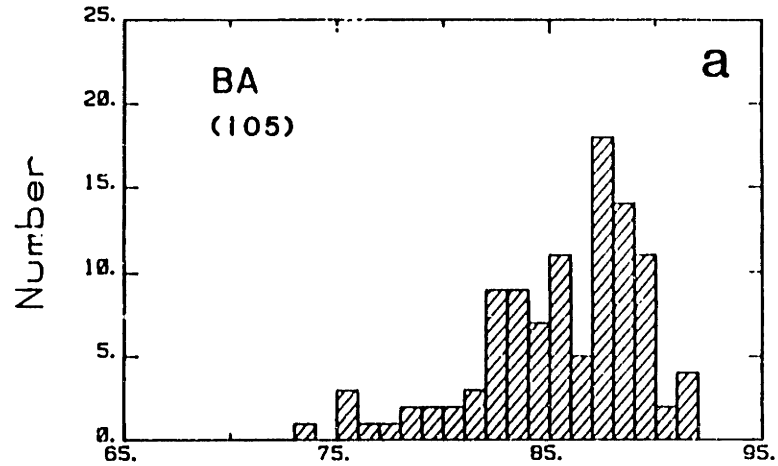

Mole % Fo

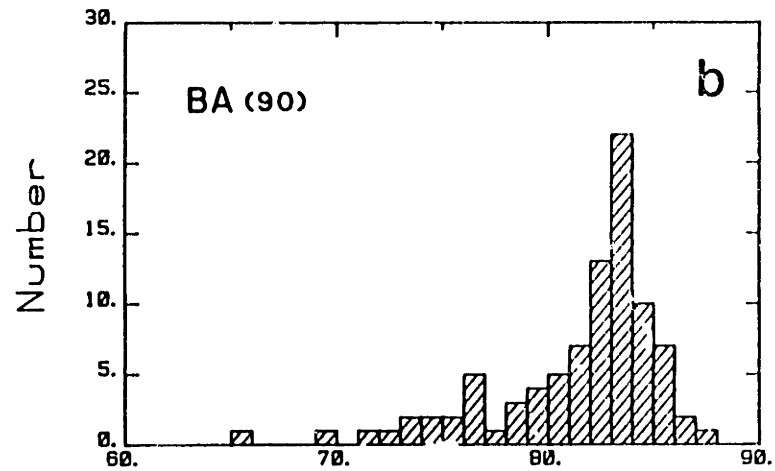

Mole % An

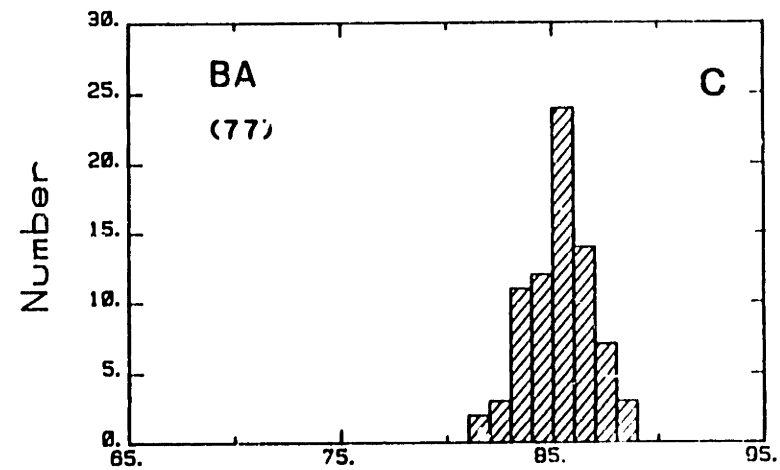

Mg# Cpx

Figure 2-4. $Mg/(Mg+Fe^{2+})$ vs $Cr/(Cr+Al)$ for spinels in the basaltic andesites. Fields for the Trinity peridotite and abyssal peridotites from Quick (1981) and Dick and Bullen (1984).

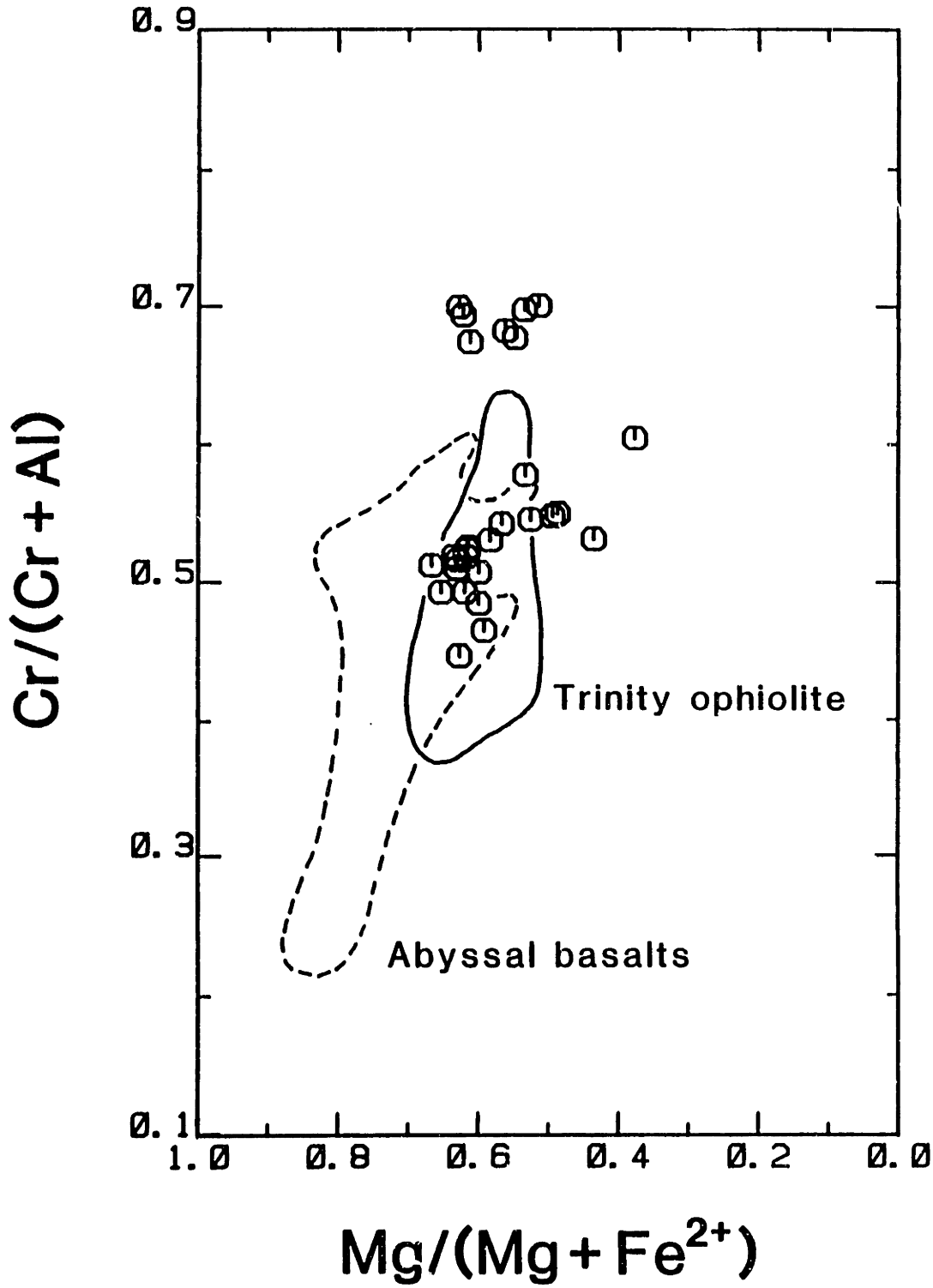
0.9
0.7
0.5
0.3
0.1
Cr/(Cr + Al)
1.0
0.8
0.6
0.4
0.2
0.0
Mg/(Mg + Fe2+)
Trinity ophiolite
Abyssal basalts

Figure 2-5. Histogram of core compositions from plagioclase phenocrysts found in the Sargents Ridge andesite and dacite lavas. Total number of analyses given in parentheses.

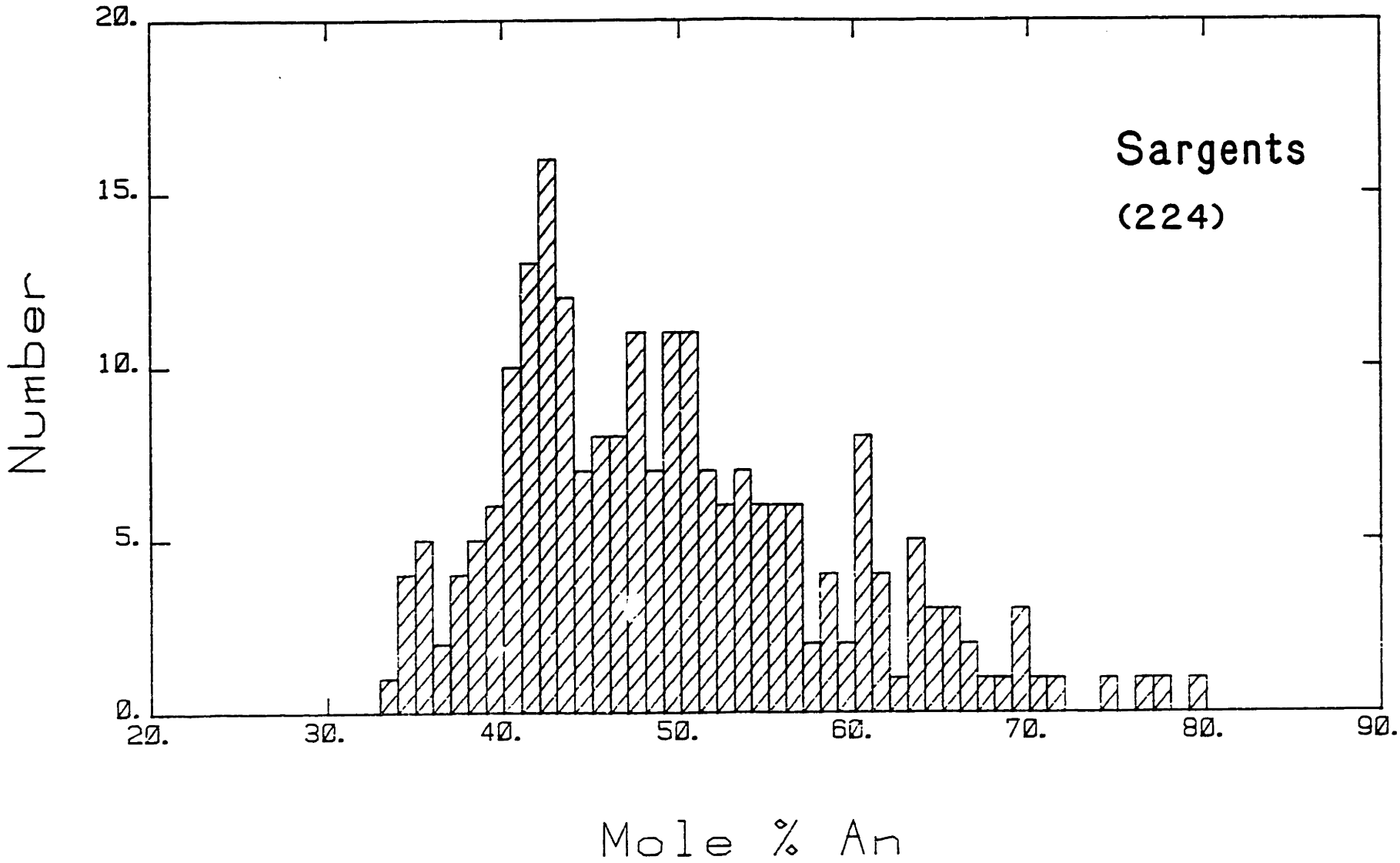
Sargents
(224)
Number
20.
15.
10.
5.
0.
20.
30.
40.
50.
60.
70.
80.
90.
Mole % An

Figure 2-6. (a) Backscattered electron image (BEI) of sieve-textured plagioclase phenocryst from 82-105. The larger light-colored inclusions are orthopyroxene. Note clear overgrowth rim. Field of view (fv) = 245 microns. (b) BEI image, plagioclase phenocryst from 85-48b showing oscillatory zoning and coarse reaction texture. Fv = 245 microns. (c) Plagioclase phenocryst showing oscillatory zoning. Zoned inclusion is orthopyroxene. BEI, fv = 164 microns. (d) BEI of plagioclase phenocryst from 82-102. Large dark interior inclusions are partially filled with SiO_2. Light colored inclusion is orthopyroxene, fv = 245 microns. (e) BEI of sector-zoned augite from 85-57. Sector boundaries are left of the white square (an electron beam location point). Fv = 82 microns. (f) Magnesian augite phenocryst in 85-48b. Note sharp growth boundaries (BEI). Fv = 377 microns.

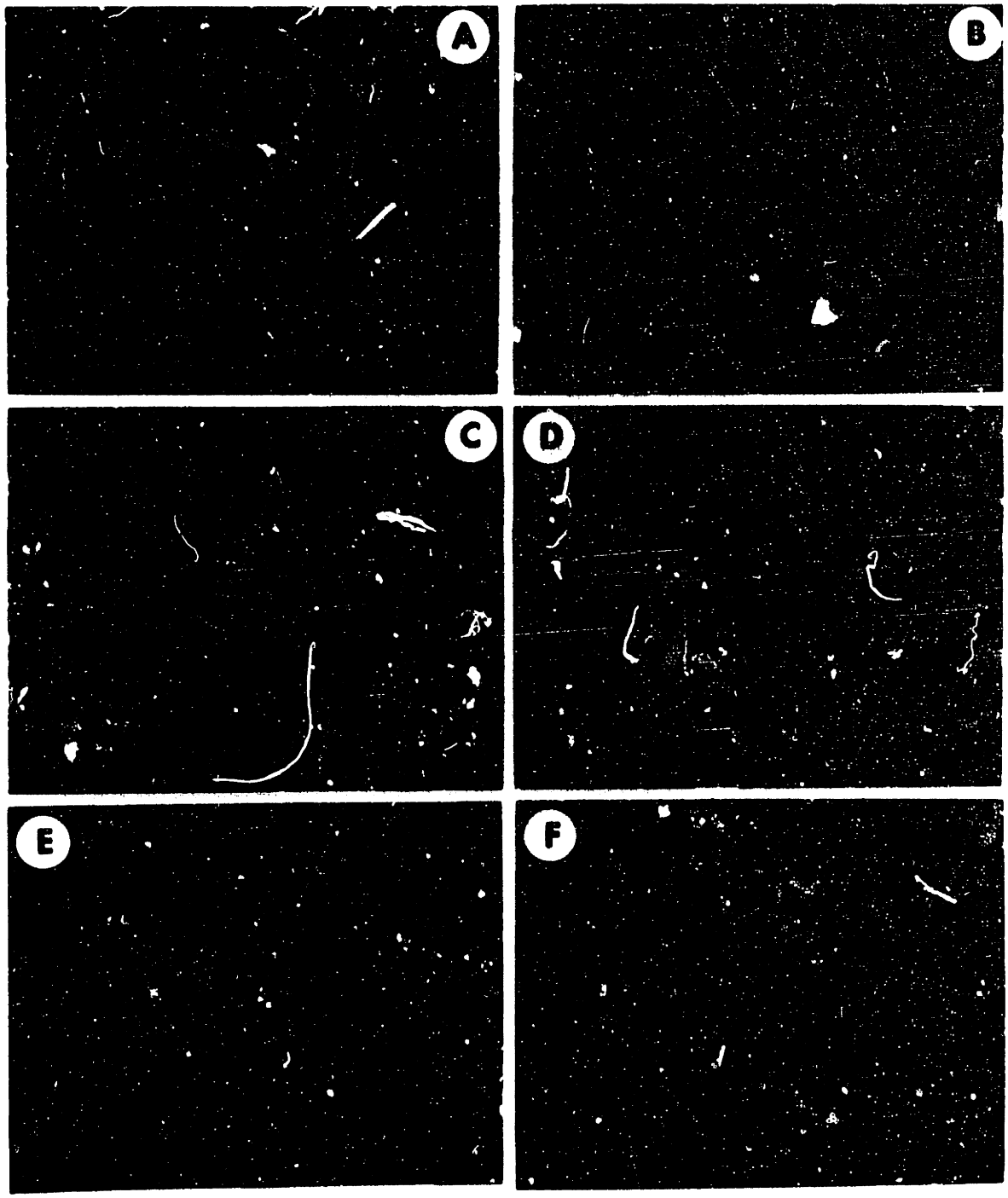
A
B
C
D
E
F

Figure 2-6. (g) BEI of augite partially overgrown by opx in 85-48b. Note oscillatory zoning and compositional discontinuities in opx, fv = 245 microns. (h) Rounded Fe-rich opx overgrown by more magnesian opx rim, 82-98. BEI, fv = 81 microns. (i) BEI of dark-colored opx partially overgrown by augite, 85-48b, fv = 122 microns. (j) Irregularly shaped Fe-rich opx with sharp magnesian opx rim in 85-57. BEI, fv = 245 microns. (k) BEI of reacted magnesian opx rimmed by magnesian augite. 85-57, fv = 245 microns. (l) BEI of oscillatory zoned opx in 82-103. Core to rim is Mg → Fe → Mg. Note both gradational and sharp compositional boundaries. Fv = 240 microns.

G
H
I
J
K
L

Figure 2-6. (m) BEI of amphibole pseudomorph from 85-57. Light regions are Fe-Ti oxides, moderate gray is pyroxene, dark gray is plagioclase, vertical fv = 245 microns. (n) BEI of amphibole from 83-57 showing outer reaction zone. vertical fv = 1225 microns. (o) Magnesian olivine with spinel inclusions (bright regions) and thin low-Ca pyroxene reaction rim, from 85-57, vertical fv = 410 microns (BEI). (p) BEI of normally zoned Fe-rich olivine with opx overgrowth, from 82-103, vertical fv = 480 microns.


M

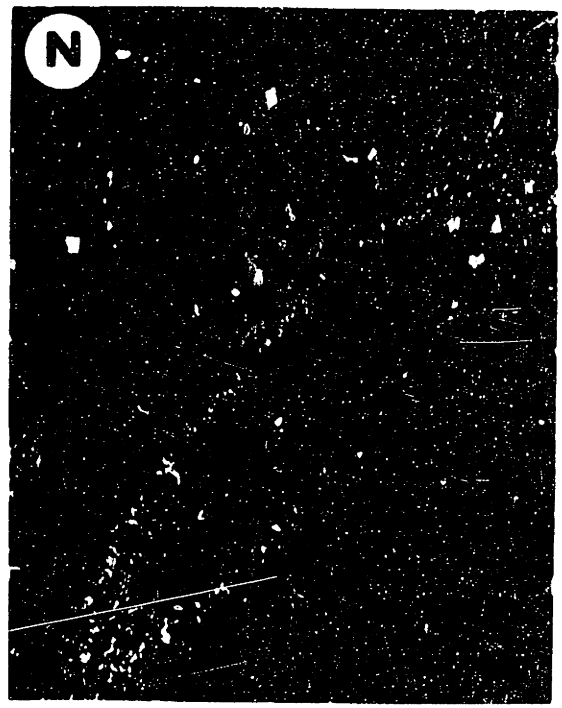
N

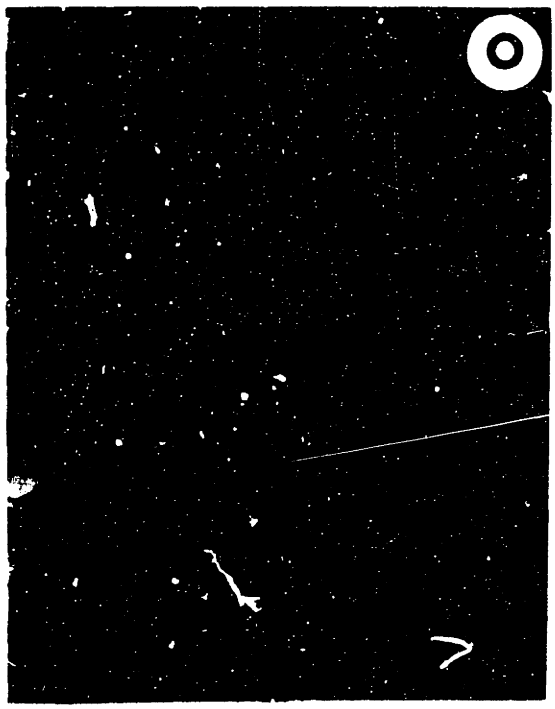
O


P

Figure 2-7. (a) Variations in Mg# for orthopyroxene phenocrysts from Sargents Ridge andesites and dacites, only core compositions are plotted. Value in parentheses equals total number of analyses. (b) Variations in Mg# for augite phenocrysts from Sargents Ridge andesites and dacites.

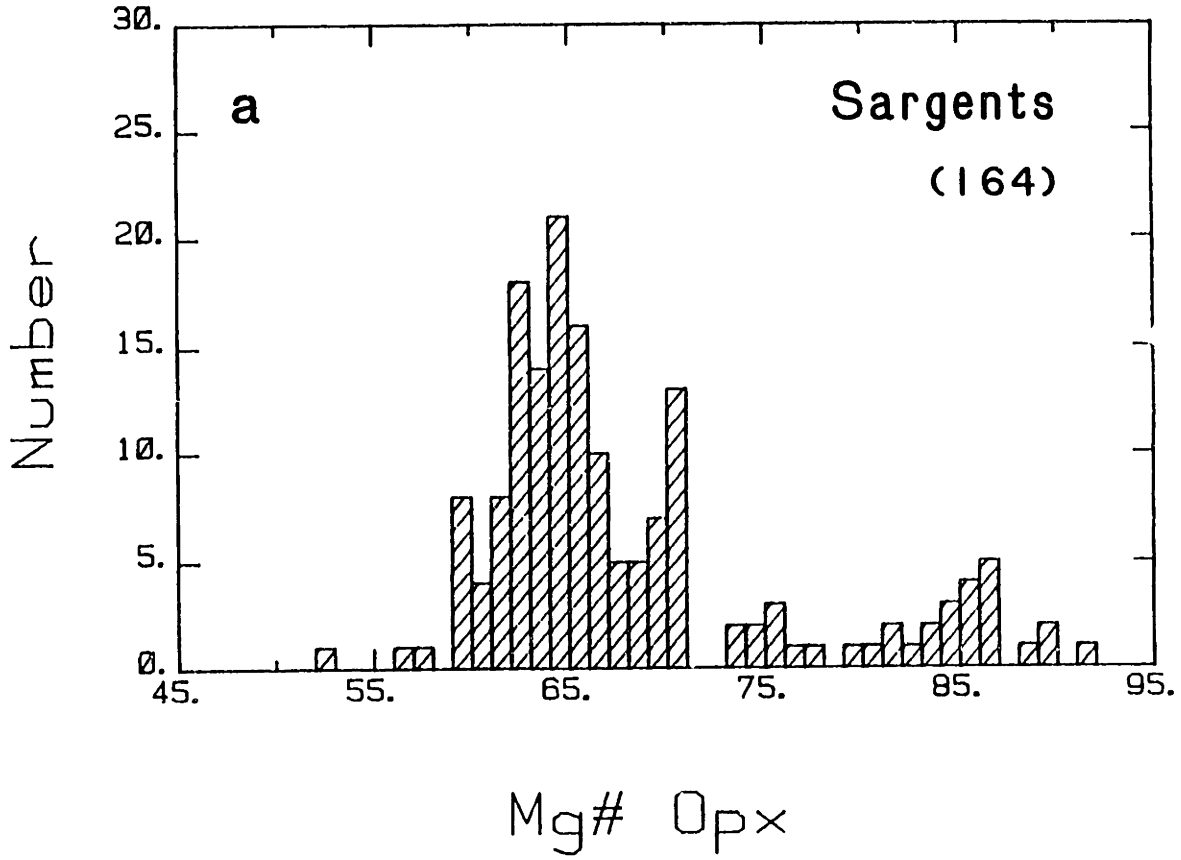
a
Sargents
(164)
Number
30.
25.
20.
15.
10.
5.
0.
45.
55.
65.
75.
85.
95.
Mg# Opx

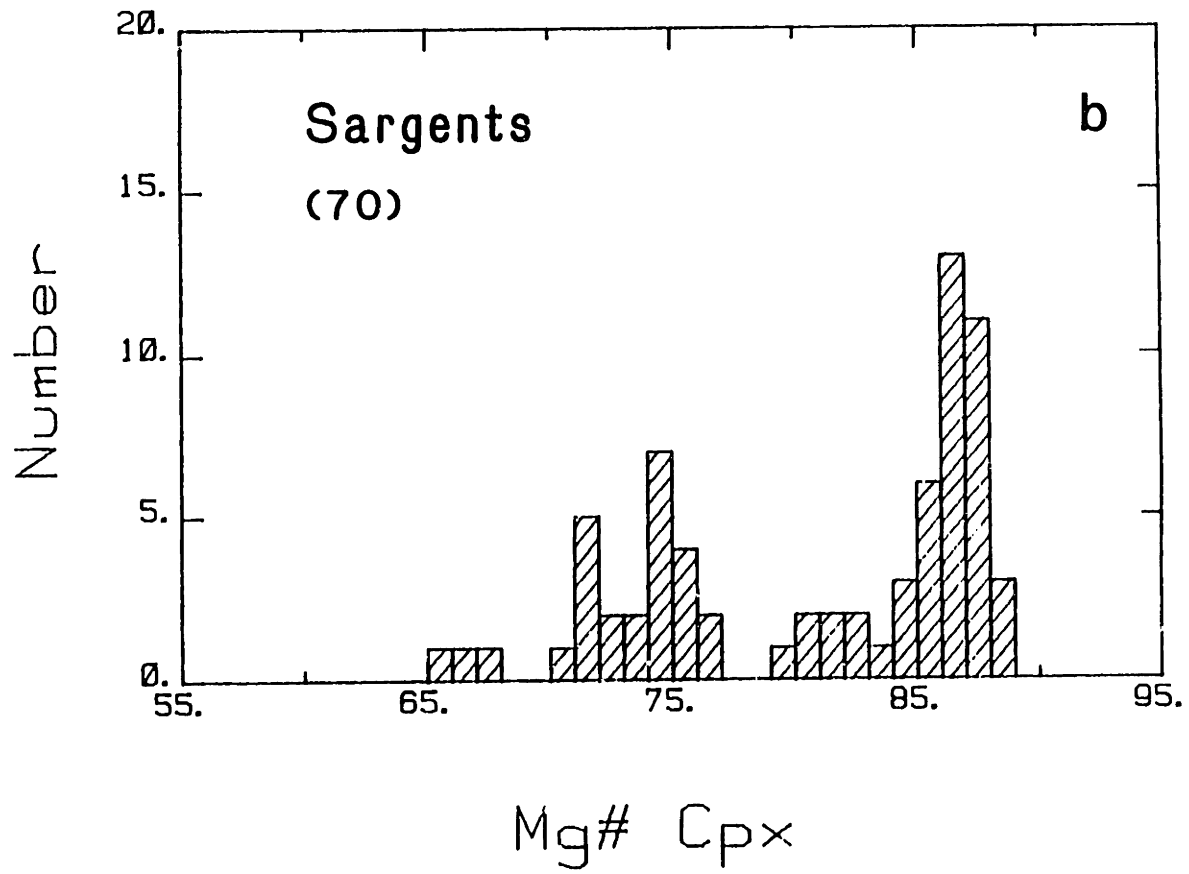
Sargents
(70)
b
Number
20.
15.
10.
5.
0.
55.
65.
75.
85.
95.
Mg# Cpx

Figure 2-8. Normalized molar abundances of Ca, Mg and Fe in amphiboles from Sargents Ridge andesite and dacite lavas.

Figure 2-8. Normalized molar abundances of Ca, Mg and Fe in amphiboles from Sargents Ridge andesite and dacite lavas.

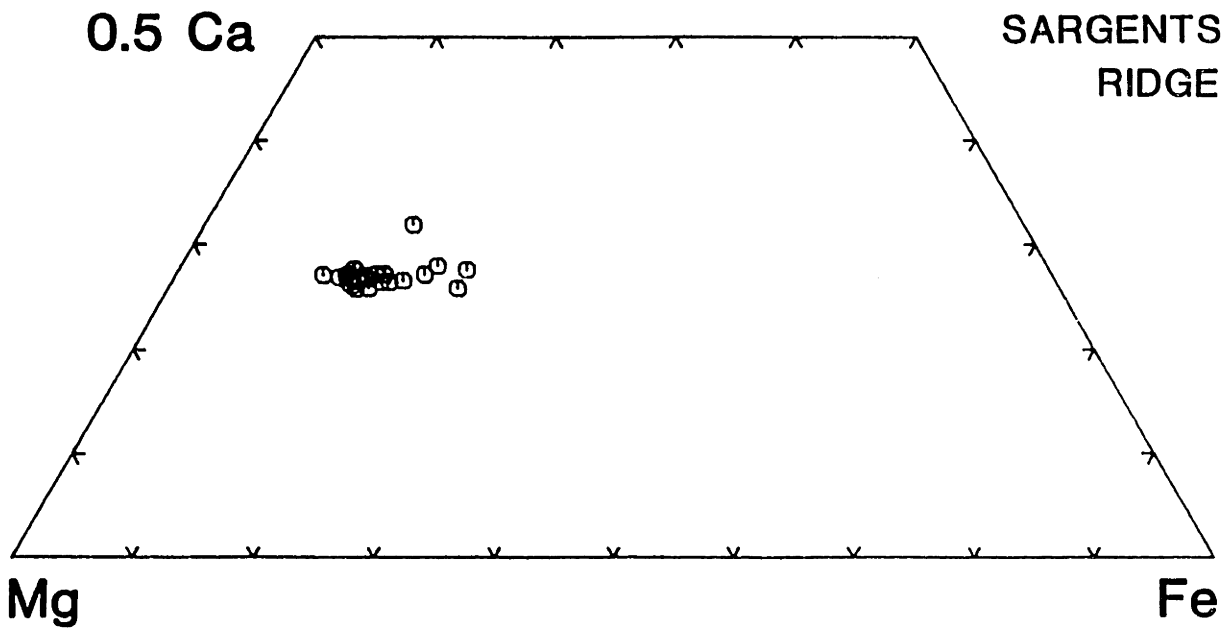
0.5 Ca
SARGENTS
RIDGE
Mg
Fe

Figure 2-9. Histogram showing distribution of plagioclase phenocryst core compositions in Misery Hill andesites and dacites. Total number of analyses given in parentheses.

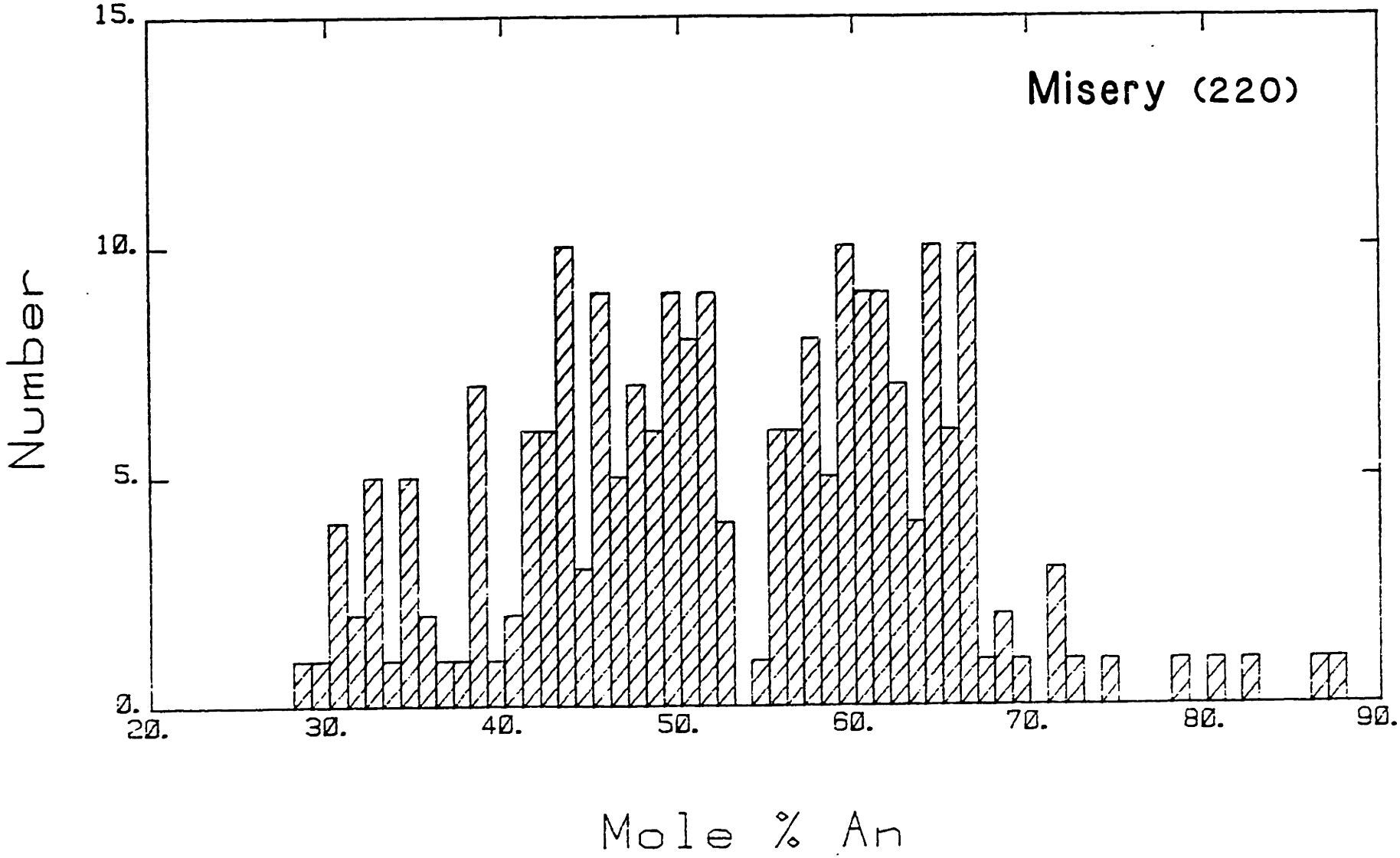
Misery (220)
Number
15.
10.
5.
0.
20.
30.
40.
50.
60.
70.
80.
90.
Mole % An

Figure 2-10. (a) Mg# distribution in orthopyroxene phenocryst cores in Misery Hill andesites and dacites. (b) Mg# distribution among augite phenocryst cores. Total number of analyses given in parentheses.

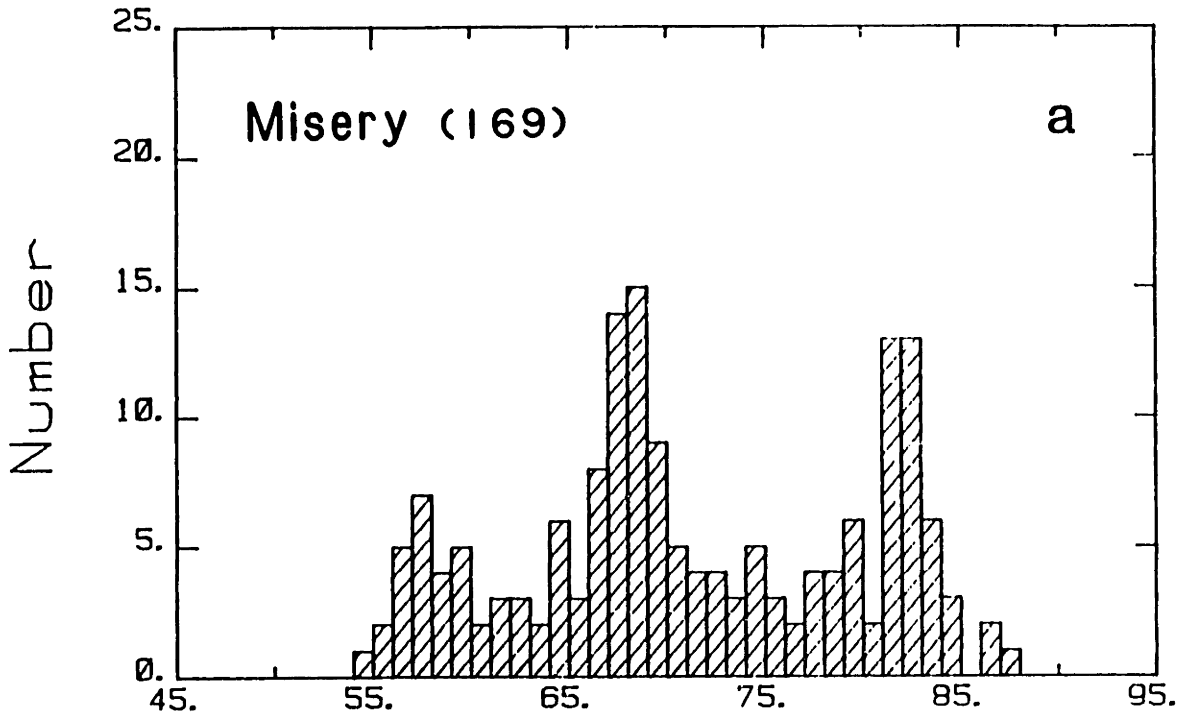
Misery (169)
a
Number
25.
20.
15.
10.
5.
0.
45.
55.
65.
75.
85.
95.
Mg# Opx

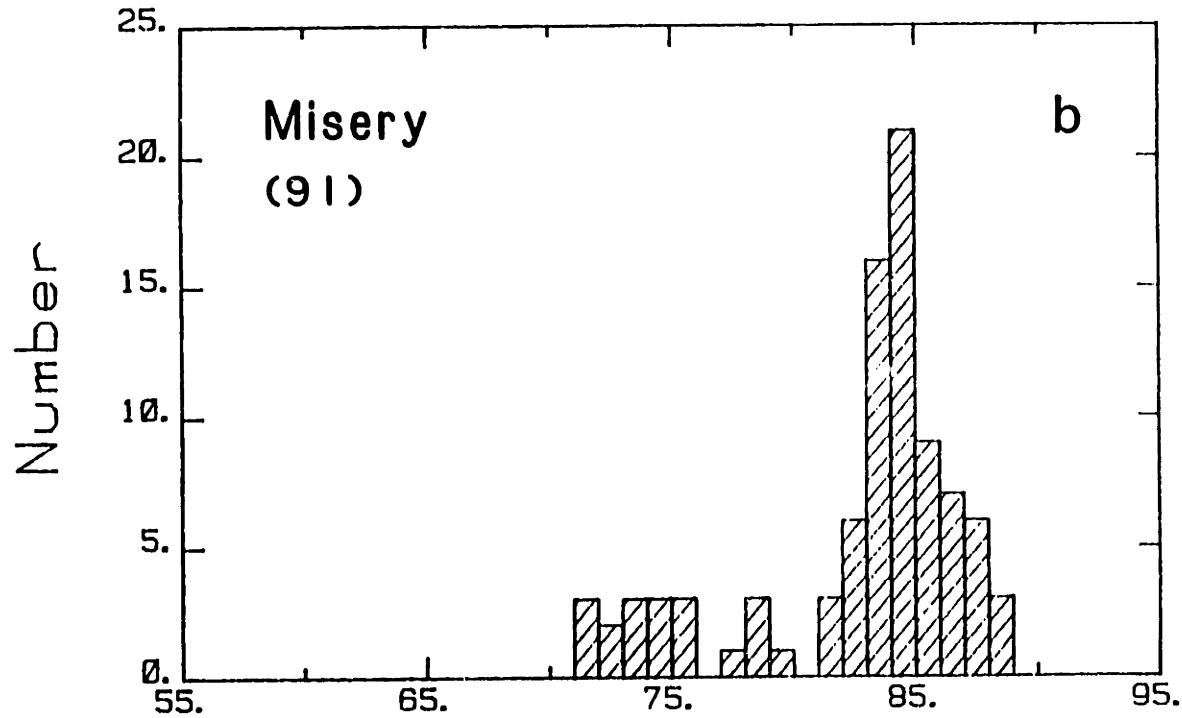
Misery
(91)
b
Number
25.
20.
15.
10.
5.
0.
55.
65.
75.
85.
95.
Mg# Cpx

Figure 2-11. Molar Ca-Mg-Fe abundances in amphibole phenocrysts from Misery Hill andesites and dacites.

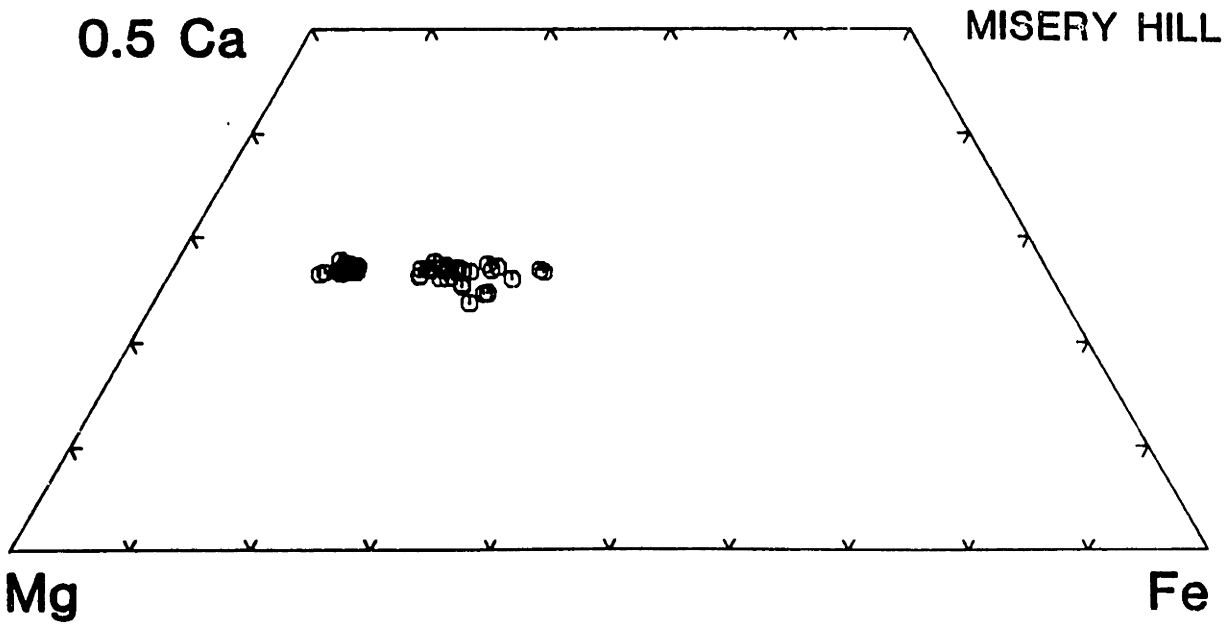
0.5 Ca
MISERY HILL
Mg
Fe

Figure 2-12. Histogram of anorthite contents in plagioclase phenocryst cores from Panther Creek andesites. Total number of analyses given in parentheses.

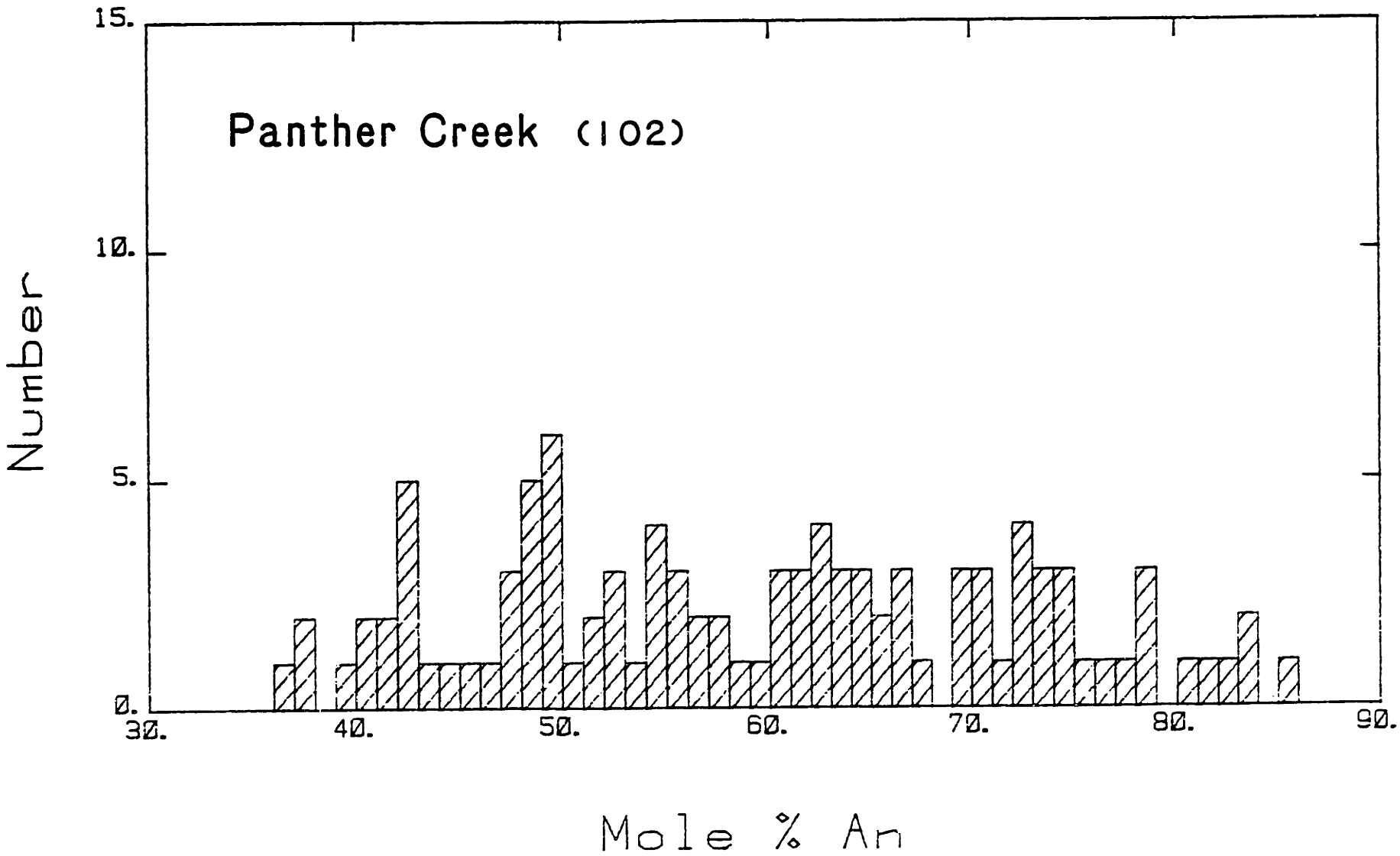
Panther Creek (102)
15.
10.
5.
0.
Number
30.
40.
50.
60.
70.
80.
90.
Mole % An

Figure 2-13. Variations in (a) Fo-content in olivine, and Mg#s in (b) orthopyroxene and (c) augite phenocrysts cores from Panther Creek andesites. Total number of analyses in each figure given in parentheses.

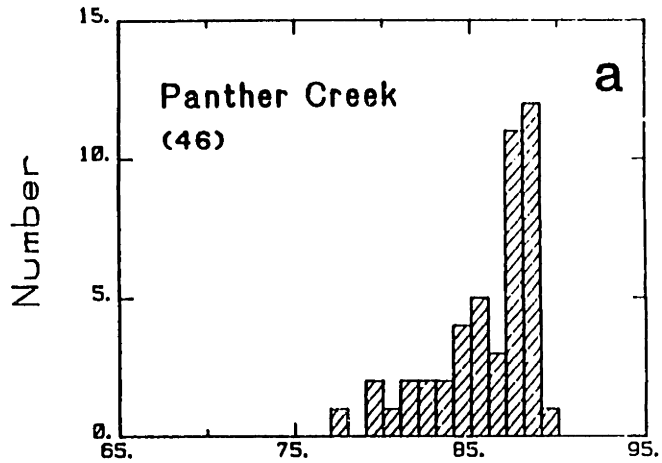

Mole % Fo

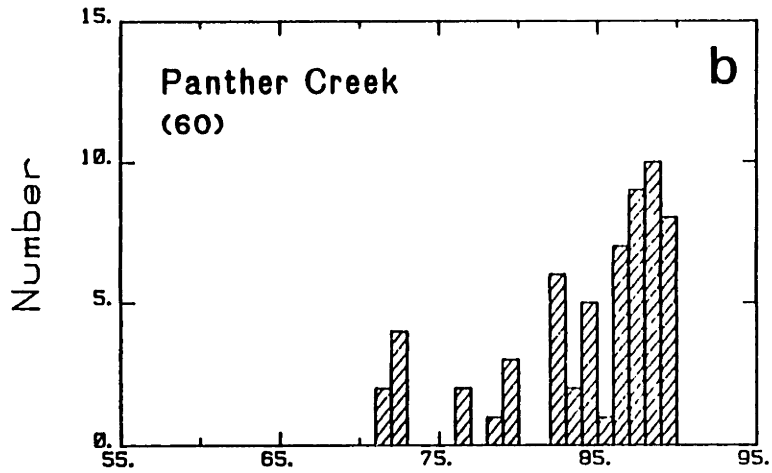

Mg# Cpx

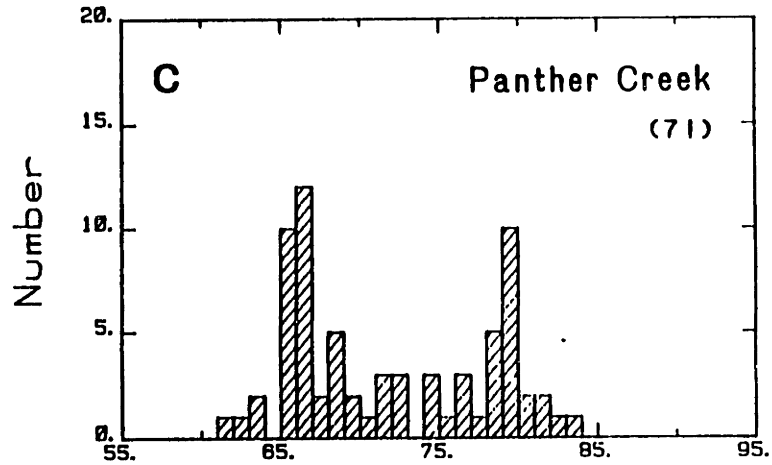

Mg# Opx

Figure 2-14. Anorthite histogram for plagioclase phenocrysts from Shastina andesites and dacites; only core compositions are plotted. Total number of analyses given in parentheses.

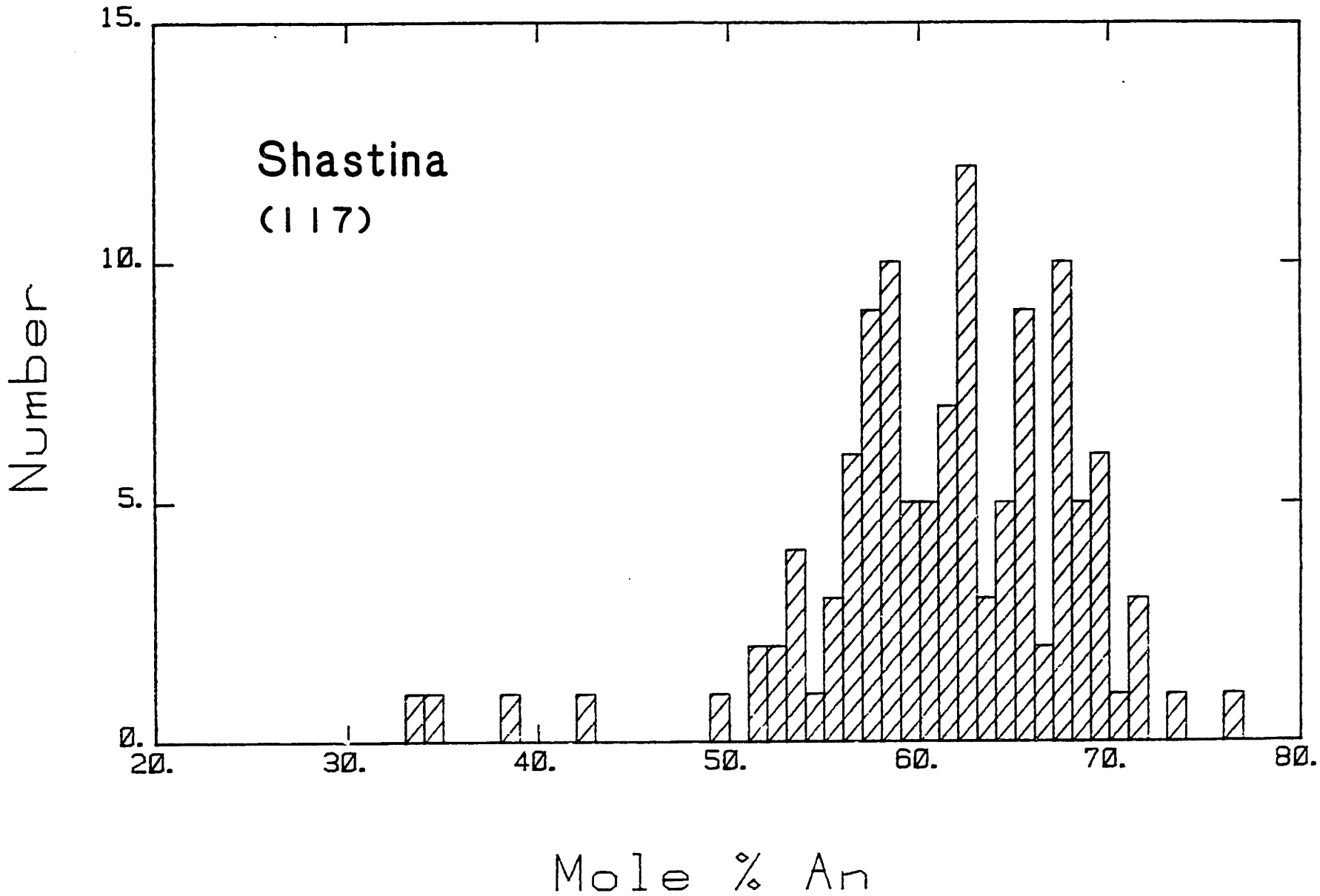
Shastina
(117)
15.
10.
5.
0.
Number
20.
30.
40.
50.
60.
70.
80.
Mole % An

Figure 2-15. Histograms of Mg# variation in (a) orthopyroxene and (b) augite phenocrysts (core compositions only, number of analyses in parentheses) from Shastina intermediate lavas.

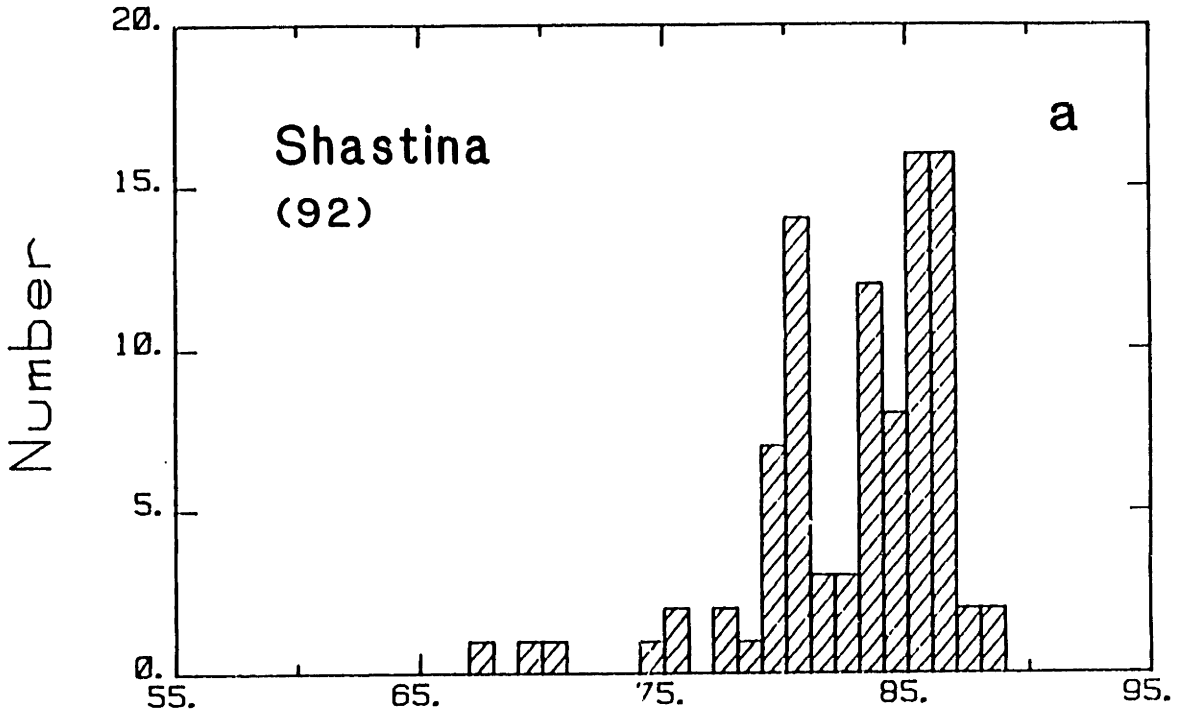
Shastina
(92)
a
Number
20.
15.
10.
5.
0.
55.
65.
75.
85.
95.
Mg# Opx

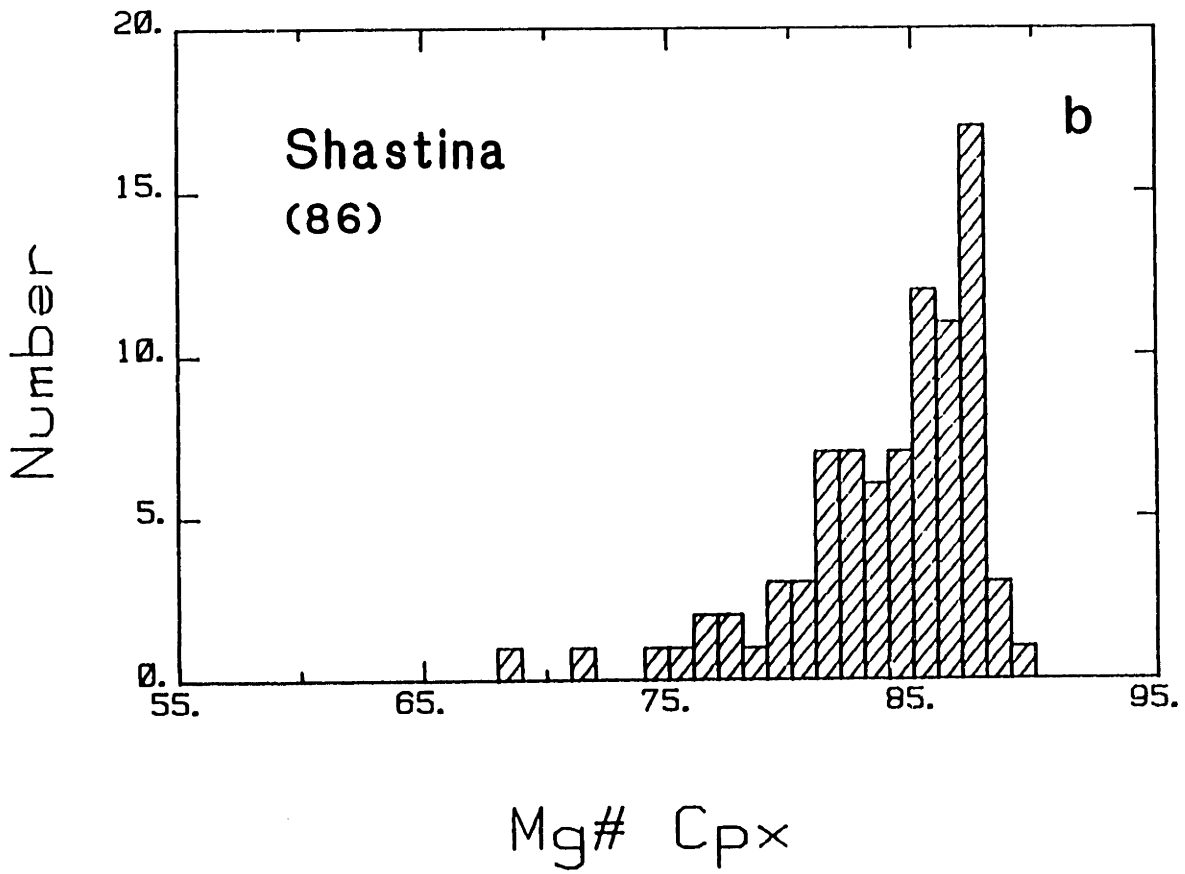
Shastina
(86)
b
Number
20.
15.
10.
5.
0.
55.
65.
75.
85.
95.
Mg# Cpx

Figure 2-16. Variations in anorthite content in plagioclase phenocrysts in andesites and dacites from Hotlum cone. Only core compositions are plotted, number of analyses given in parentheses.

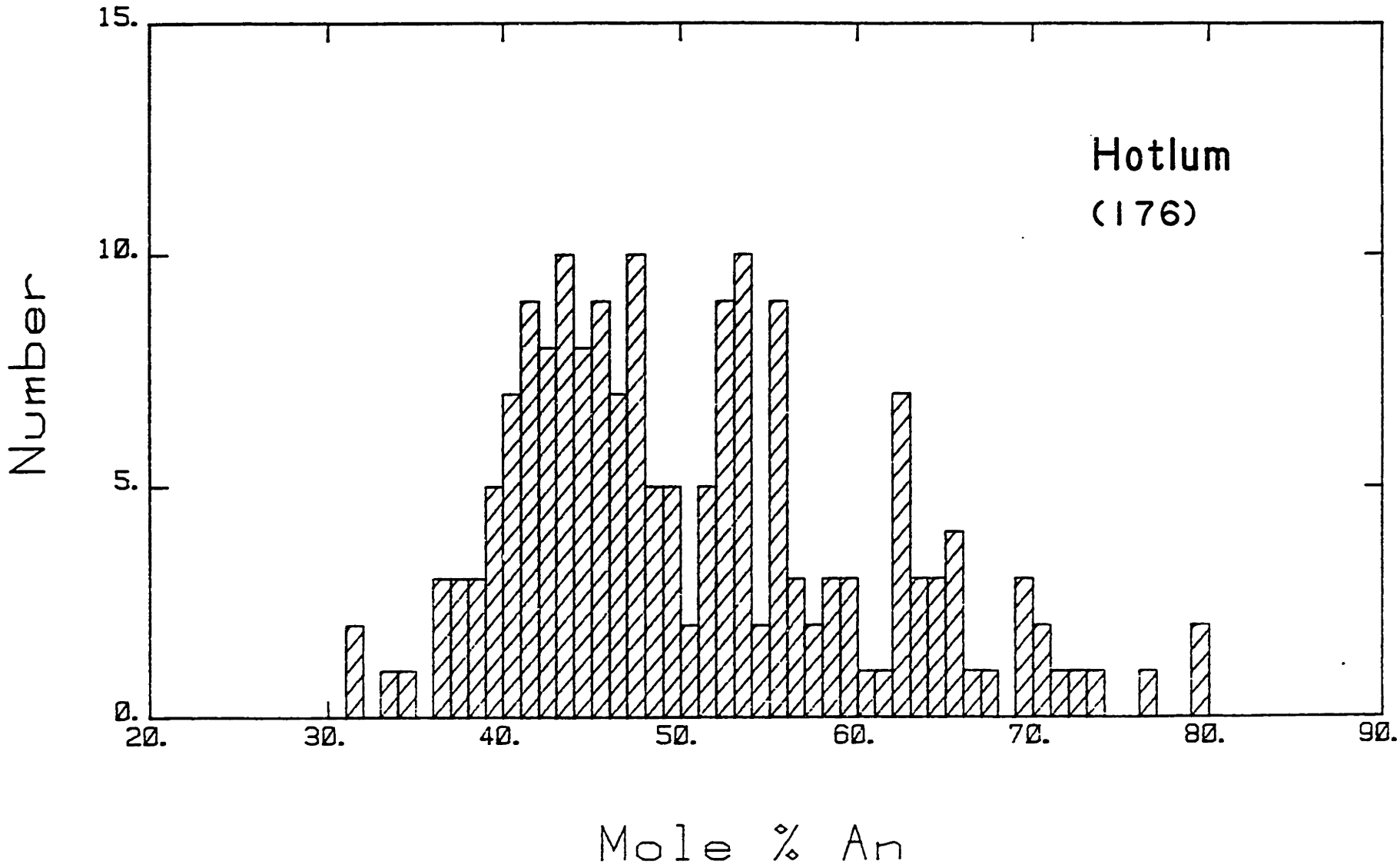
Hotlum
(176)
Number
15.
10.
5.
0.
20.
30.
40.
50.
60.
70.
80.
90.
Mole % An

Figure 2-17. (a) Mg# histogram for orthopyroxene phenocrysts and (b) augite phenocrysts (core compositions only) from Hotlum andesites and dacites. Total number of analyses given in parentheses.

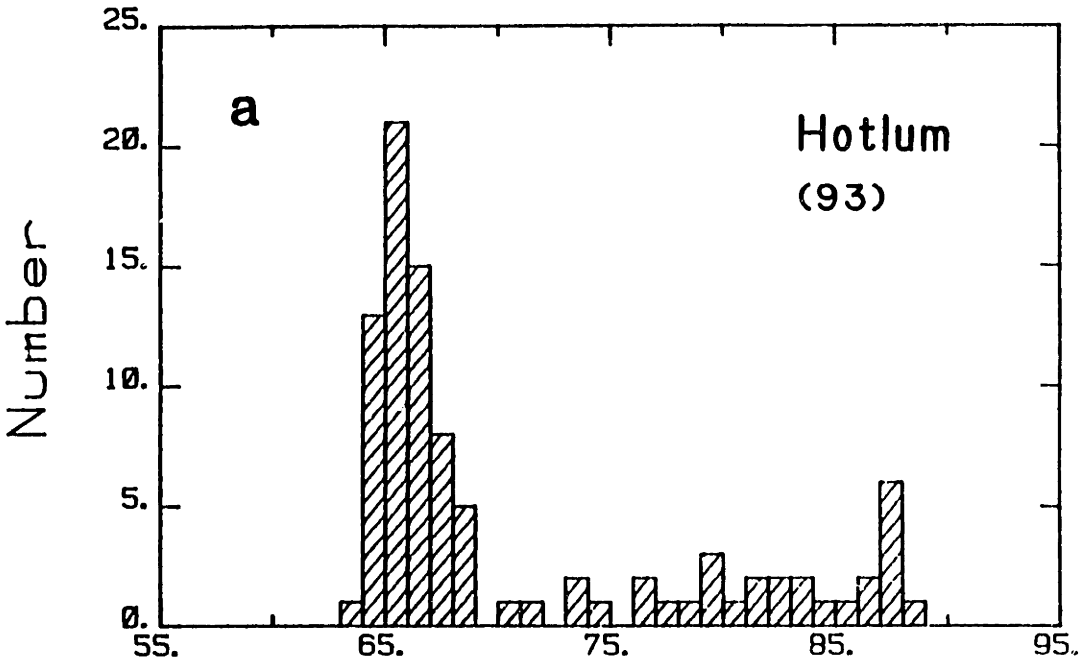
a
Hotlum
(93)
Number
25.
20.
15.
10.
5.
0.
55.
65.
75.
85.
95.
Mg# Opx

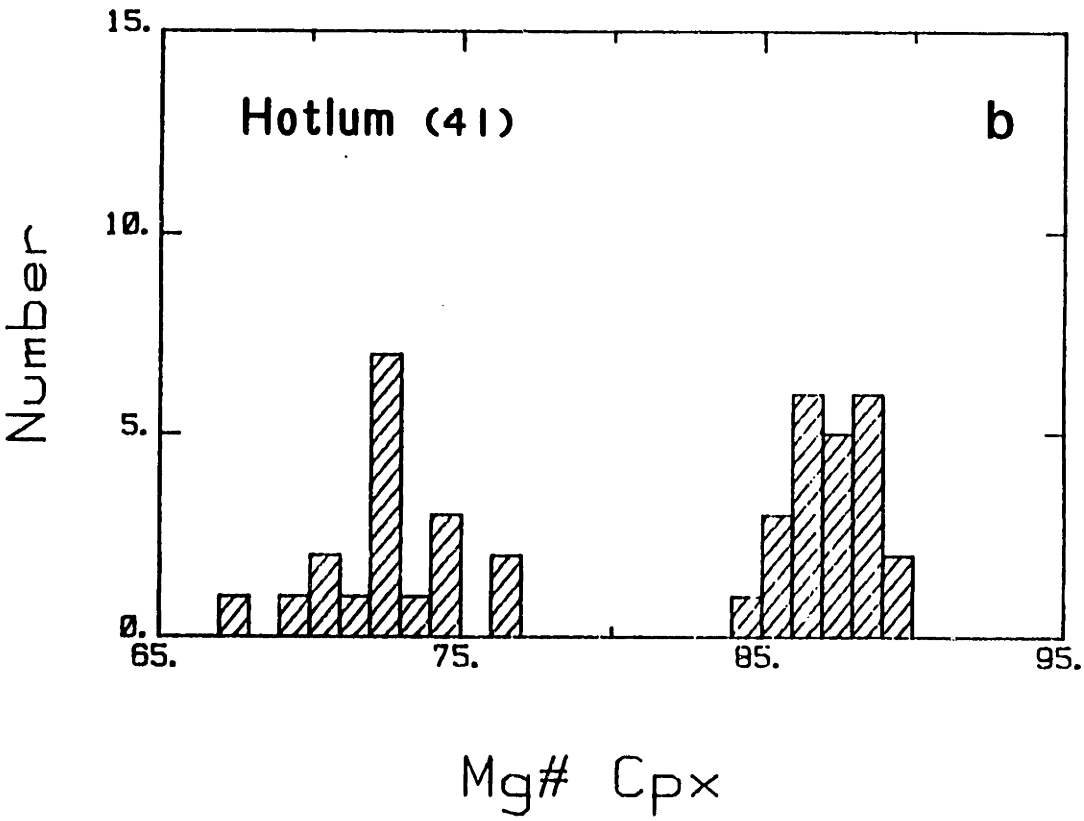
Hotlum (41)
b
Number
15.
10.
5.
0.
65.
75.
85.
95.
Mg# Cpx

Figure 2-18. (a) Plagioclase phenocryst compositions from McKenzie Butte rhyodacite plotted in terms of molar An-Ab-Or components. (b) Normalized mole fractions of Ca, Mg and Fe in orthopyroxene and amphibole phenocrysts from the rhyodacite.

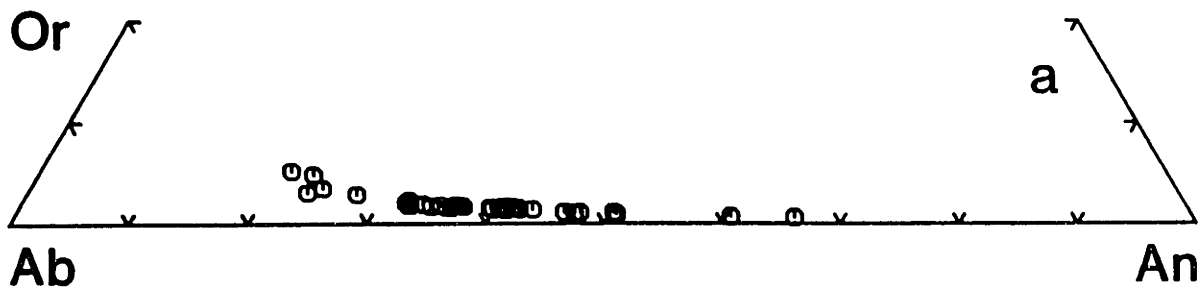
Or
a
Ab
An

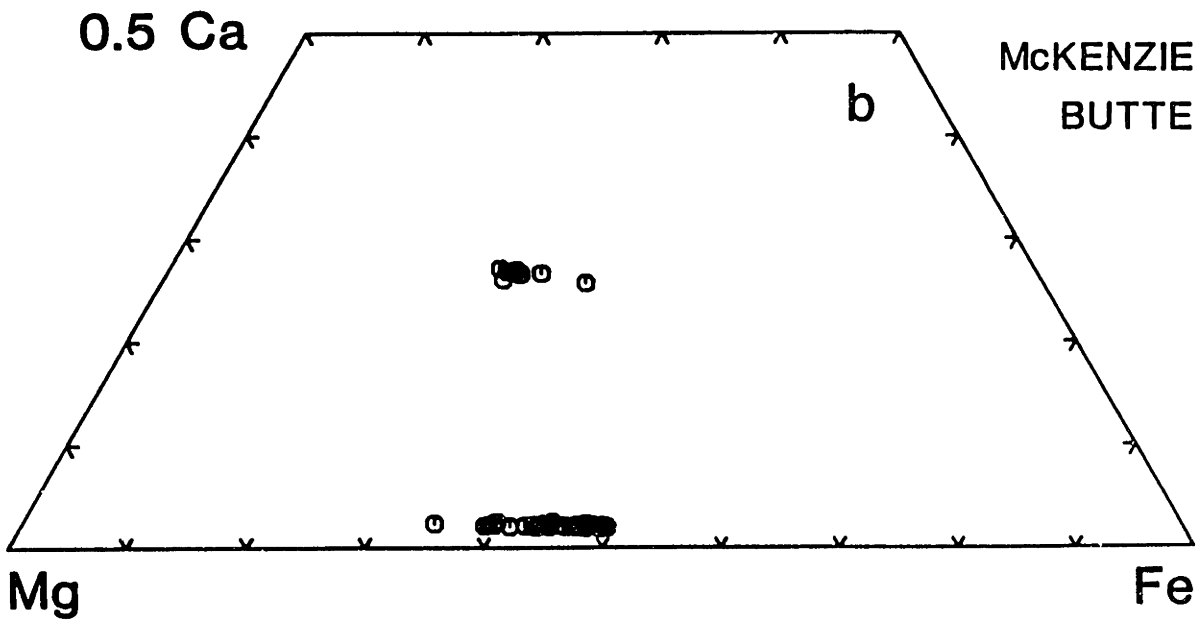
0.5 Ca
McKENZIE
BUTTE
b
Mg
Fe

Figure 2-19. Major element oxide variations in the Mt. Shasta lavas as a function of MgO content. All oxides are wt.%. Symbols for the different eruptive units are defined in the figure.

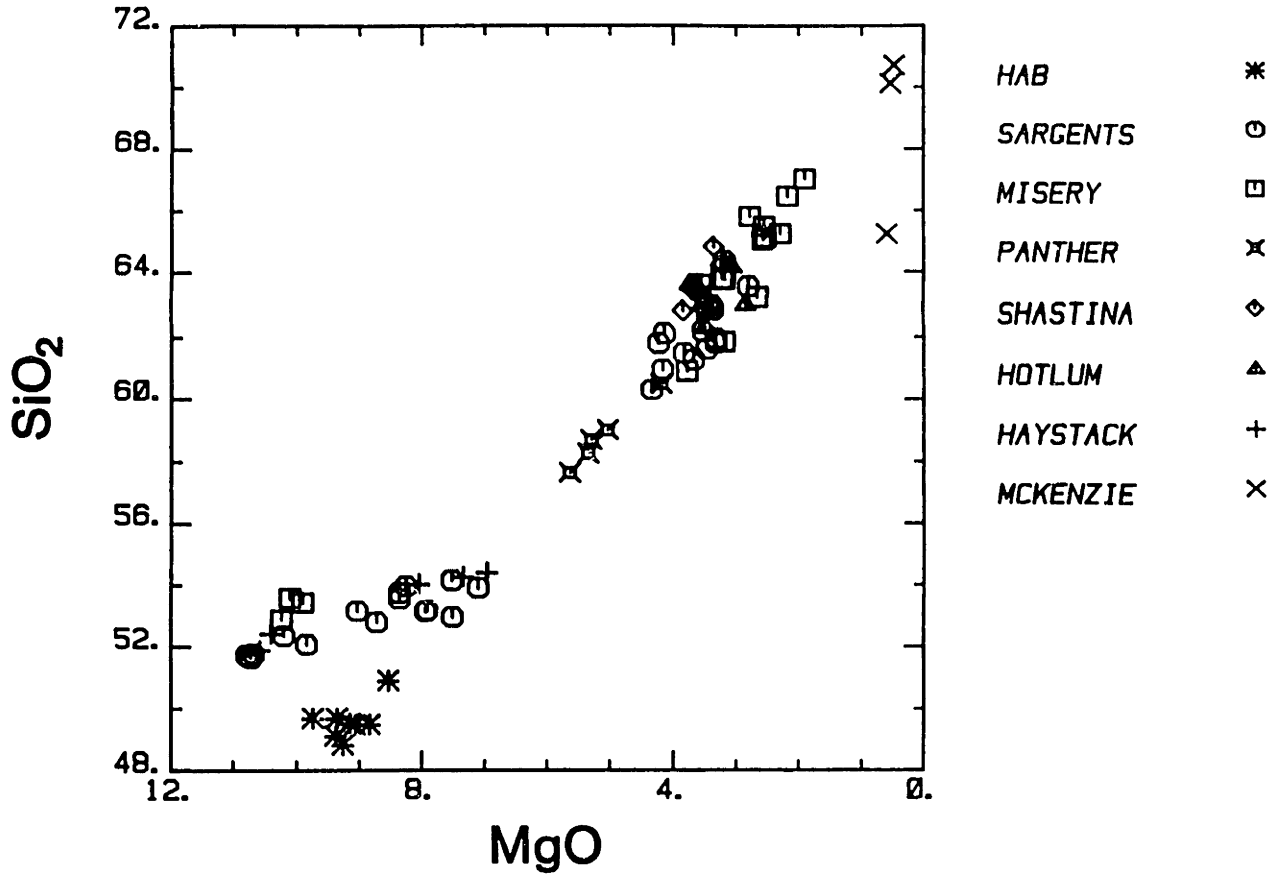
72.
68.
64.
60.
56.
52.
48.
SiO2
12.
8.
4.
0.
MgO
HAB
SARGENTS
MISERY
PANTHER
SHASTINA
HOTLUM
HAYSTACK
MCKENZIE

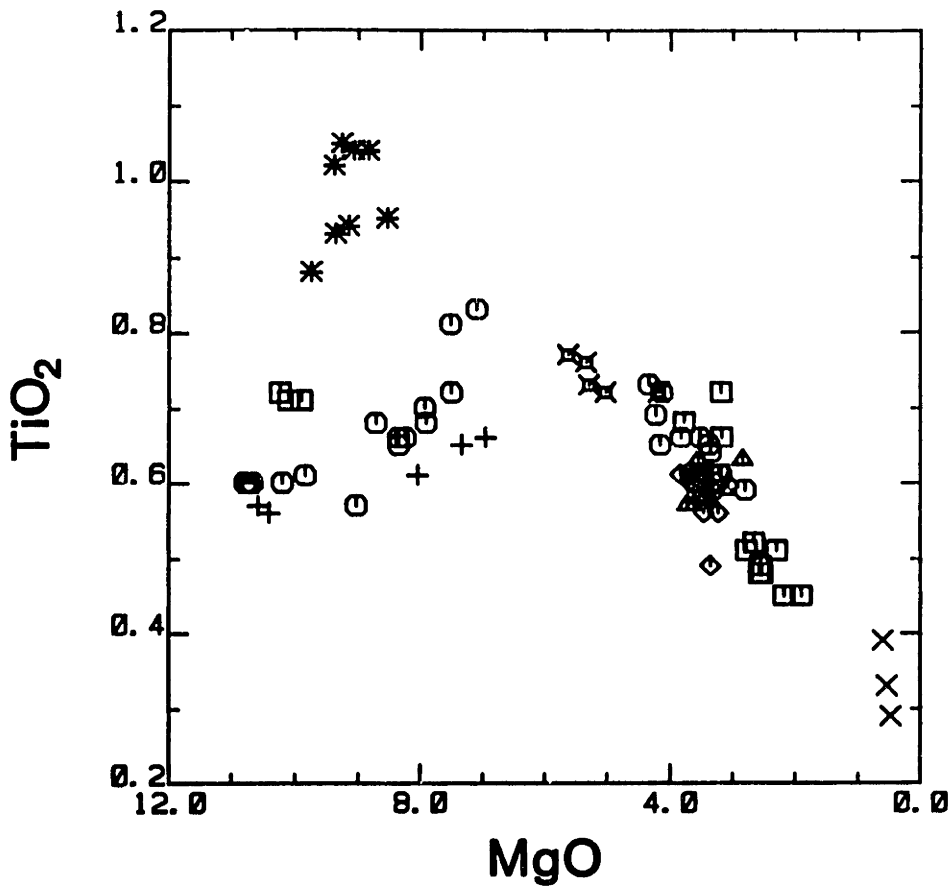
1.2
1.0
0.8
0.6
0.4
0.2
TiO2
12.0
8.0
4.0
0.0
MgO

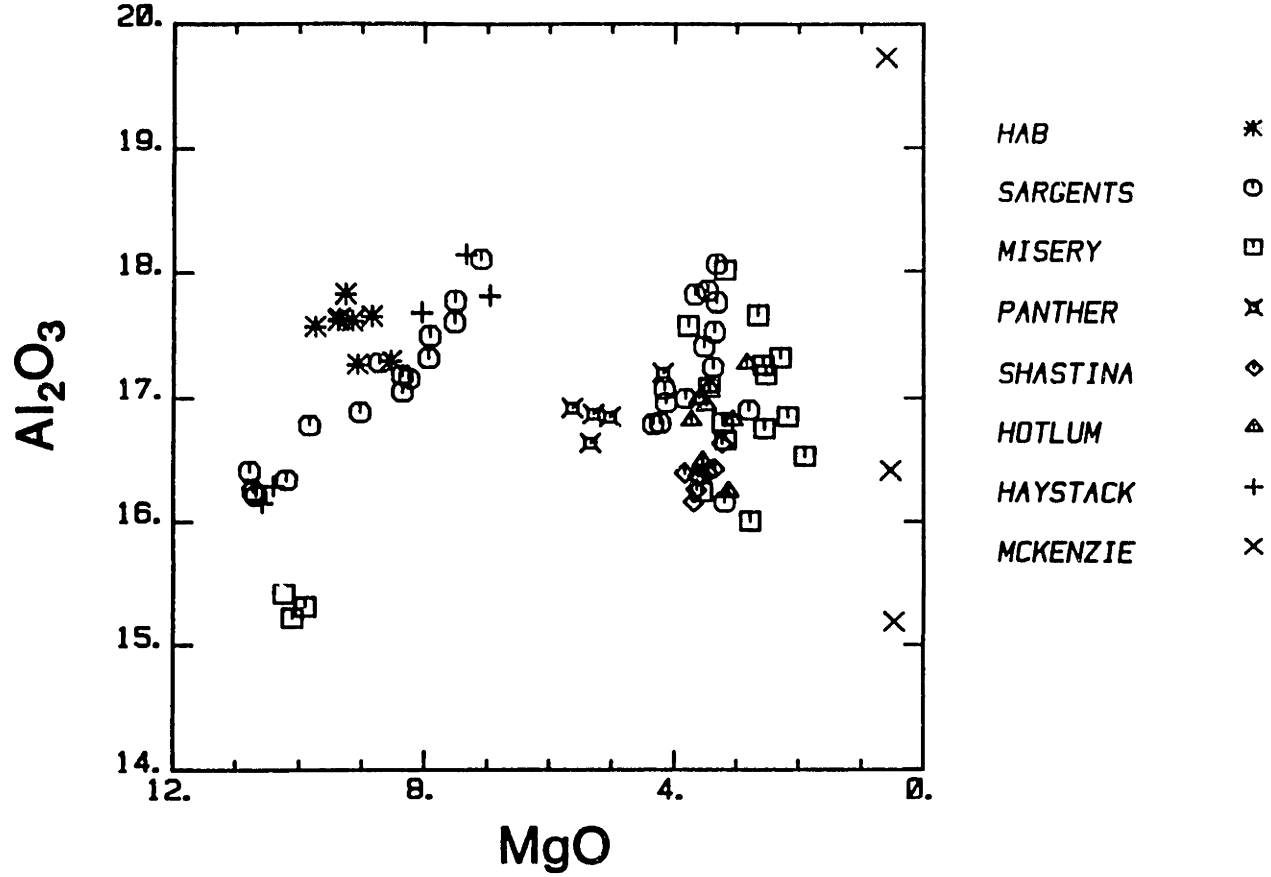
20.
19.
18.
17.
16.
15.
14.
12.
8.
4.
0.
Al_2O_3
MgO
HAB
SARGENTS
MISERY
PANTHER
SHASTINA
HOTLUM
HAYSTACK
MCKENZIE

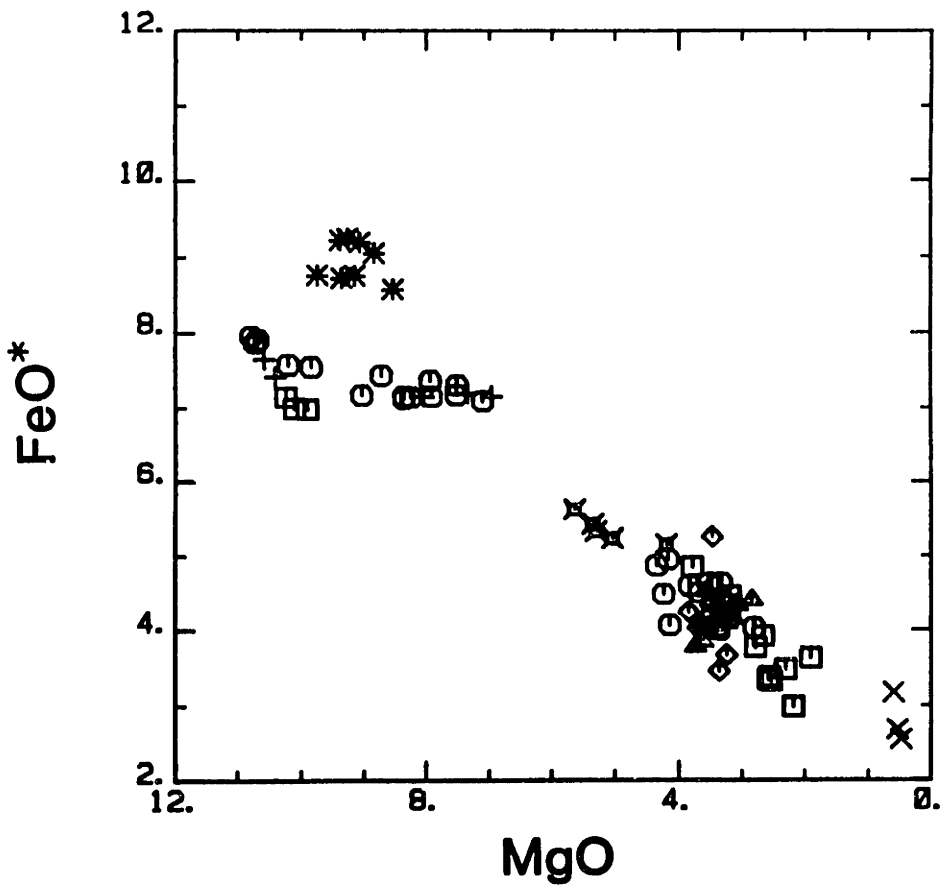
12.
10.
8.
6.
4.
2.
12.
8.
4.
0.
FeO*
MgO

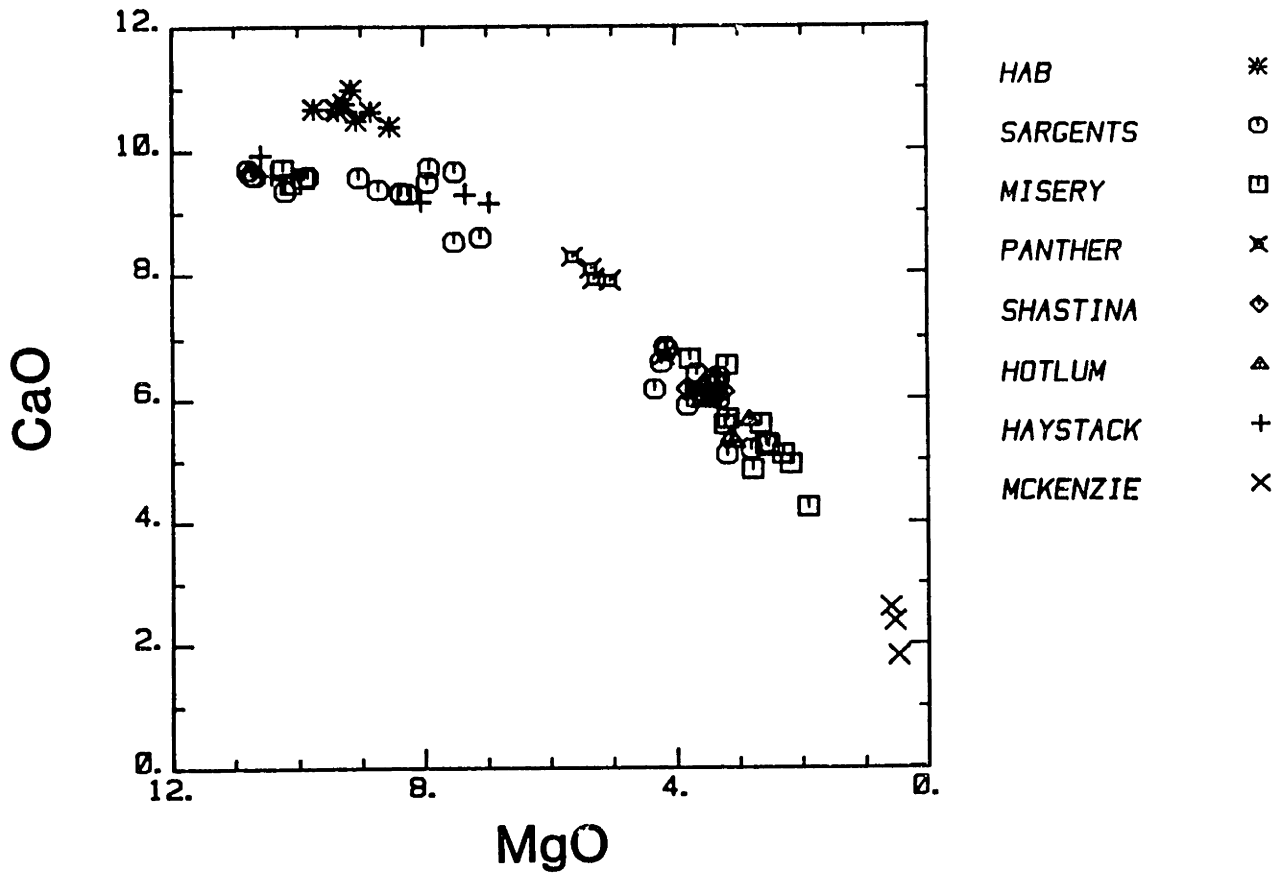
CaO
MgO
12.
10.
8.
6.
4.
2.
0.
HAB
SARGENTS
MISERY
PANTHER
SHASTINA
HOTLUM
HAYSTACK
MCKENZIE

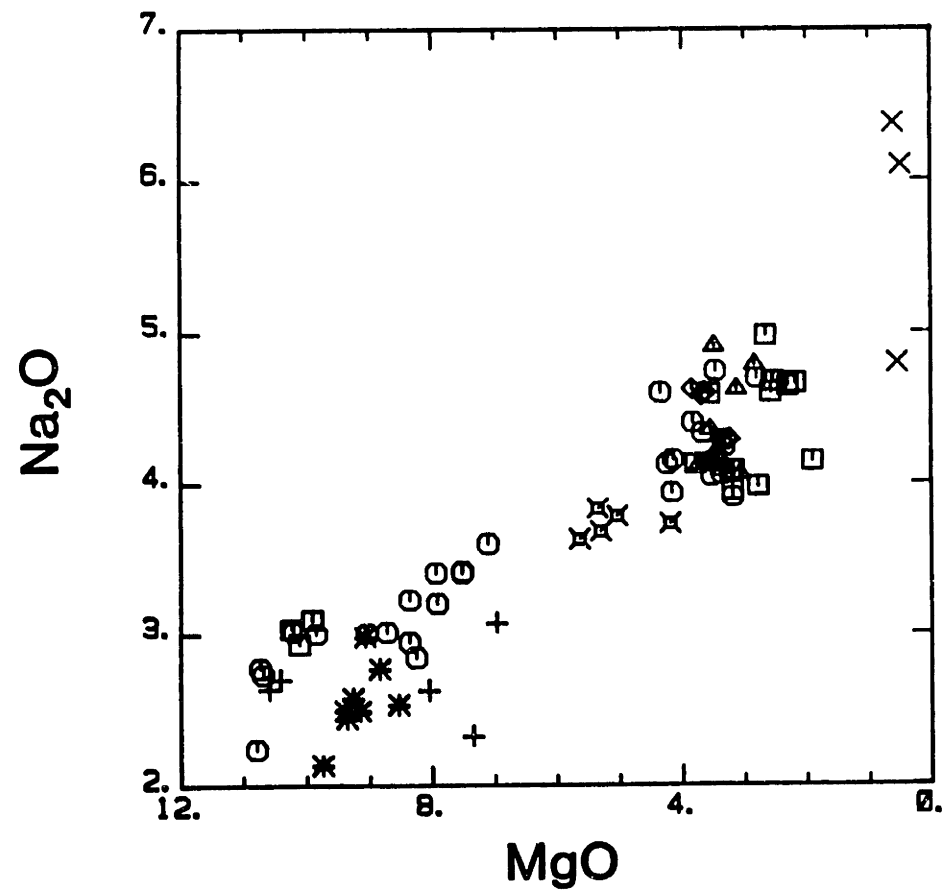
Na2O
MgO
7.
6.
5.
4.
3.
2.
12.
8.
4.
0.

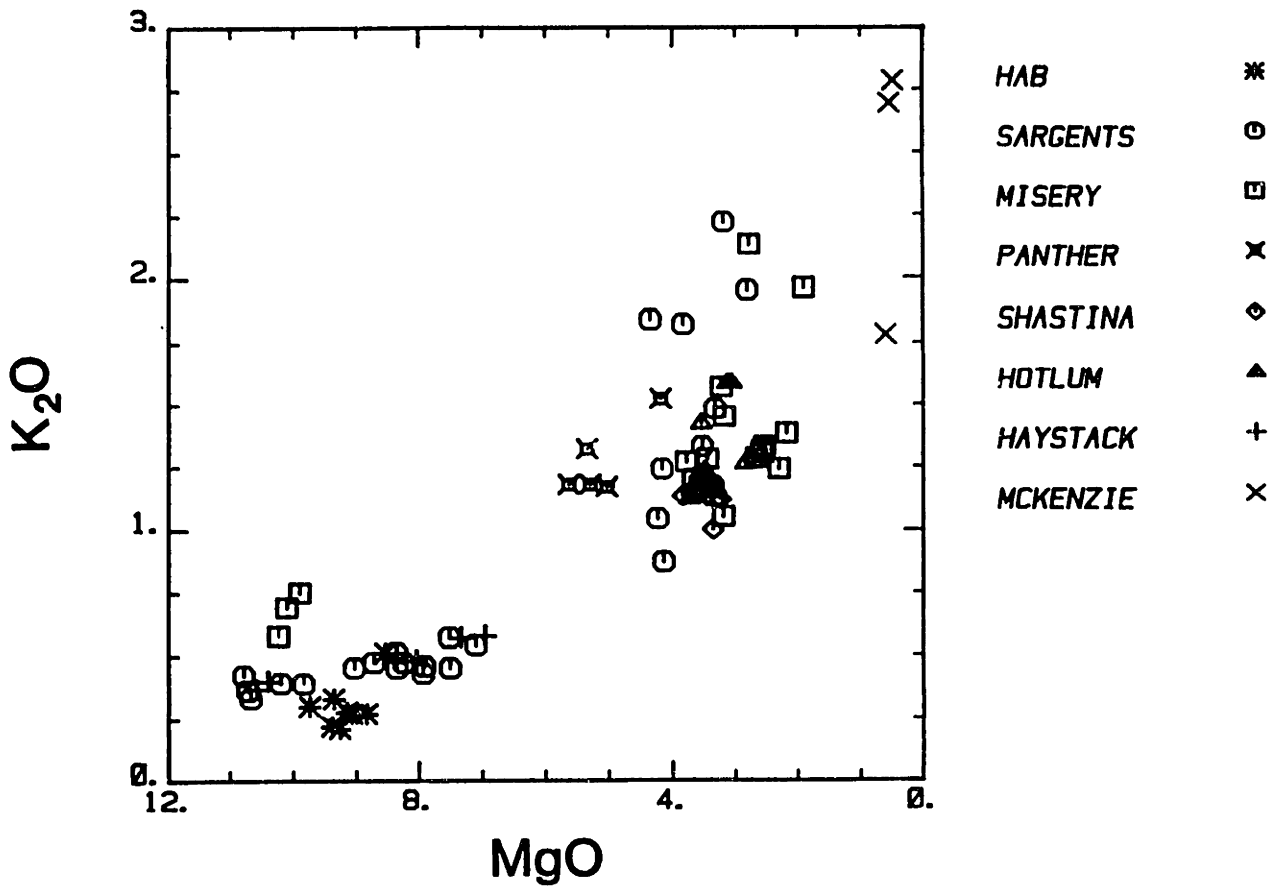
3.
2.
1.
0.
12.
8.
4.
0.
K2O
MgO
HAB
SARGENTS
MISERY
PANTHER
SHASTINA
HOTLUM
HAYSTACK
MCKENZIE

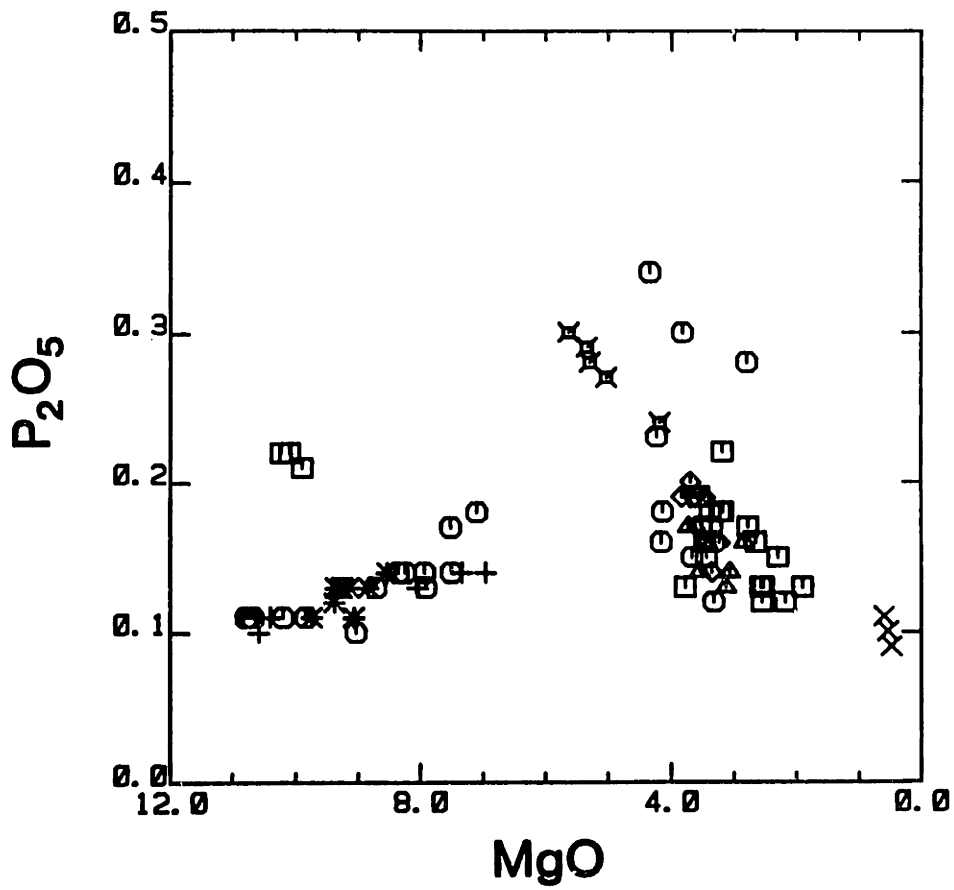
0.5
0.4
0.3
0.2
0.1
0.0
12.0
8.0
4.0
0.0
P2O5
MgO

Figure. 2-20. (a) ΔAl_2O_3 vs vol.% large plagioclase phenocrysts (>0.5 mm) in the Mt. Shasta andesites and dacites. (b) ΔAl_2O_3 vs total plagioclase phenocryst content. Modal data from Table 2-13. ΔAl_2O_3 = Al_2O_3 in a sample minus the mean Al_2O_3 for all lavas from that eruptive unit.

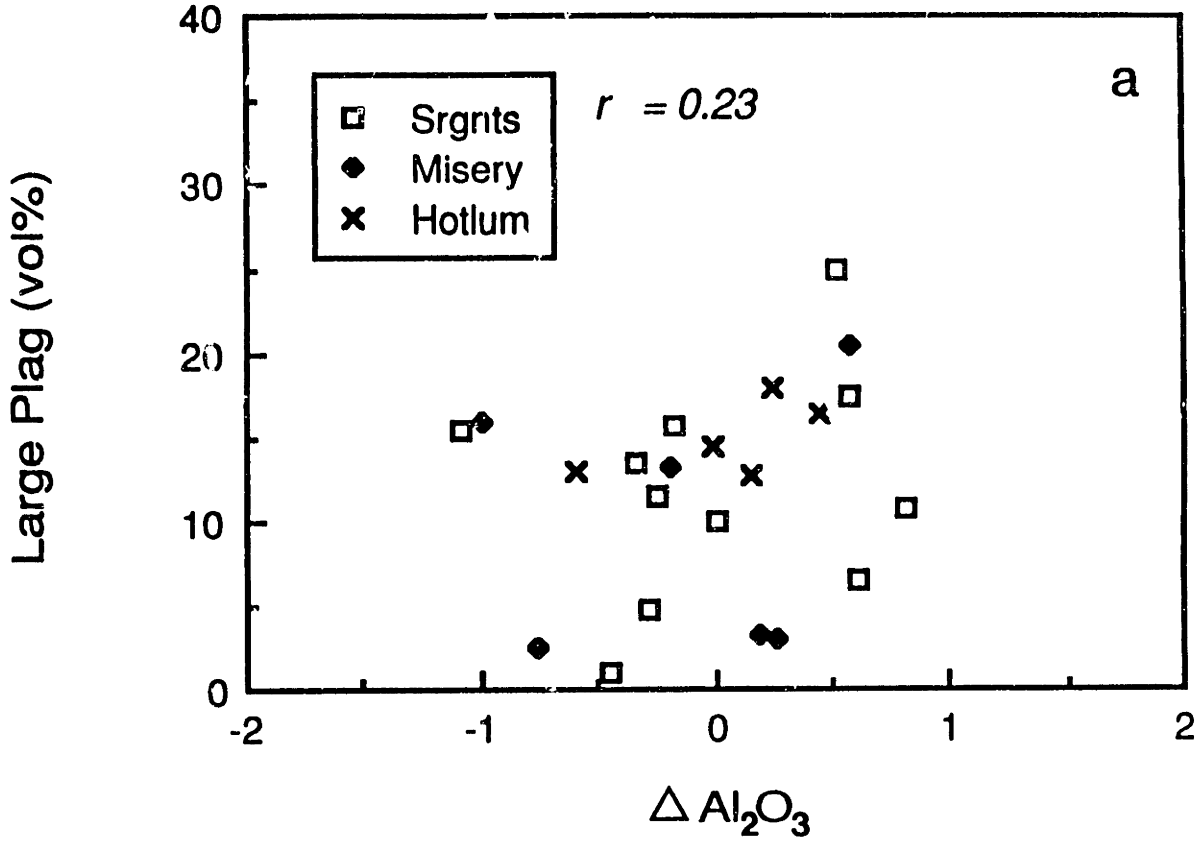
Large Plag (vol%)
40
30
20
10
0
-2
-1
0
1
2
Srgnts
Misery
Hotlum
r = 0.23
a
Δ Al2O3

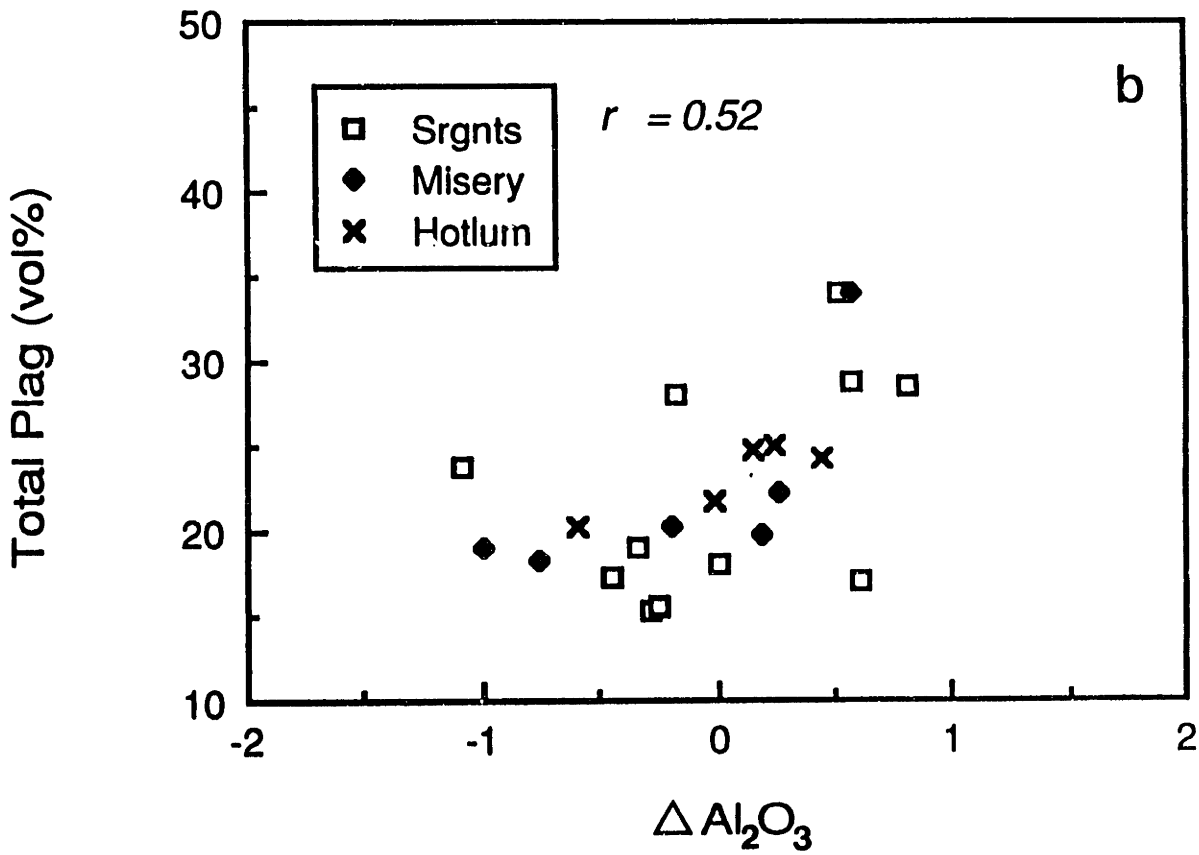
Total Plag (vol%)
50
40
30
20
10
-2
-1
0
1
2
Srgnts
Misery
Hotlum
r = 0.52
b
Δ Al2O3

Figure 2-21. Variations in SiO_2, Al_2O_3, FeO, MgO and Na_2O produced by adding and subtracting 15 wt.% plagioclase from 82-86. The plagioclase represents the average phenocryst composition found in this sample. In each figure, 82-86 is plotted as a solid circle. The field of andesite and dacite compositions at Mt. Shasta is denoted by And-Dac.

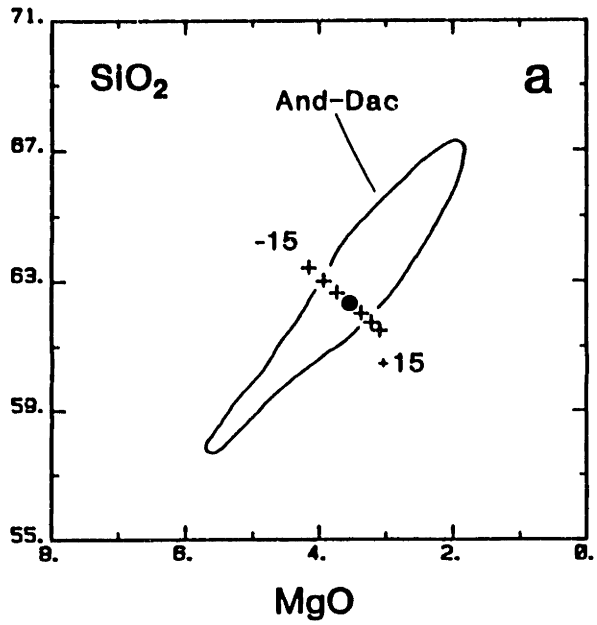
71.
67.
63.
59.
55.
SiO2
a
And-Dac
-15
+15
8.
6.
4.
2.
0.
MgO

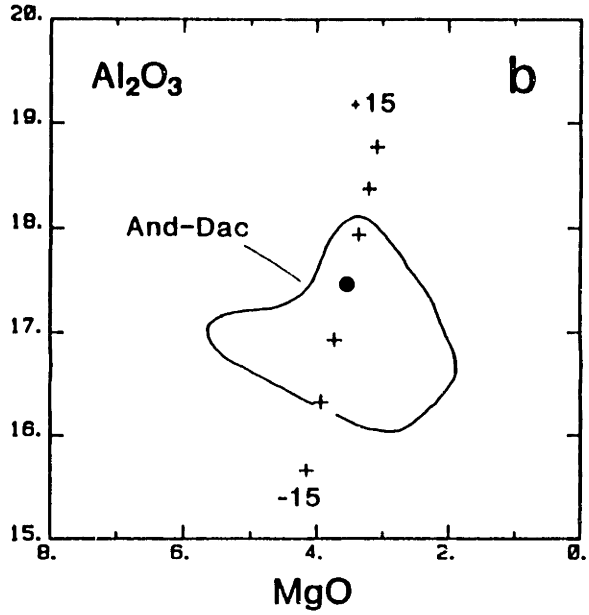
20.
19.
18.
17.
16.
15.
Al2O3
b
+15
And-Dac
-15
8.
6.
4.
2.
0.
MgO

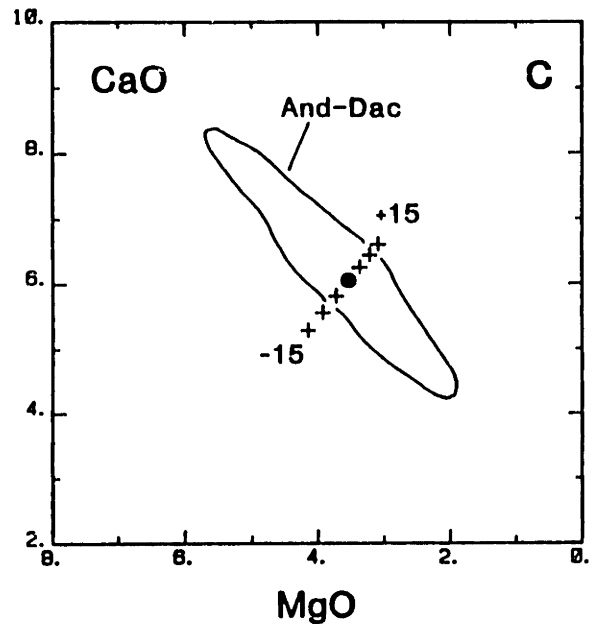
10.
8.
6.
4.
2.
CaO
c
And-Dac
+15
-15
8.
6.
4.
2.
0.
MgO

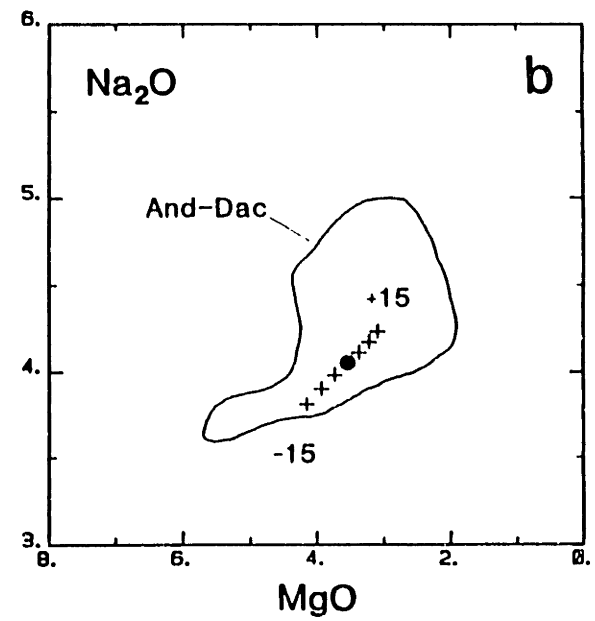
6.
5.
4.
3.
Na2O
b
And-Dac
+15
-15
8.
6.
4.
2.
0.
MgO

Figure 2-22. FeO*/MgO vs wt.% SiO_2 for all Mt. Shasta samples. The fields for Medicine Lake Highlands volcano and Crater Lake volcano are based on whole-rock analyses from Donnelly-Nolan (unpublished data) and Bacon and Druitt (1988), respectively. The dashed line with arrows is part of the Medicine Lake andesite to rhyolite fractional crystallization path from Grove and Donnelly-Nolan (1986). The dividing line between tholeiitic and calc-alkaline compositions is from Miyashiro (1974).

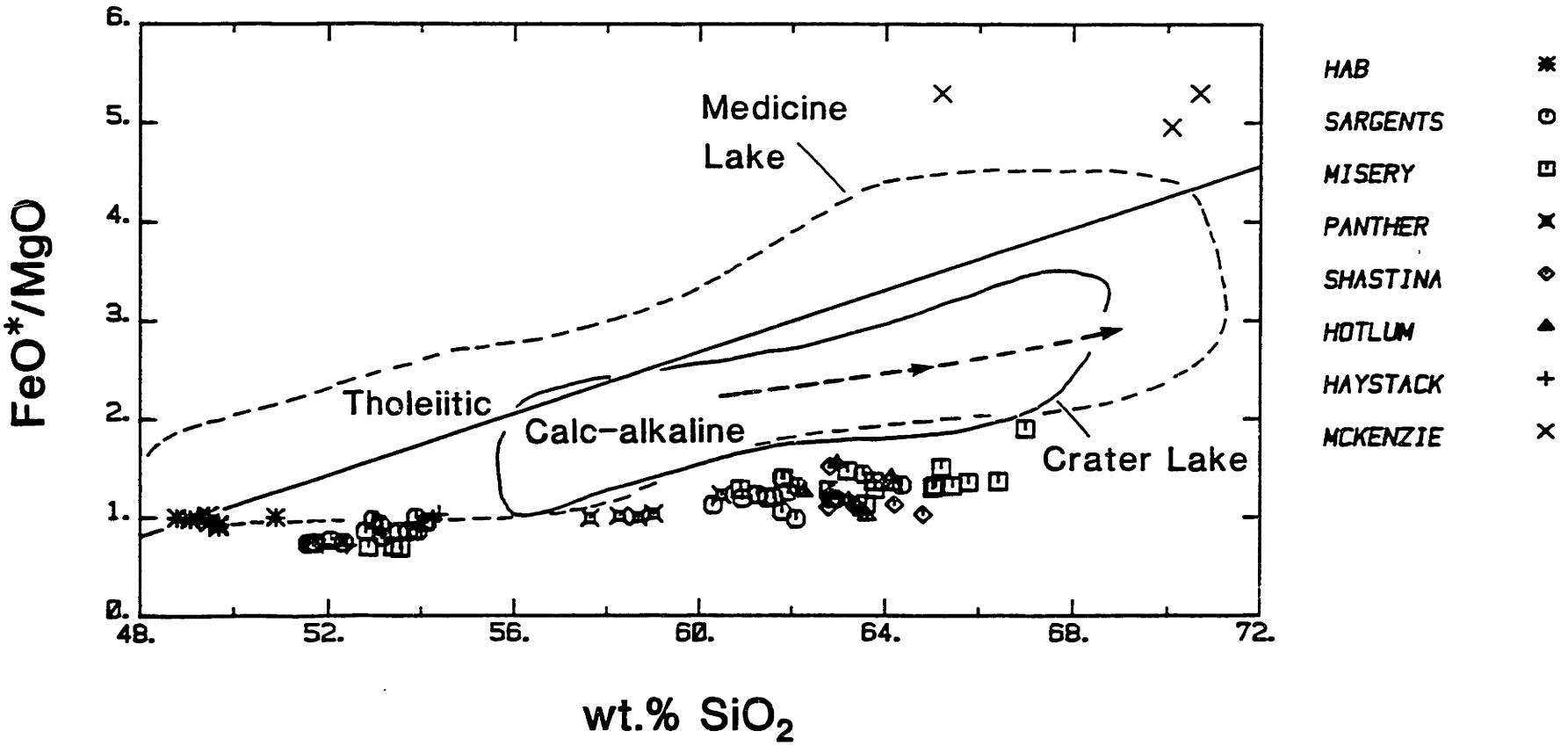
FeO*/MgO
6.
5.
4.
3.
2.
1.
0.
48.
52.
56.
60.
64.
68.
72.
wt.% SiO2
Medicine
Lake
Tholeiitic
Calc-alkaline
Crater Lake
HAB
SARGENTS
MISERY
PANTHER
SHASTINA
HOTLUM
HAYSTACK
MCKENZIE

Figure 2-23. Compatible trace element variations (a) Ni and (b) Cr in the the Mt. Shasta lavas as a function of MgO content. Trace element abundances in ppm. References for the Medicine Lake and Crater Lake fields given in Fig. 2-22.

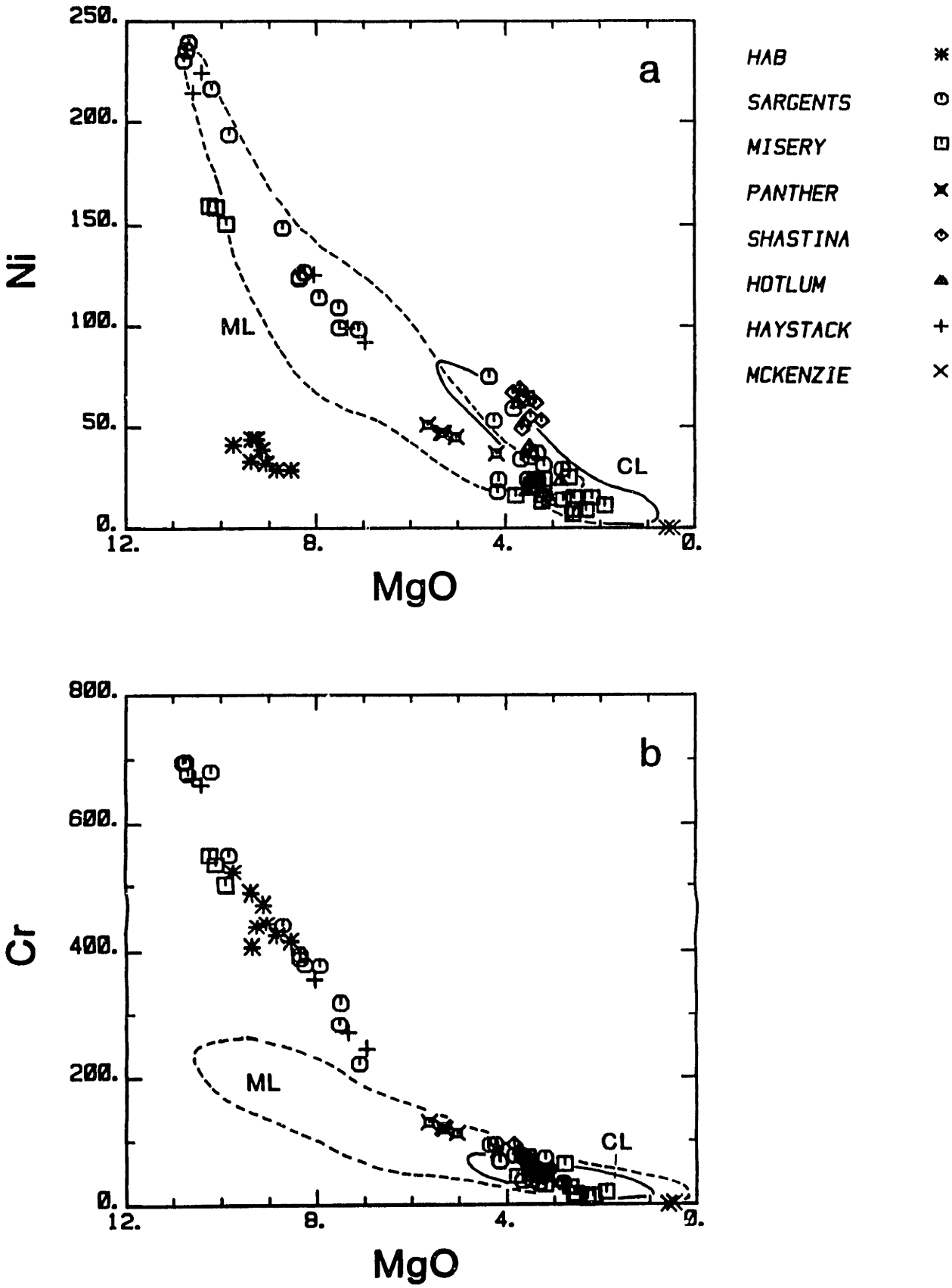
a
b
Ni
Cr
MgO
MgO
250.
200.
150.
100.
50.
0.
800.
600.
400.
200.
0.
12.
8.
4.
0.
ML
CL
ML
CL
HAB
SARGENTS
MISERY
PANTHER
SHASTINA
HOTLUM
HAYSTACK
MCKENZIE

Figure 2-24. Incompatible element abundances (ppm) as functions of wt.% MgO in the Mt. Shasta lavas. References for the Medicine Lake and Crater Lake Fields given in Fig. 2-22.

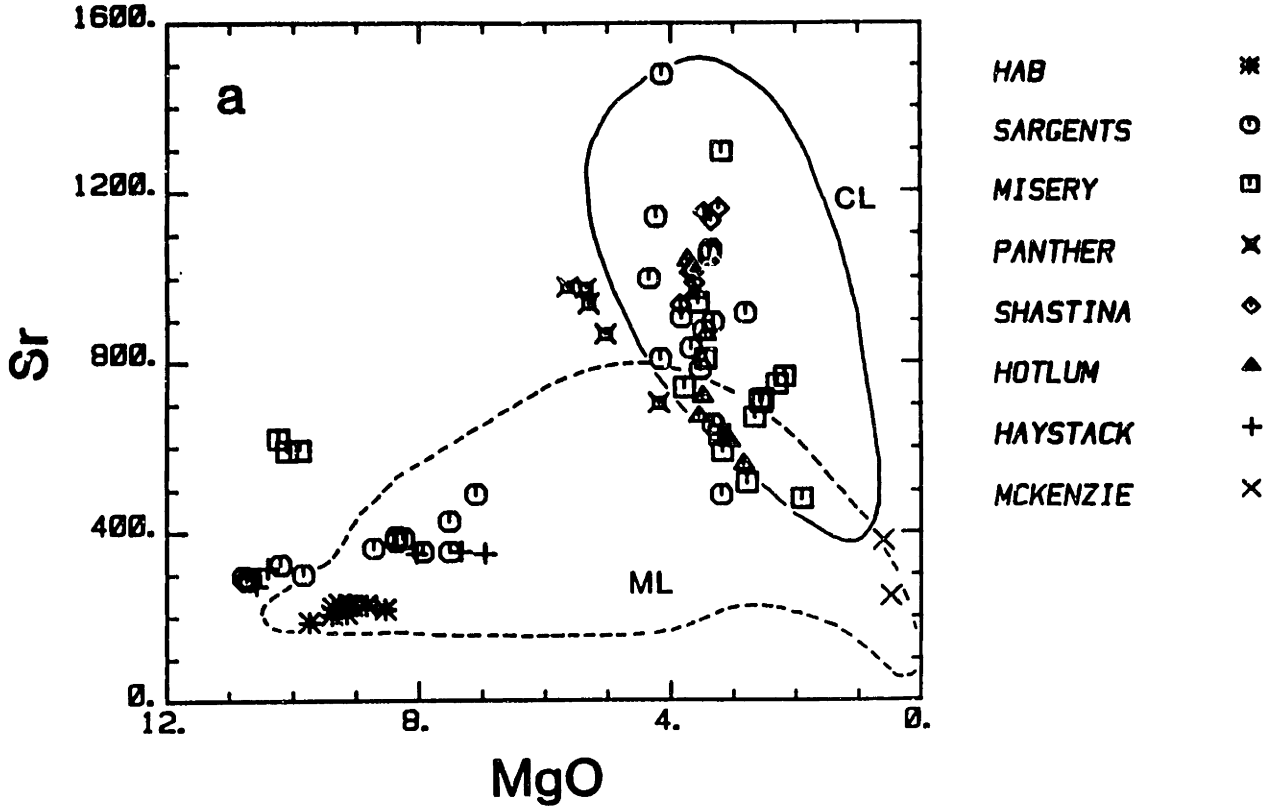
a
1600.
1200.
800.
400.
0.
Sr
12.
8.
4.
0.
MgO
CL
ML
HAB
SARGENTS
MISERY
PANTHER
SHASTINA
HOTLUM
HAYSTACK
MCKENZIE

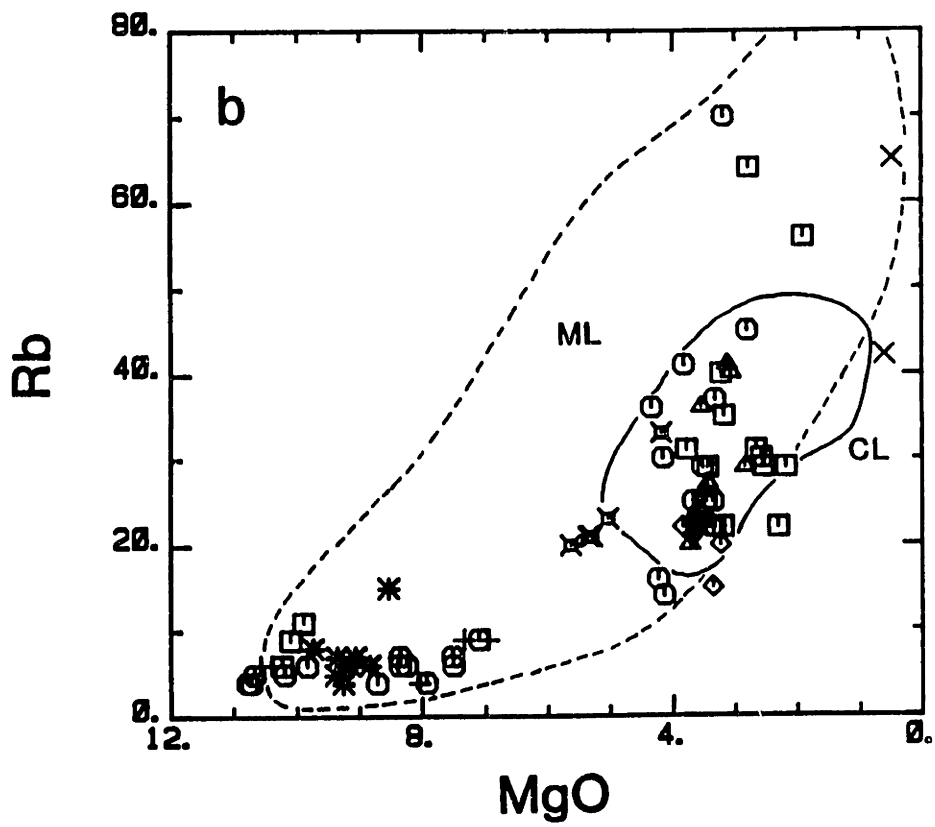
b
80.
60.
40.
20.
0.
Rb
12.
8.
4.
0.
MgO
ML
CL

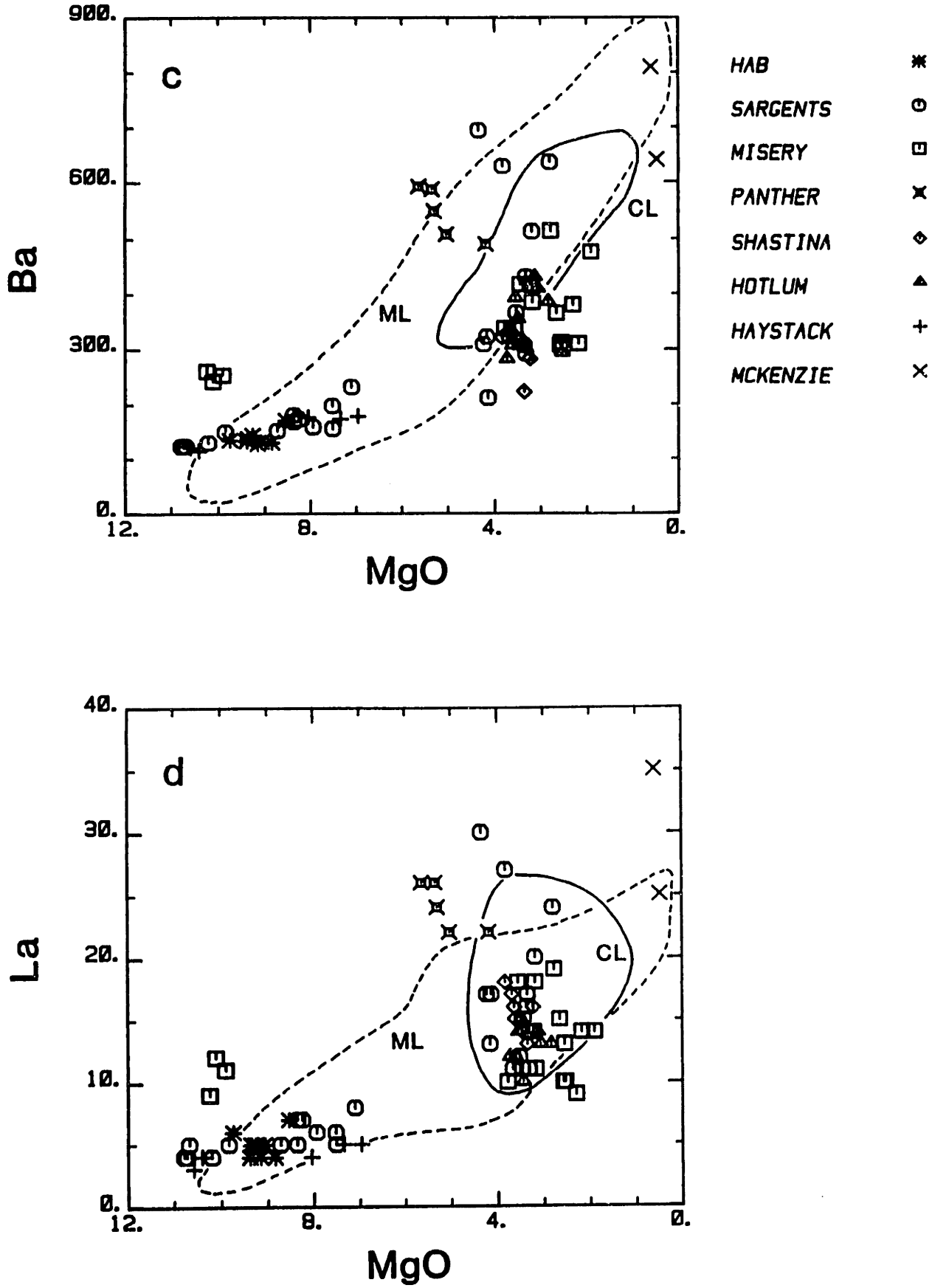
c
900.
600.
300.
0.
Ba
12.
8.
4.
0.
MgO
ML
CL
HAB
SARGENTS
MISERY
PANTHER
SHASTINA
HOTLUM
HAYSTACK
MCKENZIE
d
40.
30.
20.
10.
0.
La
12.
8.
4.
0.
MgO
ML
CL

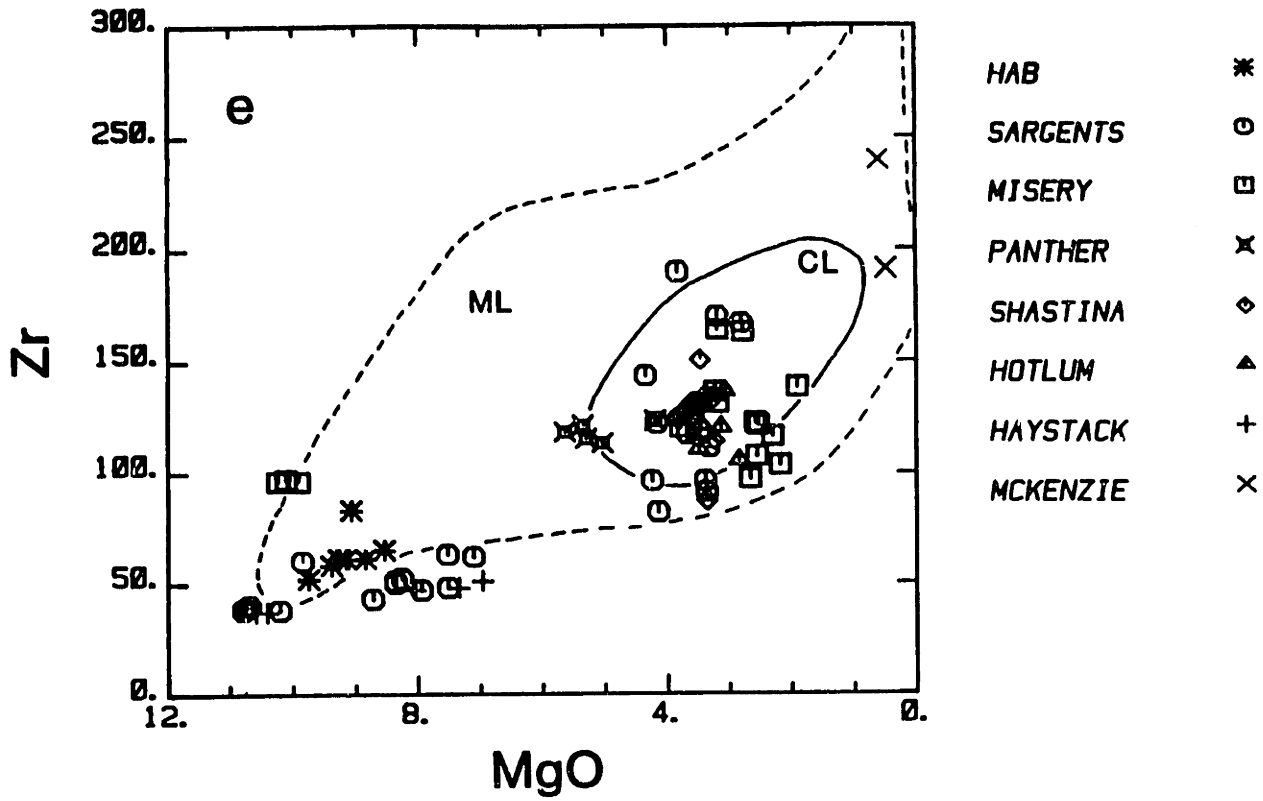
e
300.
250.
200.
150.
100.
50.
0.
Zr
12.
8.
4.
0.
MgO
ML
CL
HAB
SARGENTS
MISERY
PANTHER
SHASTINA
HOTLUM
HAYSTACK
MCKENZIE

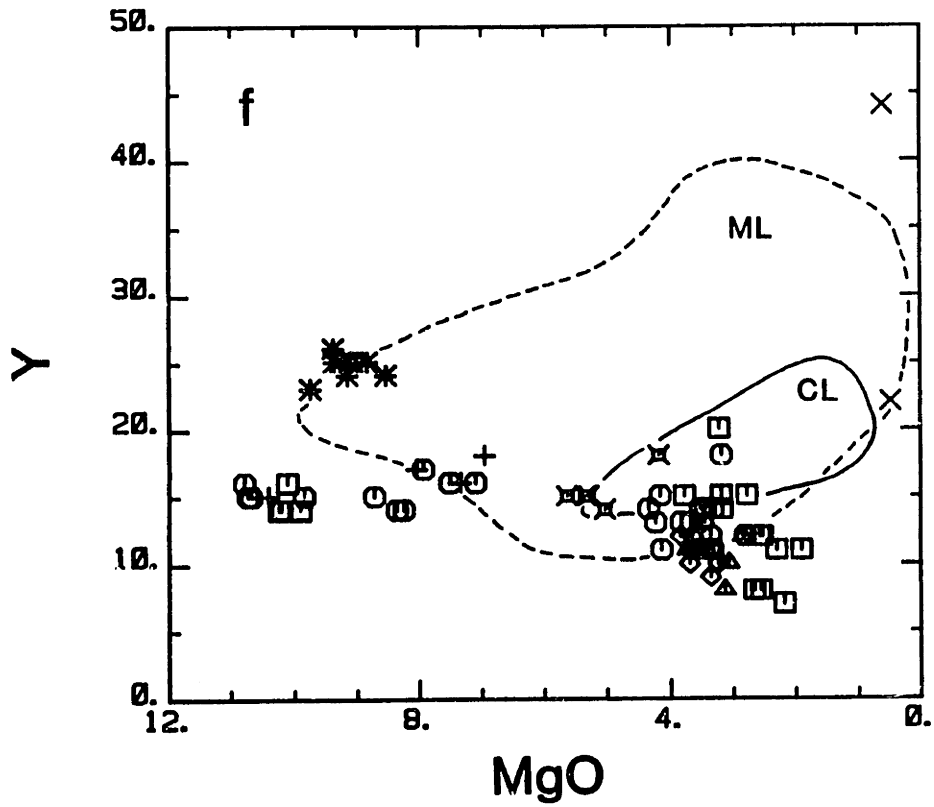
f
50.
40.
30.
20.
10.
0.
Y
12.
8.
4.
0.
MgO
ML
CL

Figure 2-25. K_2O (wt.%) vs Rb (ppm) for the Mt. Shasta lavas. Lines of constant K/Rb are labelled in the figure. References for the Medicine Lake and Crater Lake fields given in Fig. 2-22.

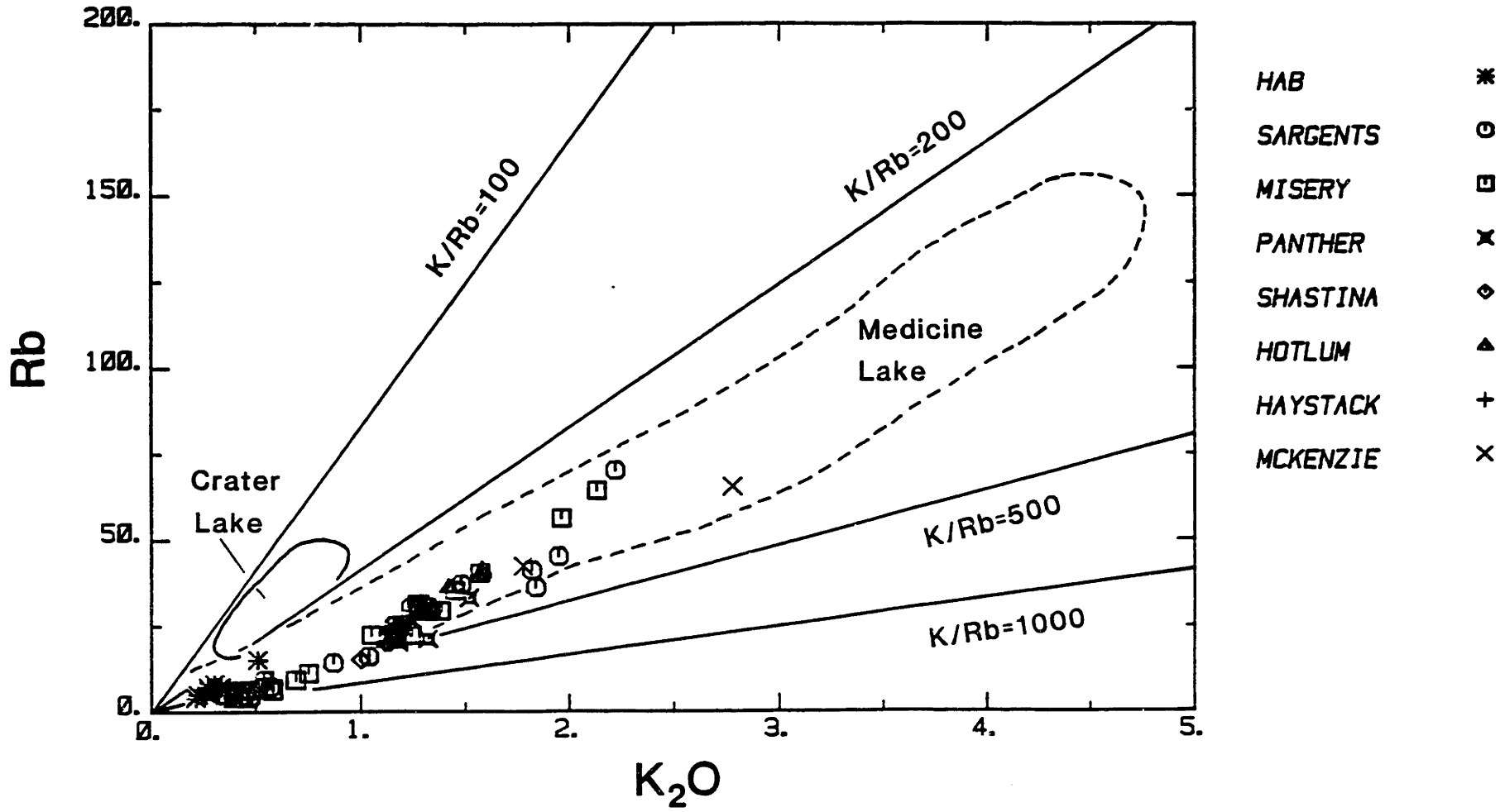
200.
150.
100.
50.
0.
Rb
0.
1.
2.
3.
4.
5.
K_2O
K/Rb=100
K/Rb=200
K/Rb=500
K/Rb=1000
Medicine Lake
Crater Lake
HAB
SARGENTS
MISERY
PANTHER
SHASTINA
HOTLUM
HAYSTACK
MCKENZIE

Figure 2-26. Ba-La ratios in the Mt. Shasta lavas. See Fig. 2-22 for the references for the Medicine Lake and Crater Lake data. Lines of constant Ba/La are labelled in the figure. The dividing line between E-type MORB and orogenic andesite from Wood et al. (1979a,b).

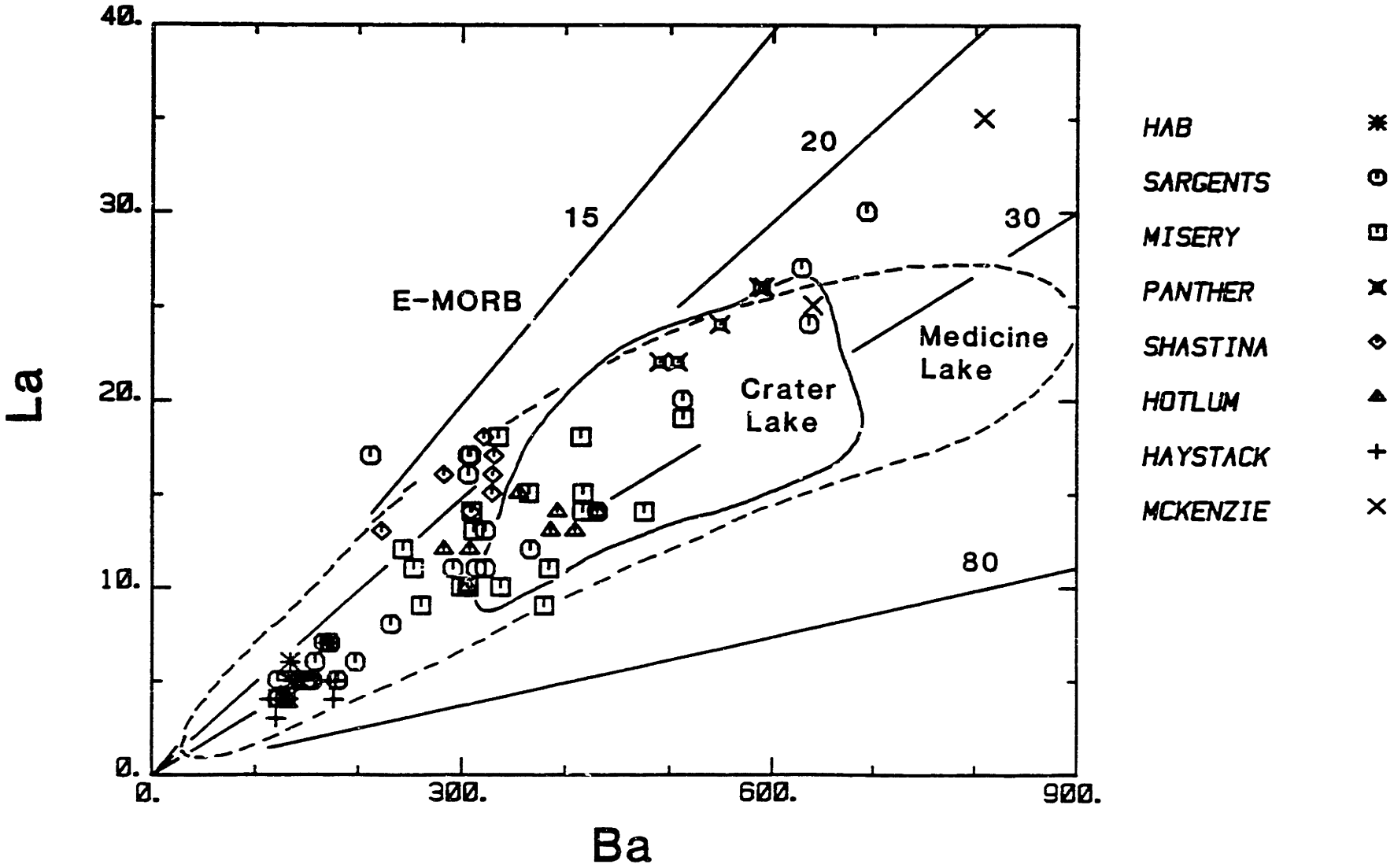
40.
30.
20.
10.
0.
La
0.
300.
600.
900.
Ba
E-MORB
15
20
30
80
Crater
Lake
Medicine
Lake
HAB
SARGENTS
MISERY
PANTHER
SHASTINA
HOTLUM
HAYSTACK
MCKENZIE

Figure 2-27. (a) $^{87/86}Sr$ vs wt.% MgO in selected basaltic andesite, andesites and dacites from Mt. Shasta. Medicine Lake field based on data from Grove et al. (1982), Kinzler (1985), Grove et al. (1988) and Chapter 1. ML = Medicine Lake. (a) $^{87/86}Sr$ vs ppm Sr in selected Mt. Shasta lavas. Sr by isotope dilution, except for samples 85-49, 85-59 and 85-55, XRF.

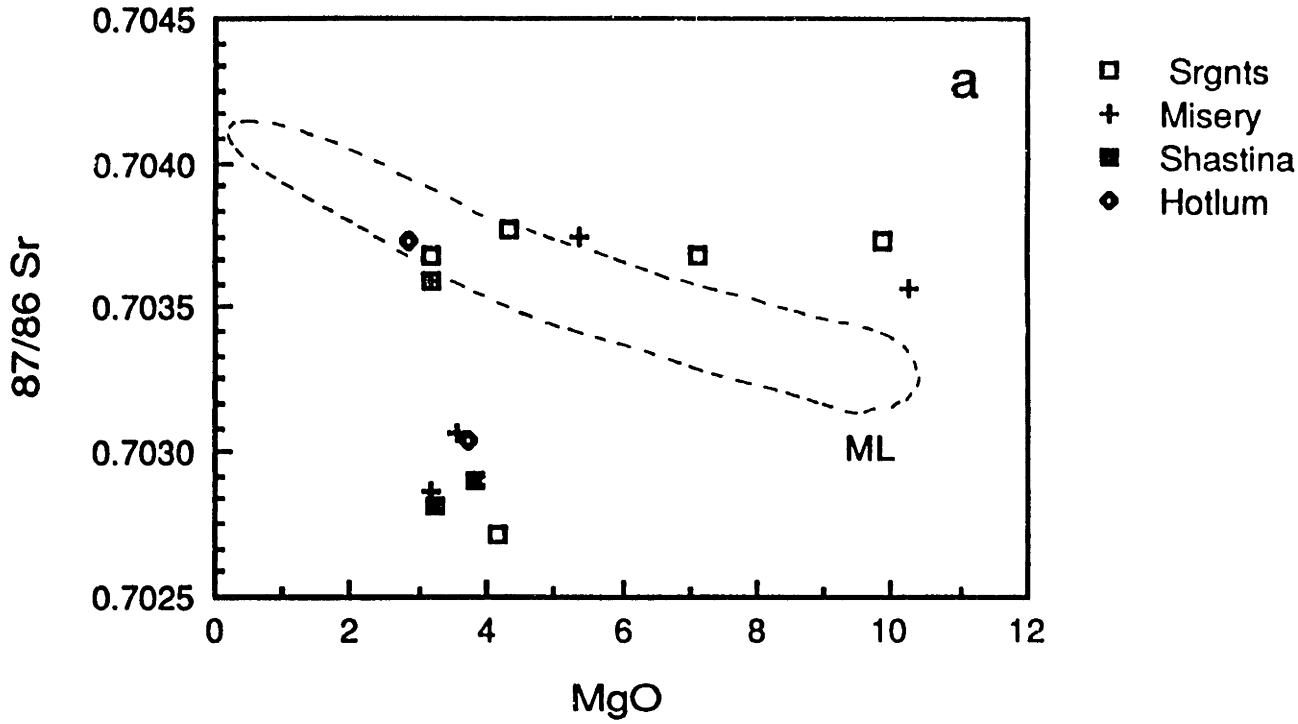
a
ML
87/86 Sr
MgO
0.7045
0.7040
0.7035
0.7030
0.7025
0
2
4
6
8
10
12
Srgnts
Misery
Shastina
Hotlum

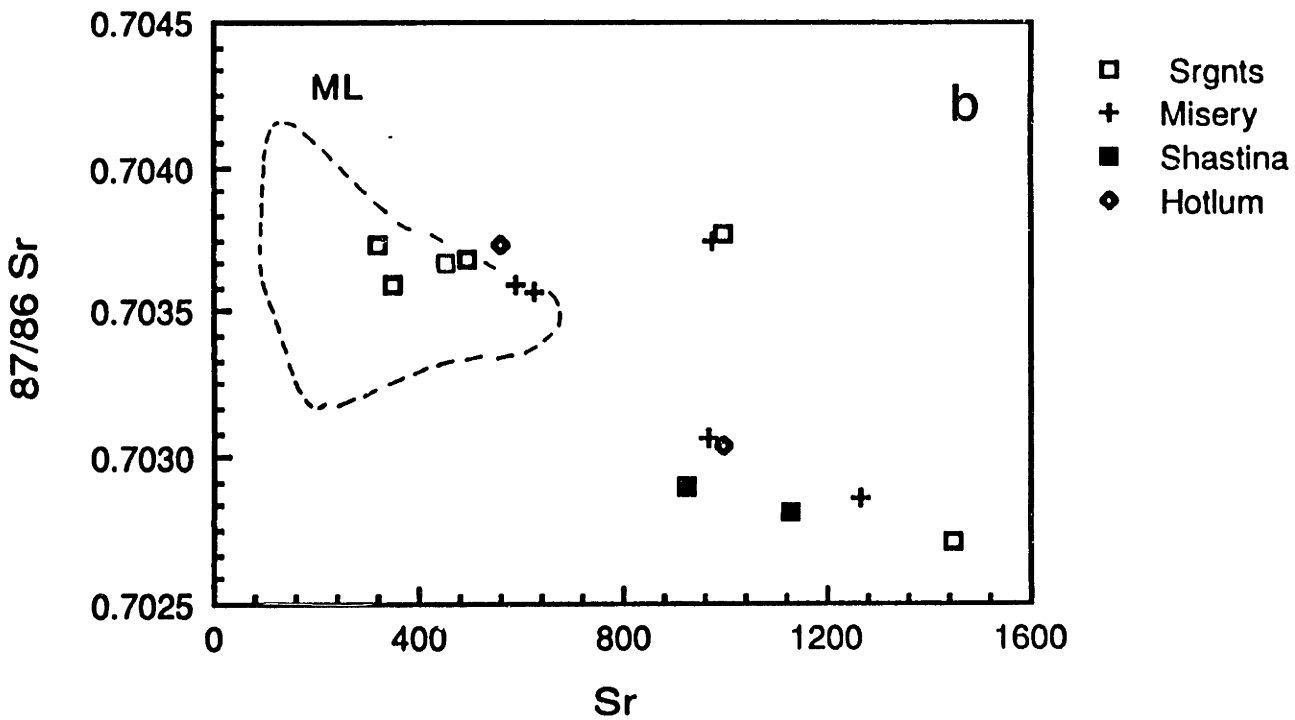
b
ML
87/86 Sr
Sr
0.7045
0.7040
0.7035
0.7030
0.7025
0
400
800
1200
1600
Srgnts
Misery
Shastina
Hotlum

Figure 2-28. Summary of 1-atm appearance temperatures (°C) for four Mt.Shasta lavas. 82-94a and 75SH-70 are basaltic andesites; 85-55 and 83-58 are low and high silica andesites, respectively.

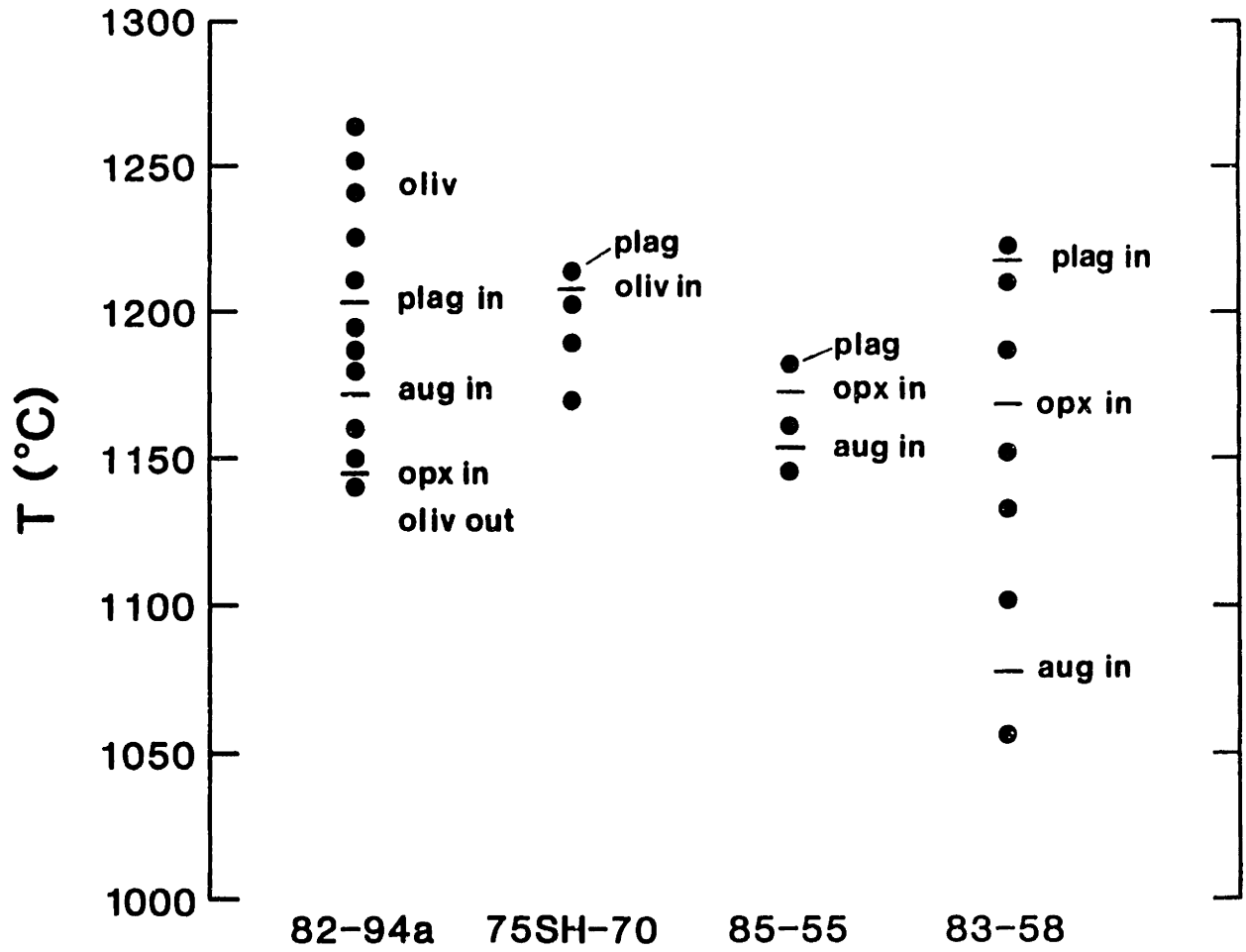
1300
1250
1200
1150
1100
1050
1000
T (°C)
oliv
plag in
aug in
opx in
oliv out
plag
oliv in
plag
opx in
aug in
plag in
opx in
aug in
82-94a
75SH-70
85-55
83-58

Figure 2-29. Experimentally produced glass compositions (Table 15) projected from plagioclase onto the olivine (Oliv) - clinopyroxene (Cpx) - quartz (Qtz). The 1-atm oliv-plag-augite (aug) and aug-plag-orthopyroxene (opx) cotectics and oliv-plag-opx reaction curve are drawn on the basis of the phase assemblage coexisting with each glass. The symbols and starting compositions are listed in the upper right hand corner of the figure. After converting oxide wt.% to mole %, and setting MF equal to MgO+FeO, the molar phase proportions are:

$$\text{Cr-sp} = [Cr_2O_3]/\text{sum}$$

$$\text{Ilm} = [TiO_2]/\text{sum}$$

$$\text{Or} = 2[K_2O]/\text{sum}$$

$$\text{Ab} = 2[Na_2O]/\text{sum}$$

$$\text{An} = \{[Al_2O_3]-[Na_2O]-[K_2O]\}/\text{sum}$$

$$\text{Cpx} = \{[CaO]+[Na_2O]+[K_2O]-[Al_2O_3]\}/\text{sum}$$

$$\text{Oliv} = 0.5\{[MF]+[Al_2O_3]-[TiO_2]-[Cr_2O_3]-[Na_2O]-[K_2O]\}/\text{sum}$$

$$\text{Qtz} = \{[SiO_2]+0.5([TiO_2]+[Cr_2O_3]-[MF]-[Al_2O_3])-1.5[CaO]-5.5\{[K_2O+Na_2O]\}/\text{sum}$$

$$\text{sum} = [SiO_2]+[Cr_2O_3]+[TiO_2]-[CaO]-4([Na_2O]+[K_2O])$$

After combining Ab+An to make Plag, each mineral component is multiplied by the number of oxygens in its mineral formula, and then normalized to 1.0.

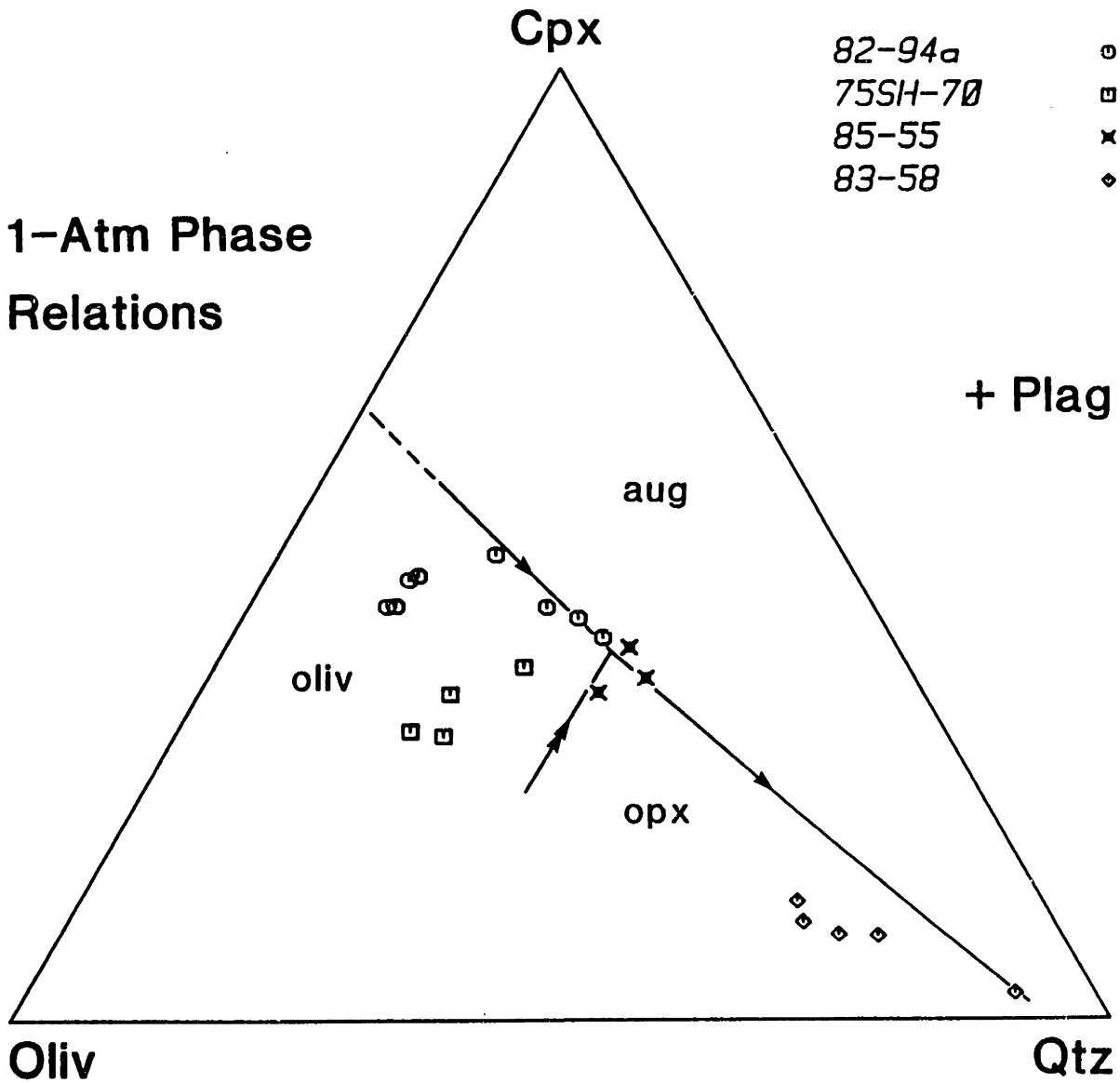
Cpx
82-94a
75SH-70
85-55
83-58
1-Atm Phase
Relations
+ Plag
aug
oliv
opx
Oliv
Qtz

Figure 2-30. Comparing the observed $Mg/(Mg+Fe^{2+})$ ratio in the liquid at the first appearance of augite at 1-atm in 82-94a with the $Mg/(Mg+Fe^{2+})$ ratio in a model liquid that would be in equilibrium with the most magnesian augite phenocrysts in 82-94a. The mole fraction of FeO in the 1-atm glass was corrected for ferric iron using Kilinc et al. (1983). The Fe^{2+}-Mg augite-liquid K_D was calculated from the 1-atm experiments on 82-94a and augite saturated 1-atm MORB experiments reported by Tormey et al. (1987) after correcting both glass and augite compositions for Fe_2O_3. The Fe-Mg $(K_D)^{aug/liq}$ has a value of 0.23±0.03.

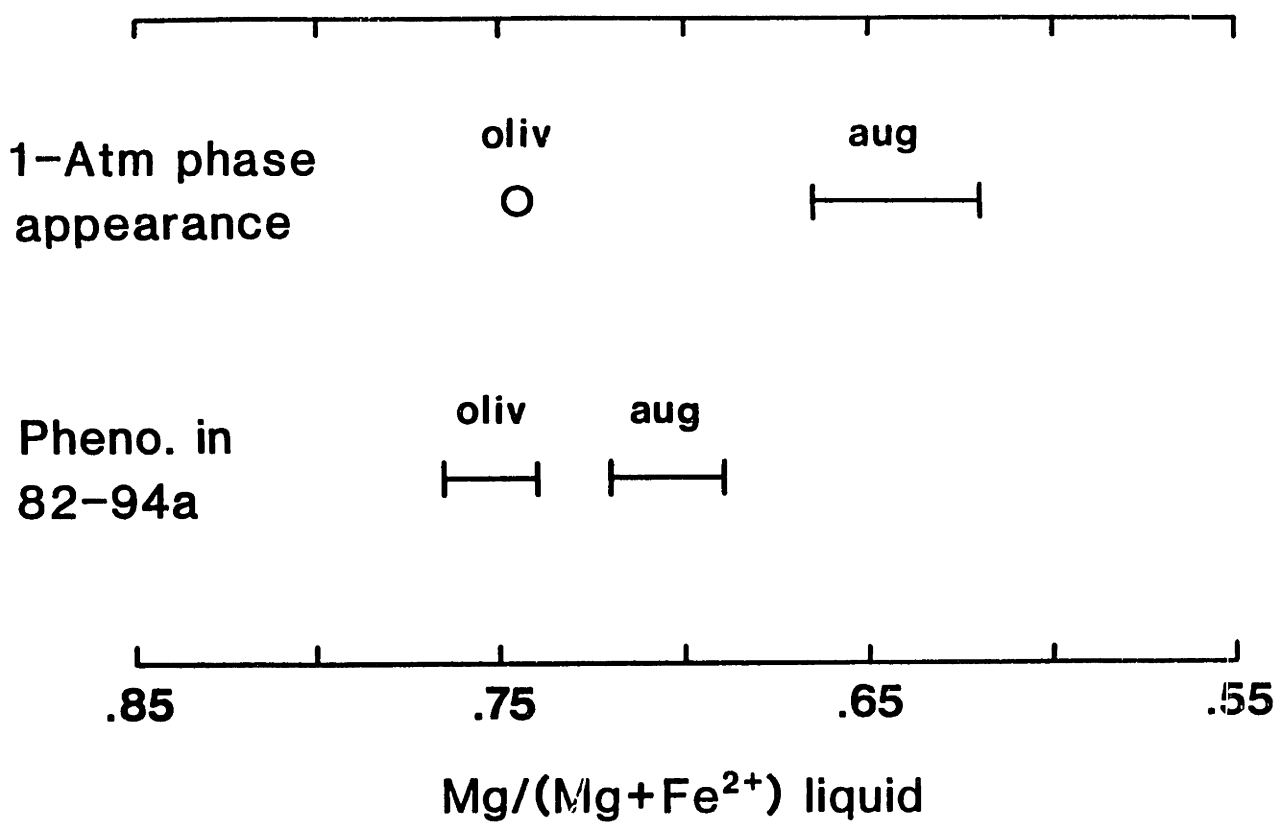
oliv
aug
1-Atm phase appearance
oliv
aug
Pheno. in 82-94a
.85
.75
.65
.55
Mg/(Mg+Fe2+) liquid

Figure 2-31. (a) CaO vs MgO and (b) Al_2O_3 vs MgO variations in the Sargents Ridge and Haystack Butte basaltic andesites and the effects of Fo_{87} addition to an intermediate BA liquid. Tick marks on the olivine addition lines are in units of weight fractions.

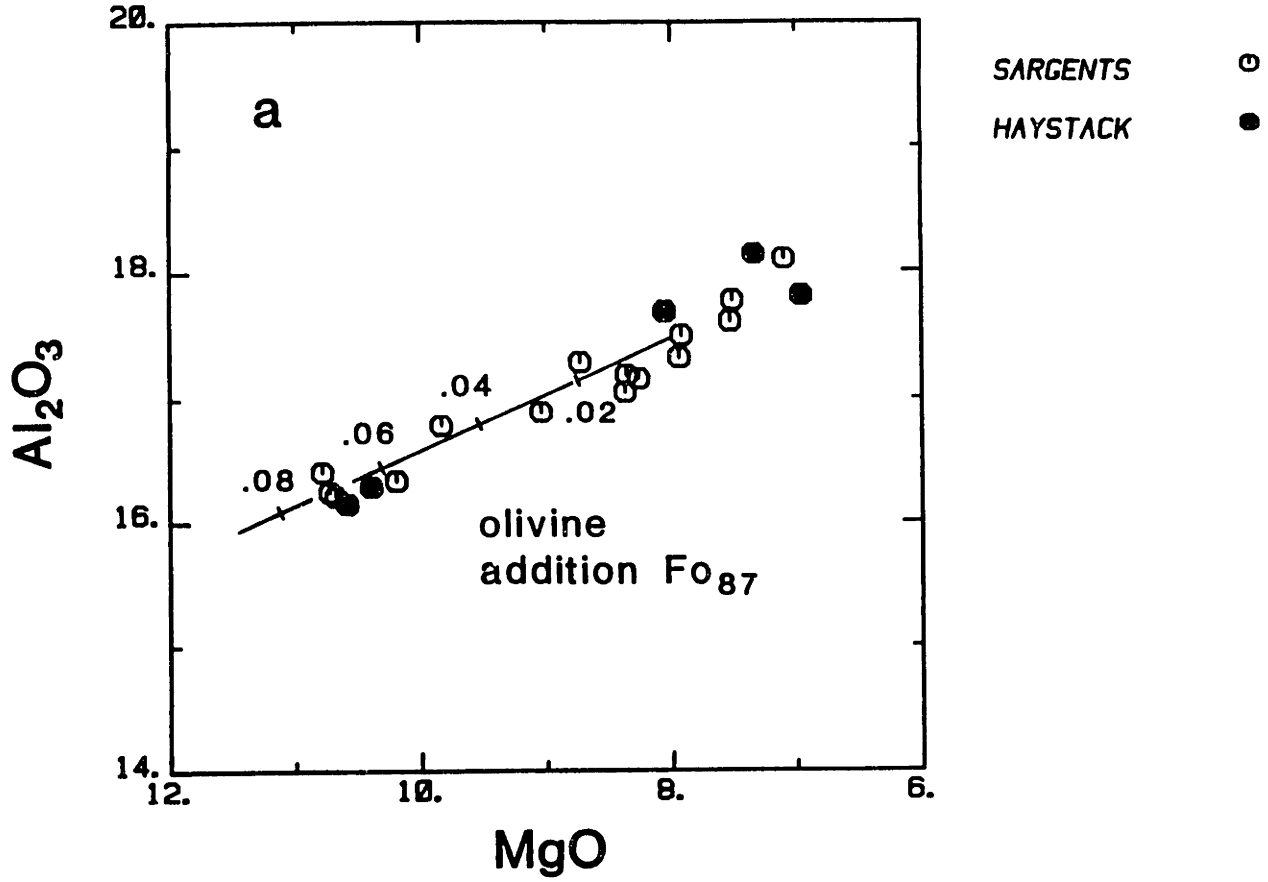
a
20.
18.
16.
14.
12.
10.
8.
6.
Al_2O_3
MgO
.08
.06
.04
.02
olivine
addition Fo_{87}
SARGENTS
HAYSTACK

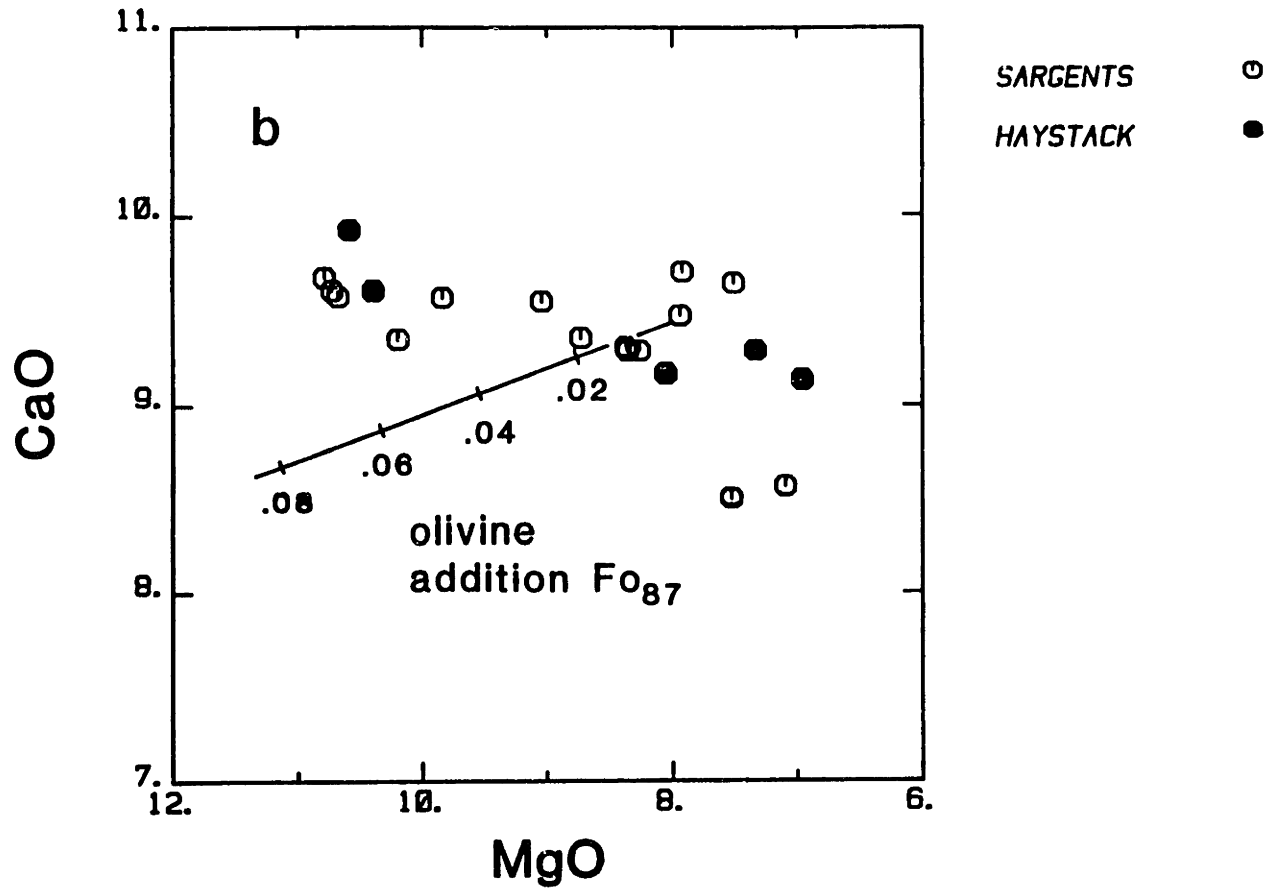
b
11.
10.
9.
8.
7.
12.
10.
8.
6.
CaO
MgO
.08
.06
.04
.02
olivine
addition Fo_{87}
SARGENTS
HAYSTACK

Figure 2-32. Calculated Fo-contents (brackets) based on bulk rock compositions compared with the average of the most magnesian olivine phenocrysts (open circles) in basaltic andesites 85-44, 85-5, 82-94a and 82-81. The brackets are calculated using an Fe^{2+}-Mg olivine-liquid K_D of 0.31±0.03 (Irvine, 1979) and bulk rock Fe^{2+}/Mg ratios calculated at QFM and NNO. The calculated brackets include errors on the bulk rock FeO and MgO values and the olivine-liquid Fe-Mg K_D.

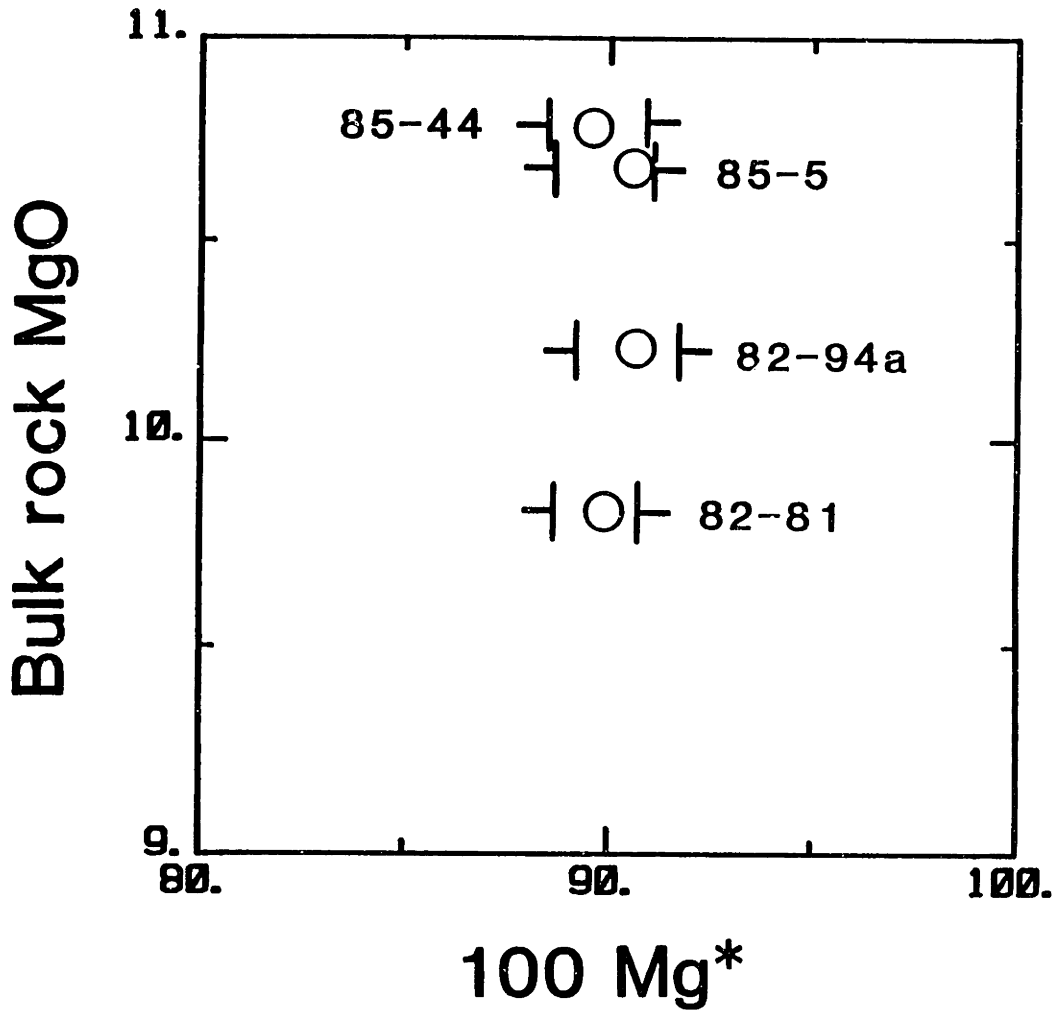
11.
10.
9.
80.
90.
100.
85-44
85-5
82-94a
82-81
Bulk rock MgO
100 Mg*

Figure 2-33. ΔT_L vs modal plagioclase for selected Mt. Shasta andesites and dacites. ΔT_L = experimentally determined 1-atm liquidus temperature minus liquidus temperature calculated from eqn (1) in the text. Experimental values from Table 17. Data on AT-1, an evolved HAB, from Baker and Eggler (1983).

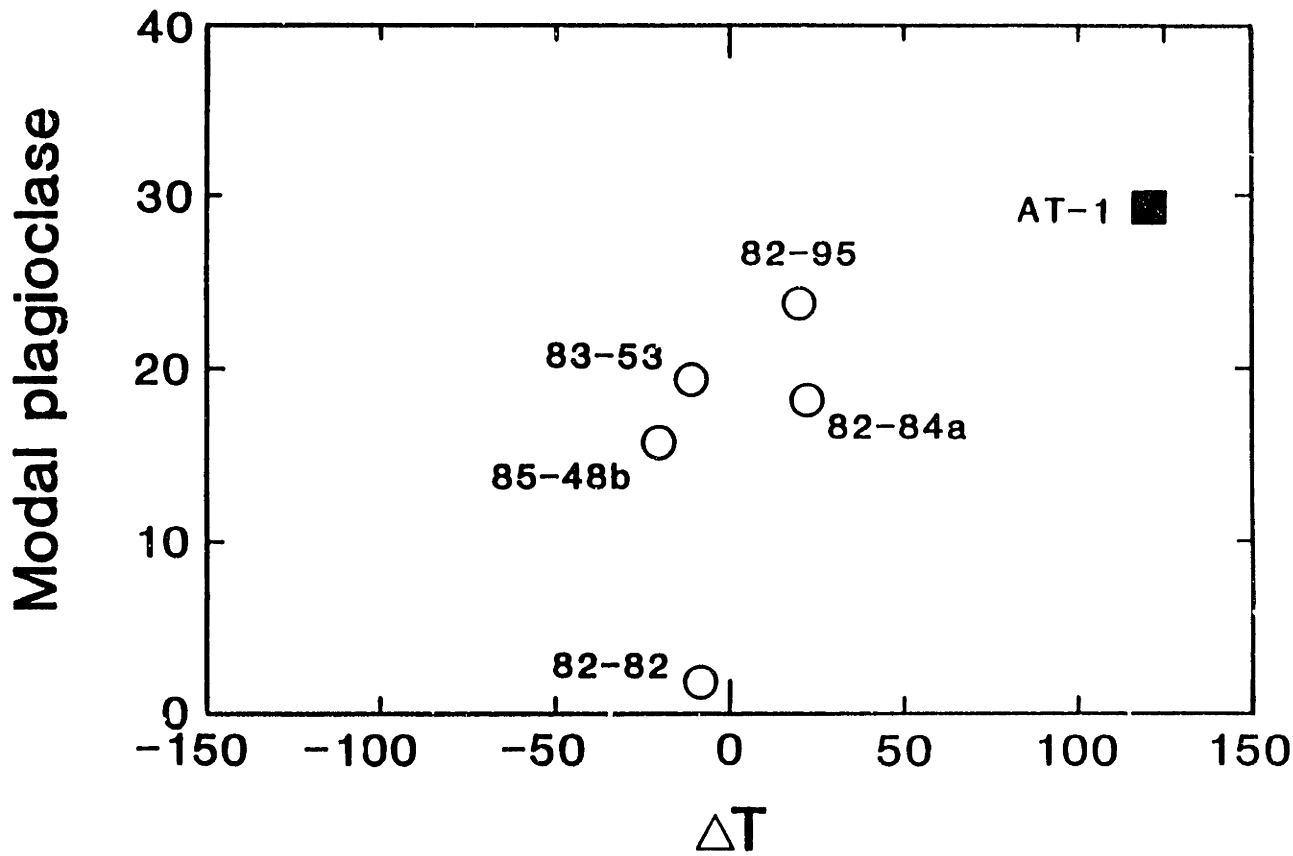
Modal plagioclase
40
30
20
10
0
−150
−100
−50
0
50
100
150
ΔT
AT−1
82−95
83−53
82−84a
85−48b
82−82

Figure 2-34. Mt. Shasta lavas projected from plagioclase onto the Oliv-Cpx-Qtz pseudoternary. 1-atm boundary curves from Fig. 2-28. Component transformation scheme given in the caption to Fig. 2-28. Arrows show the low pressure liquid line of descent for one of the primitive basaltic andesites.

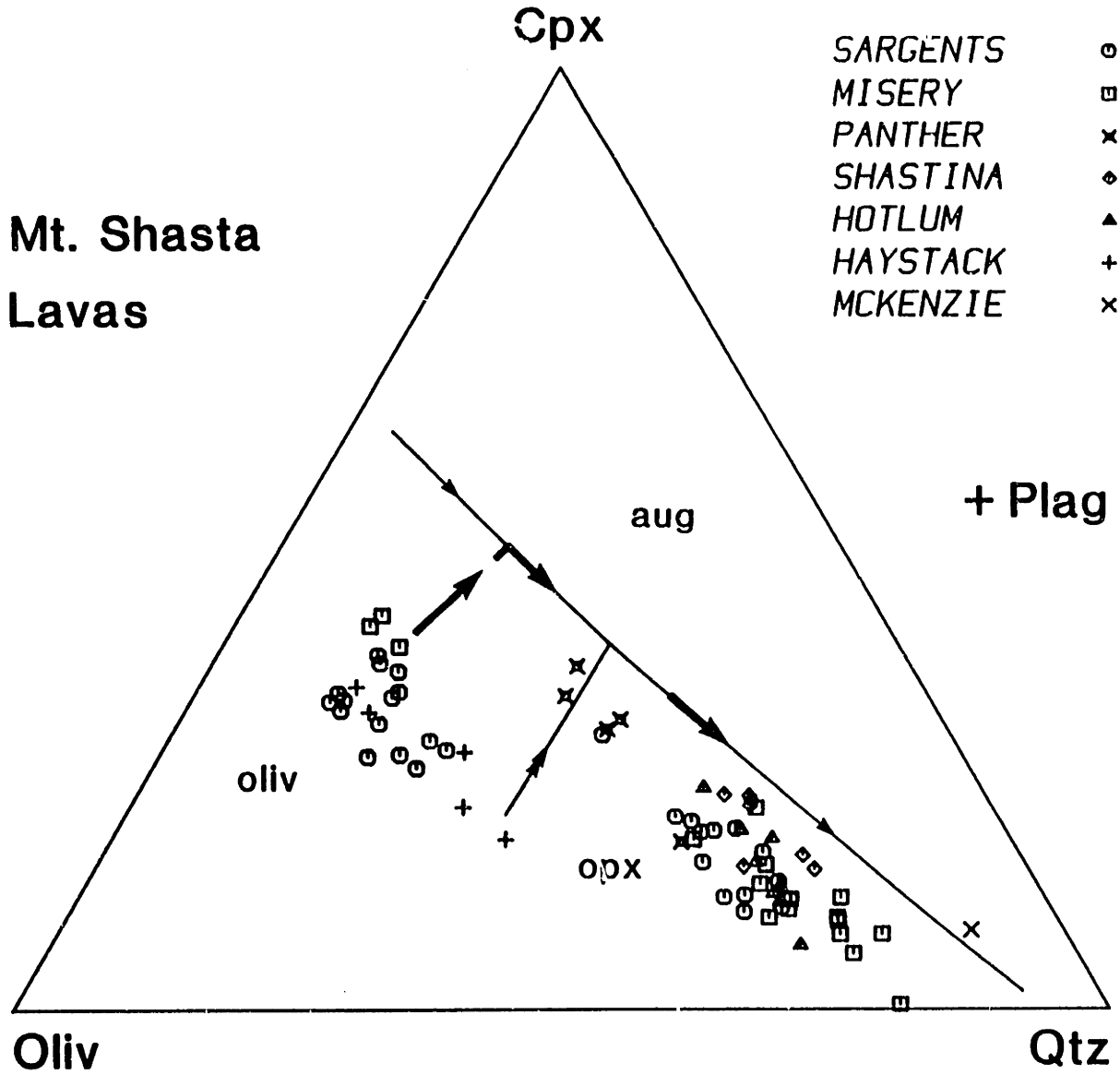
Cpx
SARGENTS
MISERY
PANTHER
SHASTINA
HOTLUM
HAYSTACK
MCKENZIE
Mt. Shasta
Lavas
aug
+ Plag
oliv
opx
Oliv
Qtz

Figure 2-35. (a) Major element fractionation calculation compared with the observed BA compositions at 7.0% MgO. Observed composition based on linear and 2nd order polynomial regressions against MgO using the Sargents Ridge and Haystack lavas (see discussion in text). The fractionation model is given in Table 2-21. (b) Comparison of observed and calculated trace element compositions in the basaltic andesites at 7.0% MgO. Trace element model reported in Table 2-21.

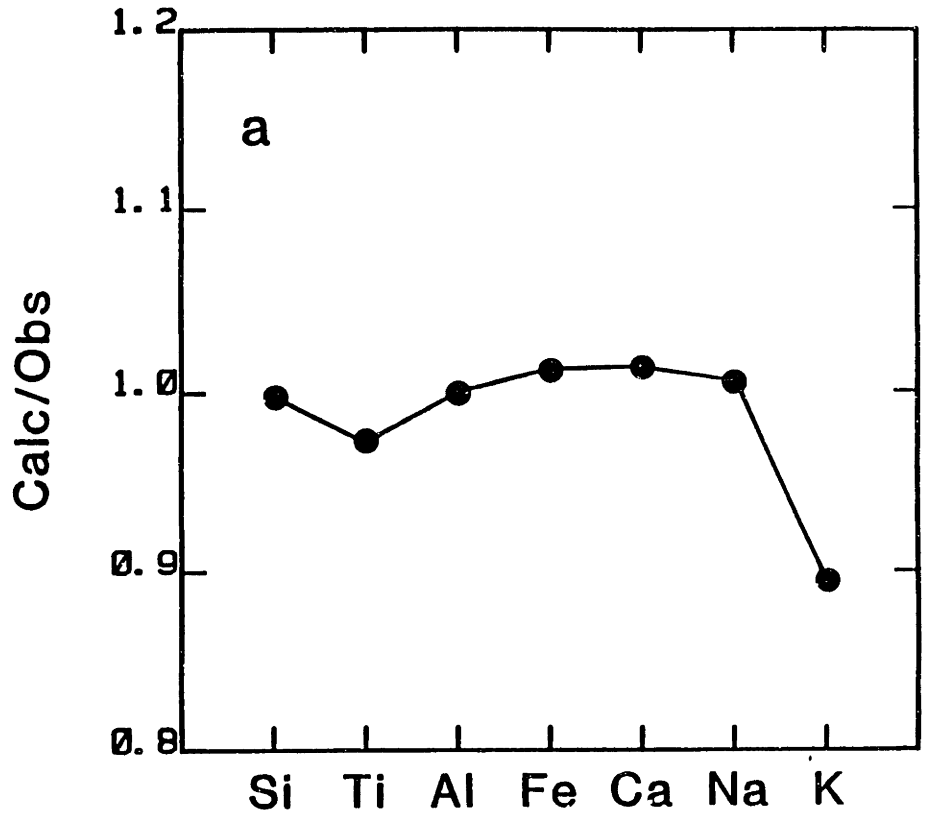
a
Calc/Obs
1.2
1.1
1.0
0.9
0.8
Si
Ti
Al
Fe
Ca
Na
K

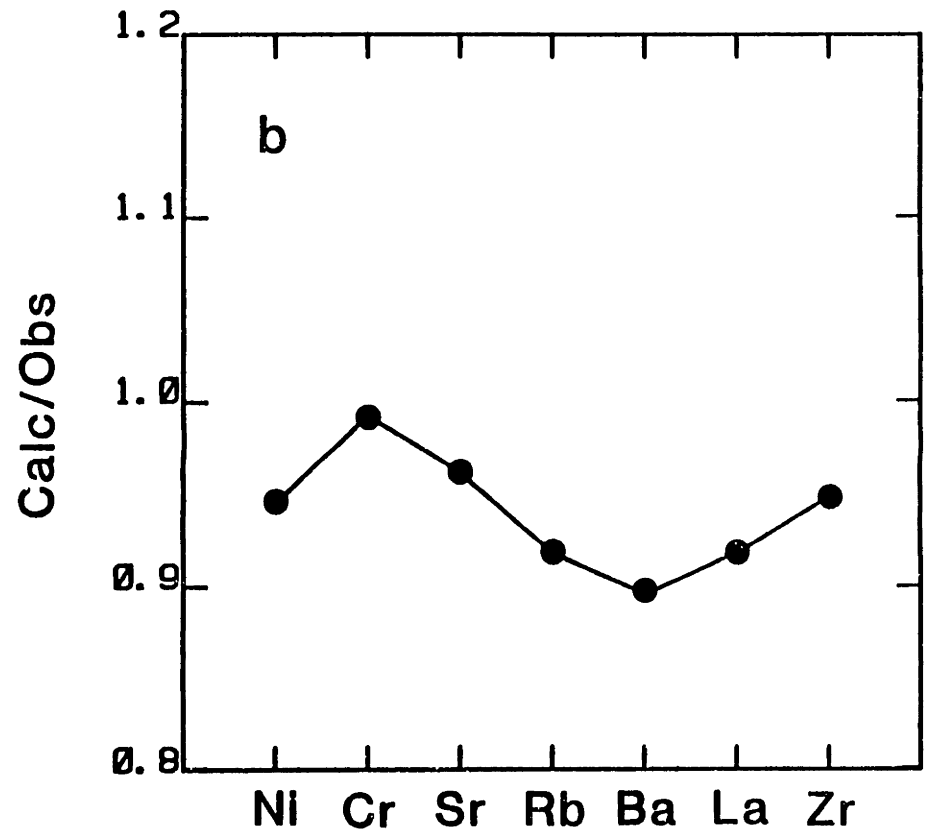
b
Calc/Obs
1.2
1.1
1.0
0.9
0.8
Ni
Cr
Sr
Rb
Ba
La
Zr

Figure 2-36. Fields for Mt. Shasta and Medicine Lake HABs the Mt. Shasta BAs projected from plagioclase onto the Oliv-Cpx-Qtz pseudoternary. Diamond labelled opx is the average of orthopyroxene analyses in the Triniy peridotite reported by Quick (1980). Vectors show the directions that residual HAB liquids woud move subject to assimilation of opx and fractionation of oliv. 1-atm boundary curves from Fig. 2-28.

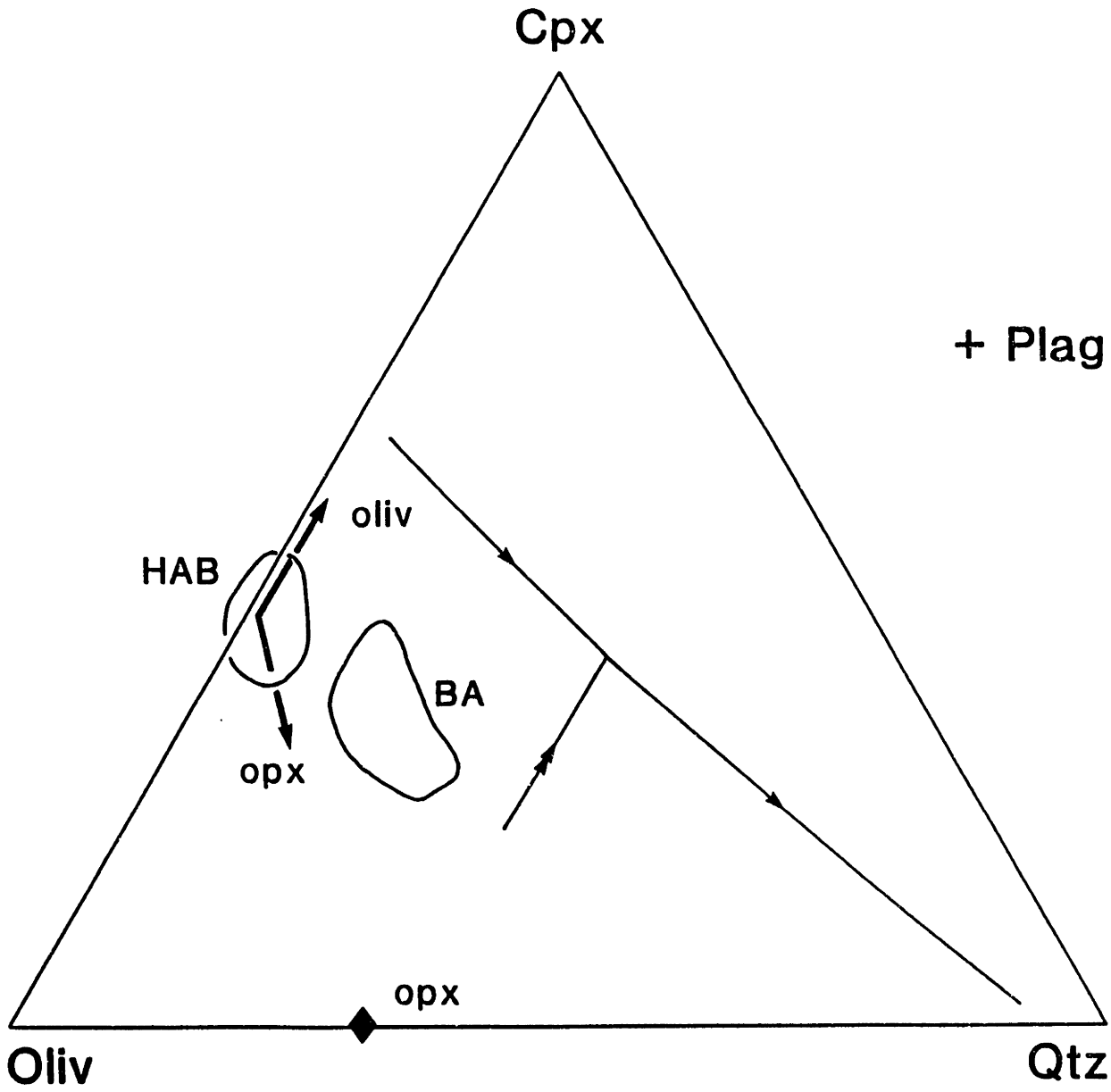
Cpx
+ Plag
oliv
HAB
BA
opx
opx
Oliv
Qtz

Figure 2-37. $MgO-SiO_2$ variation diagrams for the Mt. Shasta andesites and dacites showing the distribution of (a) quartz, (b) olivine and (c) amphibole phenocrysts and xenocrysts in the lavas.

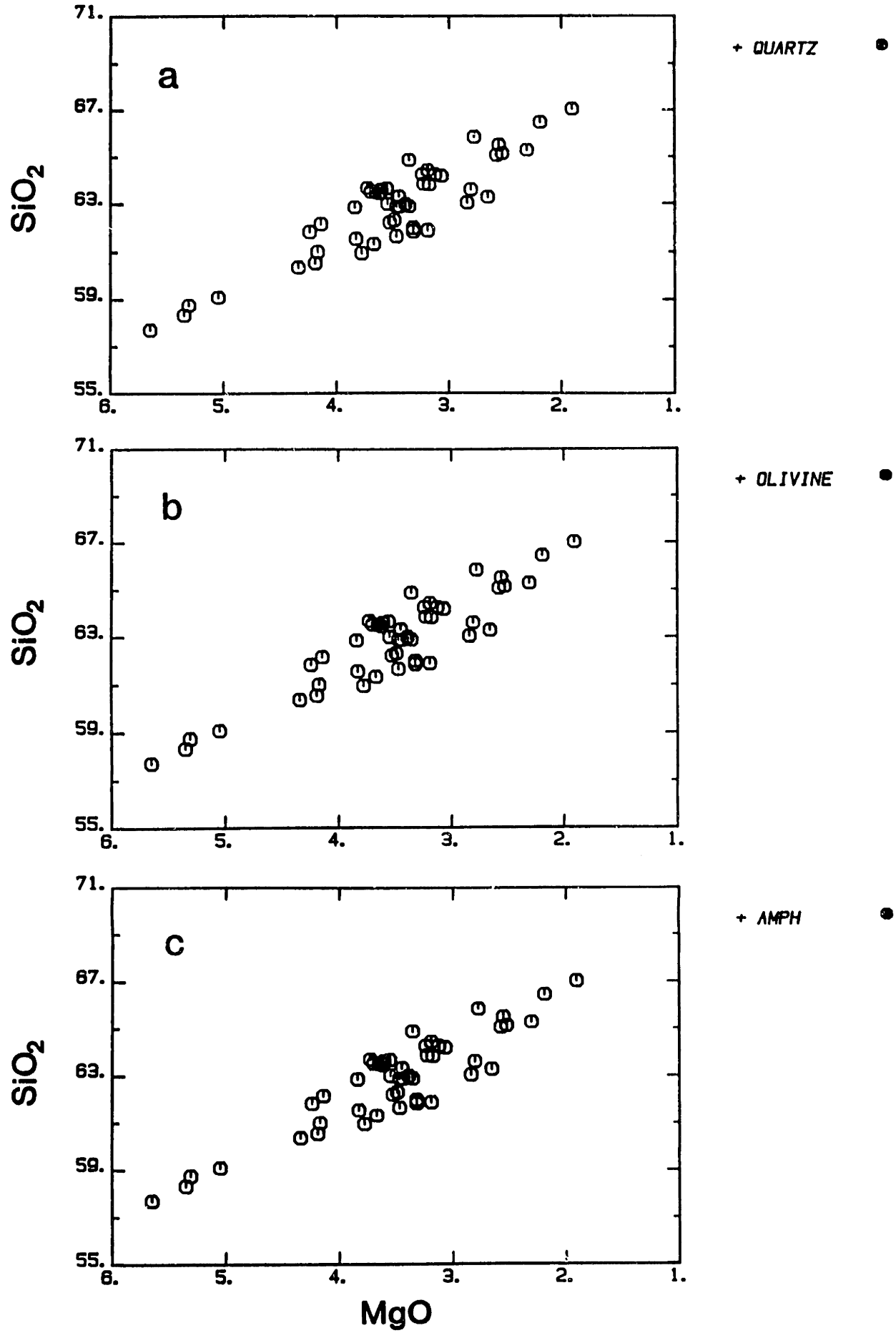
a
b
c
SiO2
71.
67.
63.
59.
55.
6.
5.
4.
3.
2.
1.
MgO
+ QUARTZ
+ OLIVINE
+ AMPH

Figure 2-38. Linear regression lines calculated from the andesites and dacites (minus Panther Creek) projected onto MgO-SiO_2, -TiO_2, -FeO and -K_2O variation diagrams. Equation parameters are listed in Table 2-23. Dashed lines are mixing lines between evolved basaltic andesite and rhyodacite. The solid circles are compositions calculated from MgO-Sr-oxide regressions at 4.5 wt.% MgO and 350 ppm Sr. Fields labeled BA, And-Dac and R-Dac represent the basaltic andesites, andesites and dacites and the rhyodacites, respectively.

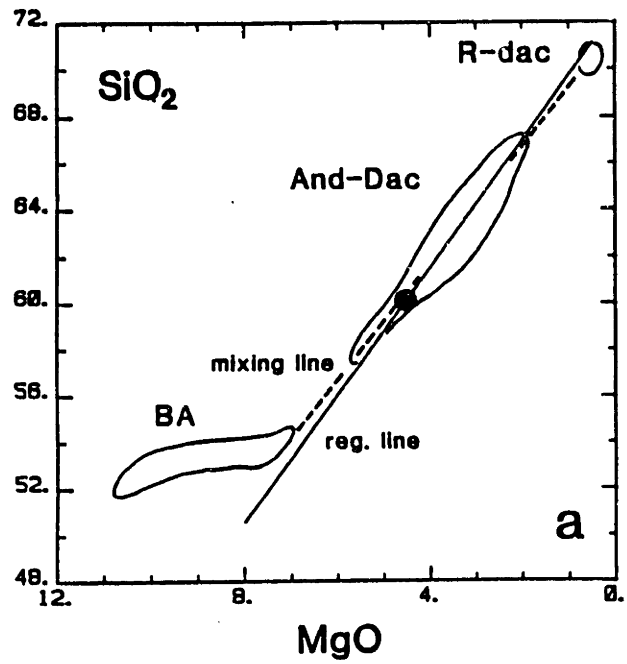
SiO2
R-dac
And-Dac
mixing line
BA
reg. line
a
72.
68.
64.
60.
56.
52.
48.
12.
8.
4.
0.
MgO

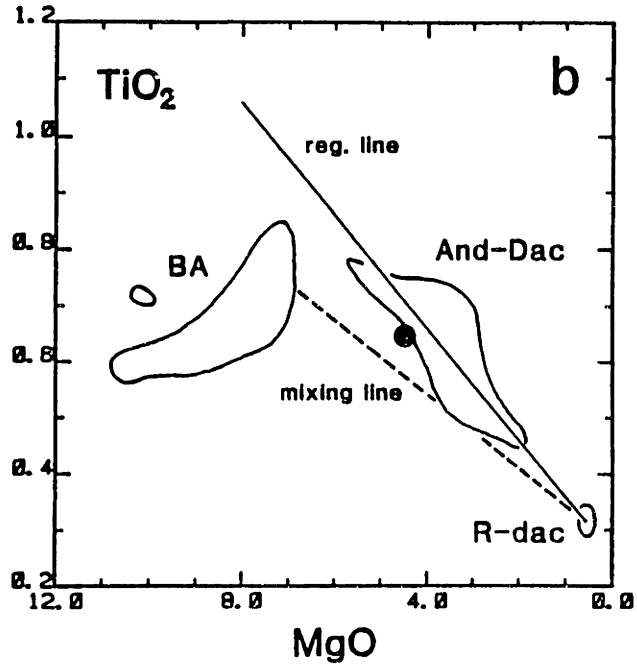
TiO2
b
reg. line
BA
And-Dac
mixing line
R-dac
1.2
1.0
0.8
0.6
0.4
0.2
12.0
8.0
4.0
0.0
MgO

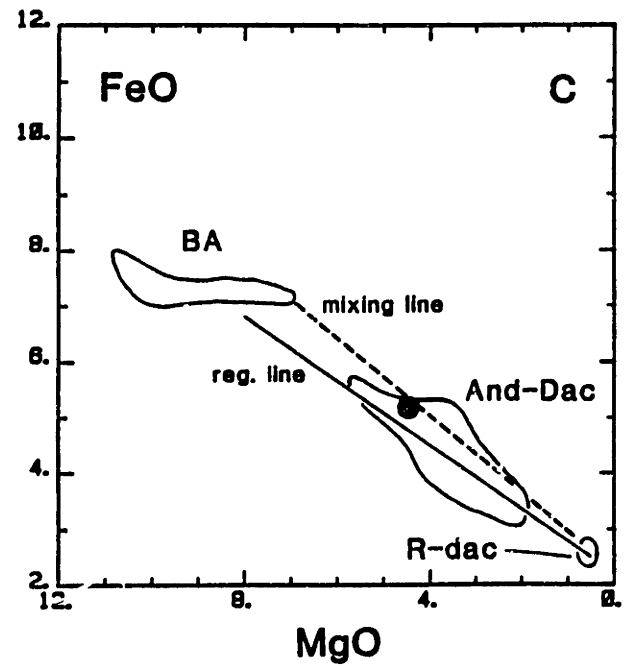
FeO
c
BA
mixing line
reg. line
And-Dac
R-dac
12.
10.
8.
6.
4.
2.
12.
8.
4.
0.
MgO

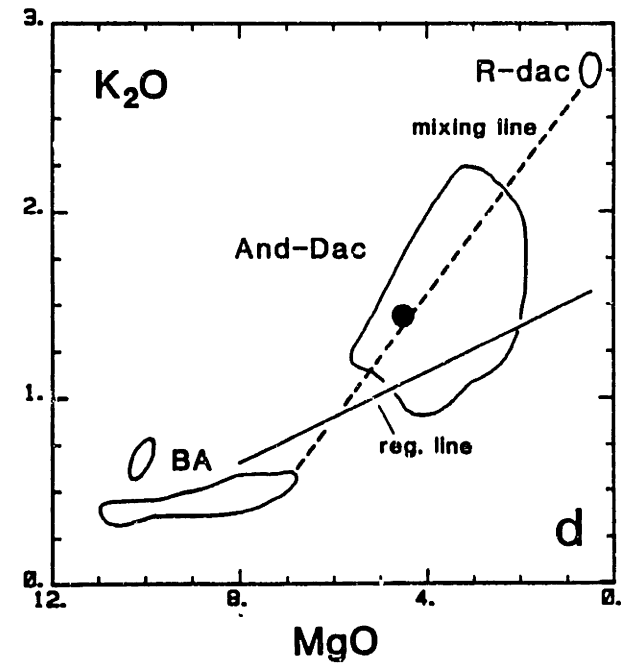
K2O
R-dac
mixing line
And-Dac
reg. line
BA
d
3.
2.
1.
0.
12.
8.
4.
0.
MgO

Figure 2-39. Location of basaltic andesite-rhyodacite mixing lines in Ba-MgO and Rb-MgO composition space relative to the andesite-dacite fields. The solid circle is calculated from MgO-Sr-trace element regression, at MgO=4.5 wt.% and 350 ppm Sr.

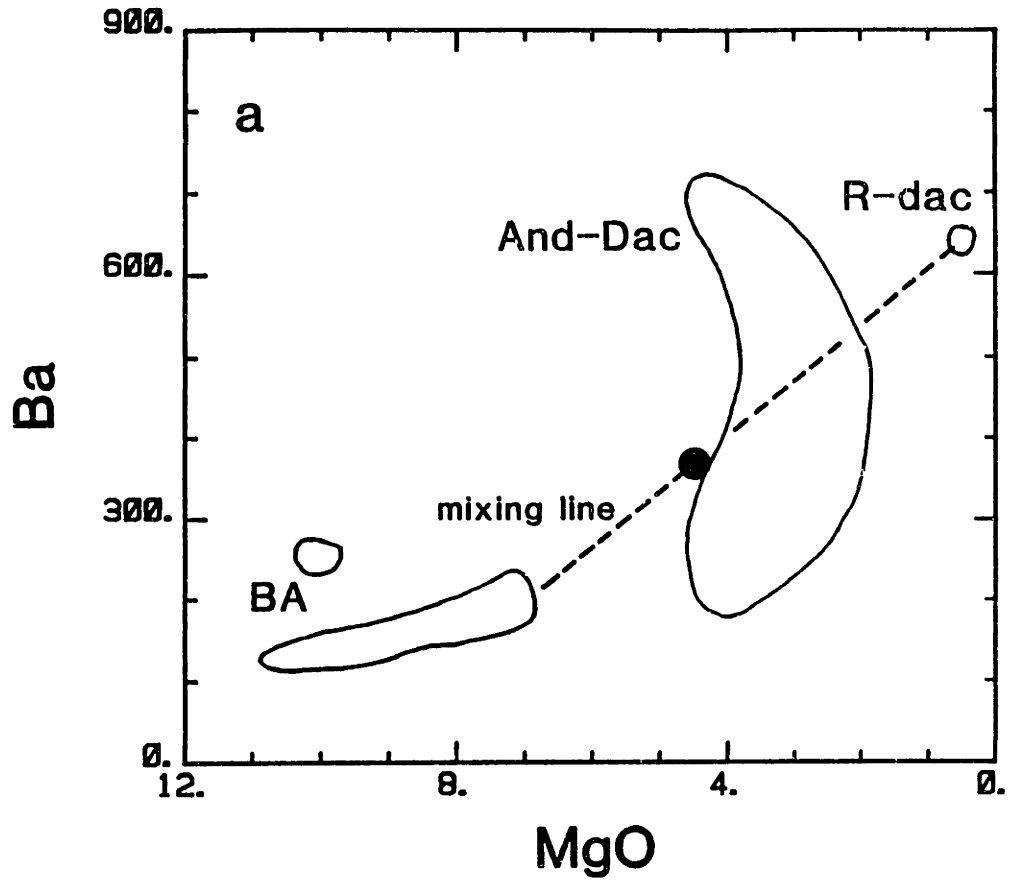
a
900.
600.
300.
0.
Ba
12.
8.
4.
0.
MgO
R-dac
And-Dac
mixing line
BA

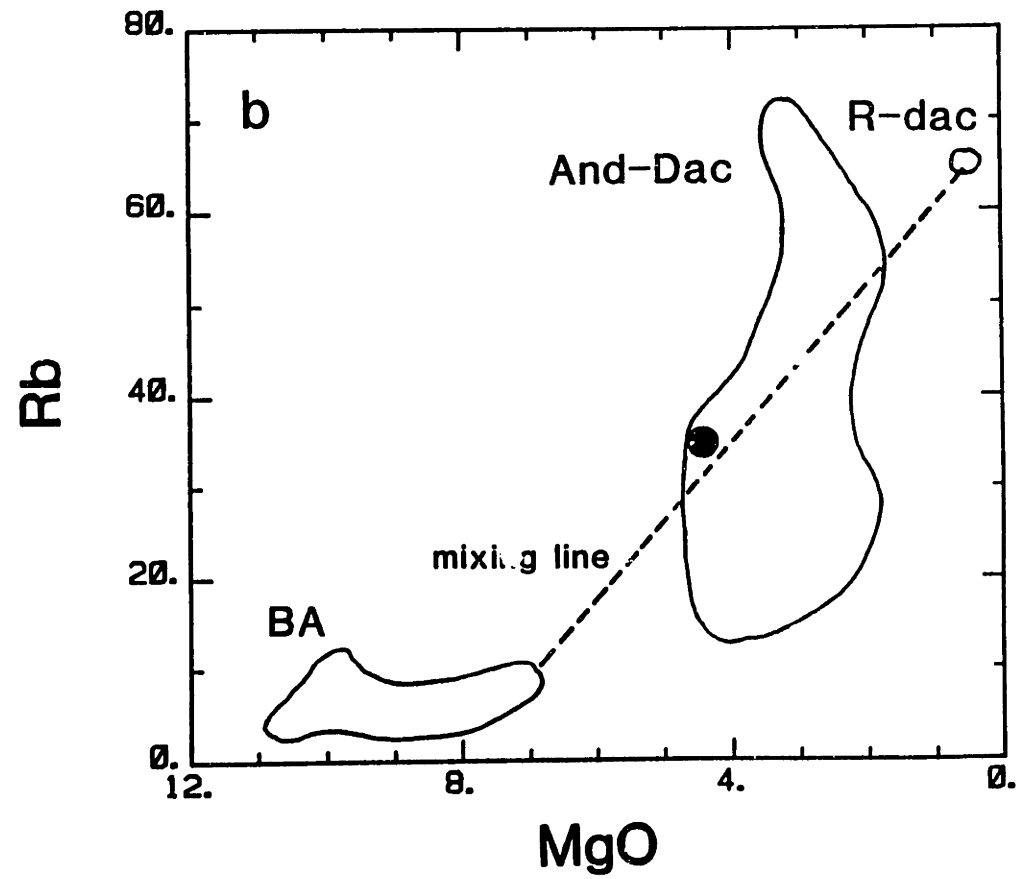
b
80.
60.
40.
20.
0.
Rb
12.
8.
4.
0.
MgO
R-dac
And-Dac
mixing line
BA

Figure 2-40. (a) wt.% K_2O vs ppm Sr in the Mt. Shasta lavas. 85-2a and 85-48b contain peridotite inclusions, sclid symbols denote the presence of quartz xenocrysts. Star represents average upper crust (Taylor and McLennan, 1985). (b) ppm Rb vs ppm Sr, symbols as in (a).

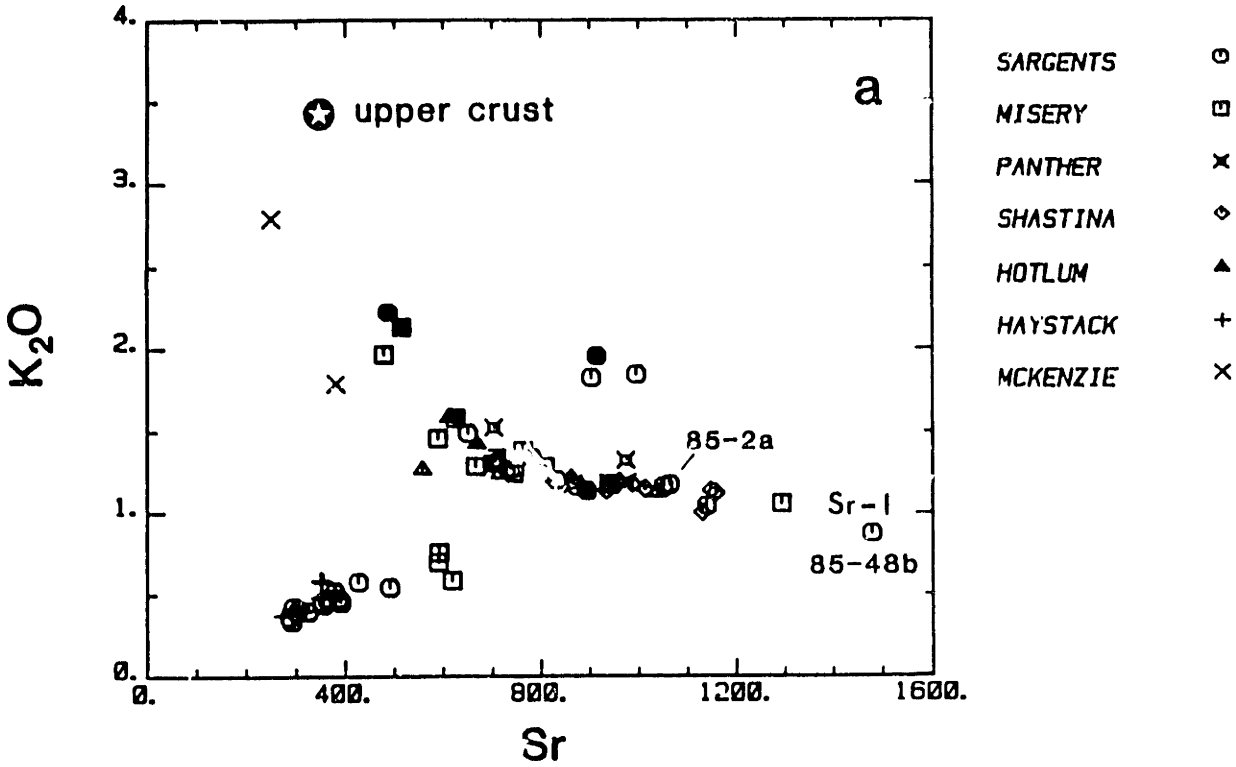
a
upper crust
K_2O
Sr
0.
400.
800.
1200.
1600.
1.
2.
3.
4.
85-2a
Sr-1
85-48b
SARGENTS
MISERY
PANTHER
SHASTINA
HOTLUM
HAYSTACK
MCKENZIE

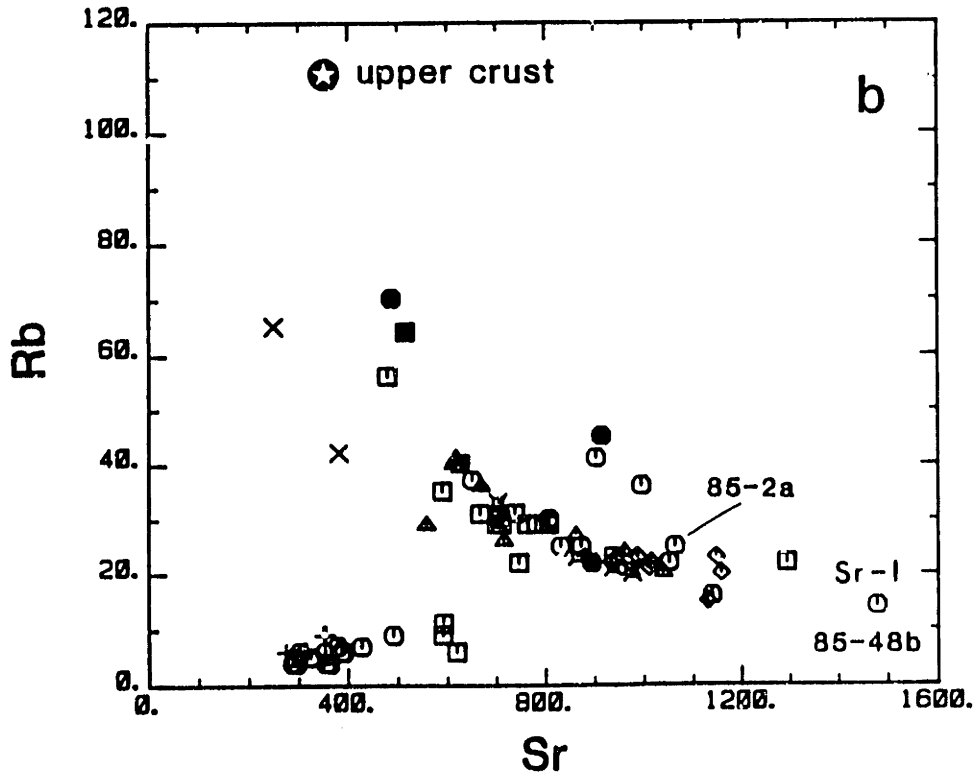
b
upper crust
Rb
Sr
0.
20.
40.
60.
80.
100.
120.
400.
800.
1200.
1600.
85-2a
Sr-1
85-48b

Figure 2-41. (a) Ba vs Sr, (b) La vs Sr, both in ppm. Symbols as in Fig. 2-39.

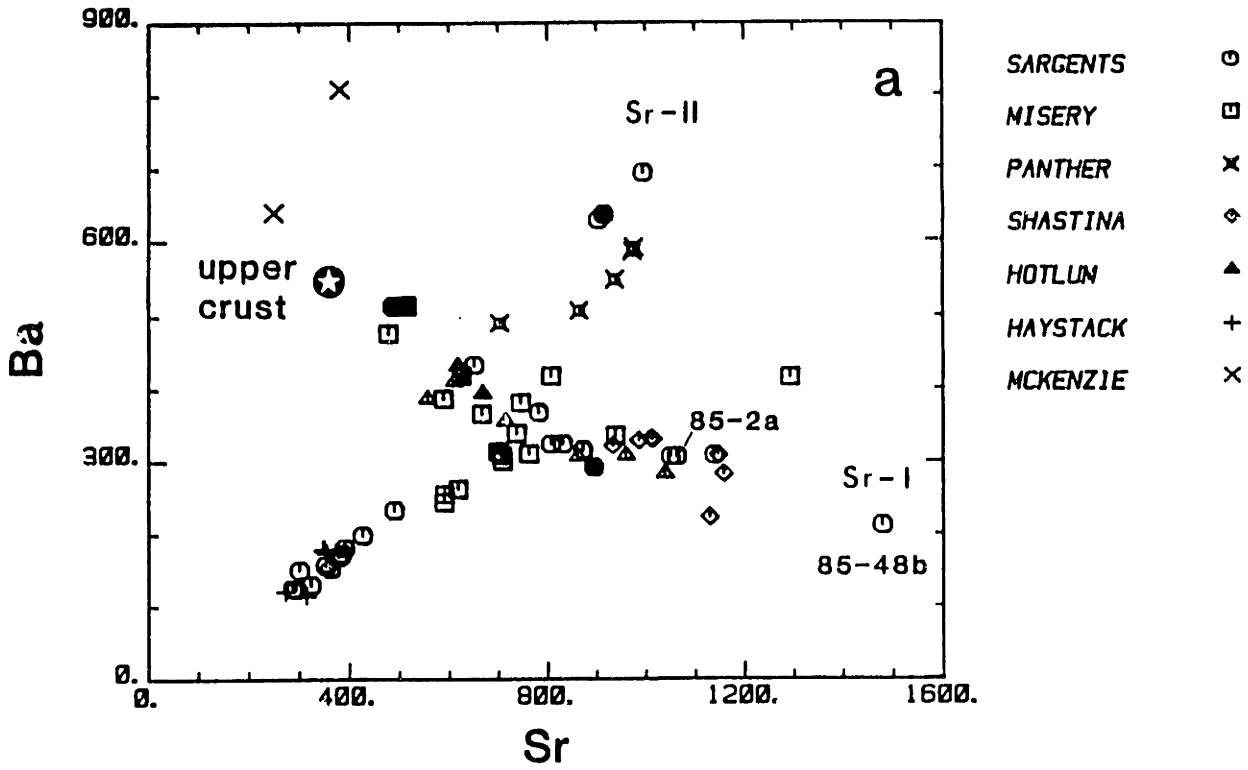
a
Sr-II
upper
crust
85-2a
Sr-I
85-48b
900.
600.
300.
0.
0.
400.
800.
1200.
1600.
Ba
Sr
SARGENTS
MISERY
PANTHER
SHASTINA
HOTLUN
HAYSTACK
MCKENZIE

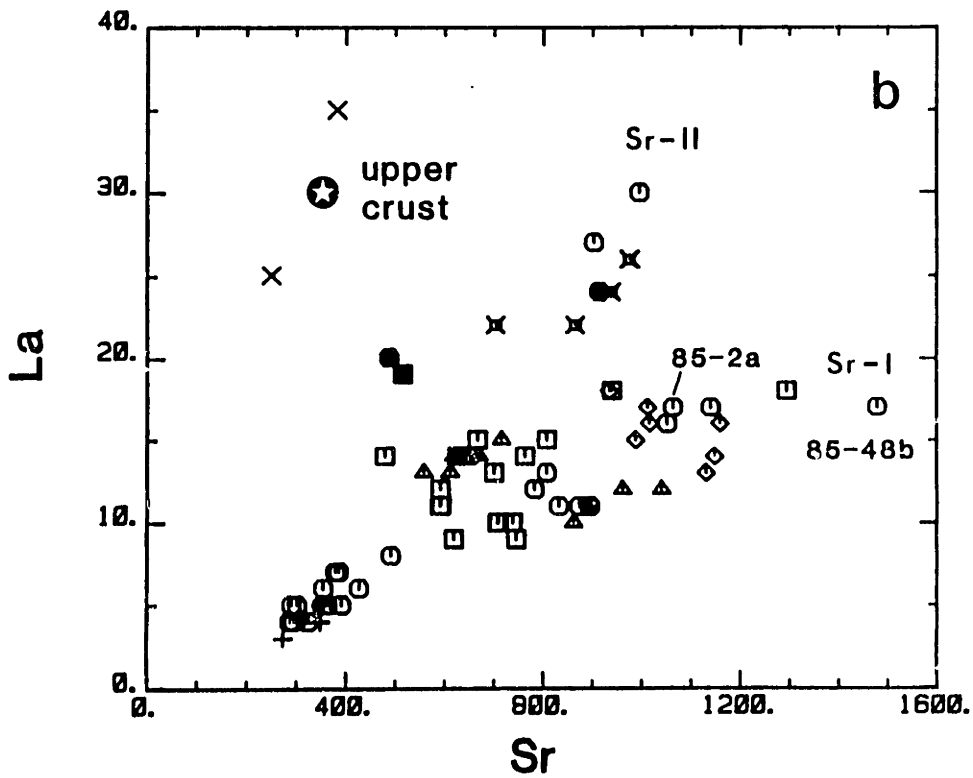
b
Sr-II
upper
crust
85-2a
Sr-I
85-48b
40.
30.
20.
10.
0.
0.
400.
800.
1200.
1600.
La
Sr

Table 2-1. Major and trace element analyses of High Alumina Basalts at Mt. Shasta[1]

Field#	83-43	85-35	85-38	85-39	85-40	85-51	85-52	85-53	BCR-1	%Error[2]
SiO_2	49.09	49.17	49.14	49.42	50.66	48.51	48.52	49.23	54.33	0.178
TiO_2	1.03	.93	.87	.92	.94	1.04	1.00	1.03	2.26	0.804
Al_2O_3	17.14	17.06	16.95	17.10	16.79	17.27	16.98	17.13	13.48	0.784
Fe_2O_3	2.51	.69	.84	1.06	.51	1.30	1.07	.91	-	
FeO	6.84	8.02	7.86	7.67	8.02	7.96	8.10	8.14	12.02	0.508
MnO	.17	.17	.18	.17	.17	.18	.18	.18	.19	2.15
MgO	9.00	9.07	9.60	9.28	8.48	9.17	9.24	8.77	3.57	0.856
CaO	10.38	10.98	10.61	10.64	10.39	10.75	10.61	10.63	6.95	0.447
Na_2O	2.96	2.47	2.11	2.43	2.52	2.55	2.46	2.74	-	3.48
K_2O	.27	.28	.30	.33	.51	.21	.22	.27	1.73	1.36
P_2O_5	.11	.13	.11	.13	.14	.13	.12	.13	.37	2.42
H_2O	.75	.69	.61	.95	1.08	.52	1.08	.56		
Ni	32	39	41	44	29	44	33	29	10.0	4.46
Cr	442	473	521	450	413	436	489	422	24.5	4.68
V	224	202	200	204	195	214	218	208	461	1.01
Zn	79	65	69	65	70	71	74	73	123	-
Ga	16	12	15	16	15	17	15	14	21.8	13.3
Rb	7	6	8	7	15	4	5	6	48.3	*
Sr	227	209	189	222	218	231	206	227	335	0.724
Ba	131	127	134	137	170	143	132	130	748	2.64
Y	25	24	23	25	24	25	26	25	34.1	3.40
Zr	03	61	52	-	65	61	58	61	204	1.82
Nb	2	4	3	-	4	3	3	4	12.2	-
La	5	4	6	5	7	5	4	4	25.5	6.19
Ce	5	14	10	14	17	8	4	12	66.0	5.55

[1] See Fig. 2-1 and Appendix 2-A for sample locations. Major and trace elements by XRF, trace elements in ppm; H_2O by gavimetric methods. Dashes indicate that element was below detectability or was not analyzed. BCR-1 represents tha average of 10 analyses.

[2] Percent error = (σ/mean)x100; based on four sets of duplicate analyses. * = 10% when concentration < 10ppm, ~1% if > 10ppm.

Table 2-2. Major element analyses of basaltic andesites at Mt. Shasta[1]

Field#	SiO_2	TiO_2	Al_2O_3	Fe_2O_3	FeO	MnO	MgO	CaO	Na_2O	K_2O	P_2O_5	H_2O
Sargents Ridge												
82-81	51.80	.61	16.69	1.83	5.84	.14	9.79	9.51	2.99	.39	.11	.53
75-70	53.2	.68	17.5	7.94	-	.13	7.93	9.71	3.2	.46	.13	-
75-317	53.2	.57	16.9	7.96	-	.13	9.05	9.55	3.0	.45	.10	-
85-4	52.13	.67	16.65	1.08	6.32	.15	8.59	9.30	2.96	.46	.13	.96
85-5	51.24	.59	15.65	2.22	5.78	.15	10.54	9.55	2.69	.33	.11	.74
85-6	52.71	.71	17.24	1.24	6.11	.14	7.45	9.66	3.38	.45	.14	.63
95-44	51.18	.59	15.84	1.31	6.65	.16	10.65	9.65	2.21	.41	.11	.92
85-45	51.13	.59	15.70	1.86	6.08	.15	10.60	9.59	2.73	.36	.11	1.02
85-46	52.09	.59	15.85	1.79	5.88	.15	10.12	9.37	2.98	.39	.11	1.09
85-47	52.67	.69	16.75	2.11	5.36	.14	7.85	9.46	3.36	.42	.14	1.22
85-48a	52.98	.65	16.45	2.25	4.98	.14	8.26	9.28	3.17	.50	.14	1.32
85-48c	53.63	.65	16.73	2.82	4.56	.14	8.32	9.33	2.92	.45	.14	.58
85-48d	53.57	.65	16.62	2.82	4.51	.14	8.18	9.29	2.81	.46	.14	.66
85-49	53.36	.68	17.47	2.03	5.15	.14	7.10	8.55	3.54	.53	.18	.86
85-50	53.58	.80	16.99	2.40	4.90	.14	7.43	8.48	3.35	.56	.17	1.37
Misery Hill												
82-94a	52.50	.72	15.30	2.93	4.43	.14	10.17	9.61	3.01	.58	.22	.51
82-94b	52.43	.70	15.02	4.99	2.34	.14	9.72	9.37	3.03	.74	.21	.73
82-94c	53.26	.71	15.13	3.75	3.56	.14	10.05	9.41	2.91	.69	.22	.48
Haystack												
85-1a	51.52	.56	15.55	1.68	6.05	.16	10.58	9.92	2.64	.38	.10	.57
85-1b	52.06	.55	15.78	1.56	5.93	.15	10.30	9.61	2.67	.40	.11	.95
85-34	53.90	.65	17.21	1.30	5.88	.14	6.88	9.11	3.03	.57	.14	1.07
85-36	53.32	.64	17.38	1.41	5.76	.14	7.19	9.19	2.28	.56	.14	1.15
85-37	53.57	.60	17.10	1.72	5.51	.14	7.96	9.16	2.60	.47	.13	.95
Replicate analyses[2]												
82-81	51.77	.63	16.26	1.85	5.84	.15	9.64	9.56	2.99	.38	.12	.51
82-87	61.42	.60	17.41	1.72	2.68	.08	3.40	6.34	4.23	1.12	.15	.60
82-84a	61.45	.59	17.34	1.49	2.80	.08	3.45	6.25	4.72	1.15	.16	.67
82-84b	53.32	.80	17.14	1.70	5.41	.13	7.15	8.38	3.68	.60	.16	.94

[1] See Fig. 2-1 and Appendix 2-A for sample locations. All elements by XRF except water which is the sum of H_2O^+ and H_2O^- and determined by gavimeteric techniques. 75-70 and 75-317 analyzed at the U.S. Geological Survey, Lakewood, Colorado; supplied by R. Christiansen.

[2] These replicates analyzed in 1987 and used to correct for systematic biases in the 1985 data set.

Dashes in columns indicate that the element was below detectability limit or was not analyzed.

Table 2-3. Trace element analyses of basaltic andesites at Mt. Shasta[1]

Field#	Ni	Cr	V	Zn	Ga	Rb	Sr	Ba	Y	Zr	Nb	La	Ce	U	Th	Pb
Sargents																
82-81	193	548	199	71	19	6	301	149	15	60	4	5	4	2	-	-
85-4	148	439	189	70	17	4	363	151	15	43	3	5	19	-	2	1
85-5	239	675	194	70	13	5	291	122	15	40	3	5	9	-	1	2
85-6	99	318	204	67	16	6	353	155	16	48	3	5	8	-	3	3
85-44	230	693	205	71	17	4	295	122	16	38	3	4	6	-	-	1
85-45	235	695	201	69	14	4	286	123	15	39	3	4	8	1	1	3
85-46	216	679	180	71	17	5	324	129	14	38	3	4	8	1	-	-
85-47	114	375	205	70	18	4	354	158	17	47	3	6	12	-	-	3
85-48a	123	386	187	63	16	7	379	167	14	50	3	7	14	-	2	2
85-48b	124	393	193	68	21	6	390	180	14	51	3	5	9	-	5	1
85-48d	126	376	187	68	15	6	385	172	14	52	3	7	13	-	-	5
85-49	98	221	176	71	18	9	491	231	16	62	3	8	14	-	5	2
85-50	109	282	162	67	21	7	427	197	16	63	3	6	15	-	3	2
Misery																
82-94a	159	548	219	77	20	6	618	260	14	96	3	9	12	3	2	4
82-94b	150	500	211	73	18	11	592	253	14	96	5	11	19	3	3	3
82-94c	158	533	205	74	17	9	590	242	16	97	3	12	15	2	-	4
Haystack																
85-1a	214	668	215	64	15	6	273	120	15	37	1	3	12	-	-	-
85-1b	224	658	210	63	14	6	315	114	15	37	2	4	9	1	-	2
85-34	92	245	207	68	17	9	349	178	18	51	3	5	8	1	5	4
85-36	99	269	208	64	19	9	354	173	16	48	3	5	14	1	-	-
85-37	125	353	185	64	17	4	348	176	17	47	3	4	14	-	1	5

[1] Trace elements by XRF; dashes in columns indicate that element was below detectability or was not analyzed. See Fig. 2-1 and Appendix 2-A for sample locations.

Table 2-4. Major element analyses of andesites and dacites from Sargents Ridge and Mckenzie Butte[1]

Field#	SiO_2	TiO_2	Al_2O_3	Fe_2O_3	FeO	MnO	MgO	CaO	Na_2O	K_2O	P_2O_5	H_2O
Sargents Ridge												
82-83	61.59	.59	17.70	1.30	3.44	.09	3.31	5.95	4.23	1.48	.16	.47
82-85	61.00	.66	16.86	.76	3.86	.08	3.80	5.83	4.37	1.81	.30	.68
82-86	61.96	.66	17.36	1.36	3.38	.09	3.52	6.00	4.03	1.33	.17	.33
82-87	61.19	.59	17.84	1.60	2.68	.07	3.28	6.27	4.23	1.12	.15	.60
82-88b	62.98	.58	16.74	1.60	2.55	.07	2.79	5.12	4.65	1.93	.28	.99
82-89	65.26	.51	15.86	3.17	.88	.07	2.76	4.80	3.94	2.11	.17	.66
82-95	63.95	.61	16.05	1.79	2.59	.08	3.17	5.05	3.88	2.21	.18	.34
82-102	60.61	.65	16.97	1.49	3.57	.09	4.15	6.79	3.91	1.23	.16	.36
82-105	60.86	.61	17.70	1.92	2.73	.08	3.65	6.36	4.30	1.19	.15	.35
85-2a	62.50	.63	16.99	.88	3.16	.07	3.33	6.22	4.01	1.16	.17	.75
85-2b	62.67	.64	16.75	.18	3.83	.07	3.36	6.28	4.07	1.15	.18	.43
85-3	61.20	.68	16.22	.67	3.81	.09	4.18	6.56	4.06	1.03	.23	1.44
85-48b	61.84	.71	16.47	1.17	2.97	.08	4.11	6.81	4.12	.86	.18	.84
85-59	59.88	.72	16.26	2.36	2.68	.09	4.29	6.14	4.55	1.82	.34	.75
McKenzie Butte												
75-22	68.8	.32	16.1	1.05	1.67	.06	.53	2.31	4.7	2.64	.10	1.76
85-42	63.48	.38	18.72	1.54	1.69	.08	.58	2.54	6.18	1.72	.11	3.09
85-43	69.89	.29	14.64	1.63	1.03	.07	.47	1.79	6.00	2.74	.09	1.24

[1] See Fig. 2-1 and Appendix 2-A for sample locations. All elements by XRF except water which is the sum of H_2O^+ and H_2O^- and determined by gavimeteric techniques.

Dashes in columns indicate that the element was below detectability limit or was not analyzed.

Table 2-5. Trace element analyses of andesites and dacites from Sargents Ridge and McKenzie Butte[1]

Field#	Ni	Cr	V	Zn	Ga	Rb	Sr	Ba	Y	Zr	Nb	La	Ce	U	Th	Pb
Sargents																
82-83	24	32	79	57	23	37	651	430	14	133	4	14	21	5	5	4
82-85	59	77	99	64	21	41	903	628	13	190	6	27	41	5	5	8
82-86	24	53	97	58	21	29	781	365	14	130	4	12	19	4	3	3
82-87	37	33	109	53	23	22	893	291	11	111	2	11	13	4	3	3
82-88b	29	33	77	57	21	45	913	635	12	167	5	24	36	4	6	8
82-89	14	64	81	50	22	64	515	513	15	163	5	19	31	4	8	7
82-95	31	73	90	52	20	70	487	512	18	170	6	20	31	4	7	11
82-102	18	69	137	55	22	30	806	322	15	122	3	13	19	4	3	6
82-105	34	36	107	53	22	25	831	322	13	117	2	11	18	3	3	4
85-2a	21	53	87	45	21	25	1062	306	12	91	4	17	31	-	6	6
85-2b	23	56	86	42	21	22	1050	306	11	96	4	16	29	1	1	3
85-3	53	94	105	51	19	16	1138	308	13	96	5	17	34	-	2	3
85-48b	24	68	102	48	18	14	1478	211	11	82	4	17	35	-	3	12
85-59	75	94	109	69	18	36	995	693	14	143	8	30	57	1	3	12
McKenzie Butte																
85-42	-	-	11	69	27	42	381	808	44	239	9	115	52	3	8	17
85-43	-	2	6	44	20	65	249	693	22	191	8	25	43	3	9	11

[1] Trace elements by XRF; dashes in columns indicate that element was below detectability or was not analyzed. See Fig. 2-1 and Appendix 2-A for sample locations.

Table 2-6. Major element analyses of Misery Hill andesites and dacites[1]

Field#	SiO_2	TiO_2	Al_2O_3	Fe_2O_3	FeO	MnO	MgO	CaO	Na_2O	K_2O	P_2O_5	H_2O
82-84a	61.37	.58	17.78	1.94	2.80	.07	3.46	6.21	4.72	1.16	.49	.67
82-92a	66.38	.45	16.37	-	3.59	.06	1.89	4.18	4.10	1.94	.13	1.30
82-94d	60.83	.71	17.71	4.14	.65	.08	3.14	6.43	3.88	1.03	.22	1.22
82-93	62.15	.64	17.23	.75	3.54	.08	3.10	5.51	3.98	1.41	.18	1.06
82-98	63.25	.60	16.65	1.37	2.87	.08	3.20	5.50	4.05	1.56	.18	.84
82-99	61.56	.60	16.74	1.55	2.89	.08	3.37	5.94	4.05	1.25	.15	1.70
82-100	63.95	.50	16.99	1.95	1.65	.07	2.27	4.98	4.55	1.22	.15	1.74
82-101	63.91	.47	16.87	2.18	1.30	.06	2.48	5.12	4.59	1.31	.13	1.13
82-103	60.47	.63	17.45	1.33	3.61	.09	3.75	6.60	4.09	1.26	.13	1.21
82-104	64.92	.48	17.23	1.27	2.19	.06	2.58	5.22	4.59	1.31	.13	.37
83-45	62.68	.52	17.51	2.93	1.24	.08	2.64	5.52	4.93	1.27	.16	.98
83-49	63.42	.60	16.19	1.63	2.54	.07	3.55	5.97	4.58	1.17	.19	.50
83-56	65.62	.44	16.64	1.76	1.36	.05	2.16	4.86	4.60	1.36	.12	1.17
83-59	65.28	.49	16.70	1.48	2.03	.06	2.55	5.23	4.66	1.30	.12	.31
Panther Creek Flow												
85-55	57.74	.75	16.08	1.23	4.23	.11	5.28	8.65	3.77	1.30	.29	1.03
85-56	56.93	.76	16.29	1.72	3.96	.11	5.55	8.21	3.56	1.16	.30	1.73
85-57a	58.07	.72	16.27	1.44	3.97	.11	5.23	7.88	3.62	1.16	.28	.91
85-57b	58.24	.71	16.21	1.61	3.68	.11	4.96	7.83	3.71	1.15	.27	.94
85-58	59.85	.71	16.60	2.05	3.22	.10	4.13	6.68	3.67	1.50	.24	.78

[1] See Fig. 2-1 and Appendix 2-A for sample locations. All elements by XRF except water which is the sum of H_2O^+ and H_2O^- and determined by gavimeteric techniques.

Dashes in columns indicate that the element was below detectability limit or was not analyzed.

Table 2-7. Trace element analyses of andesites and dacites from Misery Hill[1]

Field#	Ni	Cr	V	Zn	Ga	Rb	Sr	Ba	Y	Zr	Nb	La	Ce	U	Th	Pb
82-84a	35	37	110	56	23	25	872	314	11	118	3	11	17	4	2	8
82-92a	11	19	51	50	22	56	478	475	11	138	4	14	24	4	5	10
82-93	16	45	81	60	22	35	589	384	14	131	4	11	19	4	3	6
82-94d	24	30	98	56	26	22	1293	414	15	164	2	18	33	4	4	7
82-98	13	52	108	63	21	40	625	416	20	136	4	14	17	4	4	6
82-99	21	47	98	57	21	29	806	416	14	131	3	15	18	3	2	8
82-100	9	10	84	43	22	22	745	379	11	116	3	9	16	3	3	6
82-101	9	15	84	48	21	29	709	299	12	121	2	10	19	4	2	7
82-103	16	44	122	60	22	31	737	337	15	120	3	10	20	4	3	7
82-104	7	16	122	49	22	30	706	306	12	122	3	10	17	3	2	6
83-45	25	27	77	69	27	31	666	364	8	97	3	15	21	3	4	9
83-49	64	75	101	68	26	23	939	334	11	127	3	18	23	4	4	7
83-56	15	13	72	64	26	29	763	309	7	103	2	14	18	4	3	6
83-59	15	16	91	63	28	29	700	311	8	107	3	13	14	4	4	6
Panther Creek Flow																
85-55	47	122	161	58	17	21	973	586	15	121	5	26	46	-	2	7
85-56	51	130	171	63	17	20	976	591	15	118	4	26	52	3	4	8
85-57a	47	119	156	59	14	21	937	548	15	115	4	24	45	1	6	11
85-57b	45	113	141	56	17	23	864	507	14	113	5	22	38	1	3	4
85-58	37	85	130	59	18	33	703	490	18	123	5	22	40	2	2	11

[1] Trace elements by XRF; dashes in columns indicate that element was below detectability or was not analyzed. See Fig. 2-1 and Appendix 2-A for sample locations.

Table 2-8. Major element analyses of andesites and dacites from Shastina and Hotlum[1]

Field#	SiO_2	TiO_2	Al_2O_3	Fe_2O_3	FeO	MnO	MgO	CaO	Na_2O	K_2O	P_2O_5	H_2O
Shastina												
82-82	62.49	.56	16.31	-	5.21	.07	3.45	5.94	4.15	1.12	.19	.36
83-50	63.03	.61	16.28	1.42	2.70	.07	3.60	6.00	4.58	1.16	.19	.84
83-51	63.38	.60	16.13	1.78	2.41	.07	3.70	6.09	4.58	1.14	.20	.34
83-52	63.35	.61	16.24	1.51	2.64	.08	3.65	6.05	4.60	1.14	.19	.35
83-53	62.43	.61	16.29	1.58	2.78	.08	3.82	6.11	4.59	1.12	.19	.87
83-57	64.47	.49	16.33	1.90	1.72	.07	3.34	5.97	4.25	.99	.14	.3
83-58	63.89	.56	16.54	1.72	2.10	.07	3.22	6.06	4.27	1.11	.16	.52
Hotlum												
82-91a	63.14	.57	16.88	1.54	2.43	.07	3.59	5.89	4.11	1.18	.17	.30
82-91b	63.32	.57	16.73	1.51	2.39	.07	3.71	6.02	4.09	1.11	.17	.26
82-96	62.96	.58	17.01	1.47	2.71	.08	3.44	5.93	4.19	1.20	.16	.25
82-97	63.38	.59	16.62	3.82	.83	.07	3.03	5.19	4.00	1.56	.14	.47
83-44	62.26	.61	16.93	1.92	2.64	.08	3.49	5.99	4.60	1.23	.16	.55
83-46	62.88	.63	17.25	1.56	2.98	.09	2.84	5.61	4.77	1.26	.16	.44
83-54	63.80	.59	16.14	2.68	1.69	.08	3.11	5.31	4.59	1.57	.13	.77
83-55	62.44	.63	16.36	2.11	2.58	.08	3.52	5.89	4.32	1.41	.14	.61

[1] See Fig. 2-1 and Appendix 2-A for sample locations. All elements by XRF except water which is the sum of H_2O^+ and H_2O^- and determined by gavimeteric techniques.

Dashes in columns indicate that the element was below detectability limit or was not analyzed.

Table 2-9. Trace element analyses of andesites and dacites from Shastina and Hotlum[1]

Field#	Ni	Cr	V	Zn	Ga	Rb	Sr	Ba	Y	Zr	Nb	La	Ce	U	Th	Pb
Shastina																
82-82	55	66	82	51	23	23	1147	306	13	150	3	14	24	5	2	3
83-50	65	76	99	71	26	23	987	328	11	128	3	15	27	4	3	7
83-51	69	72	105	68	25	21	1010	330	10	127	3	17	21	4	3	10
83-52	49	74	106	71	25	22	1014	329	12	129	3	16	24	4	3	11
83-53	67	94	98	71	26	22	933	320	12	124	3	18	21	4	2	8
83-57	62	41	84	61	26	15	1129	222	9	87	1	13	18	4	2	5
83-58	53	41	85	67	27	20	1157	282	10	114	2	16	22	5	4	6
Hotlum																
82-91a	52	72	89	48	22	24	960	307	11	125	2	12	22	4	3	5
82-91b	61	85	93	46	22	20	1039	282	11	123	3	12	20	5	3	4
82-96	37	50	89	46	22	27	861	305	13	121	3	10	17	3	3	6
82-97	13	58	101	49	26	40	611	409	10	136	3	13	22	3	3	6
83-44	40	68	104	73	24	26	714	354	11	110	3	15	23	3	4	7
83-46	23	33	82	73	24	29	557	385	12	105	4	13	22	3	2	6
83-54	17	53	88	70	23	41	617	430	8	120	4	14	23	4	5	7
83-55	18	63	103	72	23	36	668	392	11	115	3	14	18	4	4	7

[1] Trace elements by XRF; dashes in columns indicate that element was below detectability or was not analyzed. See Fig. 2-1 and Appendix 2-A for sample locations.

Table 2-10. Strontium isotopic composition of Mt. Shasta samples[1]

Sample#[2]	Sr (ppm)[3]	$^{87}Sr/^{86}Sr$	wt.% SiO_2
Sargents			
82-81	320/ 301	0.70373	52.05
82-95	496/ 487	0.70368	64.35
85-48b	1446/1478	0.70272	62.08
85-49	- / 491	0.70368	53.89
85-59	- / 995	0.70377	60.29
Misery			
82-93	586/ 589	0.70359	63.75
82-94a	625/ 618	0.70357	52.86
82-94d	1262/1293	0.70287	61.82
83-49	969/ 939	0.70306	63.58
85-55	- / 973	0.70374	58.26
Shastina			
83-53	924/ 933	0.70290	62.78
83-58	1128/1157	0.70281	64.19
Hotlum			
82-91b	995/1039	0.70304	63.51
83-46	562/ 557	0.70373	62.96
Haystack			
85-34	348/ 349	0.70360	54.39
Hornbrook?			
85-1n	145/ -	0.70612	-

1 Isotopic ratios are normalized to $^{86}Sr/^{88}Sr = 0.1194$ and are corrected to 0.70800 for the Eimer and Amend $SrCO_3$ standard. All in run 2σ errors were $\leq$ 0.005%.

2 See Fig. 2-1 and Appendix 2-A for sample locations.

3 First Sr concentration is by isotope dilution with an estimated precision of ~0.5%. The second value is by XRF

Table 2-11. Representative mineral compositions from Mt. Shasta lavas.

Sample #	Mineral	Notes	SiO_2	TiO_2	Al_2O_3	Cr_2O_3	FeO	MnO	MgO	CaO	Na_2O	K_2O
HAB												
85-53	Oliv	1	39.91	-	.03	.11	13.98	.22	45.51	.27	-	-
	Plag	2	48.14	-	32.45	-	.12	-	.16	16.03	2.13	.04
Basalt. And.												
82-94a	Oliv	3	40.74	-	-	.02	9.71	.11	50.51	.09	-	-
		4	40.04	-	-	.06	16.86	.21	44.82	.15	-	-
	Aug	5	53.90	.23	1.57	.55	4.08	.16	18.44	21.67	.16	-
85-47	Oliv	6	39.41	-	.02	-	15.16	.22	44.41	.20	-	-
	Plag	7	46.42	-	33.60	-	.50	-	.10	17.29	1.52	-
	Aug	8	50.60	.37	4.17	.98	4.94	.10	16.04	21.89	.25	-
	Gl	9	56.39	1.30	15.06	-	9.10	.16	3.12	7.53	4.44	1.06
	Sp	10	.12	.30	24.58	39.31	20.72	.20	13.57	-	-	-
And/Dac												
82-95	Plag	11	57.32	-	28.55	-	.23	-	.02	8.07	6.63	.75
		12	53.14	-	31.29	-	.51	-	.04	11.23	4.97	.38
		13	49.00	-	34.27	-	.30	-	.02	13.60	3.61	.19
	Opx	14	50.79	.20	1.12	.04	20.38	.45	22.14	1.24	-	-
		15	54.09	.10	.86	.05	10.34	.14	30.89	1.86	-	-
	Aug	16	53.64	.23	1.63	.52	5.55	.10	18.89	19.13	.25	-
		17	52.08	.09	.95	.04	11.80	.25	12.95	20.79	.38	-
	Oliv	18	40.45	-	-	.02	13.51	.15	46.24	.09	-	-
	Ilm	19	.47	31.23	.17	.47	61.18	.49	1.97	.06	-	-
	Sp	20	.10	.81	13.08	44.70	28.83	.28	9.47	.02	-	-
85-56	Plag	21	47.11	-	32.46	-	.42	-	.05	16.54	2.19	.05
		22	55.19	-	26.85	-	.88	-	.07	9.92	5.34	.34
		23	46.96	-	32.85	-	.53	-	.08	16.59	1.94	.06
	Opx	24	53.19	.06	.66	-	19.98	.65	24.55	.63	-	-
		25	54.86	.15	1.44	.06	12.01	.24	29.39	1.46	.04	-
		26	53.46	.53	.94	-	15.98	.46	26.44	1.84	-	-
	Aug	27	53.53	.24	1.83	.13	3.72	.11	18.15	21.79	.19	-
		28	51.78	.46	2.73	-	6.31	.18	16.83	20.57	.24	-
	Oliv	29	40.40	-	.05	.05	11.16	.16	47.79	.15	-	-
	Sp	30	.07	.82	16.05	43.14	28.33	.27	11.20	-	-	-
85-2b	Plag	31	49.10	-	31.97	-	.47	-	.04	14.58	2.76	.12
		32	62.09	-	22.70	-	.66	-	.02	4.62	7.81	1.24
		33	56.79	-	26.47	-	.76	-	-	8.76	6.05	.43
	Opx	34	52.70	.25	.94	.02	21.97	.51	22.89	1.21	-	-
		35	54.89	.20	1.65	-	12.20	.21	30.08	1.15	-	-
	Aug	36	52.03	.32	1.45	.05	10.41	.23	13.96	20.94	.48	-
		37	53.57	.31	1.45	.06	6.12	.22	18.94	19.46	.17	-
	Mt	38	.14	9.92	1.48	.39	81.30	.22	1.53	.03	-	-
	Ilm	39	.04	42.82	.17	.10	52.34	23	2.67	.04	-	-

82-85	Plag	40	57.83	-	26.84	-	.30	-	-	8.82	6.53	.29
		41	49.02	-	32.38	-	.34	-	.02	15.22	2.77	.10
		42	54.17	-	29.29	-	.29	-	.03	11.17	4.72	.20
	Opx	43	55.56	.05	2.84	.42	7.27	.19	33.76	.48	-	-
		44	52.32	.22	.56	-	24.71	.64	21.44	.87	-	-
		45	55.64	.13	1.86	.50	9.30	.20	32.63	1.24	-	-
	Aug	46	52.85	.53	2.04	.33	5.17	.14	17.97	20.61	-	-
		47	52.45	.39	2.85	.21	5.35	.14	17.49	21.05	.41	-
	Amph	48	44.62	1.79	11.51	.34	8.34	.07	17.66	11.18	2.58	.64
		49	43.87	1.77	11.73	.38	8.78	-	17.53	11.37	2.69	.64
	Oliv	50	39.66	-	-	-	15.38	.21	45.91	.12	-	-
	Ilm	51	.10	36.49	.23	.04	57.59	.29	3.09	.05	-	-
Rhyodacite												
75SH-70	Plag	52	57.29	-	26.22	-	.23	-	.02	8.45	6.57	.23
		53	62.34	-	23.43	-	.34	-	-	4.85	8.35	.84
	Opx	54	51.16	.25	.97	-	26.81	.87	17.90	1.19	-	-
		55	51.75	.14	.86	-	24.71	.79	20.22	1.06	-	-
	Amph	56	42.57	2.35	10.67	-	14.48	.21	12.91	10.29	2.50	.38
		57	42.75	2.78	10.49	-	15.16	.29	12.41	10.52	2.40	.40
	Mt	58	.23	12.71	2.38	.05	79.30	.44	1.03	.03	-	-
	Ilm	59	.05	48.44	.17	-	48.80	.62	1.34	-	-	-

Notes

1. core, oliv + plag glomerocryst
2. core, oliv + plag glomerocryst
3. phenocryst core
4. rim of #3
5. phenocryst core
6. oliv + plag + aug glomerocryst, core comp.
7. part of glomerocryst #6, core comp.
8. part of glomerocryst #6, core comp.
9. glass in glomerocryst #6
10. included in oliv.
11. sieve-textured interior of phenocryst
12. rim on #11
13. phenocryst core
14. phenocryst core
15. rim on #14
16. augite phenocryst core
17. augite inclusion in plag, An 39-47.
18. core of olivine phenocryst.
19. ilmenite inclusion in opx, Mg* = 65-66
20. chromite included in olivine
21. plagioclase core
22. interior of #21.
23. rim of #21.
24. orthopyroxene phenocryst, core.
25. rim composition of #24.
26. orthopyroxene overgrowth on olivine, Fo 87-80.
27. augite phenocryst core.
28. augite phenocryst core.
29. olivine, core composition
30. spinel inclusion in #29.
31. core, plagioclase phenocryst.
32. sieve-textured interior of #31
33. rim of #31.
34. opx, with cpx inclusion, Mg* = 69.
35. rim of #34.
36. core of augite phenocryst
37. rim of #36.
38. mt in opx #34
39. ilm in opx #34, coexists with mt.
40. plagioclase core composition.
41. rim on plag #40.
42. plagioclase core
43. opx core, overgrowth rim has Mg* = 86
44. opx, core, with ilmenite inclusion.
45. opx rimmed by amphibole.
46. augite, attached to olivine, Fo = 90-84.
47. augite phenocryst partially rimmed by amph.
48. amphibole rimming augite # 47.
49. core of amphibole phenocryst.
50. core of oliv partially rimmed by opx, Mg* = 74.
51. ilm in opx #44.
52. core, plag partially inclosed by opx.
53. rim on plag # 52.
54. core, opx with coexisting ilm and mt.
55. opx phenocryst, core
56. amph phenocryst, core.
57. rim on #56.
58. mt in opx # 54.
59. ilm in opx # 54, coexists with # 58.

Table 2-12. Modal phase proportions in Mt. Shasta basaltic andesites[1]

		Phenocrysts			Groundmass
Sample #	MgO	Oliv	Plag	Augite	
Sargents					
82-81	9.84	8.8	-	<1	91.0
85-4	8.73	8.2	<1	<1	91.4
85-5	10.68	8.2	<1	-	91.4
85-6	7.51	6.5	7.9	2.8	82.8
85-44	10.79	9.6	-	-	90.0
85-45	10.73	8.5	<1	-	91.5
85-48a	8.37	8.0	11.5	<1	79.8
Miser/					
82-94a	10.24	8.8	<1	5.4	85.2
Haystack					
85-37	8.05	6.6	5.4	3.8	84.0

[1] Vol % based on 1000 to 1100 points per petrographic thin section. Abbreviations: Oliv = olivine, Plag = plagioclase. Dashes indicate that phase was not observed.

Table 2-13. Andesite, dacite and rhyodacite modal phase proportions.

		Phenocrysts[2]					Groundmass
Sample#[1]	SiO_2	Plag	Opx	Augite	Amph	Ilm/Mt	Oliv	
Sargents								
82-83	61.77	25.0 / 9.0	5.7	1.5	-	<1	tr	58.5
82-85	61.46	11.4 / 4.0	2.7	1.0	5.1	<1	<1	74.7
82-87	61.91	10.8 / 17.6	4.0	2.4	-	<1	-	64.9
82-88b	63.53	13.4 / 5.6	2.5	0.8	6.0	1.0	-	70.2
82-89	61.59	6.5 / 10.4	2.4	1.4	-	-	tr	79.3
82-95	64.35	15.5 / 8.3	2.5	1.4	-	<1	<1	71.2
82-102	60.93	15.8 / 12.3	4.8	2.8	-	<1	<1	63.8
82-105	61.25	17.4 / 11.4	4.8	2.4	-	<1	-	63.9
85-2b	62.93	10.1 / 8.0	3.9	3.1	-	-	-	74.9
85-3	61.77	1.0 / 16.3	3.9	3.0	-	-	-	75.8
85-48b	62.08	4.8 / 10.5	4.6	4.4	-	-	-	75.6
Misery								
82-84a	65.78	16.0 / 3.1	1.7	1.6	6.3	<1	<1	72.3
82-98	63.78	13.2 / 7.1	3.8	2.1	<1	-	-	73.6
82-101	65.08	3.2 / 16.5	4.1	1.4	-	tr	-	74.9
82-103	60.88	20.6 / 13.5	6.6	2.6	-	<1	tr	56.5
82-104	65.02	3.0 / 19.2	4.0	2.3	-	-	-	71.5
83-49	63.58	2.6 / 15.6	2.6	2.7	-	<1	-	76.3
85-55*	58.26	3.4 / 1.3	1.7	6.5	-	-	2.0	85.1
85-56*	57.63	4.4 / 1.1	2.8	7.7	-	-	1.6	82.3
Hotlum								
82-91a	63.51	12.8 / 11.9	3.9	2.4	-	<1	-	68.9
82-96	63.22	18.1 / 6.8	1.4	1.6	-	<1	-	69.0
82-97	64.12	14.6 / 7.2	3.8	1.8	tr	-	<1	70.4
83-46	62.96	16.6 / 7.7	1.1	<1	-	<1	-	70.5
83-54	64.17	13.0 / 7.2	5.2	3.4	<1	<1	-	70.0
McKenzie Butte								
75-22		9.8 / 7.3	1.0	-	<1	<1	-	81.4
83-43		8.2 / 3.8	1.2	-	<1	<1	-	85.8

[1] See Fig. 2-1 and Appendix 2-A for sample locations.

[2] Vol % calculated from 1000 to 1100 points per thin section. Abbreviations: Plag = plagioclase, Opx = orthopyroxene, Amph = amphibole, Ilm/Mt = ilmenite + magnetite, Oliv = olivine, * designates Panther Creek samples, tr = trace, present but in proportions << 1%. For plagioclase first value refers to phenocrysts > 0.5 mm in size, second value to grains between 0.05 and 0.5 mm in longest dimension.

Table 2-14a. One-atmosphere melting experiments on Mt. Shasta lavas

Sample	Run #	T(°C)	fo_2[1]	Duration[2]	Run Products[3]	Phase Proportions[4]
82-94A	10	1264	7.75	17.1	gl,ol,sp	
	7	1252	7.82	13.1	gl,ol,sp	98.4(3) 1.6(3)
	3	1241	7.91	16.0	gl,ol,sp	97.4(5) 2.6(3)
	11	1225	8.17	22.0	gl,ol,sp	95.6(4) 4.4(2)
	1	1210	8.43	22.8	gl,ol,sp	94.3(2) 5.7(2)
	5	1194	8.42	46.1	gl,ol,pl,sp	
	8	1186	8.68	48.3	gl,ol,pl,sp	
	17	1178	8.83	150.1	gl,ol,pl,sp	81.4(8) 9.6(2) 9.0(6)
	15	1160	9.03	141.8	gl,ol,pl,aug	59.7(8) 12.0(3) 21.2(6) 7.0(4)
	16	1149	9.31	239.8	gl,ol,pl,aug	46.7(7) 13.3(3) 29.0(6) 11.0(5)
	18[5]	1140	9.24	231.3	gl,ol,pl,aug,opx	41.3(7) 18.7(8) 31.7(6) 15.8(7) 0.0
75SH-70	3	1215	8.21	79.0	gl,tr pl	99.0(5) 1.0(4)
	2	1203	8.38	75.2	gl,pl,ol	89.7(8) 8.0(6) 2.2(3)
	1	1189	8.59	67.8	gl,pl,ol	77.9(9) 16.7(8) 5.4(2)
	4	1169	8.76	96.4	gl,pl,ol	66.4(6) 25.4(5) 8.3(2)
85-55	1	1181	8.70	51.3	gl,pl	
	2	1160	8.98	96.8	gl,pl,opx	
	4	1147	9.17	97.2	gl,pl,opx,aug	
83-58	7	1222	8.22	24.4	gl	
	6	1209	8.31	24.0	gl,pl	
	1	1186	8.62	24.7	gl,pl	91.8(6) 8.2(5)
	2	1151	9.16	35.0	gl,pl,opx	82.7(7) 15.3(7) 2.0(2)
	3	1132	9.30	44.5	gl,pl,opx	
	4	1102	9.75	313.4	gl,pl,opx	58(1) 34(1) 8.2(2)
	8	1055	10.28	332.4	gl,pl,opx,aug	53.4(8) 35(1) 8.9(7) 2(1)

[1] Oxygen fugacity in negative log units.

[2] Run times in hours.

[3] Abbreviations: gl=glass, ol=olivine, pl=plagioclase, sp=spinel, aug=augite, opx=orthopyroxene, tr=trace.

[4] Phase proportions calculated using phase compositions reported in Table 2-15 and a non-linear least-squares algorithm described in the text. Units in parentheses are calculated uncertainties in terms of the least units cited, e.g. 97.4(5) equals 97.4 ± 0.5.

[5] Calculated wt.% opx was negative and was set to zero.

Table 2-14b. Two kbar water-saturated melting experiment on 85-3.

Run#	T(°C)	Duration[1]	Run Products[2]	Phase Proportions[3]
4	980	48.3	gl,pl,opx,cpx	74, 11, 3.1, 7.5, (3.3)
3	960	44.8	gl,pl,opx,cpx	
5	945	72.0	gl,pl,opx,cpx	72, 11, 3.4, 8.6, (4.6)
2	930	86.7	gl,pl,opx,cpx	70, 14, 4.4, 8.4, (3.0)
1	900	85.5	gl,pl,opx,amp,ap	50, 29, 5.8, 12, 0.4, (2.2)

[1] Duration in hours

[2] Abbreviations: gl = glass, pl = plagioclase, opx = orthopyroxene, cpx = augite, amp = amphibole, ap = apatite.

[3] The mass balance calculations included "FeO" as a phase, the wt.% of FeO is given in parentheses.

Table 2-15. Electron microprobe analyses of run products from experiments on Mt. Shasta lavas[1]

Sample	Run#	Phase	SiO_2	TiO_2	Al_2O_3	Cr_2O_3	FeO	MnO	MgO	CaO	Na_2O	K_2O	P_2O_5
82-94a	7	gl(6)	53.2(2)	.74(3)	15.5(3)	.05(2)	7.22(9)	.14(3)	9.5(2)	9.9(1)	3.16(5)	.51(2)	.28(7)
		ol(3)	40.8(1)	-	.04(2)	.05(4)	10.2(2)	.18(2)	48.5(1)	.23(3)	-	-	-
	3	gl(7)	53.2(4)	.73(3)	15.8(2)	.06(5)	7.00(13)	.11(3)	9.2(2)	10.0(2)	3.12(5)	.55(3)	.33(5)
		ol(3)	40.7(5)	-	-	-	10.5(5)	.16(2)	48.4(2)	.24(3)	-	-	-
	11	gl(5)	53.0(5)	.75(2)	15.8(2)	.05(3)	6.95(8)	.11(2)	8.4(1)	10.0(2)	3.24(6)	.53(2)	.20(6)
		ol(2)	40.76(4)	-	.03(1)	-	11.2(1)	.14(6)	48.1(4)	.27(1)	-	-	-
	1	gl(6)	53.01(7)	.73(2)	16.03(7)	.04(2)	6.9(1)	.06(7)	7.86(5)	9.95(7)	3.26(7)	.61(5)	.26(2)
		ol(6)	40.7(1)	.03(2)	.07(2)	.07(2)	12.2(2)	.13(2)	46.9(3)	.29(5)	-	-	-
	17	gl(6)	54.1(2)	.89(2)	15.2(1)	.04(2)	7.1(2)	.15(2)	7.01(9)	10.17(5)	3.16(7)	.57(2)	.23(3)
		ol(3)	40.4(3)	-	.07(3)	-	13.3(1)	.21(3)	45.7(4)	.41(1)	-	-	-
		pl(6)	51.3(3)	-	29.6(4)	-	.7(2)	-	-	13.9(2)	3.34(6)	.12(2)	-
	15	gl(6)	55.9(2)	1.11(5)	14.86(5)	.05(2)	7.41(4)	.17(2)	6.00(5)	9.0(1)	3.4(1)	.81(5)	.28(2)
		ol(4)	39.9(4)	-	.16(6)	.12(2)	15.8(1)	.29(4)	43.88(6)	.4(1)	-	-	-
		pl(13)	52.8(3)	-	29.1(6)	-	.6(1)	-	.5(1)	12.7(2)	3.8(1)	.16(4)	-
		aug(5)	52.9(6)	.39(7)	2.6(6)	.6(3)	5.7(3)	.13(2)	18.0(4)	20.0(6)	.3(1)	-	-
	16	gl(13)	56.8(2)	1.36(7)	14.40(7)	-	7.8(2)	.16(4)	5.17(7)	8.3(1)	3.61(7)	.97(4)	.37(4)
		ol(5)	39.2(3)	-	.10(9)	-	18.2(2)	.32(2)	42.2(2)	.33(2)	-	-	-
		pl(7)	53.6(3)	-	28.2(3)	-	.7(1)	-	.4(1)	12.4(2)	4.18(5)	.18(3)	-
		aug(9)	52.7(6)	.46(4)	2.2(5)	.7(2)	6.7(2)	.20(3)	18.2(5)	18.2(4)	.35(9)	-	-
	18	gl(7)	57.7(4)	1.48(5)	14.44(8)	-	7.4(2)	.14(3)	4.46(5)	7.3(2)	4.0(1)	1.24(3)	.29(5)
		ol(5)	39.4(1)	-	.04(2)	-	19.39(9)	.35(2)	40.3(4)	.31(2)	-	-	-
		pl(12)	53.6(4)	-	28.2(3)	-	.61(7)	-	.29(7)	11.8(2)	4.46(7)	.20(3)	-
		aug(6)	53.0(4)	.5(1)	1.9(3)	.5(3)	7.0(2)	.16(4)	17.7(4)	18.9(7)	.25(7)	-	-
		opx(5)	55.1(3)	.29(4)	1.2(3)	.39(7)	11.55(7)	.29(4)	28.9(3)	2.4(2)	.06(2)	-	-
75-70	3	gl(4)	53.5(3)	.71(3)	17.5(1)	.12(2)	7.19(6)	.12(1)	7.80(7)	9.2(1)	3.2(2)	.49(3)	.20(5)
	2	gl(4)	54.3(1)	.72(3)	17.00(5)	.10(1)	7.26(9)	.14(4)	7.7(1)	8.99(8)	3.2(1)	.50(3)	.22(2)
		ol(4)	40.1(1)	-	.2(2)	-	12.7(2)	.19(1)	46.8(3)	.26(4)	-	-	-

		pl(3)	50.5(3)	-	31.1(3)	-	.48(8)	-	.35(5)	14.59(3)	2.93(3)	.05(2)	-
	1	gl(6)	54.9(2)	.78(4)	16.18(8)	.09(1)	8.9(1)	.13(3)	6.93(7)	8.9(1)	3.37(7)	.56(3)	.24(4)
		ol(4)	39.4(2)	-	.3(2)	.2(1)	14.7(3)	.23(3)	44.9(3)	.32(7)	-	-	-
		pl(5)	51.4(6)	-	29.8(9)	-	.53(9)	-	.27(2)	13.5(2)	3.37(6)	.06(1)	-
	4	gl(5)	55.9(2)	.95(2)	15.22(5)	.04(4)	8.4(2)	.17(1)	6.1(1)	8.98(4)	3.30(9)	.63(3)	.30(4)
		ol(4)	38.9(3)	-	.3(2)	.4(4)	16.9(2)	.26(2)	42.8(4)	.33(2)	-	-	-
		pl(6)	52.2(4)	-	29.8(3)	-	.7(1)	-	.3(1)	13.5(1)	3.50(5)	.09(1)	-
83-58	7	gl(5)	64.5(4)	.54(2)	16.9(2)	.06(2)	4.1(2)	.08(2)	3.28(2)	6.0(2)	4.2(2)	1.11(4)	.30(4)
	1	gl(4)	65.3(5)	.55(2)	16.1(1)	.05(2)	4.2(1)	.04(1)	3.6(2)	5.50(8)	4.1(2)	1.16(9)	.25(2)
	2	gl(6)	66.4(1)	.62(2)	15.12(8)	.02(2)	4.3(1)	.08(2)	3.10(4)	4.73(6)	4.1(1)	1.38(2)	.16(1)N
	3	gl(5)	67.7(2)	.74(4)	14.40(6)	.04(2)	4.6(1)	.01(2)	2.46(5)	4.35(6)	4.02(9)	1.52(7)	.18(3)N
	4	gl(6)	70.8(8)	.87(3)	12.9(2)	.05(2)	4.1(2)	.08(2)	3.28(2)	6.0(2)	4.2(2)	1.11(4)	.30(4)
	8	gl(7)	74.0(9)	.92(3)	12.0(1)	.05(2)	3.4(1)	.01(1)	.89(3)	2.36(5)	3.7(5)	2.11(7)	.4(1)
85-55	1	gl(6)	58.4(1)	.74(1)	15.78(8)	.11(2)	5.44(9)	.08(1)	5.63(9)	7.84(6)	3.59(5)	1.37(3)	.22(1)
	2	gl(5)	59.7(2)	.89(3)	15.27(5)	.03(1)	5.6(2)	.05(3)	4.66(8)	7.4(2)	3.8(3)	1.58(4)	.27(3)
	4	gl(5)	60.0(2)	.98(3)	14.9(2)	.01(2)	6.7(2)	.10(3)	4.24(7)	7.2(2)	4.0(1)	1.71(5)	.36(1)

1 Number of analyses given in parentheses following the phase abbreviation. Gl = glass, ol = olivine, pl = plagioclase, aug = augite, opx = othopyroxene. Standard deviation given in parentheses after each oxide wt.%, in terms of the least units cited.

Table 2-16. Data used to calibrate liquidus temperature (T_L) in terms of bulk composition.

Sample #	SiO_2	TiO_2	Al_2O_3	FeO	MnO	MgO	CaO	Na_2O	K_2O	T_L (°C)	Ref[1]
P12	49.35	1.23	16.39	9.41	0.18	8.15	12.59	2.27	0.35	1232±7	1
79-35g	47.61	0.58	17.94	10.79	0.16	9.84	11.30	1.69	0.09	1231±3	2
79-38b	55.19	0.87	17.32	8.31	0.18	5.92	8.50	2.68	0.91	1192±8	3
79-9c	60.53	1.47	16.39	7.00	0.16	2.79	5.81	4.18	1.39	1174±5	4
79-37i	56.40	1.08	17.35	7.74	0.15	4.68	7.90	3.66	0.93	1209±6	4
83-58	64.19	.56	16.62	3.66	0.07	3.24	6.09	4.29	1.12	1215±6	4
C8051	54.63	1.97	13.99	12.19	0.20	4.61	8.23	3.03	1.15	1140±2	5
GS104	50.92	1.40	15.33	9.00	0.17	8.03	11.80	3.06	0.22	1218±2	6
AII-78	49.10	0.99	17.33	9.31	0.17	9.53	10.53	2.91	0.11	1242±2	6
AII-96	50.63	1.45	15.37	9.29	0.17	8.53	11.20	3.14	0.12	1222±4	6
A	51.01	1.95	12.90	13.34	-	6.33	10.48	2.26	0.11	1152±3	7
Sample 1	49.22	2.54	16.14	10.49	-	6.65	10.79	3.20	0.98	1181±7	8

[1] Ref: 1 = Shibata and Fox (1975), Walker et al. (1979); 2 = Grove et al. (1982); 3 = Baker and Grove (1985); 4 = This study; 5 = Schiffman and Lofgren (1982); 6 = Tormey et al. (1987); 7 = Juster and Grove (1988); 8 = Mahood and Baker (1986).

Dash = concentration not reported.

Table 2-17. Results of experiments to determine the liquidus temperature of selected Medicine Lake and Mt. Shasta lavas.

Sample#[1]	Run#	T(°C)	log fo_2	Duration[2]	Run Products[3]
79-37i (M)	5	1215	-8.18	51.3	gl
	4	1203	-8.38	75.1	gl + plag
	2	1186	-8.60	67.?	gl + plag + oliv
79-9c (M)	47	1179	-8.69	98.0	gl
	46	1169	-8.75	96.4	gl + plag
	45	1158	-8.90	70.7	gl + plag
82-82 (S)	4	1205	-8.50	53.2	gl
	2	1196	-8.48	49.0	gl + plag
82-95 (S)	1	1195	-8.48	50.8	gl + tr plag
83-53 (S)	2	1220	-8.20	49.8	gl
	1	1203	-8.38	51.5	gl + plag
82-84a (S)	2	1213	-8.33	50.7	gl
	1	1205	-8.46	49.2	gl + plag
85-48b (S)	3	1230	-8.11	71.3	gl
	2	1210	-8.29	55.4	gl + plag

[1] (M) = Medicine Lake sample, (S) = Shasta sample. Medicine Lake bulk conmpositions given in Table 2-16, Shasta bulk compositions given in Tables 2-4, 2-6 and 2-8.

[2] Run times in hours

[3] Abbreviations: gl = glass, plag = plagioclase, oliv = olivine, tr = trace. Very rare rounded plag crystals in 82-95-1 indicate that liquidus temperature is only slightly higher than 1195°C

Table 2-18. Spearman rank-order correlation coefficients for trace element pairs and Sr-major element pairs in Sargents, Misery, Shastina and Hotlum andesites and dacites[1]

	Ba	Rb	Sr	Zr	Nb	Y	V	Cr	Ni	Cu	Zn	La	Ce	Ga
Ba	1													
Rb	.74	1												
Sr	-.54	-.81	1											
Zr	.31	.49	0	1										
Nb	.31	0	-.55	0	1									
Y	.31	0	0	.47	0	1								
V	0	0	0	0	-.40	0	1							
Cr	0	0	.36	0	0	0	.38	1						
Ni	0	-.52	.64	0	-.37	0	0	.63	1					
Cu	0	-.34	.49	0	-.47	0	0	0	.46	1				
Zn	.34	0	0	0	-.30	0	0	0	.32	.31	1			
La	.35	0	.28	.27	0	0	0	.48	.39	.32	.28	1		
Ce	.30	0	.30	.30	.27	0	0	.50	.32	0	0	.75	1	
Ga	0	-.33	0	-.26	0	-.74	0	-.29	0	0	.42	0	-.36	1

	Si	Ti	Al	Fe	Mg	Ca	Na	K	P
Sr	-.36	0	0	0	.56	.67	0	-.80	.46

[1] Correlation coefficients calculated using a subroutine from Press et al. (1986). Zero indicates that probability for the null hypothesis, i.e. no correlation, was > 10%.

Table 2-19. Results of basaltic andesite mass balance calculations I.

Phase compositions[1]

	SiO_2	TiO_2	Al_2O_3	Cr_2O_3	FeO	MgO	CaO	Na_2O	K_2O
Residual liq.	54.24	0.74	18.09	0.03	7.12	7.00	9,01	3.23	0.56
Olivine	40.08	-	-	-	14.03	45.89	-	-	-
Plagioclase	47.52	-	33.74	-	-	-	16.74	2.00	-
Augite	52.25	0.35	3.12	0.60	4.44	17.45	21.57	0.23	-
Spinel	0.09	0.40	24.30	38.26	23.86	12.68	0.02	-	-

Model: Resid. Liq. + Oliv + Aug + Sp = Parent

Parent	53.46	0.65	17.24	0.06	7.20	8.50	9.41	3.02	0.46
Calc. Parent	53.38	0.66	17.34	0.06	7.13	8.61	9.41	2.98	0.47
Difference	.08	-.01	-.10	0	.07	-.11	0	.04	-.01

Phase prop.[2] Resid liq. = 88.3 Oliv = 4.1 Plag = 3.9 Aug = 3.7 Sp = 0.3

$\chi^2 = 8.55$

$Q = 0.13$

[1] Residual and parent liquids calculated from linear or polynomial fits to the basaltic andesite data using MgO as the independent variable. Plag calculated using a Ca-Na K_D of 3.0. Fe-Mg K_Ds for oliv and cpx are 0.30, 0.25; remaining oxides in the pyroxene are based on the average of the phenocryst core compositions.

[2] Phase proportions are in wt.%.

Table 2-20. Results of basaltic andesite mass balance calculations II.

Phase compositions[1]

	SiO_2	TiO_2	Al_2O_3	Cr_2O_3	FeO	MgO	CaO	Na_2O	K_2O
Residual liq.	53.46	0.65	17.24	0.06	7.20	8.50	9.41	3.02	0.46
Olivine	40.45	-	-	-	12.04	45.51	-	-	-
Plagioclase	47.17	-	33.97	-	-	-	17.02	1.84	-
Augite	52.24	0.34	3.18	0.59	3.80	17.95	21.66	0.23	-
Spinel	0.09	0.40	24.30	38.26	23.86	12.68	0.02	-	-
Assim 1	56.17	0.09	2.01	0.49	6.71	33.44	0.98	0.02	-
Assim 2	97.00	-	2.60	-	-	0.39	-	-	-

Model 1: Resid. Liq. + Oliv + Aug + Sp - Assim 1

Parent	51.92	0.58	16.25	0.10	7.78	10.82	9.66	2.68	0.38
Calc. Parent	51.87	0.59	16.09	0.10	7.75	10.86	9.66	2.74	0.40
Difference	.05	-.01	.16	0	.03	-.04	0	-.06	-.02

Phase prop.[2] Resid liq.=92.1 Oliv=10.2 Aug=4.9 Sp=0.1 Assim 1= -7.3 R = 0.48

χ^2 = 6.4

Q = 0.27

Model 2: Resid. liq. + Oliv + Plag + Aug + Sp - Assim 1

Parent	51.92	0.58	16.25	0.10	7.78	10.82	9.66	2.68	0.38
Calc. Parent	51.81	0.59	16.23	0.10	7.73	10.86	9.65	2.72	0.40
Difference	.11	-.01	.02	0	.05	-.04	.01	-.04	-.02

Phase prop. Resid. liq=90.3 Oliv=10.4 Plag=1.8 Aug=4.2 Sp=0.1 Assim 1= -6.8 R = 0.41

χ^2 = 4.46

Q = 0.35

[1] Residual and parent liquids caclated from linear or polynomial fits to the basaltic andesite data using MgO as the independent variable. Plag calculated using a Ca-Na K_D of 3.0. Fe-Mg K_Ds for oliv and cpx are 0.30 and 0.23; remaining oxides in pyroxene are based on the average of phenocryst core compositions. Assimilant 1 is the average of the orthopyroxene analyses reported by Quick (1981). Assimilant 2 discussed in text.

[2] Phase proportions are in wt.%. R = ratio mass assimilated to mass crystallized.

Table 2-21. Basaltic andesite fractionation model.[1]

SiO_2	TiO_2	Al_2O_3	FeO	MgO	CaO	Na_2O	K_2O	Ni	Cr	Sr	Rb	Zr	Ba	La	F	Fo	An	Mg-cpx
53.49	0.65	17.25	7.20	8.51	9.42	3.02	0.46	134	410	365	6.2	48.3	163	5.3	1.00	.86	.84	.89
53.66	0.66	17.48	7.21	8.08	9.34	3.08	0.47	119	353	370					.98	.86	.83	.89
53.88	0.68	17.77	7.21	7.56	9.24	3.16	0.49	103	290	377					.95	.85	.83	.88
54.11	0.70	18.07	7.20	7.03	9.14	3.25	0.50	87	233	383	6.7	52.3	174	5.6	.92	.84	.82	.87

Phase Proportions (wt.%): Oliv = 38.2 Plag = 20.4; Cpx = 41.0; Spinel = 0.4

Exchange coefficients: Plag Ca-Na K_D=3.0; Oliv Fe-Mg K_D = 0.33; Cpx Fe-Mg K_D=0.25

[1] F = wt.% of liquid remaining; Fo = forsterite content in olivine; An = anorthite content in plagioclase; Mg-cpx = Mg/(Mg+Fe*) in the pyroxene. Major and trace element composition of starting liquid based on linear or polynomial fits to the basaltic andesite data using MgO as the independent variable. D_{Ni} from Elthon (1987), remaining partition coefficients from the compilation in Henderson (1982). Augite composition: SiO_2=52.00, TiO_2=0.20, Al_2O_3=2.50, MgO+FeO=23.17, CaO=21.90, Na_2O=0.23. Spinel composition: TiO_2=0.40, Al_2O_3=24.40, Cr_2O_3=37.41, FeO=24.95, MgO=12.73. Rb, Zr, Ba and La abundances in the residual liquid calculated using F from the major element model and the expression $C_O/C_l=F^{(D^*-1)}$, bulk distribution coefficient based on the phase proportions and oliv, plag and cpx partition coefficients from Henderson (1982). Only the final set of incompatible trace elements is calculated.

Table 2-22. Results of high alumina basalt - basaltic andesite mass balance calculations.

Phase compositions[1]

	SiO_2	TiO_2	Al_2O_3	Cr_2O_3	FeO	MgO	CaO	Na_2O	K_2O
HAB	47.99	0.59	18.56	0.03	8.21	10.54	11.81	2.17	0.07
Olivine	40.59	-	-	-	11.28	48.13	-	-	-
Orthopyroxene	56.17	0.09	2.01	0.49	6.71	33.44	0.98	0.02	-

Model : HAB - Oliv + Opx = BA

BA	51.92	0.57	16.20	0.10	7.73	10.82	9.72	2.68	0.36
Calc. BA	52.03	0.56	16.19	0.10	7.72	10.88	9.83	1.83	0.06
Difference	-.11	.01	.01	0	.01	-.06	-.11	.85	.30

Phase prop.[2] HAB 1 = 83.2 Oliv = -19.0 Opx = 35.7 R = 1.9

χ^2 = 20.7

Q = 0.004

[1] HAB is the most magnesian lava found at Giant Crater, Medicine Lake volcano, N. CA (see Chapter 1). Fe-Mg K_D for oliv is 0.30. Orthopyroxene is the average of the orthopyroxene analyses reported by Quick (1981). Uncertainties on the Na_2O and K_2O contents in the BA set equal to 1.0.

[2] Phase proportions are in wt.%.

Table 2-23 Major element variations in andesites and dacites as linear functions of MgO.[1]

Element	Slope	Intercept	r_s [2]	Technique[3]
SiO_2	-2.746	72.433	-0.73(0.33E-7)	2
TiO_2	0.0996	0.265	0.61(0.14E-4)	1
FeO	0.570	2.229	0.54(0.16E-3)	1
CaO	0.880	2.928	0.76(0.35E-8)	1
Na_2O	-0.174	4.860	-0.19(0.23)	2
K_2O	-0.123	1.633	-0.44(0.29E-2)	2
P_2O_5	0.0219	0.0908	0.48(0.10E-2)	2

[1] Data set did not include Panther Creek lavas. All compositions normalized to 100% on an MnO-free basis.

[2] r_s is the Spearman rank-order correlation coefficient; values in parentheses are probabilities that each oxide is in fact uncorrelated with MgO. Read 0.33E-7 as 0.33×10^{-7}.

[3] 1 = line fit by minimizing the sum of the squared residuals; 2 = line fit by minimizing the sum of the absolute deviations.

Table 2-24. Results of basaltic andesite - andesite mass balance calculations

Phase compositions[1]

	SiO_2	TiO_2	Al_2O_3	FeO	MgO	CaO	Na_2O	K_2O
Residual liq	60.08	0.71	17.79	4.80	4.50	6.88	4.07	1.08
Plagioclase A	51.76	-	30.88	-	-	13.40	3.96	-
Plagioclase B	49.64	-	32.31	-	-	15.07	2.98	-
Plagioclase C	48.39	-	33.15	-	-	16.06	2.40	-
Olivine	39.97	-	-	14.57	45.45	-	-	-
Clinopyroxene	52.70	0.50	2.74	4.41	18.10	21.22	0.33	-
Orthopyroxene	56.12	0.20	1.72	7.40	33.03	1.52	-	-
Magnetite	-	-	-	93.09	-	-	-	-
Ilmenite	-	52.65	-	47.35	-	-	-	-

Model 1: Resid. liq + Plag A + Oliv + Cpx + Mt + Ilm = Parent

Parent	54.23	0.74	18.09	7.12	7.00	9.01	3.23	0.56
Calc. parent	54.08	0.74	18.08	7.11	7.00	9.02	3.28	0.58
Difference	.16	0	.01	.01	0	-.01	-.05	-.02

Phase prop.[2] Resid. liq = 55.3 Plag = 26.1 Oliv = 6.6 Cpx = 8.4 Mt = 3.0 Ilm = 0.6

$\chi^2 = 4.41$

$Q = 0.22$

Model 2: Resid. Liq. + Plag A + Opx + Cpx + Mt + Ilm = Parent

Parent	54.24	0.74	18.09	7.12	7.00	9.01	3.23	0.56
Calc. Parent	54.26	0.74	17.96	7.12	6.97	9.00	3.20	0.55
Difference	-.02	0	.13	0	.03	.01	.03	.01

Phase prop. Resid. liq. = 50.6 Plag = 27.7 Opx = 9.9 Cpx = 7.6 Mt = 3.6 Ilm = 0.6

$\chi^2 = 0.92$

$Q = 0.82$

[1] Residual and parent liquids caclated from linear regression parameters given in Table 2-23. Plag A calculated using a Ca-Na K_D of 2.0; plag B using a K_D of 3.0; plag C using a K_D of 4.0. Fe-Mg K_Ds for oliv, opx and and cpx are 0.30, 0.21 and 0.23; remaining oxides in pyroxenes are based on rim compositions from 85-59, 82-102 and 85-57. Mt and Ilm are end-member compositions.

[2] Phase proportions are in wt.%.

Table 2-25. Andesite to dacite fractionation model.[1]

SiO_2	TiO_2	Al_2O_3	FeO	MgO	CaO	Na_2O	K_2O	F	An	Mg-cpx	Mg-opx
60.19	0.71	17.72	4.81	4.51	6.89	4.08	1.08	1.00	.82	.88	.89
60.67	0.74	17.63	4.91	4.12	6.57	4.23	1.14	.95	.81	.87	.88
61.16	0.77	17.55	5.00	3.71	6.23	4.38	1.20	.90	.79	.85	.86
61.78	0.81	17.45	5.08	3.22	5.82	4.56	1.27	.85	.77	.83	.84
62.43	0.85	17.35	5.14	2.72	5.40	4.75	1.35	.80	.75	.80	.82
63.12	0.90	17.26	5.17	2.22	4.96	4.95	1.43	.75	.73	.77	.78

Phase Proportions (wt.%): Plag = 55; Cpx = 17; Opx = 28

Exchange coefficients: Plag Ca-Na K_D=4.9; Cpx Fe-Mg K_D=0.23; Opx Fe-Mg K_D=0.21

[1] F = wt.% of liquid remaining; An = anorthite content in plagioclase; Mg-cpx and Mg-opx = Mg/(Mg+Fe*) in the pyroxene. See Table 2-24 for source of minor element compositions of augite and opx.

Table 2-26 Results of andesite-dacite mass balance calculations.

Phase compositions[1]	SiO_2	TiO_2	Al_2O_3	FeO	MgO	CaO	Na_2O	K_2O
Residual liq	66.94	0.46	16.51	3.37	2.0	4.69	4.51	1.39
Plagioclase A	54.71	-	28.90	-	-	11.07	5.33	-
Plagioclase B	52.22	-	30.57	-	-	13.03	4.18	-
Plagioclase C	50.64	-	31.63	-	-	14.28	3.44	-
Orthopyroxene	55.32	0.18	1.07	11.01	31.11	1.31	-	-
Clinopyroxene	53.30	0.27	1.74	6.56	17.02	20.92	0.19	-
Amphibole	46.60	1.60	10.33	10.78	16.56	11.31	2.32	0.28
Magnetite	-	-	-	93.09	-	-	-	-
Ilmenite	-	52.65	-	47.35	-	-	-	-

Model 1: Resid. liq + Plag C + Opx + Cpx + Mt + Ilm = Parent

Parent	60.08	0.71	17.69	4.80	4.50	6.88	4.07	1.08
Calc. parent	60.39	0.71	17.59	4.81	4.47	6.87	3.83	.99
Difference	-.31	0	.10	-.01	.03	.01	.24	.09

Phase prop.[2] Resid. liq = 65.8 Plag = 20.7 Opx = 8.2 Cpx = 3.3 Mt = 1.2 Ilm = 0.7

$\chi^2 = 24.47$

$Q = 0.20 \times 10^{-4}$

Model 2: Resid. Liq. + Plag B + Opx + Amp + Mt + Ilm = Parent

Parent	60.08	0.71	17.69	4.80	4.50	6.88	4.07	1.08
Calc. Parent	60.21	0.71	17.43	4.80	4.49	6.90	4.00	1.05
Difference	-.13	0	.26	0	.01	-.02	.06	.03

Phase prop. Resid. liq. = 69.4 Plag = 11.7 Opx = 0.0 Amp = 18.4 Mt = 0.7 Ilm = 0.7

$\chi^2 = 7.42$

$Q = 0.06$

[1] Residual and parent liquids caclated from linear regression parameters given in Table 2-23. Plag A calculated using a Ca-Na K_D of 2.0; plag B using a K_D of 3.0; plag C using a K_D of 4.0 Fe-Mg K_Ds for opx and and cpx are 0.21 and 0.23; remaining oxides in pyroxenes are based on rim compositions from 83-56, 82-84a and 82-92a. Amphibole is average rim composition from 83-56, 82-84a and 82-92a. Mt and Ilm are end-member compositions.

2 Phase proportions are in wt.%.

Table 2-27. Composition of the Sr-I component[1]

SiO_2	64	Sr	1450 - 1880
Al_2O_3	15	Rb	8 - 0
Na_2O	4	Ba	260 - 230
K_2O	0.8	La	21
Mg#	61	Ba/La	~12
		K/Rb	~1600
		Rb/Sr	0.006 - 0
		87/86	0.7026

[1] Calculated from element/Sr vs 1/Sr plots. Oxides in wt.%; trace elements in ppm. Maximum Sr defined by the intersection of the regression line with the y-axis in Rb/Sr - 1/Sr space. Lower Sr value from 85-48b.

APPENDIX 2-A: SAMPLE LOCATIONS

Field locations for all samples located in Tables 2-1 through 2-9 are given below. Samples are located on five 15 minute northern California quadrangle maps: Shasta, Weed, Lake Shastina, Whaleback and Bartle. Where possible samples are grouped by stratigraphic units based on the mapping of Christiansen (1977); in general, distances and elevations have been rounded to the nearest 100 feet. In cases where a sample was located between two widely spaced contours, both elevations are given.

Sargents Ridge

82-81 1200 ft south and 100 ft west from NE corner, Sec 16, T42N, R4W, Lake Shastina Quad. Sample taken from SE side railroad bed cut.

82-83 800 ft west and 2400 ft north from SE corner, Sec 33, T41N, R3W, Shasta Quad. Collected just below the 8000 ft contour at the tip of the N-S trending ridge.

82-85 1800 ft east and 600 ft south from NW corner, Sec 34, T41N, R3W, Shasta Quad. Western side of Red Butte just below northern summit.

82-86 800 ft east and 500 ft north from SW corner, Sec 27, T41N, R3W, Shasta Quad. Collected at approximately 8100 ft at the crest of the SW branch of Sargents Ridge.

82-87 1200 ft west and 2300 north from the NE corner,

Sec 21, T41N, R3W, Shasta Quad. Collected at approximately 10800 ft just below and to the SW of the lower of two domes on Sargents Ridge.

82-88 200 ft east and 1800 ft south from NW corner, Sec 22, T41N, R3W, Shasta Quad. Collected at 11000 ft to the SE of the 11267 ft dome on Sargents Ridge.

82-89 2200 ft east and 2000 ft south from NW corner, Sec 21, T41N, R3W, Shasta Quad. Collected at 10500 ft from flow exposed in glacial cirque.

82-95 1100 ft east and 400 ft from SW corner, Sec 15, T42N, R3W, Shasta Quad.

82-102 1200 ft east and 1400 ft south from NW corner, Sec 21, T41N, R3W. Sample collected at 10700 ft to the west of the ridge crest that forms the eastern border of Avalanche Gulch.

82-105 200 ft west and 600 ft south from NE corner, Sec 29, T41N, R3W, Shasta Quad. Collected at 9300 ft along crest of ridge that terminates at Green Butte.

85-2 2500 ft west and 900 ft north from SE corner, Sec 16, T42N, R4W, Weed Quad. Collected at 4500 ft from eastern side of railroad cut.

85-3 800 ft west and 500 ft north from SE corner, Sec 20, T42N, R4W, Weed Quad. Collected at 4100 ft from eastern side of railroad cut.

85-4 1500 ft west and 1700 ft south from NE corner, Sec 16, T42N, R4W, Weed Quad. Collected at 4000 ft

on south side of dirt road.

85-5 600 ft east and 2000 ft south from NW corner, Sec 15, T42n, R4W, Weed Quad. Collected at 4200 ft 200 ft south of dirt road.

85-6 2100 ft west and 1300 ft north from SE corner, SE 15, T42N, R4W, Weed Quad. Collected at 4700 ft on the SW side of large flow.

85-44 1000 ft east and 500 ft south from NW corner, Sec 22, T42N, R4W, Weed Quad. Collected at 4700 ft west of Cinder cone.

85-45 800 ft south and 2600 ft east from NW corner, Sec 22, T42N, R4W, Weed Quad. Collected at 5000 ft west of Cinder Cone.

85-46 1800 ft west and 2400 ft south from NE corner, Sec 22, T42N, R4W, Weed Quad. Collected at 4800 ft just west of cinder pit.

85-47 1200 ft west and 2500 ft south from NE corner, Sec 22, T42N, R4W, Weed Quad. Collected at 4700 ft in cinder pit.

85-48 1400 ft east and 2200 ft north from SW corner, Sec 35, T41N, R3W, Shasta Quad. Collected at 8600 ft west of ridge trending south from Green Butte.

85-49 200 ft east and 2300 ft south from NW corner, Sec 28, T41N, R3W, Shasta Quad. Collected at 9100 ft just below saddle west of Greene Butte.

85-50 2000 ft west and 2700 ft north from SW corner, Sec 29, T41N, R3W, Shasta Quad. Collected at 8700 ft.

85-59 1400 ft east and 2200 ft north from SW corner, Sec 35, T41N, R3W, Shasta Quad. Collected at 7200 ft approx.100 ft. west of Squaw Valley Creek.

Misery Hill

82-84 400 ft west and 700 ft north from SE corner, Sec 33, T41N, R3W, Shasta Quad. Collected at 8000 ft just north of the Gray Butte summit.

82-92 1000 ft east and 1400 ft north from SW corner, Sec 22, T42N, R3W, Shasta Quad. Sample collected at 7100 ft.

82-93 2500 ft west and 2500 ft south from NE corner, Sec 21, T42N, R3W, Shasta Quad. Sample collected at 6600 ft.

82-94 200 ft west and 100 ft north from SE corner Sec 16 T42N, R3W, Shasta Quad. Collected at 6300 ft from the top of small flow lobe due north of logging road.

82-98 1200 ft west from SE corner along southern boundary of Sec 9, T41N, R3W, Shasta Quad. Collected at 13800 ft due south of summit.

82-99 1200 ft west and 500 ft south from NE corner, Sec 16, T41N, R3W, Shasta Quad. Sample collected at 13600 ft from SW trending summit ridge.

82-100 2500 ft east and 2600 ft north from SW corner, Sec 16, T41N, R3W, Shasta Quad. Sample collected at 12700 ft.

82-101 2000 ft east and 1800 ft north from SW corner, Sec

16, T41N, R3W, Shasta Quad. Collected at 12000 ft.

82-103 900 ft east and 2200 ft south from NW corner, Sec 21, T41N, R3W, Shasta Quad. Sample collected at 10400 ft from crest of ridge to the east of Avalanche Gulch.

82-104 1900 ft west and 1400 ft south from NE corner, Sec 20, T41N, R3W, Shasta Quad. Collected at 10400 ft.

83-45 900 ft west and 1500 ft south from NE corner, Sec 11, T41N, R3W, Shasta Quad. Collected at 8900 ft.

83-49 2400 ft west and 300 ft north from SE corner, Sec 29, T42N, R3W, Shasta Quad. Collected at 7600 ft from western lip of Bolum Creek stream valley.

83-56 200 ft east and 100 ft south from NW corner, Sec 16, T41N, R3W, Shasta Quad. Sample collected at 12700 ft along western edge of Whitney Glacier.

83-59 1000 ft west and 1900 ft south from NE corner, Sec 19, T41N, R3W, Shasta Quad. Collected at 9200 ft along southern edge of Cascade Gulch.

85-54 1900 ft west and 800 ft south from NE corner, Sec 15, T40N, R3W, Shasta Quad. Collected at 5300 ft just north of road.

85-55 2600 ft south and 100 ft east from NE corner, Sec 2, T40N, R3W, Shasta Quad. Collected at 6800 ft.

85-56 1500 ft west and 1100 ft north from SE corner, Sec 34, T41N, R3W, Shasta Quad. Collected at 7600 ft.

85-57 1400 ft west and 1300 ft north from SE corner, Sec 34, T41N, R3W, Shasta Quad. Collected just above

7600 ft on flat nob.

85-58 1000 ft west and 1300 ft north from SE corner, Sec 34, T41N, R3W, Shasta Quad. Collected approx. 200 ft east of 85-57.

Shastina

82-82 1800 ft east and 1100 ft north from SW corner, Sec 10, T42N, R4W, Weed Quad. Collected at 4300 ft at the eastern side of railroad cut.

83-50 2100 ft east and 300 ft north from SW corner, Sec 32, T42N, R3W, Shasta Quad. Collected at 9000 ft east of Whitney Creek.

83-51 2300 ft south and 100 ft east from NW corner, Sec 5, T41N, R3W, Shasta Quad. Collected at 9300 ft.

83-52 1200 ft west and 1800 ft north from SE corner, Sec 6, T41N, R3W, Shasta Quad. Collected at 9600 ft.

83-53 2700 ft north from SE corner along eastern boundary of Sec 6, T41N, R3W, Shasta Quad. Collected at 9400 ft.

83-57 2500 ft west and 800 ft north from SE corner, Sec 8, T41N, R3W, Shasta Quad. Collected at 11900 ft in saddle between Shasta and Shastina and 600 ft SW of Sisson Lake.

83-58 800 ft east and 2200 ft north from SW corner, Sec 17, T41N, R3W, Shasta Quad. Collected at 10200 ft along the western edge of Cascade Gulch.

Hotlum

82-91 2600 ft south and 100 ft west from NE corner, Sec

24, T42N, R3W, Shasta Quad. Collected at 6400 ft from large flow that parallels Inconstance Creek.

82-96 2600 ft west and 2000 ft north from SE corner, Sec 27, T42N, R3W, Shasta Quad. Collected at 7900 ft.

82-97 1300 ft east and 1100 ft north from SE corner, Sec 9, T41N, R3W, Shasta Quad. Collected at 14160 ft from dome at summit.

83-44 1800 ft east and 1100 ft north from SE corner, Sec 12, T41N, R3W, Shasta Quad. Collected just off crest of ESE trending flow.

83-46 1800 ft east and 400 ft south from NW corner, Sec 11, T41N, R3W, Shasta Quad. Collected at 9600 ft ft N of Brewer Creek.

83-54 1000 ft west and 1400 ft north from SE corner, Sec 9, T41, R3W, Shasta Quad. Collected at 13900 ft NE of summit.

83-55 1100 ft west and 1700 ft north from SE corner, Sec 9, T41N, R3W, Shasta Quad. Collected at 13900 ft approximately 300 ft below summit at headwall of Hotlum Glacier.

McKenzie Butte

85-42 2700 ft west and 1100 ft south from NE corner, Sec 15, T40N, R3W, Shasta Quad. Collected at 5200 ft along western side of road cut.

85-43 2300 ft west and 2300 ft north from SW corner, Sec 15, T40N, R3W, Shasta Quad. Sample collected from northern side of road embankment at 5200 ft.

Whaleback

85-41 2100 ft north and 1500 ft west from SE corner, Sec 13, T43N, R3W, Whaleback. Collected at 5800 ft at northern side of small hill.

Cinder Cone north of Haystack

85-1 500 ft east and 2500 ft north from SW corner, Sec 26, T43N, R4W, Lake Shastina Quad. Collected at 3700 ft from western side of dome NNW of Haystack.

85-34 1300 ft west and 2800 ft north from SE corner, Sec 27, T43N, R4W, Lake Shastina Quad. Collected at 3600 ft from flow on western side of cinder cone.

85-36 300 ft east and 1500 ft south from NW corner, Sec 26, T43N, R4W, Lake Shastina Quad. Collected at 3600 ft from flow on NNE side of cinder cone.

85-37 400 ft west and 2000 ft south from NW corner, Sec 27, T43N, R4W, Lake Shastina Quad. Collected at 3800 ft on eastern side of cinder cone.

85-60 Same location as 85-1.

High Alumina Basalts

85-35 400 ft west and 700 ft south from NE corner, Sec 27, T43N, R4W, Lake Shastina Quad. Collected at 3400 ft north of cinder cone.

85-38 1600 ft east and 2300 ft south from NW corner, Sec 24, T43N, R4W, Lake Shastina Quad. Collected at 3700 ft just north of 99-97 cutoff by caves.

85-39 300 ft west and 1500 ft south from NE corner, Sec 9, T43N, R4W, Lake Shastina Quad. Collected

between 3080 and 3040 ft along northern side of 99-97 cutoff.

85-40 1600 ft east and 1000 ft north from SW corner, Sec 20, T43N, R3W, Whaleback Quad. Collected between 4280 and 4240 ft along south side of Route 97.

85-51 1700 ft west and 900 ft south from NE corner, Sec 24, T41N, R2W, Shasta Quad. Collected at 5000 ft NE of Sugar Pine Butte.

85-52 1800 ft east and 2600 ft north from SE corner, Sec 13, T41N, R2W, Shasta Quad. Collected between 4800 and 4720 ft.

85-53 2100 ft east and 1400 ft south from NW corner, Sec 10, T41N, R2W, Shasta Quad. Collected at 5400 ft just west of dirt road

CHAPTER 3

Calculating Liquid and Solid Compositions Produced by Equilibrium Crystallization and Melting: A Numerical Technique with Applications

INTRODUCTION

This Chapter presents a simple numerical technique for calculating the compositions of liquids and solids produced by equilibrium crystallization and melting. Using the proportions of liquid and solid phases and the bulk chemistry of the system, the algorithm calculates the equilibrium liquid, olivine (oliv), plagioclase (plag), augite (aug) and low-Ca pyroxene (opx) compositions using exchange coefficients (K_Ds), distribution coefficients (Ds), mineral stoichiometries and mass balance equations. Coupled with pseudoternary phase diagrams (e.g. Walker et al., 1979; Grove and Bryan, 1983; Sack et al., 1987) the 1-atmosphere crystallization paths may be calculated for a wide range of basaltic to andesitic melts.

Using this algorithm, we compare the residual liquids produced by equilibrium and fractional crystallization, and determine the point at which these two endmember crystal-liquid processes produce divergent residual liquids for an identical starting composition. Calculations using both a primitive and an evolved mid-ocean ridge basalt show that the resulting liquids do not begin to differ substantially until after 30 to 40% crystallization. These results indicate that numerical techniques based on either perfect equilibrium or fractional crystallization can accurately model the early to middle stages of the natural process.

In addition, we use our model to calculate the compositions of liquids produced by low degrees of partial melting of a depleted mantle peridotite, and to investigate

liquid compositional changes as a function of the residual oliv, opx and cpx proportions. Recent dynamic treatments of mantle partial melting suggest that a variety of liquid compositions may be produced within an ascending mantle diapir (Ahern and Turcotte, 1979; McKenzie, 1984; Klein and Langmuir, 1987). The refractory quartz tholeiites found in some ophiolite sequences (Duncan and Green, 1980; 1987; Cameron, 1985) represent one melt composition proposed as a partial melt from a MORB depleted mantle. We are able to reproduce the estimated parental quartz tholeiite liquids in the Troodos massif by 6% melting of a depleted mantle composition. The final residue is a harzburgite, 84% olivine, 14% orthopyroxene and 2% clinopyroxene.

A critical assumption of the equilibrium model presented here is that Fe-Mg and Ca-Na exchange reactions are approximately independent of temperature and bulk composition. This assumption is widely accepted for olivine-liquid equilibria, and experimental data on natural basaltic to andesitic melts support a similar conclusion for Fe-Mg exchange between augite and liquid over the interval 1250 to 1080°C. Data for Ca-Na partitioning between plagioclase and varying melt compositions suggests a weak temperature effect but a strong bulk compositional effect. We present a preliminary model that describes the changing plagioclase K_D as a function of melt composition. Since exchange coefficients are much less dependent on temperature and liquid composition than are simple distribution coefficients or formation

reactions (e.g. Roeder and Emslie, 1970; Longhi et al., 1978), temperature is not a variable in our model. In contrast, the empirical formulations of Nathan and Van Kirk (1978), Langmuir and Hanson (1981) and Nielsen and Dungan (1983) use expressions of the form,

$$\ln(K) = A/T + B \qquad (1)$$

to describe the partitioning of major elements between crystals and liquid, where K is either a distribution coefficient or a formation reaction for a specific mineral, T is the absolute temperature, and A and B are constants determined by a least-squares fit to a set of experimental data. The regression equations that form the basis of these models provide a means for calculating the temperature at which a given phase becomes saturated, and the changing phase proportions and liquid compositions as crystallization proceeds. However, the data base used to calibrate these models consists almost exclusively of anhydrous one-atmosphere experiments, which limits the application of these models to cases of low-pressure anhydrous crystallization.

The advantage of our method compared to the ln K models is its simplicity. The disadvantage of our method is in the loss of temperature information. Nevertheless, our model can be used to "test" different liquid lines of descent by specifying different sets of equilibrium phase proportions. Coupled with the currently qualitative understanding of how

cotectic phase proportions change as a function of the total pressure (P) and partial pressure of water (pH_2O), our K_D model provides a simple approach for directly observing how changes in phase proportions affect liquid lines of descent.

MODELING EQUILIBRIUM AND FRACTIONAL CRYSTALLIZATION

Equilibrium Crystallization

The starting point for the equilibrium model is the mass balance equation,

$$F(C_\alpha)^{liq} = (C_\alpha)^{bulk} - (1 - F)(C_\alpha)^{xtl} \qquad (2)$$

where $(C_\alpha)^{liq}$, $(C_\alpha)^{xtl}$ and $(C_\alpha)^{bulk}$ are the concentrations of component α in the liquid, crystal and bulk system respectively, and F represents the mass fraction of liquid. Modeling the liquid produced by either equilibrium crystallization or melting of a bulk composition involves two steps. The first step is to calculate the compositions of olivine, plagioclase, augite and low-Ca pyroxene at a specific value of F using eqn (2) and exchange and single-element distribution coefficients. The second step involves calculating the residual liquid by subtracting the composition of each phase weighted by its mass fraction from the bulk composition. The liquid is then normalized to 100%. In the model equations derived below all concentrations are expressed in units of cation mole percent.

Fe-Mg exchange: The model currently handles three iron-magnesium silicates; olivine, augite and low-Ca pyroxene. The Mg/(Mg+Fe) ratios in all three phases are evaluated simultaneously using a single mass balance equation. The equation for the case where olivine is the only Fe-Mg silicate present in the system is developed first.

The cation sum of FeO + MgO in an olivine with the formula $(MgFe)_2SiO_4$ is 66.67 with SiO_2 comprising the remaining 33.33 percent. If X equals the Mg/(Mg+Fe) ratio in olivine in equilibrium with a silicate melt, then the cation mole percents of MgO and FeO in the olivine are 66.67(X) and 66.67(1-X), and the following two expressions describe MgO and FeO mass balance in the bulk system:

$$F[Mg]^{liq} = [Mg]^{bulk} - [X(66.67)](1-F) \qquad (3)$$

$$F[Fe]^{liq} = [Fe]^{bulk} - [(1-X)(66.67)](1-F) \qquad (4)$$

The square brackets in eqns (3) and (4) denote cation mole percents. Computing the ratio between these equations removes F from the left-hand side and gives the following expression,

$$\frac{[Mg]^{liq}}{[Fe]^{liq}} = \frac{[Mg]^{bulk} - [X(66.67)](1-F)}{[Fe]^{bulk} - [(1-X)(66.67)](1-F)} \qquad (5)$$

Rearranging the olivine-liquid Fe-Mg exchange coefficient yields,

$$\frac{[Mg]^{liq}}{[Fe]^{liq}} = \frac{(K_D)^{ol/liq}\ (X)}{(1-X)} \qquad (6)$$

Combining eqns (5) and (6), we derive an expression containing a single unknown, X, which may be written as a quadratic polynomial,

$$AX^2 + BX + C = 0 \qquad (7)$$

where

$$A = (66.67)\{K_D(1 - F) + F - 1\}$$

$$B = K_D[Fe]^{bulk} + [Mg]^{bulk} + (66.67)\{FK_D - K_D - F + 1\}$$

$$C = [Mg]^{bulk}$$

Since the experimentally determined parameter $K_D^{ol/liq}$ is nearly independent of temperature and liquid composition (Roeder and Emslie, 1970; Longhi et al., 1978; Hoover and Irvine, 1978), eqn (7) can be solved for X, given the cation fraction of olivine crystallized, (1-F), and the cation percents of MgO and FeO in the bulk system. X in turn fixes the composition of the equilibrium olivine.

In order to add augite to eqns (3) and (4), we assume that the cation sum of MgO+FeO in the clinopyroxene is constant over a given crystallization interval. We also assume that the cation percent of CaO in the augite is constant. One-atmosphere experimental data suggests that these two

assumptions are not unreasonable, especially for augites co-existing with olivine and plagioclase. Mean and 1σ values for FeO+MgO and CaO (both in cation mole %) from augites produced in melting experiments on ocean floor and high alumina basalts over the temperature interval 1193 to 1137°C are 28.22 ± 0.76 and 19.59 ± 0.76, respectively (Grove et al, 1982; Grove and Bryan 1983; Tormey et al, 1987).

Following the steps outlined for olivine, let $[MF]^{cpx}$ equal the cation sum of MgO and FeO. Thus, MgO and FeO in a given augite will be $(Mg^*)^{cpx}[MF]^{cpx}$ and $(Fe^*)^{cpx}[MF]^{cpx}$, where $(Mg^*)^{cpx}$ equals Mg/(Mg+Fe). Adding these two terms to eqns (3) and (4) yields expressions describing the MgO and FeO mass balance between olivine, augite, liquid and the bulk system.

$$F[Mg]^{liq} = [Mg]^{bulk} - (1-F)\{[X(66.67)(P)^{ol}] + (Mg^*)^{cpx}[MF]^{cpx}(P)^{cpx}\} \quad (8)$$

$$F[Fe]^{liq} = [Fe]^{bulk} - (1-F)\{[(1-X)66.67(P)^{ol}] + (Fe^*)^{cpx}[MF]^{cpx}(P)^{cpx}\} \quad (9)$$

Computing the ratio of these equations and replacing the LHS with the RHS from eqn (6) we have,

$$\frac{X(K_D)^{ol/liq}}{(1-X)} =$$

$$\frac{[Mg]^{bulk}-(1-F)\{[X(66.67)](P)^{ol}+(Mg^*)^{cpx}[MF]^{cpx}(P)^{cpx}\}}{[Fe]^{bulk}-(1-F)\{[(1-X)66.67](P)^{ol}+(Fe^*)^{cpx}[MF]^{cpx}(P)^{cpx}\}} \qquad (10)$$

where $(P)^{ol}$ and $(P)^{cpx}$ are the cation fractions of olivine and augite in the equilibrium assemblage and $\Sigma(P)^{i} = 1$. In order to solve eqn (10), $(Mg^*)^{cpx}$ and $(Fe^*)^{cpx}$ must be defined in terms of x, the Mg-number of the equilibrium olivine. Equating the K_D expressions for olivine and augite through their common quotient, $(Mg^*)^{liq}/(Fe^*)^{liq}$, produces,

$$\frac{(K_D)^{ol/liq}\ (X)}{(1-X)} = \frac{(K_D)^{cpx/liq}\ (Mg^*)^{cpx}}{(1 - Mg^*)^{cpx}} \qquad (11)$$

Manipulating eqn (11) yields $(Mg^*)^{cpx}$ as a function of x, and the two parameters $(K_D)^{ol/liq}$ and $(K_D)^{cpx/liq}$.

$$(Mg^*)^{cpx} = \frac{(K_D)^{ol/liq}\ (X)}{(K_D)^{ol/liq}\ (X) + (K_D)^{cpx/liq}\ (1-X)} \qquad (12)$$

Substituting eqn (12) and its equivalent for $(Fe^*)^{cpx}$ back into eqn (10) produces a cubic polynomial in X. For a given bulk composition, cation liquid fraction and proportions of olivine and augite in the equilibrium assemblage, eqn (10) can be solved for x, which in turn in turn fixes the proportions

of MgO, FeO and SiO_2 in the olivine and the cation abundances of MgO and FeO in the augite.

Ca, Na, Al, Ti and Si are also included in the augite calculation. The cation percents of TiO_2, $AlO_{1.5}$ and $Na_{1.5}O$ in an equilibrium augite are determined using mass balance equations and cation-based distribution coefficients. At present these distribution coefficients are assumed to be constant over the crystallization interval. Experimental augite-liquid data summarized in the next section show these partition coefficients depend on temperature and/or bulk composition, although the variation in the D-values is not extreme in the basalt to andesite range. Future implementations of our equilibrium model will include terms for the compositional dependence of the partition coefficients, e.g. Lesher (1986), and the Ca-content in the pyroxenes, e.g. Longhi (1982). At present, the equations for Ti and Al in augite are derived from eqn (2) and the definition of D.

$$[Ti]^{cpx} = \frac{(D_{Ti})^{cpx}[Ti]^{bulk}}{\{F + (D_{Ti})^{cpx}(P)^{cpx}(1-F)\}} \qquad (13)$$

$$[Al]^{cpx} = \frac{(D_{Al})^{cpx}\{[Al]^{bulk} - [Al]^{pl}(P)^{pl}(1-F)\}}{\{F + (D_{Al})^{cpx}(P)^{cpx}(1-F)\}} \qquad (14)$$

$[Al]^{pl}$ is fixed by the stoichiometry and Ca/(Ca+Na) ratio of the equilibrium plagioclase. The expression for $[Na]^{cpx}$ is developed in the section on Ca-Na exchange. After calculating Ti, Al and Na abundances, the cation % of SiO_2 in the augite is determined by difference, i.e. 100 - sum of all other cations, which ensures a stoichiometric phase.

Adding a low-Ca pyroxene to eqn (10) follows the same procedure as developed for augite. The resulting equation is a fourth order polynomial in X. However, since solutions of geologic interest lie in the interval $0 \leq X \leq 1$, the polynomial is most easily solved by bracketing and bisection methods (e.g. Press et al., 1986). These techniques do not require calculating derivatives.

Ca-Na Exchange: $Ca_yNa_{1-y}Al_{1+y}Si_{3-y}O_8$, describes plagioclase compositions that lie along the join Anorthite - Albite, where y equals the ratio Ca/(Ca+Na). For this stoichiometry, the cation mole percents of calcium and sodium are 20(y) and 20(1-y), respectively. If plagioclase and augite are the only Ca- and Na-bearing phases that are crystallizing, then the following two expressions describe the mass balance for CaO and $Na_{1.5}O$ in the bulk system,

$$F[Ca]^{liq} = [Ca]^{bulk} - (1-F)\{[20y](P)^{pl} + [Ca]^{cpx}(P)^{cpx}\} \quad (15)$$

$$F[Na]^{liq} = [Na]^{bulk} - (1-F)\{[20(1-y)](P)^{pl} + [Na]^{cpx}(P)^{cpx}\} \quad (16)$$

Again, [Ca] and [Na] are the cation mole percents of Ca and Na in liquid, augite and the bulk system, respectively, and $(P)^{pl}$ and $(P)^{cpx}$ are the fractions of plagioclase and augite in the crystallized assemblage. Using the Ca-Na exchange reaction between plagioclase and liquid $K_D=(y/(1-y))^{pl}/([Ca]/[Na])^{liq}$, we may compute the ratio of eqns (15) and (16) to produce a expression which will be quadratic in y, the Ca/(Ca+Na) ratio in the equilibrium plagioclase.

$$\frac{y}{(1-F)K_D} = \frac{[Ca]^{bulk}-(1-F)\{[20y](P)^{pl}+[Ca]^{cpx}(P)^{cpx}\}}{[Na]^{bulk}-(1-F)\{[(1-y)20](P)^{pl}+[Na]^{cpx}(P)^{cpx}\}} \quad (17)$$

$[Ca]^{cpx}$ is a constant in eqn (17), while $[Na]^{cpx}$ is a function of the unknown liquid composition. The functional relationship between $[Na]^{cpx}$ and y is given by,

$$[Na]^{cpx} = \frac{(D_{Na})^{cpx}\{[Na]^{bulk}-(1-F)(P)^{pl}(1-y)20\}}{\{F+(D_{Na})^{cpx}(P)^{cpx}(1-F)\}} \quad (18)$$

Substituting (18) into eqn (17) produces an algebraic expression which may also be solved by bracketing and bisection.

After calculating the equilibrium compositions of olivine, plagioclase, augite and low-Ca pyroxene, the liquid

composition is determined by subtracting from the bulk system a sum for each oxide given by the cation % of the oxide in the each phase times its respective mass fractions, multiplied the total fraction of solids, (1-F). The resulting liquid is normalized to 100%, and may at this point be converted to oxide wt.%.

Fractional Crystallization

The fractional crystallization calculation models the process as one of compositional zoning overgrowth (Bowen, 1928; p. 74). The basic procedure has been discussed by Grove and Baker (1984) and Grove and Donnelly-Nolan (1986) and will be briefly reviewed here. As in the case of the equilibrium model, all calculations are carried out in units of cation mole percent. Olivine, plagioclase and augite are removed as $(Mg,Fe)_2SiO_4$, $Ca_yNa_{1-y}Al_{1+y}Si_{3-y}O_8$ and $(Ca,Na,Al,Fe^{+2},Mg,Ti,Si)_4O_6$, respectively. The composition of the starting liquid and the appropriate K_D expressions are used to calculate the compositions of the olivine, plagioclase, and the Fe and Mg contents in the augite. The cation sum of MgO and FeO in the augite is held constant as is the CaO value. Augite-liquid distribution coefficients are used to calculate the cation abundances of Ti, Al and Na in the pyroxene. The percent of SiO_2 in the augite is determined by difference. Fractionation is carried out by subtracting the amount given by the sum for all phases of the cation mole % in each phase multiplied by the fraction of each phase multiplied

by 0.01 for each cation. The resulting residual liquid is normalized to 100%. For each new liquid, the Fe-Mg and Ca-Na exchange K_Ds and pyroxene Ti, Al and Na distribution coefficients are used to calculate new equilibrium phase compositions.

In contrast to the case of equilibrium crystallization, fractional crystallization results in two compositional parameters for each phase, the instantaneous and cumulative phase compositions. The instantaneous composition is in equilibrium with liquid at each increment of crystallization, while the cumulative composition represents the phase's integrated compositional profile for a given interval of crystallization. As long as the proportion of the phase in the crystallizing assemblage is constant over the interval of interest, the phase's cumulative composition is calculated by summing its composition at each increment within the interval and dividing by the number of increments. If the proportion of the phase changes within the interval, the cumulative composition is calculated by combining the average compositions from above and below the point of change, normalized to the mass fraction of the phase crystallized within each sub-interval.

Olivine, Augite and Plagioclase Exchange and Distribution Coefficients

Both the equilibrium and the fractional crystallization calculations assume that Fe-Mg K_Ds for olivine and augite and

the Ca-Na K_D for plagioclase are constant over a specific crystallization interval. The minor element contents in augite are also modeled assuming constant distribution coefficients.

Numerous studies at 1-atmosphere have shown that the Fe^{+2}-Mg exchange coefficient for olivine is nearly independent of temperature and liquid composition, and is equal to 0.30 ± 0.03 (e.g. Roeder and Emslie, 1970; Longhi et al., 1978; Sack et al., 1987). The mean of 64 $(K_D)^{ol/liq}$ values from olivine tholeiites to ferro-basalts and basaltic andesites is 0.29 ± 0.01 (Grove and Bryan, 1983; Tormey et al., 1987; Juster and Grove, 1988; data from Chapter 2). K_Ds were calculated with all Fe as FeO and cover the temperature interval between 1252 and 1100°C.

Fe-Mg partitioning between augite and natural basaltic and andesitic melts is summarized in Fig. 3-1a. Liquid compositions ranged from terrestrial and lunar basalts (Grove and Bryan, 1983; Tormey et al, 1987; Juster and Grove, 1988; Biggar et al., 1971; Ho, 1973; O'Hara et al., 1974; Lindstrom, 1976; Walker et al., 1976) to low silica andesites (Chapter 2). The mean for the 62 augite-liquid pairs is 0.23 ± 0.02. The data suggest that K_D decreases slightly with decreasing temperature, from ~0.24 at 1200°C to ~0.21 at 1100°C. Given the large compositional differences between the terrestrial and lunar samples, the limited variability displayed by the K_D values suggests that augite and liquid Fe-Mg exchange is relatively insensitve to liquid composition in the range basalt to andesite.

Augite-liquid distribution coefficients for TiO_2 and $AlO_{1.5}$ determined on terrestrial starting compositions are plotted as a function of run temperature in Figs. 3-1b,c. D_{Ti} shows a modest temperature effect, decreasing from ~ 0.29 at ~1200°C to ~0.21 at 1100°C. D_{Al} shows appreciable scatter in Fig. 3-1c and no clear temperature dependence. Calculated D_{Na} values are even more variable. Some of this variability may reflect disequilibrium and/or analytical error. For the equilibrium crystallization calculations presented in this paper, we have averaged the data for each partition coefficient. These mean values are 0.26 ± 0.05 D_{Ti}, 0.19 ± 0.04 D_{Al} and 0.09 ± 0.03 D_{Na}.

Ca-Na exchange reactions for plagioclase-liquid vary as a function of temperature (Drake, 1976). However, recent experimental data has shown that much of the observed temperature variation in minor and trace element distribution coefficients can be related to changes in melt composition, and by inference, melt structure (e.g. Watson, 1977; Hart and Davis, 1978; Lesher, 1986). Fig. 3-2a shows plagioclase K_Ds calculated from experiments over the same temperature interval on basaltic to andesitic liquids. At a constant temperature, K_D increases with increasing silica content, varying from ~0.9 for the ferro-basaltic compositions to ~1.9 for the andesitic liquids. Fig. 3-2b shows calculated plagioclase K_Ds plotted against the mole percent of network-forming melt species, NF (Bottinga and Weill, 1972; data sources are given in the figure caption and include the experiments in Chapter 2). Also

shown are the exchange coefficients calculated from the 1250 and 1300°C experiments of Murphy (1977) in the system Di-An-Ab. The above data indicate that, under anhydrous 1-atm conditions, plagioclase K_D increases monotonically with increasing melt polymerization in both simple and natural systems. The implications of these results for melt structure will be discussed elsewhere (Baker and Grove, in prep.). Close examination of the limited data suggests a weak temperature dependence. Since most basaltic liquids are ~ 70% network-forming components, the plagioclase K_D will be ~1 for these compositions under low pressure anhydrous conditions. Due to the scatter at ~ 70% network-formers and the small number of compositions included in the present data set, we have not incorporated a function for $(K_D)^{pl/liq}$ into the equilibrium or fractional crystallization models, although such a relationship would be easy to include. However, as we will show in the following section, the mole fraction of network-forming species in a basaltic liquid does not increase during low pressure cotectic crystallization of olivine + plagioclase ± augite. Thus, until the appearance of an Fe-Ti oxide phase, the plagioclase K_D should remain relatively constant.

APPLICATIONS

Low Pressure Equilibrium vs Fractional Crystallization

In order to compare liquid compositions produced by equilibrium and fractional crystallization as a function of F, we have chosen two mid-ocean ridge basalts, 418A-52-5

(Staudigel and Bryan, 1981) (???) and AII78-3-102 (Grove and Bryan (1983). Bulk compositions are given in Table 3-1, along with the K_Ds, Ds and pryoxene parameters used in both calculations. We compare liquid compositions produced by both processes along their respective liquid lines of descent in Figs. 3-3 and 3-4. Liquid compositions calculated at F-values of 0.9 to 0.5 are given in Tables 3-2 and 3-3.

The liquid lines of descent for the two bulk compositions were calculated in the following manner. Olivine and plagioclase are the sole phenocryst phases in the more evolved 418A-52-5 and were removed in the proportion 34:66. Plagioclase joins olivine ~5°C below the liquidus in the more primitive AII78-3-102 (Tormey et al, 1987), however, for this calculation both phases were assumed to appear simultaneously and were removed in the proportions 35:65. These phase proportions are consistent with the results of 1-atmosphere melting experiments on both compositions (Grove and Bryan, 1983; Tormey et al., 1987). In principal, experimentally produced equilibrium liquids may be compared to the calculated fractional liquid lines of descent, however Na_2O loss during the course of 1-atmosphere experiments produces an enrichment in normative quartz which makes direct comparison difficult. The Fe-Mg K_Ds used for olivine and augite were 0.29 and 0.23, respectively. The average values for the augite-liquid Ti, Al and Na distribution coefficients were 0.26, 0.19 and 0.09 (Table 3-1). The Ca-Na exchange coefficient used to model plagioclase crystallization was 1.1, a value consistent with

K_Ds calculated from 1-atm experiments on these compositions (Grove and Bryan, 1983; Tormey et al., 1987).

The point at which augite joined the crystallizing assemblage for each bulk composition was determined by plotting the residual liquids from varying degrees of equilibrium and fractional crystallizaion on the Oliv-Cpx-Qtz and Oliv-Plag-Qtz pseudoternaries (Walker et al., 1979; Grove et al., 1982; Grove and Bryan, 1983), and noting when the compositions crossed the oliv+plag+augite cotectic. Crystallization of olivine, plagioclase and augite in the proportions 11.5:50.3:38.2 constrained 418A-52-5 residual liquids to remain on the cotectic in both the Oliv-Cpx-Qtz and Oliv-Plag-Qtz projections. Cotectic proportions for AII78-3-102 were 11.3:50.8:37.9. Augite appears after 7% crystallization of 418A-52-5, compared to ~46% crystallization in the case of AII78-3-102. Calculations were carried out to F=0.5 for both starting liquids.

Figs. 3-3 and 3-4 compare equilibrium and fractional liquids at F-values of 0.8, 0.6 and 0.5 for both starting compositions. FeO, MgO, CaO and Na_2O show the greatest fractionation between the two processes. FeO and Na_2O are enriched while MgO and CaO are depleted in liquids produced by fractional compared to equilibrium crystallization. However, the Equil/Fract ratios for FeO, MgO and Na_2O have not substantially diverged from 1.0 until F-values of 0.7 to 0.6. The ratio for Al_2O_3 remains close to 1.0 until F=0.6; for SiO_2 the ratio remains close to 1.0 even after 50% crystallization.

These results are consistent with Langmuir and Hanson (1981), who noted that approximately 30% equilibrium and fractional crystallization of olivine and plagioclase from a mid-ocean ridge basalt produced similar residual liquids.

We generalize these results with the aid of Fig. 3-5 which shows the ratio $(C_l)^{eq}/(C_l)^{fr}$ as a function of liquid fraction remaining for different bulk distribution coefficients. $(C_l)^{eq}$ and $(C_l)^{fr}$ are the normalized concentrations (C_o=1) calculated with the standard equilibrium and fractional crystallization equations (e.g. Allegre and Minster, 1978; Haskin, 1983). As F varies from 1.0 to 0.4, $(C_l)^{eq}/(C_l)^{fr}$ remains less 1.2 for bulk cation distribution coefficients between 1 and 2. Table 3-4 summarizes the range of cation-based bulk distribution coefficients ($D^* = \Sigma X_i D_i$) calculated along the equilibrium and fractional liquid lines of descent for both starting compositions. Each element displays a restricted range of values, e.g. $(D_{Mg})^*$ for both compositions is between 1.47 and 1.78. Thus if two liquids are related by less than 40 to 50% cotectic crystallization (e.g. oliv+plag+aug) either a mass balance or a Rayleigh fractionation model should adequately match the data.

Fig. 3-6 shows fractional liquid lines of descent for the two MORB compositions in mole % NF vs liquid Mg# space. For both compositions the decrease in mole percent of network-forming species during low pressure crystallization, correlates with the steadily dropping Al_2O_3 content in each liquid. The drop in Al_2O_3 is a function of the abundant

plagioclase that crystallizes from both basalts. The small change in mole % NF suggests that under anhydrous low pressure conditions the plagioclase K_D should remain relatively constant over the initial crystallization interval for most basalts.

Figs. 3-7a,b and 3-8a,b show the Fo and An contents produced by equilibrium and fractional crystallization of the two MORB samples plotted against F. Both cumulative and instantaneous olivine and plagioclase compositions are shown for fractional crystallization. The cumulative compositions plotted in Figures 3-7 and 3-8 are calculated from F=1.0 to each respective F-value; for example, a cumulative olivine composition at F=0.5 represents the average olivine composition produced during crystallization over the interval F=1.0 to 0.5.

For both starting compositions, the instantaneous fractional Fo and An contents do not begin to deviate from the bulk equilibrium values until 0.7 to 0.6. With further crystallization the instantaneous olivine and plagioclase compositions become increasingly more Fa- and Ab-rich compared to the equilibrium phase compositions. This observation is consistent with the differences observed between instantaneous and bulk equilibrium plagioclase compositions determined graphically in the simple system Di-An-Ab (Morse, 1980), and reflects the steadily increasing differences in Fe/Mg and Na/Ca ratios produced in liquids by fractional vs. equilibrium crystallization. In constrast, the cumulative olivine and

plagioclase compositions are always more Fo- and An-rich than the bulk equilibrium phase compositions at the same degree of crystallization (Figs. 3-7 and 3-8). It is this difference between the cumulative fractional composition and the bulk equilibrium crystal composition that drives residual liquids produced by fractional crystallization to higher FeO and Na_2O contents compared to equilibrium liquids at the same value of F. Morse (1980; p.103-110) has demonstrated the same principle in the system Di-An-Ab. Starting with a plagioclase saturated liquid in this simple system geometrical constructions show that the mean plagioclase composition produced by fractional crystallization must be more An-rich than the plagioclase produced by equilibrium crystallization. This in turn means that the fractional liquid must be more Ab-rich.

Crystallization in Hawaiian Lava Lakes

An analysis of olivine, pyroxene and plagioclase zoning trends in Hawaiian lava lakes suggests that both bulk and surface equilibrium processes will control differentiation trends in small magmatic systems (Moore and Evans, 1967; Evans and Moore, 1968; Helz, 1987a,b). For example, olivine in the Kilauea Iki lava lake appears to re-equilibrate with liquid during solidification, indicating a close approach to bulk equilibrium over a temperature interval of 1180 to 1050°C (Helz, 1987a,b). In contrast to olivine, plagioclase grains are zoned on the order of 10 to 20 mole % An (Helz, 1987a). The slow rate of coupled CaAl-NaSi diffusion in plagioclase

(Grove et al., 1984) indicates that crystals should retain any zoning produced during solidification. Pyroxenes exhibit compositional variability intermediate between olivine and plagioclase (Helz, 1987a).

The zoning trends discussed above suggest that hypabyssal fractionation of olivine, plagioclase and augite is best approximated by bulk equilibrium crystallization for olivine and Rayleigh fractionation for plagioclase and augite. However, the Al_2O_3, CaO and Na_2O contents in low pressure residual liquids are not very sensitive to the crystallization process along the oliv-aug-plag cotectic. Only MgO and FeO display $(C_l)^{eq}/(C_l)^{fr}$ ratios that substantially differ from 1.0. Since the MgO and FeO contents in a liquid on the 3-phase cotectic will be largely controlled by olivine, a differentiation scheme that involves equilibrium olivine and fractional plagioclase and augite crystallization may be modeled by assuming a bulk equilibrium process for all three phases. We have tested this assumption using the bulk composition, glass chemistry and modal proportions from a Kilauea Iki lava lake core sample reported by Helz and Thornber (1987) and Helz (1987a). The quenched basalt is saturated with olivine, plagioclase and augite and contains ~40 wt.% glass (Helz and Thornber, 1987). The calculated glass composition at a cation liquid fraction of 0.39 is strikingly close to the observed composition (Fig. 3-9), and with the exception of K_2O, all differences are less than 5%. The deviations in the ratio of calculated to observed oxide

percents are consistent with the fractional crystallization of augite and plagioclase (see Figs. 3-3 and 3-4). The (Calc/Obs) values are also much smaller than those expected if the observed glass was the product of fractional crystallization. The K_2O content in the calculated glass is much higher than in the observed glass, 1.04 to 1.24 wt.%. This discrepency is a result of the low bulk distribution coefficient for K_2O in our model, $(D_K)^*=0.0$. Using the phase proportions and potassium distribution coefficients (Henderson, 1982), a more realistic $(D_K)^*$ value is 0.1, which lowers the calculated K_2O content in the glass to 1.11 % and the (Calc/Obs) ratio from 1.2 to 1.1 (Fig. 3-9).

Modeling Low Degrees of Equilibrium Melting

The equilibrium model may also be used to calculate the compositions of liquids produced by batch melting. A specific liquid may be calculated for a given bulk composition and melt percentage if the proportions of phases in the residual solid assemblage are known. However, even when the residual phase proportions are not known the model can be used to calculate a range of permissible liquids at a specific value of F. The fundamental constraint is that all of the oxide values for the calculated liquid must be positive. As an example of this approach we will calculate equilibrium liquids produced by 6% melting within the plagioclase lherzolite field of a depleted mantle peridotite. In particular, we will model the major element chemistry of a parental magnesian quartz tholeiite

from the Troodos ophiolite (Duncan and Green, 1987). This composition is inferred to represent relatively low pressure partial melts from a mantle source which has been depleted by extraction of a parental MORB liquid (Smewing et al., 1975; Kay and Senechal, 1976; Duncan and Green, 1980; Cameron, 1985; Duncan and Green, 1987). The depleted mantle composition is given in Table 3-5, and represents a sample of the Ronda peridotite (Frey et al, 1985; Table 3-2). The exchange and distribution coefficients for clinopyroxene and orthopyroxene are also listed in Table 3-5 and are based on the the data compiled in Chapter 4. Since residual phase proportions at low degrees of melting are not well known for natural peridotites, our approach is to define the region in the oliv - opx - cpx space where all the oxides in the calculated liquid have positive values. If the bulk composition is capable of producing a liquid similar to the magnesian quartz tholeiites, the proportions of residual oliv, opx and cpx must lie within this region. Phase fractions of .84 oliv, .14 opx and .02 cpx at 6% melt produced a liquid which is quite similar to the parent composition given in Table 3-5. The calculated and observed composition are compared in Fig. 3-10. Differences are generally between 0.98 and 1.06; TiO_2 and K_2O in the calculated melt composition are low relative to the average parental liquid. A minor increase in the Ti and K abundances in the bulk mantle or a decrease in the percentage of melting would improve the fit for these two elements. Al_2O_3 in the calculated composition is high relative to the observed

liquid; a small amount of spinel in the residual assemblage would correct this error. Our calculated harburgite residue is consistent with moderate pressure phase equilibria for a similar quartz tholeiite composition (Duncan and Green, 1987). Estimated melting percentages for the magnesian quartz tholeiites are ~10% (Duncan and Green, 1987) which is close to our F-value of 0.06. Partial melting calculations using the bulk mantle given in Table 3-5 indicate that it becomes very difficult to generate a liquid with greater than 52% SiO_2 and 10% MgO at liquid fractions greater than 0.10. The problem reflects the rapid decrease in the leverage that olivine exerts on the silica content in the melt relative to the MgO content as the fraction of liquid increases. At low melt percentages, increasing the mass of residual olivine, increases SiO_2 and decreases MgO in the liquid by roughly equivalent amounts. At higher liquid fractions (e.g. >0.10), increasing the mass of residual olivine produces a moderate increase in SiO_2 in the liquid, but a substantial decrease in MgO. We believe that 10% represents an upper limit on the degree of melting capable of producing magnesian quartz tholeiites from a strongly depleted mantle.

The phase proportions necessary to model the observed liquid composition in the above example were determined by trial and error. However, if F is held constant, the equilibrium melting equations are linear with respect to the cation phase fractions. Thus, the equilibrium melting problem could be solved by linear programing techniques. Future work

will involve implementing a least-squares approach for modeling specific liquid compositions.

CONCLUSIONS

In this Chapter we develop a simple algorithm for calculating liquid and solid phase compositions produced by equilibrium crystallization and present several applications. A review of experimental data on Fe-Mg exhange for augite and liquid shows that the K_D is fairly independent of temperature and liquid composition. We also demonstrate a functional relationship between plagioclase K_D and the percentage of network-forming melt species.

A comparison between equilibrium and fractional liquid lines of descent shows that residual liquid compositions remain similar down to F ~0.6 to 0.7. Our equilibrium model also provides a technique for calculating the compositions of partial melts for different bulk systems. We successfully model the magnesian quartz tholeiites found in the Troodos ophiolite by 6% melting of a strongly depleted mantle. The calculated harzburgite residue is consistent with moderate pressure phase relations for these lavas.

REFERENCES

Ahern, J.L. and Turcotte, D.L. (1979) Magma migration beneath an ocean ridge. Earth Planet. Sci. Lett. 45, 114-122.

Allegre, C.J. and Minster, J.F. (1978) Quantitative models of trace element behavior in magmatic processes. Earth Planet. Sci. Lett. 38, 1-25.

Bigger, G.M., O'Hara, M.J., Peckett, A. and Humphries, D.J. (1971) Lunar lavas and the achondrites: petrogenesis of protohyperthene basalts in the maria lavas lakes. Proc. Lunar Sci. Conf. 2, 617-643.

Bottinga, Y. and Weill, D.F. (1972) The viscosity of magmatic silicate liquids: a model for calculation. Am. J. Sci. 272, 438-475.

Bowen, N.L. (1928) The Evolution of the Igneous Rocks. Reprinted, Dover Publications, Inc., 251 pp.

Cameron, W.E. (1985) Petrology and origin of primitive lavas from the Troodos ophiolite, Cyprus. Contrib. Mineral. Petrol. 89, 239-255.

Drake, M. (1976) Plagioclase-melt equilibria. Geochim Cosmochim. Acta 40, 457-466.

Duncan, R.A. and Green, D.H. (1980) The role of multi-stage melting in the formation of the oceanic crust. Geology 8, 22-26.

Duncan, R.A. and Green, D.H. (1987) The genesis of refractory melts in the formation of the oceanic crust. Contrib. Mineral. Petrol. 96, 326-342.

Evans, B.W. and Moore, J.G. (1968) Mineralogy as a function of depth in the prehistoric Makaopuhi tholeiitic lava lake, Hawaii. Contrib. Mineral. Petrol. 17, 85-115.

Frey, F.A., Suen, C.J. and Stockman, H.W. (1985) The Ronda high temperature peridotite: Geochemistry and petrogenesis. Geochim. Cosmochim. Acta 49, 2469-2491.

Grove, T.L and Baker, M.B. (1984) Phase equilibrium controls on the tholeiitic versus calc-alkaline differentiation trends. Jour. Geophys. Res. 89, 3253-3274.

Grove, T.L and Bryan, W.B. (1983) Fractionation of pyroxene-phyric MORBs at low pressure: an experimental study. Contrib. Mineral. Petrol. 84, 293-309.

Grove, T.L. and Donnelly-Nolan, J.M. (1986) The evolution of young silicic lavas at Medicine Lake volcano, California: Implications for the origins of compositional gaps in calc-alkaline series lavas. Contrib. Mineral. Petrol. 92, 281-302.

Grove, T.L., Baker, M.B. and Kinzler, R.J. (1984) Coupled CaAl-NaSi diffusion in plagioclase feldspar: Experiments and applications to cooling rate speedometry. Geochim. Cosmochim. Acta 48, 2113-2121.

Grove, T.L., Gerlach, D.C. and Sando, T.W. (1982) Origin of calc-alkaline series lavas at Medicine Lake volcano by fractionation, assimilation and mixing. Contrib. Mineral. Petrol. 80, 160-182.

Hart, S.R. and Davis, K.E. (1978) Nickel partitioning between olivine and silicate melt. Earth Planet. Sci. Lett. 40, 203-219.

Haskin, L.A. (1984) Petrogenetic modelling - use of rare erth elements. In Rare Earth Element Geochemistry - Developments in Geochemistry, 2. ed. Henderson, P., Elsevier Sci. Pub., 510 pp.

Helz, R. (1987b) Diverse olivine types in lavas of the 1959 eruption of Kilaeua volcano and their bearing on eruption dynamics. In U.S. Geological Survey Professional Paper 1350, Volcanism in Hawaii, vol.I, ed. Decker, R.W., Wright, T.L. and Stauffer, P.H., 839 pp.

Helz, R.T. (1987a) Differentiation behavior of Kilauea Iki lava lake, Kilauea Volcano, Hawaii: An overview of past and current work. In Magmatic Processes: Physicochemical Principles, ed. B.O. Mysen, The Geochemical Society, 500 pp.

Helz, R.T. and Thornber, C.R. (1987) Geothermometry of Kilauea Iki lava lake, Hawaii. Bull. Volcanol. 49, 651-668.

Henderson, P. (1982) "Inorganic Geochemistry" Pergomon Press, 353 pp.

Ho, C.O. (1973) Experimental study of plagioclase/liquid and clinopyroxene/liquid distribution coefficients for Sr and Eu in oceanic ridge basalt system. Master's Thesis, Lamont-Doherty Geological Observatory, Columbia University.

Hoover, J.D. and Irvine, T.N. (1978) Liquidus relations and Mg-Fe partitioning on part of the system Mg_2SiO_4 - Fe_2SiO_4 - $CaMgSi_2O6$ - $CaFeSi_2O_6$ - $KAlSi_3O_8$ - SiO_2. Carnegie Inst. Washington Year Book 77, 774-783.

Huebner, J.S and Turnock, A.C. (1980) The melting relations at 1 bar of pyroxenes composed largely of Ca-, Mg- and Fe-bearing components. Amer. Mineral. 65, 255-271.

Juster, T. and Grove, T.L. (1988) Experimental constraints on the generation of Fe-Ti basalts, andesites and rhyodacites at the Galapagos Spreading Center, 85°W and 95°N. Jour. Geophys. Res., submitted.

Kay, R.W. and Senechal, R.G. (1976) The rare earth geochemistry of the Troodos ophiolite complex. J. Geophys. Res. 81, 964-970.

Klein, E.M. and Langmuir, C.H. (1987) Global correlations of ocean ridge basalt chemistry with axial depth and crustal thickness. Jour. Geophys. Res. 92, 8089-8115.

Langmuir, C.H. and Hanson, G.N. (1981) Calculating mineral-melt equilibria with stoichiometry, mass balance and single-component distribution coefficients. In Thermodynamics of Minerals and Melts, ed. R.C. Newton, A. Navrotsky, B.J. Wood. Springer-Verlag, 304 pp.

Lesher, C.E. (1986) Effects of silicate liquid composition on mineral-liquid element partitioning from Soret diffusion studies. J. Geophys. Res. 91, 6123-6141.

Lindstrom, D.J. (1976) Experimental study of the partitioning of the transition metals between clinopyroxene and co-

existing silicate liquids. Ph.D. Thesis, University of Oregon.

Longhi, J. (1982) Effects of fractional crystallization and cumulus processes on mineral composition trends of some lunar and terrestrial rock series. Proc. Lunar Planet. Sci. Conf. 13th, A54-A64.

Longhi, J., Walker, D. and Hays, J.F. (1978) Fe and Mg distribution between olivine and lunar basaltic liquids. Geochim. Cosmochim. Acta 42, 1545-1558.

McKenzie, D.P. (1984) The generation and compaction of partially molten rock. J. Petrol. 25, 713-765.

Moore, J.G. and Evans, B.W. (1967) The role of olivine in the crystallization of the prehistoric Makaopuhi lava lake, Hawaii. Contrib. Mineral. Petrol. 15, 202-223.

Morse, S.A. (1980) Basalts and Phase Diagrams: An Introduction to the Quantitative Use of Phase Diagrams in Igneous Petrology. Springer-Verlag, 493 pp.

Murphy, W.M. (1977) An experimental study of solid-liquid equilibria in the albite-anorthite-diopside system. M.S. Thesis, University of Oregon.

Nathan, H.D. and Van Kirk, C.K. (1978) A model of magmatic crystallization. J. Petrol. 19, 66-94.

Nielson, R.L. and Dungan, M.A. (1983) Low pressure mineral-melt equilibria in natural anhydrous mafic systems. Contrib. Mineral. Petrol. 84, 310-326.

O'Hara, M.J., Biggar, G.M., Hill, P.G., Jefferies, B. and Humphries, D.G. (1974) Plagioclase saturation in lunar

high titanium basalts. Earth Planet. Sci Lett. 21, 253-264.

Press, W.H, Flannery, B.P., Teukolsky, S.A. and Vetterling, W.T. (1986) "Numerical Recipes: The Art of Scientific Computing." Cambridge University Press, 818 pp.

Roeder, P.L. and Emslie, R.F. (1970) Olivine-liquid equilibrium. Contrib. Mineral. Petrol. 29, 275-289.

Sack, R.O.,Walker, D. and Carmichael, I.S.E. (1987) Experimental petrology of alkalic lavas: constraints on cotectics of multiple saturation in natural basaltic liquids. Contrib. Mineral. Petrol. 96, 1-23.

Smewing, J.D., Simonian, K.O. and Gass, I.G. (1975) Metabasalts from the Troodos Massif, Cyprus: genetic implications deduced from petrography and trace element geochemistry. Contrib. Mineral. Petrol. 51, 49-64.

Staudigel, H and Bryan, W.B. (1981) Constrasting glass-whole rock compositions and phenocryst redistribution, IPOD sites 417 and 418. Contrib. Mineral. Petrol. 78, 255-262.

Tormey, D.R., Grove, T.L. and Bryan, W.B. (1987) Experimental petrology of normal MORB near the Kane Fracture Zone: 22°-25°N, mid Atlantic ridge. Contrib. Mineral. Petrol. 96, 121-139.

Walker. D., Shibata, T. and Delong, S.E. (1979) Abyssal tholeittes from the oceanographer fracture zone. II. Phase equilibria and mixing. Contrib. Mineral. Petrol. 70, 111-1125.

Walker, D., Kirkpatrick, R.J., Longhi, J. and Hays, J.F. (1976) Crystallization history of lunar picritic basalt sample 1002: phase equilibria and cooling rate studies. Geol. Soc. Am. Bull. 87, 646-656.

Watson, E.B. (1977) Partitioning of manganese between forsterite and silicate liquid. Geochim. Cosmochim. Acta 41, 1363-1374.

Figure 3-1. (a) Augite-liquid Fe-Mg exchange coefficients vs. temperature (°C). K_D = $(Fe/Mg)^{aug}/(Fe/Mg)^{liq}$, molar, calculated with all Fe as FeO. (b) Augite-liquid distribution coefficient for Ti calculated on a cation basis plotted against run temperature. (c) D_{Al} for augite-liquid vs run temperature. Data from experiments on tholeiitic basalts, ferro-basalts and basaltic andesites (Ho, 1973; Lindstrom, 1976; Grove and Bryan, 1983; Tormey et al., 1987; Juster and Grove, 1988; Chapter 2).

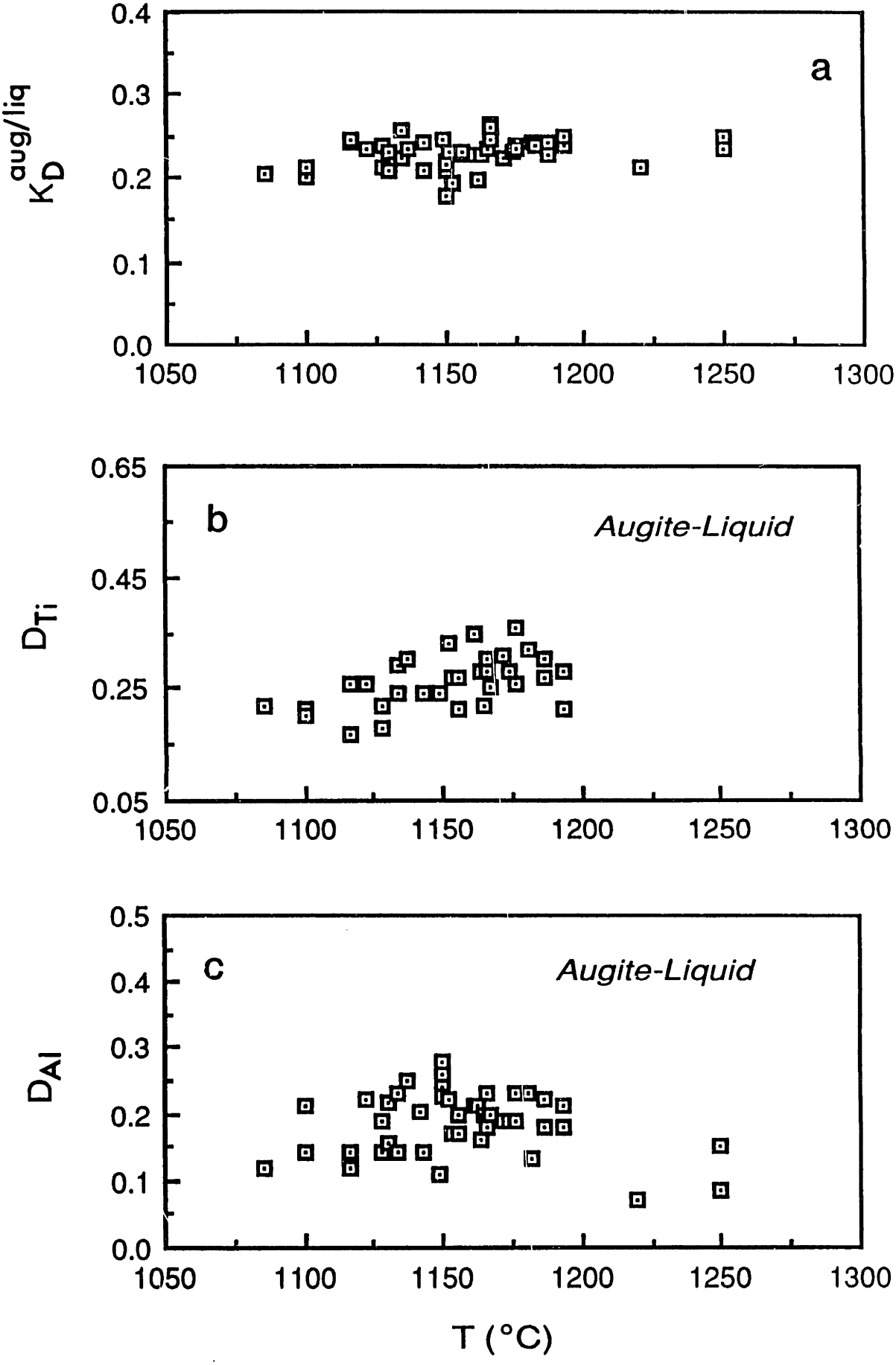
a
b
Augite-Liquid
c
Augite-Liquid
$K_D^{aug/liq}$
D_{Ti}
D_{Al}
T (°C)
0.0
0.1
0.2
0.3
0.4
0.05
0.25
0.45
0.65
0.5
1050
1100
1150
1200
1250
1300

Figure 3-2. (a) Calculated plagioclase K_Ds vs run temperature for three different compositional groups. Data from Juster and Grove (1987); Grove (unpublished data); Chapter 2. $K_D = (Ca/Na)^{pl}/(Ca/Na)^{liq}$, molar. B-Andesite = basaltic andesite. (b) Plagioclase K_D vs mole% of network-forming species in the melt. NF = 100(NF/(NF+NM), where NF = (Si+Al) and NM = Ca+Mg+Mn+Fe +Ti-0.5(Al-Na-K); all concentrations in cation mole fractions. Data from Grove and Bryan (1983), Tormey et al. (1987) and references in Fig. 3-3a. Curve labelled Di-An-Ab represents K_Ds calculated from the 1250 and 1300°C experiments of Murphy, (1977)

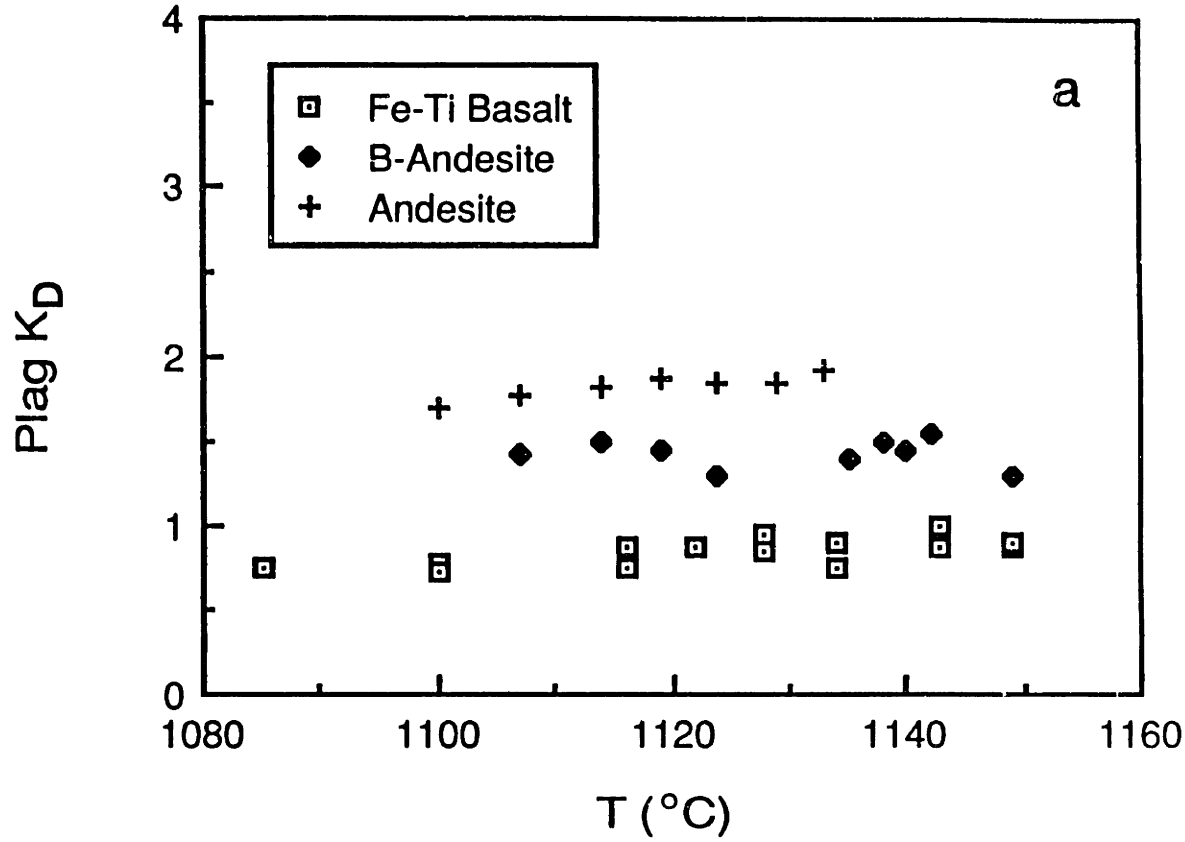
a
Fe-Ti Basalt
B-Andesite
Andesite
Plag K_D
T (°C)
0
1
2
3
4
1080
1100
1120
1140
1160

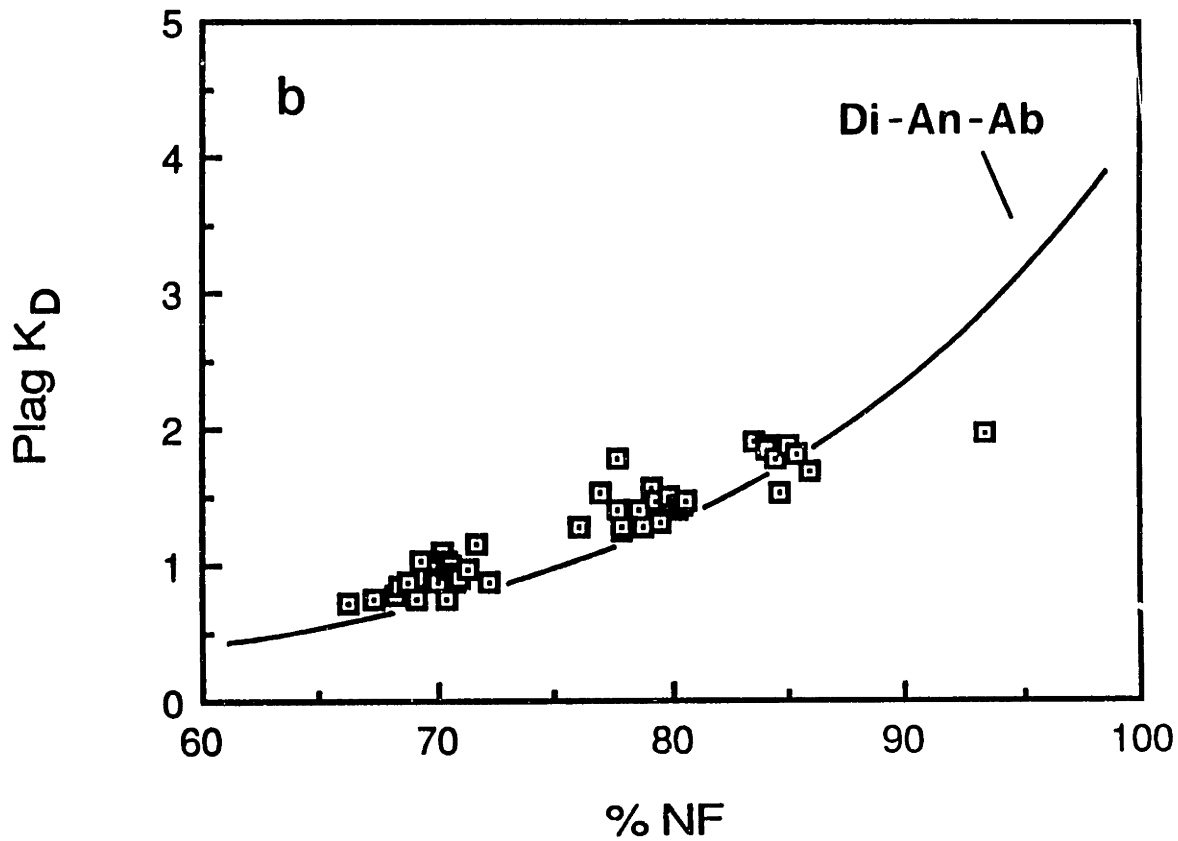
b
Di-An-Ab
Plag K_D
% NF
0
1
2
3
4
5
60
70
80
90
100

Figure 3-3. Comparison of liquids generated by equilibrium vs fractional crystalliation for AII78-3-102 at F-values of 0.8, 0.6 and 0.5. The number plotted for each major element on the y-axis is the ratio of the oxide value in the equilibrium liquid to the oxide value in the fractional liquid. Models are given in Table 3-2.

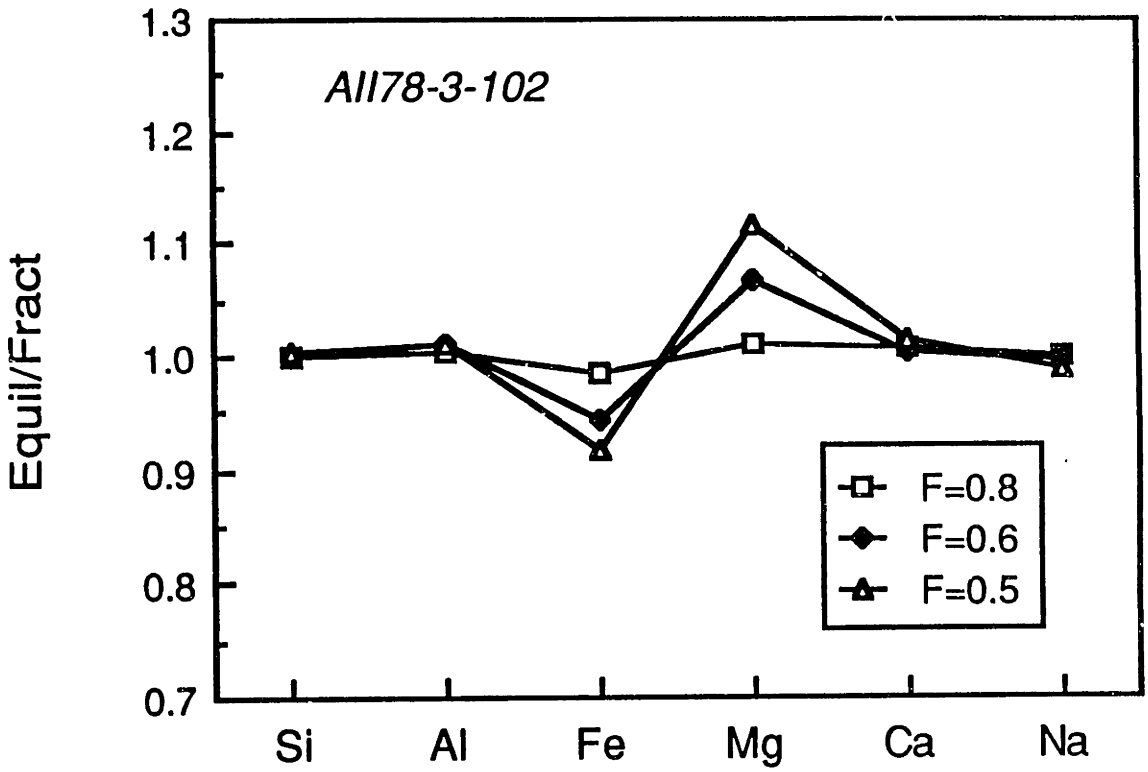
All78-3-102
Equil/Fract
1.3
1.2
1.1
1.0
0.9
0.8
0.7
Si
Al
Fe
Mg
Ca
Na
F=0.8
F=0.6
F=0.5

Figure 3-4. Comparison of equilibrium liquids to fractional liquids for 418A-52-5; models in Table 3-3.

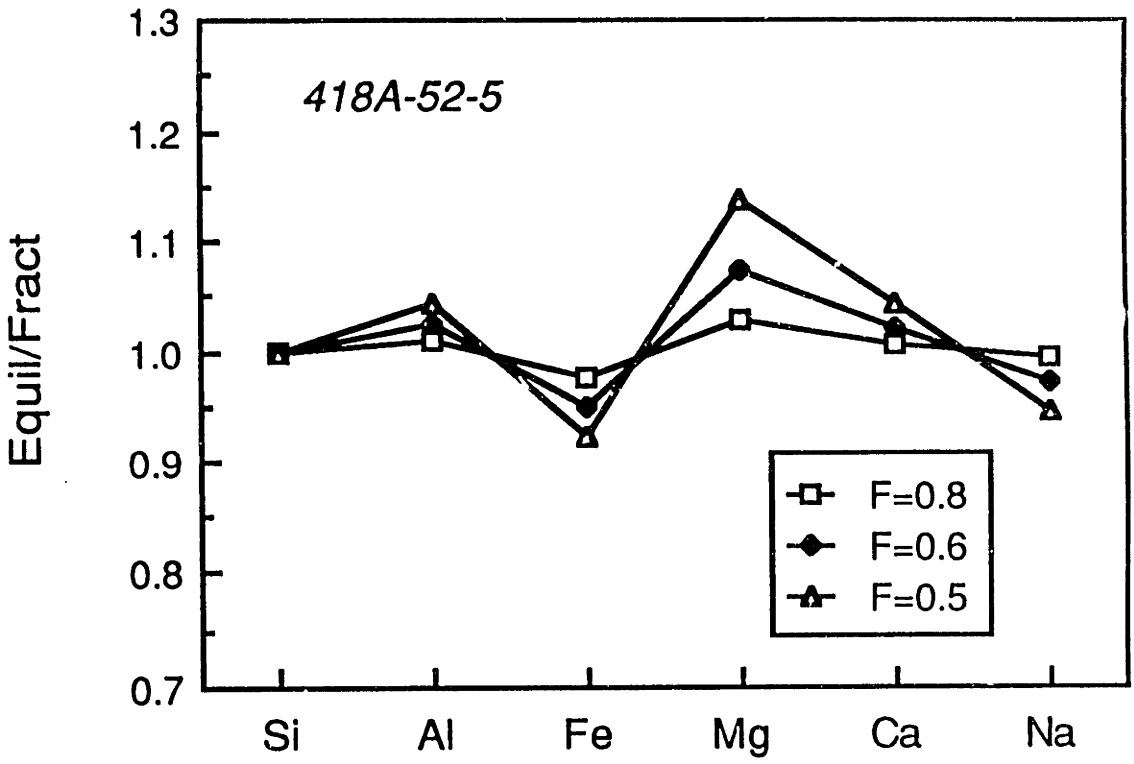
418A-52-5
Equil/Fract
1.3
1.2
1.1
1.0
0.9
0.8
0.7
Si
Al
Fe
Mg
Ca
Na
F=0.8
F=0.6
F=0.5

Figure 3-5. Differences between equilibrium and fractional liquids vs liquid fraction remaining for different bulk distribution coefficients. Numbers by each curve are the bulk Ds.

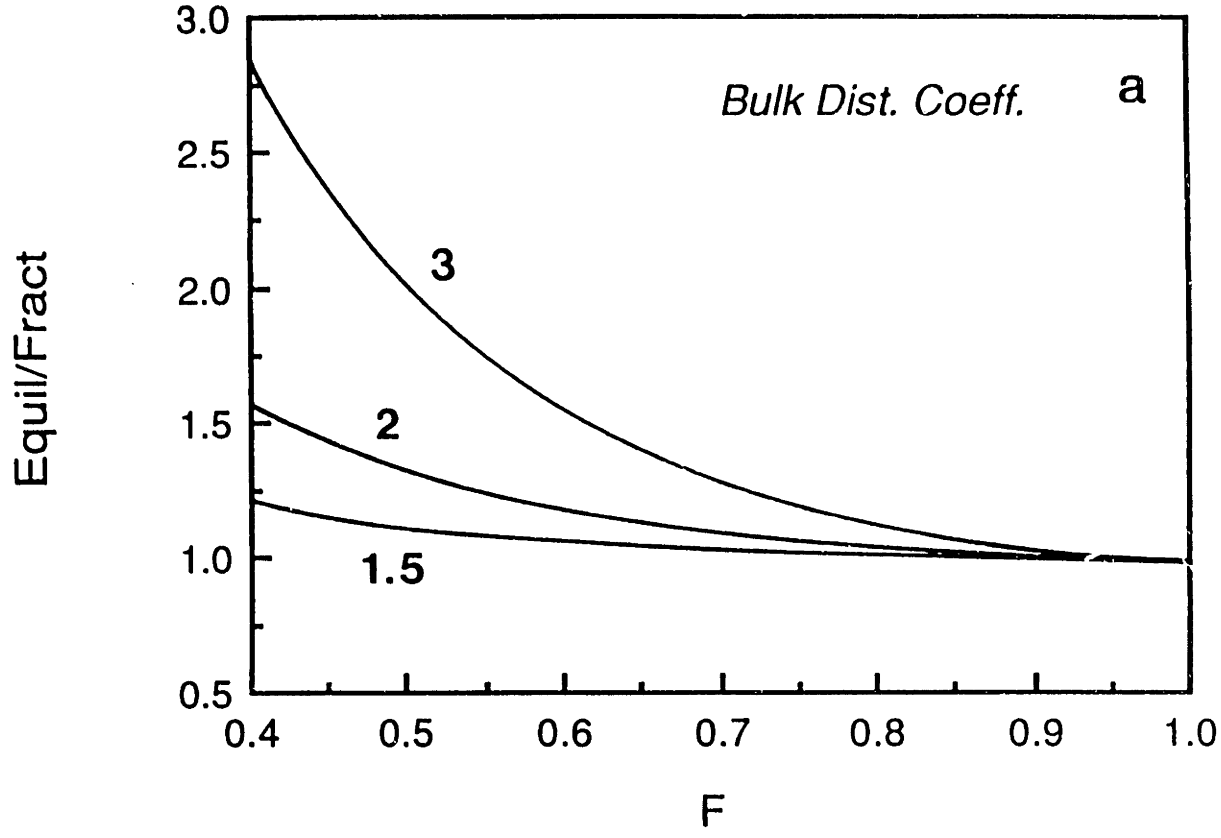
Bulk Dist. Coeff.
a
3
2
1.5
Equil/Fract
F
3.0
2.5
2.0
1.5
1.0
0.5
0.4
0.5
0.6
0.7
0.8
0.9
1.0

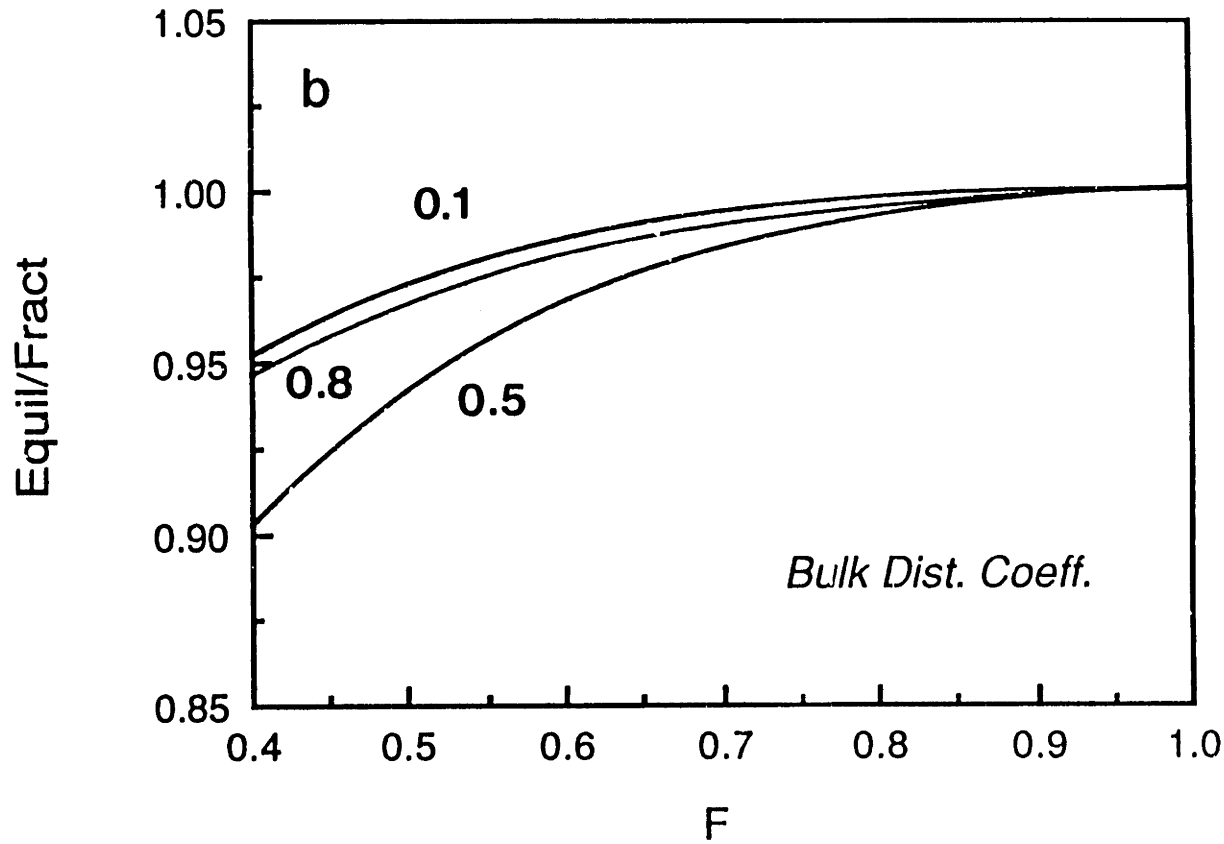
b
0.1
0.8
0.5
Bulk Dist. Coeff.
Equil/Fract
F
1.05
1.00
0.95
0.90
0.85
0.4
0.5
0.6
0.7
0.8
0.9
1.0

Figure 3-6. Mole% NF vs Mg/(Mg+Fe*) in the liquid for the calculated fractional liquid lines of descent given in Tables 3-2 and 3-3. NF defined in the caption to Fig. 3-3b.

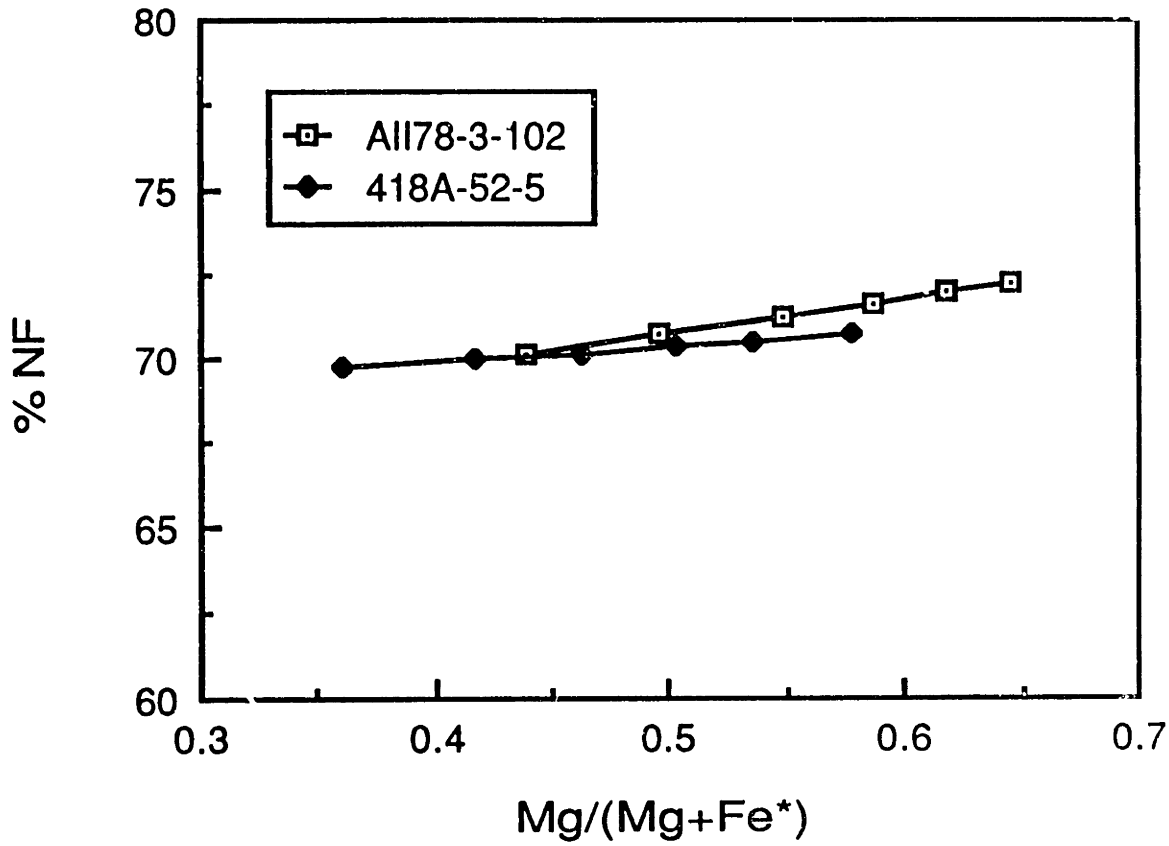
80
75
70
65
60
% NF
0.3
0.4
0.5
0.6
0.7
Mg/(Mg+Fe*)
AII78-3-102
418A-52-5

Figure 3-7. Compositions of olivine and plagioclase produced by equilibrium and fractional crystallization of AII78-3-102 at F ranging from 1.0 to 0.4. Equil = equilibium crystallization. Frac. inst. and frac. cum. are the instantaneous and cumulative phase compositions produced by fractional crystallization. Cumulative compositions represent the integrated sum of all prior crystallization of each phase.

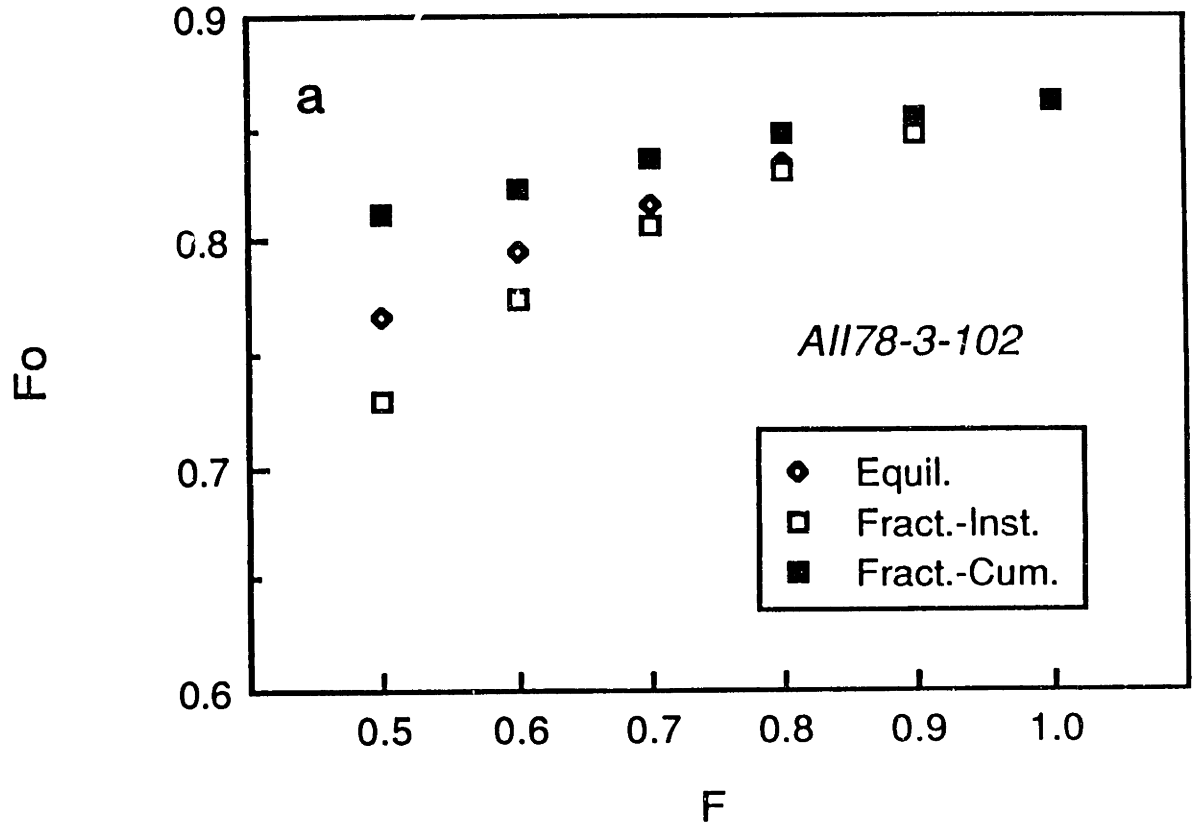
a
Fo
F
0.9
0.8
0.7
0.6
0.5
0.6
0.7
0.8
0.9
1.0
All78-3-102
Equil.
Fract.-Inst.
Fract.-Cum.

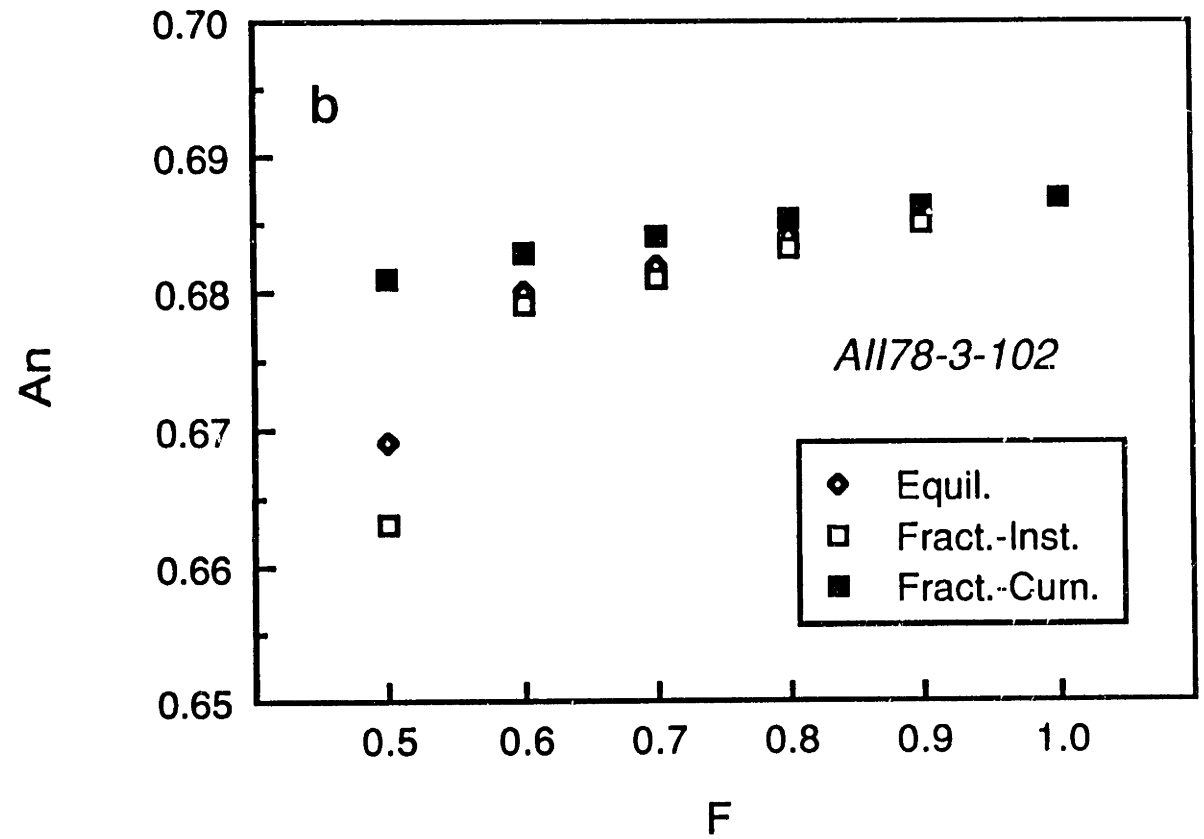
b
An
F
0.70
0.69
0.68
0.67
0.66
0.65
0.5
0.6
0.7
0.8
0.9
1.0
All78-3-102
Equil.
Fract.-Inst.
Fract.-Cum.

Figure 3-8. Calculated olivine and plagioclase compositions plotted against F for 418A-52-5.

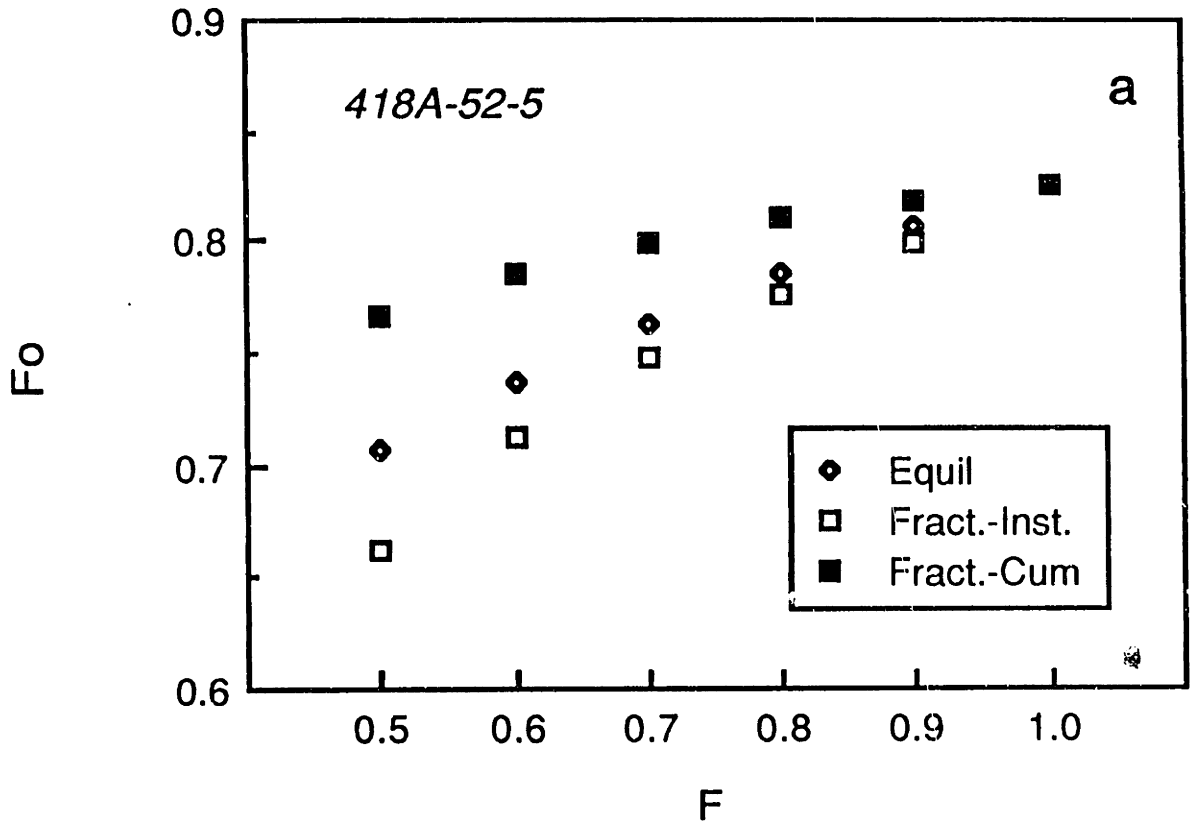
418A-52-5
a
Fo
F
0.9
0.8
0.7
0.6
0.5
0.6
0.7
0.8
0.9
1.0
Equil
Fract.-Inst.
Fract.-Cum

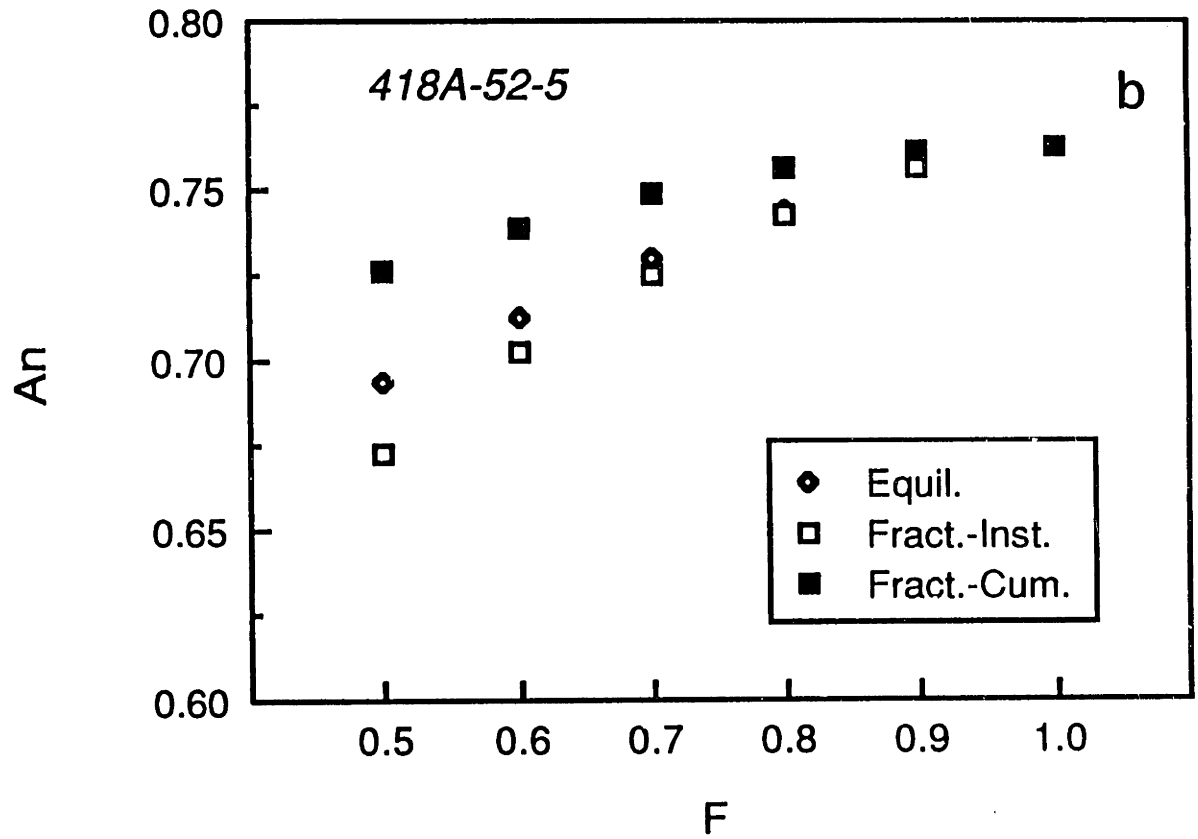
418A-52-5
b
An
F
0.80
0.75
0.70
0.65
0.60
0.5
0.6
0.7
0.8
0.9
1.0
Equil.
Fract.-Inst.
Fract.-Cum.

Figure 3-9. Comparison of calculated (Calc) to observed (Obs) oxide concentrations for a residual glass from the Kilaeua Iki lava lake. Model discussed in text.

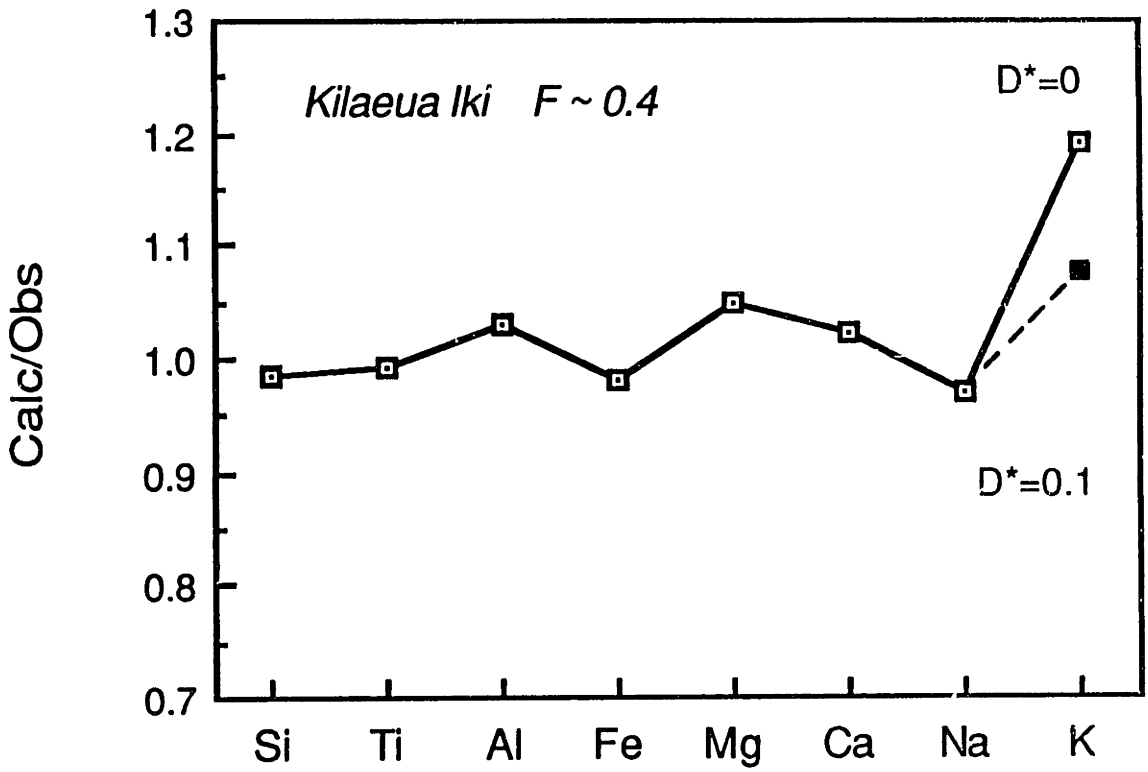
Kilaeua Iki F ~ 0.4
D*=0
D*=0.1
Calc/Obs
1.3
1.2
1.1
1.0
0.9
0.8
0.7
Si
Ti
Al
Fe
Mg
Ca
Na
K

Figure 3-10. Fit between calculated partial melt at F = 0.06 and the average of the magnesian quartz tholeiite parental liquids given in Duncan and Green (1987). Melting model discussed in text, model parameters given in Table 3-4.

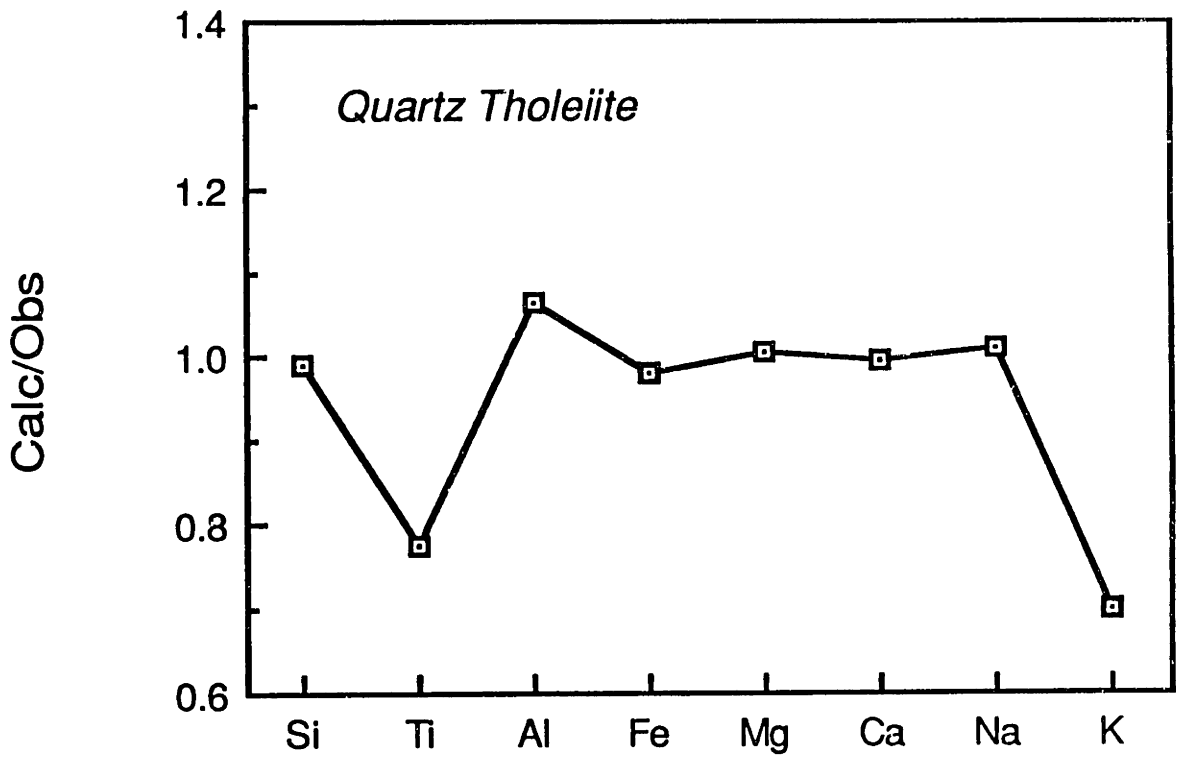
Quartz Tholeiite
Calc/Obs
1.4
1.2
1.0
0.8
0.6
Si
Ti
Al
Fe
Mg
Ca
Na
K

Table 3-1. Bulk compositions of 418A-52-5 and AII78-3-102 and model parameters.

Major element chemistry[1]

	SiO_2	TiO_2	Al_2O_3	FeO	MgO	CaO	Na_2O	K_2O
418A	50.66	1.23	14.95	10.49	8.04	12.22	2.31	0.10
AII78	49.19	0.99	17.36	9.33	9.55	10.55	2.92	0.11

Exchange coefficients

$(K_D)^{ol/liq} = 0.29$ $(K_D)^{pl/liq} = 1.1$ $(K_D)^{aug/liq} = 0.23$

Augite distribution coefficients

$D_{Ti} = 0.26$ $D_{Al} = 0.19$ $D_{Na} = 0.09$

[1] Compositions from Staudigel and Bryan (1981), 418A-52-5 and Grove and Bryan (1983), AII78-3-102. Analyses normalized to 100%.

Table 3-2. Equilibrium and fractional crystallization models for AII78-3-102

SiO_2	TiO_2	Al_2O_3	FeO	MgO	CaO	Na_2O	K_2O	Oliv[1]	Plag	Aug	F
Equil. Crystal.											
								33.0	67.0	00.0	
49.19	0.99	17.36	9.33	9.55	10.55	2.92	0.11	86.3	68.7		1.0
49.37	1.10	16.90	9.85	9.05	10.64	2.97	0.12	85.5	68.5		0.9
49.61	1.23	16.34	10.39	8.50	10.77	3.03	0.14	83.4	68.4		0.8
49.94	1.40	15.64	10.93	7.90	10.94	3.10	0.16	81.6	68.2		0.7
50.41	1.62	14.74	11.43	7.23	11.19	3.20	0.18	79.5	68.0		0.6
								11.3	50.8	37.9	
50.87	1.92	13.80	12.15	6.49	11.19	3.36	0.21	76.6	66.9	47.5	0.5
Fract. Crystal.											
								33.0	67.0	00.0	
49.19	0.99	17.36	9.33	9.55	10.55	2.92	0 11	86.3	68.7		1.0
49.39	1.11	16.84	9.92	8.98	10.64	2.98	0.12	84.8	68.5		0.9
49.61	1.24	16.28	10.53	8.39	10.76	3.03	0.14	83.0	68.3		0.8
49.92	1.42	15.55	11.26	7.66	10.92	3.11	0.16	80.7	68.1		0.7
50.35	1.64	14.60	12.09	6.78	11.15	3.21	0.19	77.5	67.9		0.6
								11.3	50.8	37.9	
50.70	1.96	13.65	13.25	5.81	11.01	3.40	0.22	72.9	66.3	45.6	0.5

1. Phase proportions (cation %) used in calculations. Oliv = olivine, Plag = plagioclase, and Aug = augite. Numbers below phase proportions give the forsterite (Oliv), anorthite (Plag) and enstatite contents (Aug, enstatite value is normalized Wo-En-Fs). F = cation fraction of liquid remaining.

Table 3-3. Equilibrium and fractional crystallization models for 418A-52-5

SiO_2	TiO_2	Al_2O_3	FeO	MgO	CaO	Na_2O	K_2O	Oliv[1]	Plag	Aug	F
Equil. Crystal.											
								35.0	65.0	00.0	
50.66	1.23	14.95	10.49	8.04	12.22	2.31	0.11	82.5	76.3		1.0
								11.5	50.3	38.2	
51.05	1.36	14.35	11.03	7.47	12.25	2.38	0.11	80.6	75.8	49.6	0.9
51.21	1.50	13.97	11.79	7.05	11.87	2.48	0.13	78.6	74.4	48.6	0.8
51.40	1.68	13.56	12.61	6.60	11.40	2.58	0.14	76.3	73.0	47.4	0.7
51.61	1.92	13.08	13.49	6.13	10.93	2.68	0.17	73.6	71.3	46.0	0.6
51.87	2.22	12.52	14.44	5.65	10.33	2.77	0.20	70.6	69.4	44.4	0.5
Fract. Crystal.											
								35.0	65.0	00.0	
50.66	1.23	14.95	10.49	8.04	12.22	2.31	0.10	82.5	76.3		1.0
								11.0	50.3	38.7	
51.10	1.38	14.22	11.20	7.40	12.20	2.39	0.11	80.2	75.6	49.4	0.9
51.22	1.53	13.83	11.99	6.97	11.80	2.49	0.13	78.1	74.2	48.3	0.8
51.45	1.71	13.36	12.93	6.47	11.32	2.61	0.15	75.5	72.5	46.9	0.7
51.70	1.97	12.73	14.15	5.83	10.68	2.76	0.17	71.7	70.2	44.9	0.6
52.01	2.30	11.98	15.59	5.10	9.89	2.93	0.20	66.8	67.2	42.3	0.5

[1] Phase proportions (cation %) used in calculations. Oliv = olivine, Plag = plagioclase, and Aug = augite. Numbers below phase proportions give the forsterite (Oliv), anorthite (Plag) and anstatite contents (Aug, enstatite value is normalized Wo-En-Fs). F = cation fraction of liquid remaining.

Table 3-4. Bulk Distribution Coefficients for Equilibrium and Fractional Crystallization of 418A and AII78.

	F[1]	SiO_2	TiO_2	Al_2O_3	FeO	MgO	CaO	Na_2O
418A Fract.								
	.9	.943	.098	1.211	.374	1.470	1.238	.606
	.7	.936	.099	1.254	.403	1.586	1.295	.621
	.5	.926	.099	1.332	.452	1.782	1.409	.648
418A Equil.								
	.9	.944	.100	1.194	.373	1.466	1.234	.601
	.7	.937	.100	1.232	.399	1.569	1.288	.625
	.5	.928	.098	1.290	.430	1.694	1.378	.639
AII78 Fract.								
	.9	.928	0	1.241	.441	1.520	.878	.798
	.7	.911	0	1.328	.488	1.681	.843	.766
	.5	.965	.099	1.193	.430	1.694	1.280	.588
AII78 Equil.								
	.9	.929	0	1.238	.438	1.512	.879	.800
	.7	.912	0	1.324	.479	1.652	.844	.766
	.5	.965	.098	1.189	.405	1.595	1.272	.586

[1] F = cation fraction of liquid remaining. Other abbreviations: Fract.= fractional crystallization, Equil.= equilibrium crystallization.

Table 3-5. Melting calculation: bulk and liquid compositions

	SiO_2	TiO_2	Al_2O_3	FeO	MgO	CaO	Na_2O	K_2O
Bulk comp.[1]	44.14	.03	1.38	7.59	45.53	1.24	.08	.009
Calc. liq.	52.20	.31	12.72	8.08	15.55	9.85	1.16	.14
Obs. liq.[2]	52.65	.40	11.95	8.25	15.50	9.91	1.15	.20

Cation Liquid Fraction = .06

Residual Phase Assemblage: Oliv = .840 Opx = .138 Cpx = .022

Phase Parameters: $(K_D)^{ol/liq} = .31$ $(K_D)^{pyx/liq} = .27$

Cpx: $D_{Ti} = 0.39$ $D_{Al} = 0.41$ $D_{Na} = 0.17$

Opx: $D_{Ti} = 0.17$ $D_{Al} = 0.23$

[1] Bulk composition is R347 from Ronda peridotite (Frey et al., 1985).

2 Observed liquid is average of two parental liquids in Duncan and Green (1987; Table 2).

CHAPTER 4

Major Element Constraints on the Compositions and Melt Percentages of Primary Mid-Ocean Ridge Basalts

INTRODUCTION

The chemical characteristics and degree of partial melting of primary mid-ocean ridge basalts (MORB) are fundamental questions for understanding the evolution of the earth's mantle. These two questions are at the center of the debate on whether liquids parental to the bulk of ocean floor basalts are picritic or tholeiitic in composition. Picritic magmas (12-20% MgO) are thought to represent high degrees of partial melting at pressures between 15 and 30 kbars (O'Hara, 1968; Green et al., 1979; Stolper, 1980; Elthon and Scarfe, 1984; Elthon, 1986). High pressure melting experiments on peridotites suggest that these MgO-rich liquids represent from > 25% (Mysen and Kushiro, 1977) to 30 to 40% melt (Jaques and Green, 1980). Tholeiitic primary magmas are believed to have compositions similar to the most primitive lavas sampled at mid-ocean ridges (Presnall et al., 1979; Fujii and Bougault, 1983; Takahashi and Kushiro, 1983; Fujii and Scarfe, 1985; Presnall and Hoover, 1984; 1987). Based on trace element and phase equilibrium studies, such primary magmas are thought to represent between 5 and 30% partial melting of peridotite at 7 to 11 kbars (Bender et al., 1984; Jaques and Green, 1980; Presnall et al., 1979; Presnall and Hoover, 1987).

Using major element abundances and mass balance constraints, we evaluate whether various magmas could be primary mantle melts and what melt fractions these magmas would

$$\text{liq} + \text{oliv} + \text{opx} \pm \text{cpx} \pm \text{sp} = \text{primitive mantle} \qquad (1)$$

for the proportions of phases using different liquid and bulk mantle compositions. Statistical criteria provide a test of the "goodness of fit" for each model. The liquids range from experimental glasses with 11 to 17 wt.% MgO (Fujii and Scarfe, 1985; Green et al., 1979) to a series of compositions (9.7 to 13.3% MgO) generated by adding olivine and spinel to an average primitive mid-Atlantic ridge basaltic glass. Using existing high-pressure experimental data, we develop a simple series of algorithms for calculating the solid phase compositions necessary to solve eqn (1). Our results indicate that the most primitive mid-Atlantic ridge glasses are not primary melts of spinel lherzolites. However, these basaltic liquids may have evolved from melts with 11 to 13% MgO by moderate amounts of olivine + spinel fractionation (5 to 10%). Picritic magmas with > 15% MgO may also be parental to the MORB glasses. Uncertainties in the major element composition of the MORB source region limit the determination of melt percentages for a given basalt to within a factor of 1.5. Our preferred estimate of melting for liquids with 11 to 13% MgO is 6 to 12%. This range is consistent with recent modelling of trace element abundances in MORB by Jochum et al. (1983), Hoffman (1983), Bender et al. (1984) and Galer and O'Nions (1986).

A fundamental assumption inherent in our solution to eqn

(1) is that melt generation is an isobaric, bulk equilibrium process. A number of recent papers have invoked more complicated, and perhaps more realistic, scenarios for mantle partial melting, e g. variable melting as a function of position within a diapir (O'Hara, 1985) and continuous adiabatic melting of an ascending mantle diapir (Ahern and Turcotte, 1979; McKenzie, 1984; Klein and Langmuir, 1987). All of these models involve pooling liquids formed by different degrees of melting at various pressures. Thus, magmas parental to MORBs may be a blend of liquids and might not reflect any single pressure of equilibration. However, numerical calculations by Richter (1986) and Maaloe and Johnston (1986) show that, compared to dynamic models, the bulk equilibrium melting expression is surprisingly successful in recovering actual melting percentages and source region compositions. We conclude that eqn (1) is an appropriate starting point for investigating questions of primary magma composition and melt percentages.

MIXING COMPONENTS

Basalts

Table 4-1 lists the major element compositions and associated uncertainties for the six basalts used in the mass balance calculations. The bulk compositions range from olivine tholeiites to picritic basalts and are representative of the magma types which may be parental to the vast majority of ocean ridge basalts. Basalts 1 and 2 are experimental run products, produced by equilibrating an olivine tholeiite with the

assemblage olivine, orthopyroxene, clinopyroxene and spinel at 10 kbars and temperatures of 1275 and 1290°C (Fujii and Scarfe, 1985). Except for their high Mg/(Mg+ΣFe) ratios of 0.74 to 0.75, these experimental liquids are similar in composition to primitive MORB glasses (column 4). Both of these experimental liquids were in equilibrium with a spinel lherzolite assemblage and thus provide information on the percentages of liquid which may co-exist with oliv + opx + cpx + sp at high pressures. Basalt 3 is a picritic basalt (16.7% MgO) and is in equilibrium with olivine and orthopyroxene at 20 kbars (Green et al., 1979). O'Hara (1968) and more recently Stolper (1980) and Elthon and Scarfe (1984) have argued that such MgO-rich compositions are parental to most ocean floor basalts. Estimated melting percentages necessary to produce such magnesian liquids range from 25 to 40 (Mysen and Kushiro, 1977; Jaques and Green, 1980).

Basalt 4 is the average of 32 primitive Atlantic MORB glasses compiled by Presnall and Hoover (1987; Appendix 1). All of these glasses have Mg/(Mg+0.86Fe) > 0.70, and are potential primary magmas which may evolve to normal MORBs by low pressure fractional crystallization. Basalts 5 and 6 are two synthetic basalts intermediate between the average ocean-floor glasses (column 4) and the MgO-rich picrite (column 3). These two compositions were calculated by adding 5 and 10 wt.% of the assemblage 98% olivine and 2% spinel to glass #4. The olivine and spinel were added in 1 wt.% increments and both phases were calculated to be in equilibrium with the changing liquid composition at each increment (see Grove and Baker,1984; the

spinel calculation is discussed below). Crystallization of olivine + spinel is one of the most simple high pressure fractionation scenarios, and is consistent with the expansion of the olivine primary phase volume during magma ascent (e.g. O'Hara, 1968). High pressure crystallization of clinopyroxene may also be important in the evolution of normal MORBs. However, since the cotectic proportions of olivine and clinopyroxene are poorly constrained at high pressure, we have not attempted to calculate a more MgO-rich liquid using these two phases. For these last three basalts, there are no experimental constraints on the high pressure equilibrium phase assemblage and we have solved eqn (1) for each liquid using the following sets of phases: oliv + opx + cpx + sp, oliv + opx + cpx, and oliv + opx. These three sets of phases represent the inferred order in which mantle minerals melt out with increasing temperature within the spinel stability field.

In the mineral and mass balance balance calculations discussed below, all iron in the melt is assumed to be present as FeO. We are forced to make this assumption because fO_2 and Fe^{3+}/Fe^{2+} ratios are poorly known in most high pressure piston cylinder experiments, although they are presumed to be low. This includes those experiments that supply the major element crystal-liquid partitioning data for this study. For example, graphite capsules at 10 kbars and 1100 to 1450°C impose oxygen fugacities that lie somewhere in the wustite stability field (Thompson and Kushiro, 1972). The oxidation state of the mantle is currently a subject of active debate, with estimates ranging

from close to iron-wustite (IW) to quartz-fayalite-magnetite (QFM) (e.g. Mathez, 1984; Arculus, 1985; Mattioli and Wood, 1986; Sen and Jones, 1988). However recent determinations of $Fe^{3+}/\Sigma Fe$ ratios in mid-ocean ridge basaltic glasses suggest that the oxidation state for the sub-oceanic mantle is at least 1 to 2 log units below QFM (Christie et al., 1986). Under these fO_2 conditions, < 5% of the total iron will be present as Fe_2O_3 (molar), and thus our assumption that $Fe_2O_3 = 0$ in the melt is not unreasonable.

Bulk Mantle Estimates

Table 4-2 lists eight recent estimates of the major element chemistry of the earth's primitive mantle (Hutchison, 1974; Ringwood, 1979; Jagoutz et al., 1979; Wanke, 1981; Sun, 1982; Palme and Nickel, 1985; Hart and Zindler, 1986). Most of these bulk silicate earth estimates are based on chondritic abundances, elemental ratios and the compositions of mantle lherzolites. Al_2O_3 and CaO show the greatest variation among the different models, with concentrations differing by a factor of ~1.5; 3.3 to 4.8 wt.% Al_2O_3 and 2.8 to 4.4 wt.% CaO. Also listed in Table 4-2 is a calculated depleted mantle composition (column H), derived from primitive mantle F by subtracting 4% basaltic melt following the methods described in Hart and Zindler (1986). This depleted composition represents one possible estimate of the bulk chemistry of the MORB source region. CaO and Al_2O_3 in mantle H are ~12 and 11% lower than the values in mantle F. Although the MORB source region has long been characterized as

being depleted in incompatible elements (e.g. Tatsumoto et al., 1965; Kay et al., 1970), its major element abundances may not be substantially different from bulk earth estimates (Hart and Zindler, 1988).

The compositions from Table 4-2 are projected from spinel onto the base of the Oliv - Opx - Cpx - Sp pseudoquaternary system in Fig. 4-1; the letter by each point refers to a column heading in Table 4-2. The projection scheme transforms the wt.% oxides into the mineral components $(MgFe)_2SiO_4$, $(MgFe)_2Si_2O_6$, $Ca(MgFe)Si_2O_6$, $NaAlSi_2O_6$, $(MgFe)Al_2O_4$ and $(MgFe)Cr_2O_4$. After multiplying each component by the number of oxygens in its formula, diopside-hedenburgite and jadeite are combined to form Cpx, and spinel-hercynite and picrochromite-chromite are summed to form Sp. The four new components are then normalized to 1. Oliv and Opx make up between 74 and 82% of each mantle composition, with Cpx and Sp comprising between 12 to 20 and 5 to 7%, respectively. The Oliv/Opx ratio varies considerably among the different compositions, ranging from 2.2 in mantle B to 1.2 in mantle G. Using Fig. 4-1 as a guide, we selected the primitive mantles B, D and F, as well as the depleted composition (H) to use in the mass balance calculations. These four mantle compositions should indicate the extent to which calculated liquid proportions for a given basalt vary in response to changes in the bulk chemistry of the system. Regardless of the extent of major element depletion in the MORB source region, the primitive mantle estimates will place upper limits on the percentage of melting necessary to generate a

given primary basalt.

Estimated fractional uncertainties for all of the mantle compositions are given in the final column in Table 4-2. Lacking formal error estimates for each model composition, we assume that the variability shown by SiO_2, TiO_2, Cr_2O_3, FeO, MgO and Na_2O is representative of the uncertainty which may be associated with these oxides in each model. For these oxides the reported uncertainties are the fraction errors (σ/mean) for the seven primitive mantle compositions (column H was not included). For Al_2O_3 and CaO, which show large variation among the different models, the 5% error estimates are based on the uncertainties in the chondritic abundances of these elements (Anders and Ebihara, 1982).

CALCULATING RESIDUAL PHASE COMPOSITIONS

The following section presents a series of simple algorithms for calculating the compositions of olivine, orthopyroxene, clinopyroxene and spinel which may be in equilibrium with a basaltic melt at high pressures, as well as our technique for estimating the uncertainties in the composition of each phase.

Olivine

Equilibrium olivine was calculated assuming a stoichiometry of $(MgFe)_2SiO_4$. This formula fixes the mole percent sum of FeO and MgO at 66.67 and the mole % of SiO_2 at 33.33. The Fe-Mg exchange coefficient for olivine-liquid is defined as,

$$K_D^{ol/liq} = \frac{(X_{Fe})^{ol}(X_{Mg})^{liq}}{(X_{Mg})^{ol}(X_{Fe})^{liq}} \qquad (2)$$

where X_{Mg} = Mg/(Mg + Fe) molar. $K_D^{ol/liq}$ is approximately independent of temperature and bulk composition and only weakly dependent upon pressure (Roeder and Emslie, 1970; Longhi et al., 1977; Grover et al., 1980, Takahashi and Kushiro, 1983). Rearranging eqn (2) yields the olivine Mg-number as a function of the Fe-Mg K_D and the liquid Mg/(Mg+Fe) ratio.

$$X_{Mg}^{ol} = \frac{X_{Mg}^{liq}}{X_{Fe}^{liq} K_D^{ol/liq} + X_{Mg}^{liq}} \qquad (3)$$

Thus for a given liquid composition and K_D value, eqn (3) provides the Mg-number of the equilibrium olivine, which in turn fixes the mole % of MgO and FeO in the olivine at $(X_{Mg}^{ol})66.67$ and $(1-X_{Mg}^{ol})66.67$. The mole % SiO_2 remains constant at 33.33. Multiplying the MgO, FeO, and SiO_2 mole percents by the gram-formula weights for these oxides and normalizing to 100% yields the olivine composition in oxide wt.%.

Orthopyroxene

Table 4-3 summarizes the published experimental data on orthopyroxene - liquid equilibria in ocean floor basalts at ~ 10 and 20 kbars. $[MF]^{opx}$ equals the mole% sum of MgO and FeO, and $[CaO]^{opx}$ is the mole% of CaO in each opx. The exchange coefficient $[K_D^{opx/liq} = (X_{Fe})^{opx}(X_{Mg})^{liq}/(X_{Mg})^{opx}(X_{Fe})^{liq}]$ and the single element distribution coefficients for TiO_2, Al_2O_3, Cr_2O_3 and Na_2O ($D_i = X_i^{opx}/X_i^{liq}$) are all calculated on a mole % basis. Note that none of the experiments contain clinopyroxene, and thus the Wo content in the orthopyroxenes is not constrained by opx-cpx equilibria. $[CaO]^{opx}$ ranges from 0.75 to 2.68 mole% and is negatively correlated with run temperature (Fig. 4-2a). For orthopyroxene in equilibrium with augite, Wo increases with increasing temperature at constant pressure (e.g. Lindsley, 1980; Lindsley and Anderson, 1983). $[MF]^{opx}$ is inversely correlated with [CaO] (Fig. 4-2b); the total variation in MgO + FeO among the six experiments is ~3.5% of the average value. The calibration of Lindsley and Anderson (1983) suggest that the Wo content in a magnesian opx (Mg# = 0.90) in equilibrium with clinopyroxene at 1200 to 1300°C and 10 kbars will lie in the range 0.05 to 0.10. Since a majority of the mass balance calculations involve opx + cpx, only the three orthopyroxenes with the highest Wo content were used to compute the final 10 kbar averages for $[MF]^{opx}$ and $[CaO]^{opx}$ in Table 4-3.

With the exception of D_{Cr}, the exchange and distribution coefficients are fairly constant within each pressure interval. The large variation in the chrome partition coefficient most likely reflects analytical uncertainties due to the low Cr_2O_3

abundances in the melts. For the 10 to 11 kbar data, mean and 1 σ values for K_D and the distribution coefficients are listed in Table 4-3. The mean for D_{Cr} is based on the three highest calculated values.

The 20 kbar data is limited to two opx-glass pairs. For most of the parameters, the calculated values for these two experiments overlap with those determined from the ~ 10 kbar data. Thus with the exception of $K_D^{opx/liq}$ and D_{Al}, averages for each parameter are based on the 10-11 kbar data and the 20 kbar values. Mean $K_D^{opx/liq}$ and D_{Al} values are computed using only the two 20 kbar opx-glass pairs.

To calculate the composition of an orthopyroxene in equilibrium with a basaltic liquid at 10 or 20 kbars, the liquid composition is first converted from wt.% to oxide mole %. The Mg-number of the equilibrium orthopyroxene is given by,

$$X_{Mg}^{opx} = \frac{X_{Mg}^{liq}}{X_{Fe}^{liq} K_D^{opx/liq} + X_{Mg}^{liq}} \qquad (4)$$

The mole % of MgO and FeO in the opx is $X_{Mg}^{opx}[MF]$ and $(1-X_{Mg}^{opx})[MF]$, respectively. The CaO content in the opx is constant and is equal to the mean value for $[CaO]^{opx}$ determined from the experimental data. The mole percents of TiO_2, Al_2O_3, Cr_2O_3 and Na_2O in the opx are fixed by the D values and the composition of the liquid. Mole % SiO_2 is determined by difference, i.e. 100 -

(sum of all other oxides), which ensures a stoichiometric orthopyroxene. The oxide mole percents are converted to weight percents using the oxide gram-formula weights as outlined for olivine.

Clinopyroxene

$[MF]^{cpx}$, $[CaO]^{cpx}$ and calculated exchange and distribution coefficients for 12 clinopyroxene-liquid pairs from 10 to 12 kbar experiments on tholeiitic basalts are compiled in Table 4-4. Mole % CaO in the pyroxenes shows a negative correlation with run temperature (Fig. 4-3). $[MF]^{cpx}$ and $[CaO]^{cpx}$ are also negatively correlated (Fig. 4-4) and range from ~28 to 39 and ~10 to 19 mole %, respectively. Fe-Mg exchange coefficients show substantial scatter and only a very weak correlation with temperature; values cluster at ~0.30 and 0.23. With the exception of one or two experiments, calculated clinopyroxene-liquid distribution coefficients for TiO_2, Al_2O_3 and Na_2O are relatively constant.

Calculated regression lines for $[CaO]^{cpx}$ vs T(°C) and $[MF]^{cpx}$ vs $[CaO]^{cpx}$ are given in Figs. 4-3 and 4-4. [CaO] values from experiments 35 and 5590 (crosses) plot substantially off the trend in Fig. 4-3 and were not included in the linear fit. Using clinopyroxene compositions calculated with the mean [MF] and [CaO] values, initial mass balance solutions for basalts 1 through 6 produced liquid fractions between 0.07 and 0.27. These melt fractions may be approximately related to temperature using the peridotite melting experiments of Jaques and Green (1980),

and correspond to temperatures of ~1225 to 1325°C. A mean melting temperature of 1280°C was used to calculate new $[CaO]^{cpx}$ and $[MF]^{cpx}$ values which were used in all subsequent calculations. The uncertainties given for $[MF]^{cpx}$ and $[CaO]^{cpx}$ in Table 4-4 reflect a ±20°C temperature variation. Based on the scatter in Fig. 4-3, the exchange and partition coefficients from runs 35 and 5590 were not included in the calculated means and 1σ for K_D, D_{Ti}, D_{Al} and D_{Na}. The average values and their uncertainties are given in Table 4-4. Based on partition coefficients reported in Henderson (1982; Bougault and Hekinian, 1974), D_{Cr} was set equal to 10±3. For a given melt composition, the equilibrium clinopyroxene composition was calculated in the same manner as outlined for orthopyroxene.

Spinel

Al_2O_3, Cr_2O_3, ΣFe and MgO comprise between 98 and 99 wt % of spinels analyzed from abyssal peridotites; Fe_2O_3 is generally between 3 and 4 wt.% (Bonatti and Hamlyn, 1981; Dick and Bullen, 1984). Assuming all iron as FeO the stoichiometric formula $(MgFe)(AlCr)_2O_4$ covers a major portion of abyssal spinel composition space. In one of the few high pressure studies to have produced spinel-liquid pairs over a range of bulk compositions and temperatures, Fujii and Scarfe (1985) found that the Cr/(Cr+Al) ratio in spinel varies linearly with the Al_2O_3 content in the co-existing basaltic melt. We digitized the data points from their Fig. 6 (spinel analyses were not reported) and calculated the following regression line,

$$Y_{Cr}^{sp} = 1.977 - 0.1054(Al_2O_3, \text{ wt.\%}) \qquad (5)$$

where Y_{Cr}^{sp} is the Cr/(Cr+Al) ratio in the spinel. The standard errors on the two regression parameters are 0.075 and 0.0047, respectively, and the fit has a linear correlation coefficient of 0.986. At present there is very little data that can be used to check eqn (5) independently. Y_{Cr}^{sp} calculated from a 10 kbar melt composition reported by Takahashi (1986) is 0.11 ± 0.11. The Cr/(Cr+Al) ratio in the coexisting spinel is 0.14, well within the uncertainty of the calculated value.

The lack of reported spinel compositions in equilibrium with basaltic melts at high pressures precludes calibrating an Fe-Mg K_D for spinel and liquid. However, since olivine will always be a residual phase during mantle partial melting, the olivine-spinel Fe-Mg exchange reaction can be used to calculate the Mg-number of a spinel in equilibrium with co-existing olivine and liquid. The distribution of FeO and MgO between olivine and spinel is,

$$K_D^{ol/sp} = \frac{X_{Mg}^{ol} \, X_{Fe}^{sp}}{X_{Fe}^{ol} \, X_{Mg}^{sp}} \qquad (6)$$

Substituting the $K_D^{ol/liq}$ expression into eqn (6) we can write

$$K_D^{ol/sp} = \frac{X_{Mg}^{liq}\, X_{Fe}^{sp}}{X_{Fe}^{liq}\, K_D^{ol/liq}\, X_{Mg}^{sp}} \qquad (7)$$

Rearranging eqn (7) yields X_{Mg}^{sp} as a function of liquid composition, $K_D^{ol/liq}$ and $K_D^{ol/sp}$.

$$X_{Mg}^{sp} = \frac{X_{Mg}^{liq}}{K_D^{ol/sp}\, K_D^{ol/liq}\, X_{Fe}^{liq} + X_{Mg}^{liq}} \qquad (8)$$

As noted earlier, $K_D^{ol/liq}$ is nearly independent of temperature and bulk composition and only weakly dependent on pressure. Engi (1983) has calibrated $K_D^{ol/sp}$ as a function of temperature and Y_{Cr}^{sp}. We digitized at 0.1 Y_{Cr} intervals the 1100, 1200, 1300 and 1400°C isotherms from his Fig. 13, ($\ln K_D^{ol/sp}$ vs Y_{Cr}^{sp}), and fitted the points with the following polynomial expression,

$$\ln K_D^{ol/sp} = -1.247 + 2.634(Y_{Cr}) - 0.762(Y_{Cr})^2 + 2.130(10^3/T\ ^\circ K) \qquad (9)$$

Standard errors on the fitting parameters are 0.046, 0.057, 0.056 and 0.067. Eqn (9) reproduces the digitized data with an average error of ~ 1.4%.

The composition of a spinel in equilibrium with a given liquid is calculated using eqns (5), (8) and (9). The wt.% Al_2O_3

in the liquid fixes Y_{Cr}^{sp} in the spinel through eqn (5). At a specific temperature and pressure, $K_D^{ol/sp}$ is calculated using eqn (9), Y_{Cr}^{sp} and the pressure correction given by Engi (1983; Appendix). Finally, substituting $K_D^{ol/sp}$, $K_D^{ol/liq}$ and X_{Mg}^{liq} into eqn (8) yields the Mg-number of the equilibrium spinel. Once Y_{Cr}^{sp} and X_{Mg}^{sp} are known, the mole percents of MgO, FeO, Al_2O_3 and Cr_2O_3 are:

$$MgO = X_{Mg}^{sp}(33.33)$$

$$FeO = (1-X_{Mg}^{sp})(33.33)$$

$$Al_2O_3 = Y_{Cr}^{sp}(66.67)/2$$

$$Cr_2O_3 = (1-Y_{Cr}^{sp})(66.67)/2$$

As with the previous mineral phases the oxide mole percents are converted to weight percents by multiplying by the appropriate oxide gram formula weights and normalizing to 100.

Error Propogation and Computed Mineral Compositions

The mineral calculations discussed above depend on experimentally determined parameters which have significant uncertainties. There are also uncertainties associated with all of the basalt compositions, representing either analytical error or variation about a mean. We use Monte Carlo techniques to determine how both sets of uncertainties propagate through the mineral calculation scheme and manifest themselves as uncertainties in the mineral compositions. Our procedure is: (1) using random numbers create a synthetic data set of 400 values

normally distributed about the mean of each input parameter based on its 1σ. (2) Calculate 400 mineral compositions based on the synthetic data set. (3) Calculate the mean and standard deviation for each oxide for the 400 mineral compositions. Convergence tests showed that 400 iterations were sufficient to produce a constant standard deviation for a given mineral algorithm.

Input parameters for the olivine calculation are FeO and MgO contents in the liquid (in wt.%) and $K_D^{ol/liq}$. Using the pressure calibration of Takahashi and Kushiro (1983), $K_D^{ol/liq}$ is equal to 0.32 ± 0.03 at 10 kbars and 0.34 ± 0.03 at 20 kbars. The 10 kbar value agrees with the olivine-liquid data of Fujii and Scarfe (1985) collected at the same pressure, and was used to calculate olivines in equilibrium with all of the compositions in Table 4-1 except basalt 3. The 20 kbar value was used to calculate the equilibrium olivine composition for the picritic liquid. The pyroxene calculations require the liquid composition in wt.%, $[MF]^{pyx}$, $[CaO]^{pyx}$, $K_D^{pyx/liq}$, D_{Ti}, D_{Al}, D_{Cr} and D_{Na}. Uncertainties on these values are given in Tables 4-1, 4-3 and 4-4. Input parameters for the spinel calculation are Al_2O_3, FeO and MgO contents in the liquid, temperature, and the regression coefficients for eqns (5) and (9). A temperature of 1280 ± 20°C and a pressure of 10 kbars were used for all spinel calculations.

Mineral compositions calculated to be in equilibrium with the six basalts are given in Table 4-5. Uncertainties on oxide values vary from <0.5% for SiO_2 in olivine to <27% for Al_2O_3 and

<58% for Cr_2O_3 in the spinels. Forsterite content in the equilibrium olivines varies from 87 (basalt 4) to 92 (basalt 3), in general agreement with accepted mantle values. Fig. 4-5 shows calculated alumina contents in the orthopyroxenes and spinels in equilibrium with basalts 1, 2, 4, 5 and 6, with the fields defined by Al_2O_3 in coexisting orthopyroxenes and spinels from subcontinental ultramafic inclusions (Frey and Prinz, 1978) and abyssal and Alpine peridotites (Dick and Fisher, 1984) plotted for comparison. The slope of the calculated trend is nearly parallel to the inclusion data, although the calculated values only partial intersect the ultramafic field. Nevertheless, Fig. 4-5 suggests that $^{Y}Cr_{sp}$ and $(D_{Al})^{opx}$ determined from the 10 kbar experimental data may be used to match observed alumina trends in co-existing orthopyroxenes and spinels from ultramafic rocks. Mg- and Cr-numbers in the spinels calculated for basalts 4 through 6 are compared with the spinel field from abyssal peridotites (Dick and Bullen, 1984) in Fig. 4-6. The calculated compositions fall within the observed field, although the synthetic spinels define a more vertical trend. Although the uncertainty associated with each calculated spinel composition is quite large, the overall match in Fig. 4-6 suggests that the spinel-olivine algorithm is able to reproduce the observed compositional variations.

ESTIMATING MELTING PERCENTAGES FOR MID-OCEAN RIDGE BASALTS

Mass Balance Algorithm

Equation 1 can be written in matrix notation as

$$\mathbf{Ax} = \mathbf{Y} \tag{10}$$

where each column in the **A** matrix is the composition of one of the phases on the left-hand side of eqn (1), the vector **Y** is a bulk mantle composition and the vector **x** contains the unknown phase proportions. We have used the least-squares algorithm presented by Albarede and Provost (1977) to solve the overdetermined system of equations represented by (10). The advantage of this method for solving the inverse problem is that it handles the uncertainties on all phases in the **A** matrix, and not just those of the vector **Y**. In the traditional least-squares approach, oxides in the coefficient matrix **A** are weighted by the uncertainties for each oxide in the solution vector **Y**, and the best fit parameters are those values of x_i that minimizes the merit function, χ^2,

$$\chi^2 = \Sigma[(Y_i - \Sigma A_{ij}x_j)/\sigma_i]^2 \tag{11}$$

where A_{ij} is the observed oxide value in the i^{th} column and j^{th} row in **A** and σ_i is the standard error associated with the i^{th} oxide in **Y**. The merit function which incorporates uncertainties on each oxide in **A** and **Y** is (Albarede and Provost, 1977),

$$\chi^2 = \Sigma \frac{[Y_i - \Sigma A_{ij}x_j]^2}{[\Sigma(\sigma_{ij}x_j)^2 + \sigma_i]} \tag{12}$$

where σ_{ij} represents the uncertainty associated with the A_{ij} oxide term. Eqn (12) may be rewritten as,

$$\chi^2 = \Sigma\{[(\Sigma a_{ij}x_j - Y_i)/\sigma_i]^2 + \Sigma[(A_{ij} - a_{ij})/\sigma_{ij}]^2\} \qquad (13)$$

where A_{ij} is defined above and a_{ij} are the oxide values that minimize (13) for a given $\mathbf{x}$ vector. Albarede and Provost (1977) give a series of expressions for calculating the matrix $\mathbf{a}$ once (12) is minimized. Eqn (13) demonstrates how the uncertainties in the phase compositions contribute to the value of χ^2. In order to discuss the error in each phase composition, we define the quantity $(\delta_i)^{xtl}$, where

$$(\delta_i)^{xtl} = A_{ij} - a_{ij} \qquad (14)$$

We refer to the phase compositions given by A_{ij} as the observed compositions; the phase chemistries given by a_{ij} will be called the calculated compositions.

Equation 12 is non-linear and we minimize χ^2 using the downhill simplex algorithm (Nelder and Meade, 1965). The subroutine is from Press et al. (1986). A penalty function of the form $\alpha(1-\Sigma x_i)^2$ was added to eqn (12) to ensure that the phase proportions sum to 1.0. α was set to 10^6 for all calculations. Using eqn (54) from Albarede and Provost (1977) we

calculate $\partial(\chi^2)^2/\partial x_i \partial x_j$, the Hessian matrix at the χ^2 minimum. The inverse of the Hessian matrix supplies the variance-covariance matrix for the fitted parameters; the diagonal elements of this inverse matrix are the standard errors on the x_i's.

In order to evaluate each of the mass balance solutions statistically, we use the probability function $Q(\chi^2|\nu)$ as a quantitative measure of the goodness-of-fit (Bevington, 1969), where ν is the degrees of freedom in the model, i.e. the number of oxides plus 1 minus the number of phases. Q is the probability that the sum of the squares of ν random normal variables of unit variance will be greater than the χ^2 calculated for the specific model. If this probability is low for the given model, then the differences between the supplied and calculated mineral and bulk chemistries are not the result of inherent uncertainties in the phase compositions, and either the model can be statistically rejected or the errors on the phase compositions have been under-estimated. Since Monte Carlo methods tend to overestimate errors when applied to closed data sets (McKenna, per. com.), small Q-values are not the result of underestimated errors on phase compositions. We reject models with Q-values < 0.05. This is equivalent to a 95% confidence level for the more commonly tabulated function P = (1-Q).

Results

Table 4-6 summarizes the results of the mass balance calculations for the two 10 kbar experimental glasses from Fujii

and Scarfe (1985), and the picritic liquid from Green et al. (1979). Table 4-6 and all subsequent tables report mantle compositions calculated from each regression, the proportions of phases and their errors, χ^2 and the value of the probability function Q.

The experimental configuration of Fujii and Scarfe (1985) constrains the mass balance expression for basalts 1 and 2 as liq + oliv + opx + cpx + spinel = bulk mantle. All four mantle compositions provide acceptable fits for basalt 1, with liquid percentages varying from 14.5 (mantle B) to 6.4 (mantle H). The calculated solid phase proportions are all greater than zero and statistically significant, i.e. the standard errors are smaller than the calculated weight fractions. The decrease in calculated melt fraction with changing bulk composition reflects the difference in cpx + sp content between mantles B and H (Fig. 4-1). The relative proportions of olivine and orthopyroxene in each residual assemblage is directly correlated with the oliv/opx ratio in each bulk mantle composition. Oliv and opx comprise ~70 and 18% of the residue with mantle B (bulk oliv/opx ~ 2.2), compared to ~57 and 33% respectively for mantle H (bulk oliv/opx ~ 1.5). For basalt 2, calculated liquid percentages range from 21 (mantle B) to 11 (mantle H). Again all four models are statistically significant at the 95% confidence level and all of the solid phases have positive values. Compared to basalt 1, the fractions of clinopyroxene and spinel in the solid assemblage have decreased by approximately a factor of 2. The proportions of clinopyroxene and spinel in the four residues

range from 3.6 to 7.3 and 0.5 to 0.9 wt.%, respectively.

Calculated liquid, olivine and orthopyroxene proportions for the picritic basalt are also presented in Table 4-6. Based on the 20 kbar experimental results of Green et al. (1979), the appropriate mass balance expression is liquid + oliv + opx = mantle. Only mantle F produces a fit that which is significant at the 95% confidence level (Q ~ .26). Liquid comprises ~ 21% of the bulk system by weight and the normalized oliv and opx proportions are 63 and 36%. Comparing calculated and observed phase compositions in the unsuccessful models reveals that FeO in the olivine and CaO in the orthopyroxene calculated from each regression are higher than the values used to calculate the fit. The discrepency in FeO content suggests that the 20 kbar Fe-Mg K_D for olivine and liquid maybe >0.34.

Tables 4-7 through 4-9 summarize least-squares fits for basalts 4, 5 and 6 and three different sets of mantle phases. There are no experimental constraints for selecting the residual phase assemblage for these three basalt compositions. For each liquid we used the following phase combinations in eqn (1): oliv + opx, oliv + opx + cpx and oliv + opx + cpx + sp. Liquid percentages vary from ~18 to 10% for basalt 4 + oliv + opx compared to 16 to 7% when the solid phases are oliv + opx + cpx + sp. However all 12 models failed the χ^2 significance test at the 95% confidence level.

$(\delta_{FeO})^{ol}$ and $(\delta_{Cr2O3})^{opx,cpx}$ represent the largest contributions to χ^2 in all eight liq + oliv + opx ± cpx models. $(\delta_{FeO})^{ol}$ is positive, that is, FeO in the calculated olivine is

lower than in the observed olivine. $(\delta_{Cr})^{opx,cpx}$ is negative, suggesting that spinel must be an important residual phase for primary basalts with ~10 wt.% MgO. When spinel is added to the residual assemblage, chromium differences between calculated and observed pyroxenes vanish. $(\delta_{Fe})^{ol}$ remains the largest single error, comprising more than 50% of the observed χ^2 value.

Mass balance results for basalt 5 are given in Table 4-8. Degrees of melting fall in the range 21 to 12% when the residual assemblage is olivine and orthopyroxene, although none of these models are statistically significant. Basalt 5 represents 18 to 10% melt for the residual assemblage oliv + opx + cpx. Among these four models, only the fit using mantle F resulted in a Q value > 0.05 (Q ~ 0.06). For both sets of residual phases, $(\delta_{Fe})^{ol}$ is positive and $(\delta_{Cr})^{sp}$ is negative. In the unsuccessful models, these two errors contribute ~ 50% of the total value of χ^2.

When spinel was added to mass balance equation, calculated melt percentages for basalt 5 were 19 to 9%, and Q was > 0.05 for all four mantle compositions. In each of these successful models, the calculated residual assemblage is a harzburgite containing 90 to 92 wt.% oliv + opx. Residual cpx and sp lie in the range 6 to 9 and 0.8 to 1.1 wt.%, respectively.

Mass balance results using basalt 6 and the three different mantle assemblages are given in Table 4-9. Out of 12 models, only the liq + oliv + opx regressions calculated with mantles D and H had Q-values < 0.05 and could be rejected. Liquid percentages for the accepted calculations ranged from 24 to 19

(oliv + opx), 21 to 12 (oliv + opx +cpx) and 22 to 11 (oliv + opx + cpx + sp). Again, all of the residual assemblages are harzburgites. Although cpx varies from 4 to 8% in the residues, the majority of models have cpx abundances in the range of 4 to 5 wt.%. Approximately 1% of the calculated residual mantles is spinel.

DISCUSSION

Isobaric and Dynamic Melting Models

The results presented above are based on the simple model of isobaric, bulk equilibrium melting. Recent investigations suggest that this model is a poor physical description of melt generation during the adiabatic ascent of mantle material (e.g. Ahren and Turcotte, 1979; McKenzie, 1984; Ribe, 1987). Dynamic calculations show that small percentages of melt will ascend rapidly relative to the mantle matrix, and if these melt fractions are pooled prior to eruption, the final magma will represent a mixture of all liquids produced throughout the melting column. Thus the erupted basalt may not represent a liquid that was ever in equilibrium with a specific parcel of mantle at some P and T as required by the batch equilibrium equation. Furthermore, if melt migration is rapid relative to crystalline diffusion rates, then bulk equilibrium will not hold at any pressure and temperature.

Richter (1986) and Maaloe and Johnston (1986) have calculated and compared synthetic liquid compositions using melt segregation models and the simple equations for perfect

equilibrium and fractional melting. Using incompatible element concentrations from the segregation models as input, the bulk equilibrium equation recovers the melting percentages to within 10 to 50% (Richter, 1986). For compatible elements and melt fractions < 0.20, the segregation and batch equilibrium models yield very similar liquid compositions (Maaloe and Johnston, 1986). For bulk distribution coefficients in the range 0.1 to 10, the batch melting equation is also quite successful in recovering the source composition when supplied with a synthetic liquid generated by a melt segregation process (Richter, 1986; Maaloe and Johnston. 1986). Major element bulk distribution coefficients calculated for the oliv + opx + cpx ± sp assemblages and basalts 1 through 6 lie in the range 0.02 to 8, suggesting that our mass balance approach should be able to recover the major element chemistry of each observed mantle. The ability to reproduce a mantle composition is part of the test of the goodness-of-fit. The numerical analysis of Richter (1986) indicates that, for diffusion rates on the order of 10^{-17} m^2/sec, grain sizes ≤ 1 cm will be in chemical equilibrium with the liquid, and thus partial melting should approach bulk equilibrium.

The degree of partial melting calculated for each basalt in this Chapter is in general agreement with results presented by Klein and Langmuir (1987). Using high pressure experimental data, they calculate the compositions of liquids produced by mean percentages of dynamic melting. Klein and Langmuir (1987) find that as the mean melt percentage increases, the calculated

liquids become more magnesian and have lower alumina and silica contents. Similarly in this study, for a given mantle composition, calculated melt fractions increase as the basalts become richer in normative olivine content.

Implications for MORB Petrogenesis

We draw three important conclusions from the mass balance calculations reported in Tables 4-6 through 4-9. The first is that mid-Atlantic ridge basaltic glasses with ~ 9.5 wt.% MgO are not primary liquids from a spinel lherzolite mantle. All of the mass balance calculations using basalt 4, the average of 32 of these glasses, failed the χ^2 significance test at the 95% confidence level, and all but one model give Q-values < 0.01. These results are consistent with high pressure experimental data which show that MgO-rich MORB glasses are not saturated with opx at 10 kbars (Green et al. 1979; Bender et al., 1978). The fact that the addition of olivine to basalt 4 produces compositions which yield satisfactory fits is also consistent with the experimental data. Green et al. (1979) found that the addition of 17% olivine to a magnesian MORB glass stabilized orthopyroxene on the liquidus. In our numerical experiments, only a small amount of olivine (~5%) needs to be added to basalt 4 to produce acceptable solutions. Neither basalt 5 or 6 with MgO contents in the range 11 to 13 wt.% is a picritic parent in the sense of O'Hara (1968) or Elthon and Scarfe (1984). This discussion does not preclude deriving ocean floor basalts from magmas with ≥ 16% MgO. In fact, mass balance calculations show

that basalt 3, the 16% MgO picrite, can evolve to the average of the primite MORB glasses via olivine + spinel fractionation.

Our results also indicate that spinel is minor but important residual phase for partial melts with up to ~11 wt% MgO, and that spinel may still be present at the degrees of melting necessary to produce liquids with 13 to 14% MgO. The calculated spinel residues for the basalt compositions 1 and 2 and 4 through 6 lie in the range 0.5 to 1.3 wt%. In the case of basalt 5, spinel is necessary to produce acceptable mass balance solutions. These results are consistent with the observed Cr anomaly in normalized transition metal patterns in MORBs, which have been attributed to residual spinel + cpx (Langmuir et al., 1977). Nesbitt and Sun (1976) have also argued that Cr in terrestrial basalts with less than 15 wt.% MgO is controlled by spinel and clinopyroxene.

The uncertainty in the major element composition of the MORB source region makes it impossible to place narrow constraints on the percentage of melting for any primary magma. The percentage of melting required to produce a given liquid is quite sensitive to the extent of major element depletion in the source region. For example, $CaO+Al_2O_3$ is ~14% lower in mantle H relative to mantle D, while liquid fractions calculated using the same two mantles are ~30 to 40% lower. CaO and Al_2O_3 are both major constituents of basaltic liquids, and are substantially depleted in a source region by basalt extraction. Fig. 4-7 shows that acceptable mass balance solutions for basalts 1, 2, 5 and 6 define a curved band in melt fraction-bulk

$CaO+Al_2O_3$ composition space. As the wt.% of lime and alumina decreases in the bulk system, the melt fraction necessary to produce a given basaltic liquid also decreases. Fig. 4-7 demonstrates that if $CaO + Al_2O_3$ is ~ 7 wt.% in the MORB mantle, then basalts with between 11 and 13 wt.% MgO could be produced by 9 to 16% melting. However, if $CaO+Al_2O_3$ is ~ 6 wt.%, then the same basalts could be produced by 5 to 10% melting. Trace element and isotopic systematics have shown that the MORB source region is depleted in LIL-elements relative to a chondritic source (e.g. Gast, 1968; Allegre et al., 1983; Hart and Zindler, 1988). As discussed above, certain major elements, e.g TiO_2, Al_2O_3, CaO and Na_2O, should also be relatively depleted in the MORB mantle compared to bulk earth estimates. If mantle F is a reasonable approximation of the major element composition of the source region for mid-ocean ridge basalts, then primary basaltic liquids with 11 to 13 wt% MgO may represent between 6 to 12% melt. This range is substantially lower than the 20% value which is often quoted in the literature (e.g. BVSP, 1981). However, 6 to 12% melting is consistent with recent estimates based on trace element abundances (Jochum et al., 1983; Galer and O'Nions, 1986). These studies show that the variations in highly incompatible element abundances in MORBs cannot be produced by variable degrees of melting of a homogeneous mantle, but may be modelled by mixtures of high and low percentage melts or by ~10% melting of a source containing both a depleted component and an enriched residual liquid. For example, Rb/K vs Rb variations in MORBs lie along mixing lines between low (≤0.01%) and high

(~10%) percentage melts (Galer and O'Nions, 1986). The major element composition of the resulting mixture will reflect the composition of the 10% melt.

Fig. 4-8 shows K_2O abundances in basalts 1-3 and 5 and 6, calculated using the melt fractions from Tables 4-6 to 4-9, bulk mantle potassium contents (Table 4-2) and the equilibrium melting equation,

$$C_l = \frac{C_o}{F + D^*(1 - F)} \qquad (15)$$

C_l and C_o are the liquid and bulk concentration, respectively, D^* is the bulk partition coefficient for the element in question and F is the weight fraction of liquid. D^* is defined as $\Sigma X_i(D_i)$, where D_i is the crystal-liquid partition coefficient for phase i and X is the weight fraction of i in the residual assemblage. D^* was set equal to 0.001 for all of the calculations (Jochum et al., 1983). The stippled band represents the 1σ variation in wt.% K_2O in the primitive mid-Atlantic glasses compiled by Presnall and Hoover (1987). The melt fractions for basalts 1, 2, 5 and 6 calculated using mantle H coupled with an estimated K_2O content of 0.005% in the depleted mantle (Jochum et al., 1983) reproduce the lower range of observed potassium abundances in the primitive mid-Atlantic ridge glasses. The mixing processes, such as those presented by Jochum et al. (1983) and Galer and O'Nions (1986) could produce the upper range of K_2O contents observed in the primitive

glasses. As expected, calculated potassium contents using the three primitive mantle compositions plot at the top of the stippled field or well above it.

CONCLUSIONS

In this Chapter, we used major element abundances and mass balance constraints to investigate whether different mid-ocean ridge basalts could represent primary partial melts of different spinel lherzolite compositions. The average of 32 primitive mid-Atlantic ridge glasses does not appear to be a primary magma. However, the addition of 5 and 10 wt.% olivine + spinel to this composition produces liquid which may represent primary magmas. The calculated melting proportions for each basalt is directly correlated with the calcium plus alumina content in the bulk mantle. Using all of the successful mass balance solutions we define a band in % liquid vs CaO + Al_2O_3 composition space. Based on current estimates of the calcium and alumina content in the MORB source region, we estimate that primary mid-ocean ridge magmas represent 6 to 12% partial melting. This range is consistent with recent models of the trace element variations in MORBs.

REFERENCES

Ahern, J.L. and Turcotte, D.L. (1979) Magma migration beneath an oceanic ridge. Earth Planet. Sci. Lett. 45, 115-122.

Albarede, F. and Provost, A. (1977) Petrologic and geochemical mass-balance equations: An algorithm for least-squares fitting and general error analysis. Computers Geoscience 3, 309-326.

Allegre, C.J., Hart, S.R. and Minster, J.-F. (1983) Chemical structure and evolution of the mantle and continents determined by inversion of Nd and Sr isotopic data, II. Numerical experiments and discussion. Earth Planet. Sci. Lett. 66, 191-213.

Anders, E. and Ebihara, M. (1982) Solar system abundances of the elements. Geochim. Cosmochim. Acta 46, 2363-2380.

Arculus, R.J. (1985) Oxidation state of the earth's mantle: Past and present. Ann. Rev. Earth Planet. Sci. 13, 75-95.

Basaltic Volcanism Study Project (1981) "Basaltic Volcanism on the Terrestrial Planets". Pergamon Press, Inc., 1286 pp.

Bender, J.F., Hodges, F.N. and Bence, A.E. (1978) Petrogenesis of basalts from the project FAMOUS area: Experimental sudy from 0 to 15 kbars. Earth Planet. Sci. Lett. 41, 277-302.

Bender, J.F., Langmuir, C.H. and Hanson, G.N. (1984) Petrogenesis of basalt glasses from the Tamayo region, East Pacific Rise. Jour. Petrol. 25, 213-254.

Bevington, P.R. (1969) "Data Reduction and Error Analysis for the Physical Sciences". McGraw-Hill, 336 pp.

Bonatti, E. and Hamlyn, P.R. (1981) Oceanic ultramafic rocks. In The Sea, vol. 7, The Oceanic Lithosphere. ed. C. Emiliani. Wiley, 1738 pp.

Bougault, H. and Hekinian, R. (1974) Rift valley in the Atlantic Ocean near 36°50'N: Petrology and geochemistry of basaltic rocks. Earth Planet. Sci. Lett. 24, 249-261.

Christie, D.M., Carmichael, I.S.E. and Langmuir, C.H. (1986) Oxidation states of mid-ocean ridge basalt glasses. Earth Planet. Sci. Lett. 79, 397-411.

Dick, H.J.B. and Bullen, T. (1984) Chromian spinels as a petrogenetic indicator in abyssal and alpine-type peridotites and spatially associated lavas. Contrib. Mineral. Petrol. 86, 54-76.

Dick, H.J.B. and Fisher, R.L. (1984) Mineralogic studies of the residues of mantle melting: abyssal and alpine-type peridotites. In "Kimberlites II: The Mantle and Crust-Mantle Relationships." ed. Kornprobst, J., Elsevier, 393 pp.

Dunn, T. (1987) Partitioning of Hf, Lu, Ti, and Mn between olivine, clinopyroxene and basaltic liquid. Contrib. Mineral. Petrol. 96, 476-484.

Elthon, D. (1986) Comments on "Composition and depth of origin of primary mid-ocean ridge basalts" by D.C. presnall and J.D. Hoover. Contrib. Mineral. Petrol. 94, 253-256.

Elthon, D. and Scarfe, C.M. (1984) High pressure phase equilibria of a high-magnesia basalt and the generation of primary oceanic basalts. Amer. Mineral. 69, 1-15.

Engi, M. (1983) Equilibria involving Al-Cr spinel: Fe-Mg exchange with olivine. Experiments, thermodynamic analysis and consequences for geothermometry. Am. J. Sci 283-A, 29-71.

Frey, F.A. and Prinz, M. (1978) Ultramafic inclusions from San Carlos, Arizona: Petrologic and geochemical data bearing on their petrogenesis. Earth Planet. Sci Lett. 38, 129-176.

Fujii, T. and Bougault, H. (1983) Melting relations of a magnesian abyssal tholeiite and the origin of MORBs. Earth Planet. Sci. Lett. 62, 283-295.

Fujii, T. and Scarfe, C.M. (1985) Composition of liquids coexisting with spinel lherzolite at 10 kbar and the genesis of MORBs. Contrib. Mineral. Petrol. 90, 18-28.

Galer, S.J.G. and O'Nions, R.K. (1986) Magmagenesis and the mapping of chemical and isotopic variations in the mantle. Chem. Geol. 56, 45-61.

Gast, P.W. (1968) Trace element fractionation and the origin of tholeiitic and alkaline magma types. Geochim. Cosmochim. Acta 32, 1057-1086.

Green, D.H., Hibberson, W.O. and Jaques, A.L. (1979) Petrogenesis of mid-ocean ridge basalts. In, The Earth: Its Origin, Structure and Evolution. ed. M.W. McElhinny, Academic Press, 500 pp.

Grove, T.L. and Baker, M.B. (1984) Phase equilibrium controls on the tholeiitic versus calc-alkaline differentiation trends. J. Geophys. Res. 89, 3253-3274.

Grove, T.L. and Bryan, W.B. (1983) Fractionation of pyroxene-phyric MORBs at low pressure: an experimental study. Contrib. Mineral. Petrol. 84, 293-309.

Grover, J.E., Lindsley, D.H. and Bence, A.E. (1980) Experimental phase relations of olivine vitrophyres from breccia 14321: The temperature- and pressure-dependence of Fe-Mg partitioning for olivine and liquid in a highlands melt rock. Proc. Lunar Planet. Sci. Conf. 11th, 179-196.

Hart, S. and Zindler, A. (1988) Constraints on the nature and development of chemical heterogeneities in the mantle. In Mantle Convection. ed. D. Peltier. (in press).

Hart, S.R. and Zindler, A. (1986) In search of a bulk-earth composition. Chem. Geol. 57, 247-267.

Henderson, P. (1982) "Inorganic Geochemistry" Pergamon Press, 353 pp.

Hoffman, A.W. (1983) Buffered and unbuffered elements in MORB. EOS 64, 345.

Hutchison, R. (1974) The formation of the earth. Nature 250, 556-558.

Jagoutz, E., Palme, H., Badenhausen, H., Blum, K., Cendales, M., Dreibus, G., Spettel, G., Lorenz, V. and Wanke, H. (1979) The abundances of major and trace elements in the Earth's mantle as derived from primitive ultramafic nodules. Proc. Lunar Planet. Sci. Conf. 10th, 2031-2050.

Jaques, A.L. and Green, D.H. (1980) Anhydrous melting of peridotite at 0-15 kb pressure and the genesis of tholeiitic basalts. Contrib. Mineral. Petrol. 73, 287-310.

Jochum, K.P., Hofmann, A.W., Ito, E. Seufert, H.M. and White, W.M. (1983) K, U and Th in mid-ocean ridge basalt glasses and heat production, K/U and K/Rb in the mantle. Nature 306 431-436.

Kay, R., Hubbard, N.J. and Gast, P.W. (1970) Chemical characteristics and origin of oceanic ridge volcanic rocks. Jour. Geophys. Res. 75, 1585-1613.

Klein, E.M. and Langmuir, C.H. (1987) Global correlations of ocean ridge basalt chemistry with axial depth and crustal thickness. Jour. Geophys. Res. 92, 8089-8115.

Langmuir, C.H., Bender, J.F., Bence, A.E. and Hanson, G.N. (1977) Petrogenesis of basalts from the Famous area: mid-Atlantic ridge. Earth Planet. Sci. Lett. 36, 133-156.

Lindsley, D.H. (1980) Phase equilibria of pyroxene at pressures > 1 atmosphere. In "Reviews in Mineralogy, vol 7, Pyroxenes". Mineralogical Society of America, 525 pp.

Lindsley, D.H. and Andersen, D.J. (1983) A two-pyroxene thermometer. Proc. Lunar Planet. Sci. Conf. 13th, A887-A906.

Longhi, J., Walker, D. and Hays, J.F. (1977) Fe and Mg distribution between olivine and lunar basaltic liquids. Geochim. Cosmochim. Acta 42, 1545-1558.

Maaloe, S and Johnston, A.D. (1986) Geochemical aspects of some accumulation models for primary magmas. Contrib. Mineral. Petrol. 93, 449-458

Mathez, E.A. (1984) Influence of degassing on oxidation states of basaltic magmas. Nature 310, 371-375.

Mattioli, G. and Wood, B.J. (1986) Upper mantle oxygen fugacity recorded by spinel lherzolites. Nature 322, 626-628.

McKenzie, D.P. (1984) The generation and compaction of partially molten rock. J. Petrol. 25, 713-765.

Mysen, B.O. and Kushiro, I. (1977) Compositional variations of coexisting phases with degree of melting of peridotite in the upper mantle. Amer. Mineral. 62, 843-865.

Nelder, J.A. and Meade, R. (1965) A simplex method for function minimization. Computer Journal 7, 308-313.

Nesbitt, R.W. and Sun, S-S. (1976) Geochemistry of Archean spinifex textured peridotites and magnesian and low magnesian tholeiites. Earth Planet. Sci. Lett. 31, 433-453.

O'Hara, M.J. (1985) Importance of the 'shape' of the melting regime during partial melting of the mantle. Nature 314, 58-62.

O'Hara, M.J.(1968) The bearing of phase equilibria studies on the origin and evolution of basic and ultrabasic rocks. Earth Sci. Rev. 4, 69-133.

Palme, H. and Nickel, K.G. (1985) Ca/Al ratio and composition of the Earth's upper mantle. Geochim. Cosmochim. Acta 49, 2123-2132.

Presnall, D.C. and Hoover, J.D. (1984) Composition and depth of origin of primary mid-ocean ridge basalts. Contrib. Mineral. Petrol. 87, 170-178.

Presnall, D.C. and Hoover, J.D. (1987) High pressure phase equilibrium constraints on the origin of mid-ocean ridge basalts. In "Magmatic Processes: Physicochemical

Principles". ed. B.O. Mysen, The Geochemical Society, 500 pp.

Presnall, D.C., Dixon, J.R., O'Donnell, T.H. and Dixon, S.A. (1979) Generation of mid-ocean ridge tholeiites. Jour. Petrol. 20, 3-35.

Press, W.H., Flannery, B.P., Teukolsky, S.A. and Vetterling, W.T. (1986) "Numerical Recipes: The Art of Scientific Computing". Cambridge University Press, 818 pp.

Ribe, N.M. (1987) Theory of melt segregation - a review. J. Volcan. Geotherm. Res. 33, 241-253.

Richter, F.M. (1986) Simple models for trace element fractionation during melt segregation. Earth Planet. Sci. Lett. 77, 333-344.

Ringwood, A.E. (1975) "Composition and Petrology of the Earth's Mantle". McGraw-Hill, N.Y. 618 pp.

Ringwood, A.E. (1979) "Origin of the Earth and Moon". Springer-Verlag, 295 pp.

Roeder, P.L. and Emslie, R.F. (1970) Olivine-liquid equilibria. Contrib. Mineral. Petrol. 29, 275-289.

Sen, G and Jones, R.E. (1988) Exsolved silicate and oxide phases from clinopyroxenes in a single Hawaiian xenolith: Implications for oxidation state of the Hawaiian upper mantle. Geology 16, 69-72.

Shibata, T. and Thompson, G. (1986) Peridotites from the mid-Atlantic ridge at 43°N and their petrogenetic relationship to abyssal peridotites. Contrib. Mineral. Petrol. 93, 144-159.

Stolper, E. (1980) A phase diagram for mid-ocean ridge basalts: Preliminary results and implications for petrogenesis. Contrib. Mineral. Petrol. 74, 13-27.

Sun, S-S. (1982) Chemical composition and origin of the Earth's primitive mantle. Geochim. Cosmochim. Acta 46, 179-192.

Takahashi, E. (1986) Melting of a dry peridotite KLB-1 up to 14GPa: Implications on the origin of peridotitic upper mantle. Jour. Geophys. Res. 91, 9367-9382.

Takahashi, E. and Kushiro, I. (1983) Melting of dry peridotite at high pressures and basalt magma genesis. Amer. Mineral. 68, 859-879.

Tatsumoto, M, Hedge, C.E. and Engel, A.E.J. (1965) Potassium, rubidium, strontium, thorium, uranium and the ratio of strontium-87 to strontrium-86 in oceanic tholeiitic basalts. Science 150, 886-888.

Thompson, R.N. and Kushiro, I. (1972) The oxygen fugacity within graphite capsules in piston-cylinder apparatus at high pressures. Carnegie Inst. Wash. Yearbook 71, 615-616.

Wanke, H. (1981) Constitution of terrestrial planets. Phil. Trans. R. Soc. Lond. A303, 287-302.

Figure 4-1. Primitive mantle compositions (Table 4-2) projected from spinel onto the plane olivine - clinopyroxene - orthopyroxene. Mineral components are calculated using oxide mole percents and the following expressions:

$$Oliv = -[SiO_2]-[Al_2O_3]-[Cr_2O_3]+[MgO]+[FeO]+[CaO]+0.5[Na_2O]$$

$$Opx = [SiO_2]+0.5\{[Al_2O_3]+[Cr_2O_3]-[MgO]-[FeO]\}-1.5[CaO]-4.5[Na_2O]$$

$$Cpx = [CaO]$$

$$Jd = 2[Na_2O]$$

$$Sp = [Al_2O_3]-[Na_2O]$$

$$Her = [Cr_2O_3]$$

The components are then weighted by the number of oxygens in each mineral formula, Cpx and Jd are combined to form a new Cpx component, Sp and Her are combined to form a new Sp component and then Oliv, Opx, Cpx and Sp are normalized to 1.

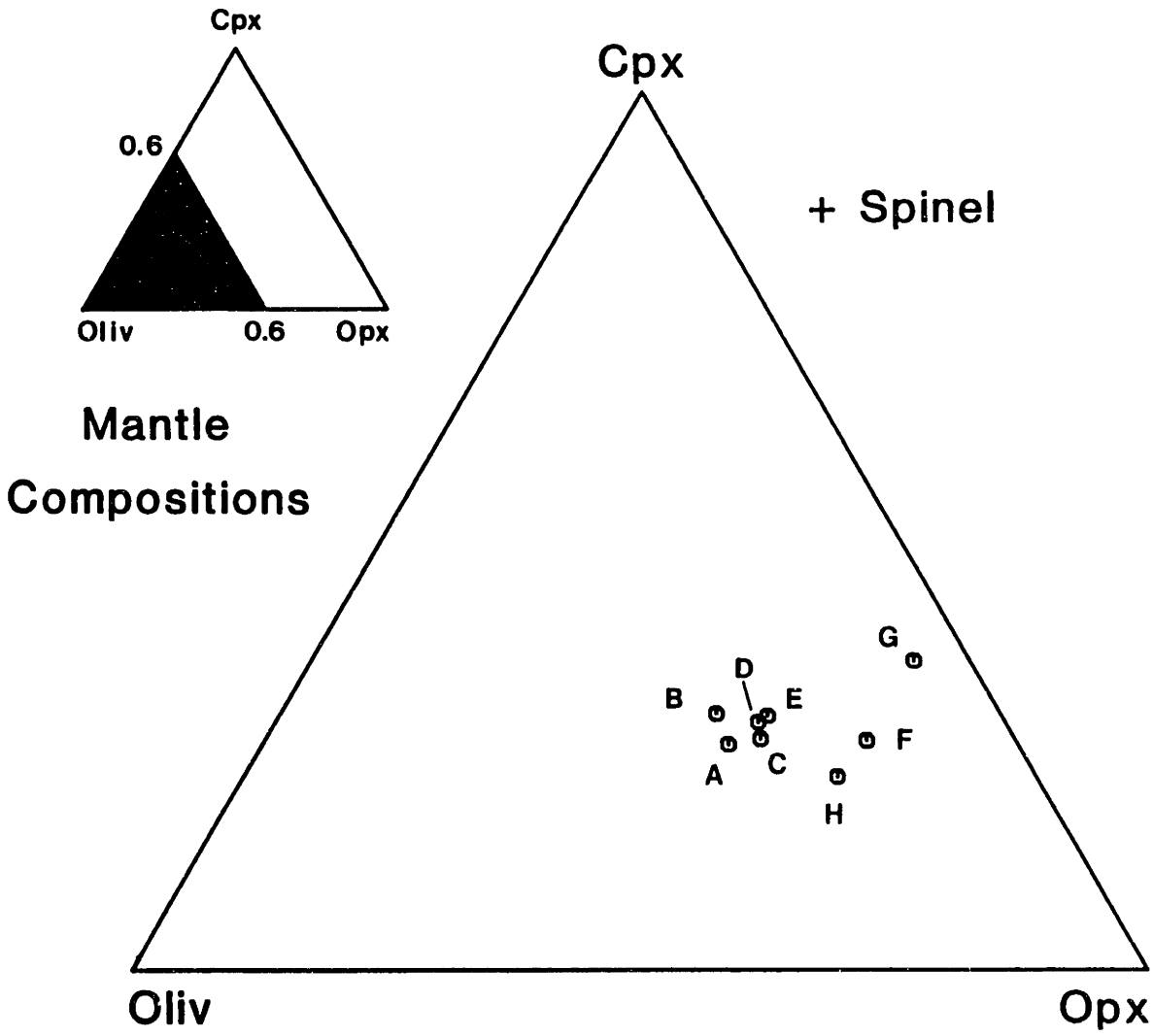
Cpx
0.6
Oliv
0.6
Opx
Mantle
Compositions
Cpx
+ Spinel
A
B
C
D
E
F
G
H
Oliv
Opx

Figure 4-2. (a) CaO (mole%) in orthopyroxenes vs. run temperature in °C from 10 kbar basalt melting experiments. Data from Table 4-3. (b). MgO+FeO plotted against CaO (both in mole%) in opx from 10 kbar basalt melting experiments; Table 4-4.

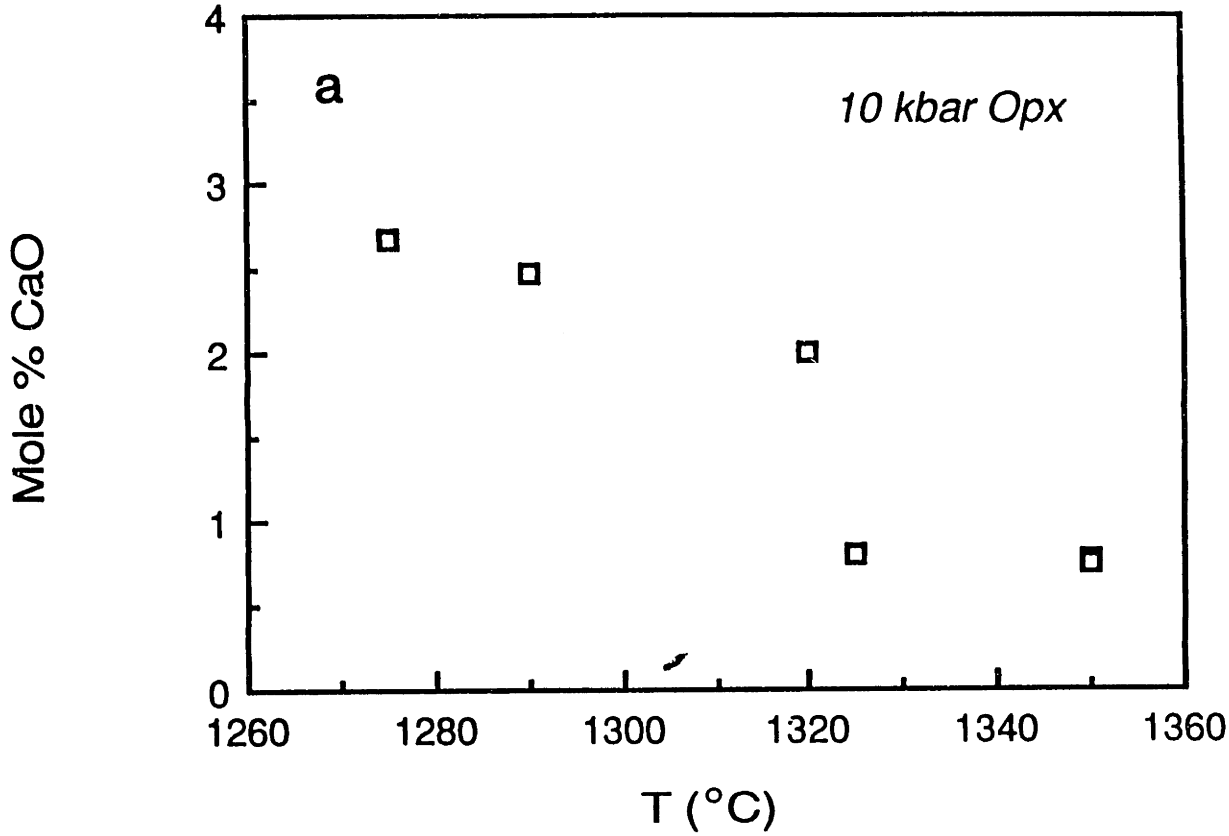
a
10 kbar Opx
Mole % CaO
T (°C)
0
1
2
3
4
1260
1280
1300
1320
1340
1360

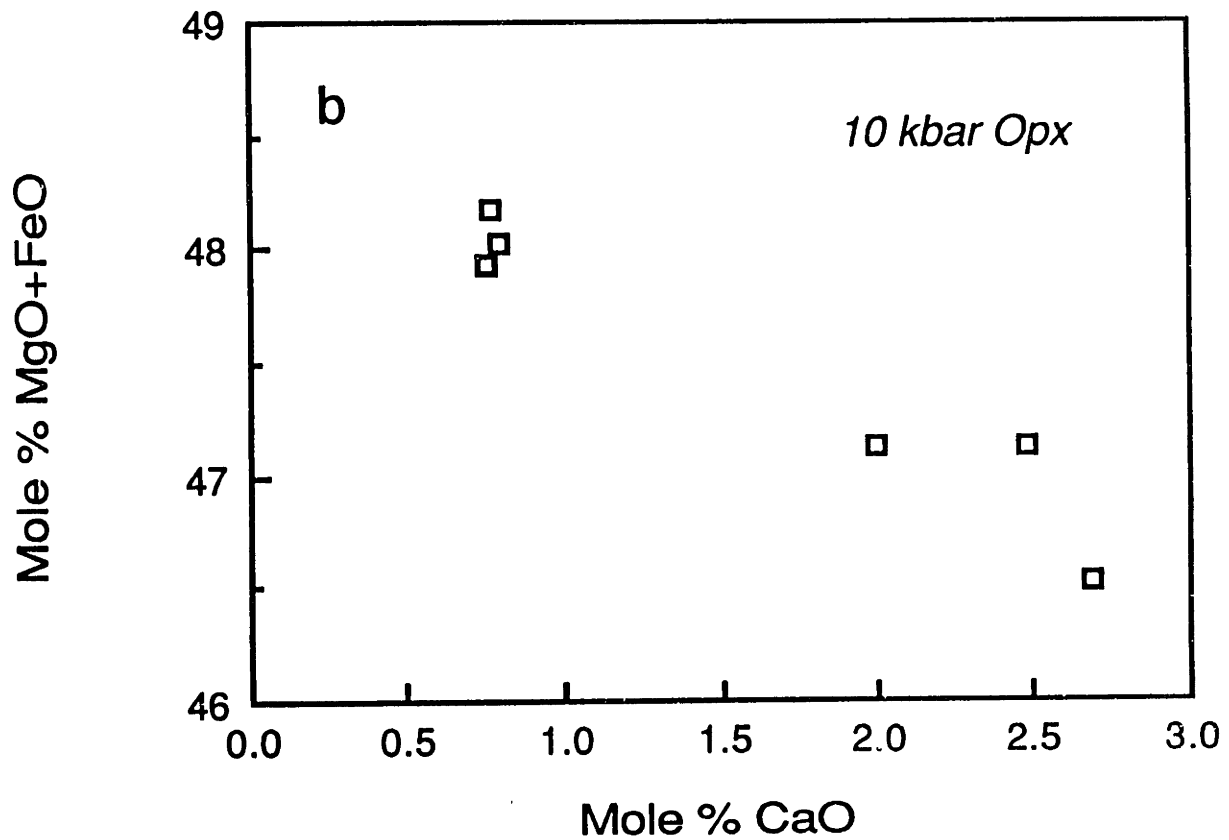
b
10 kbar Opx
Mole % MgO+FeO
Mole % CaO
46
47
48
49
0.0
0.5
1.0
1.5
2.0
2.5
3.0

Figure 4-3. Clinopyroxene CaO contents (mole%) as a function of experimental run temperature (°C) at ~10 kbars; data from Table 4-4. Regression equation based on open and closed squares. Closed square is the average of 4 1250°C experiments from Dunn (1987). Crosses represent disequilibrium clinopyroxenes.

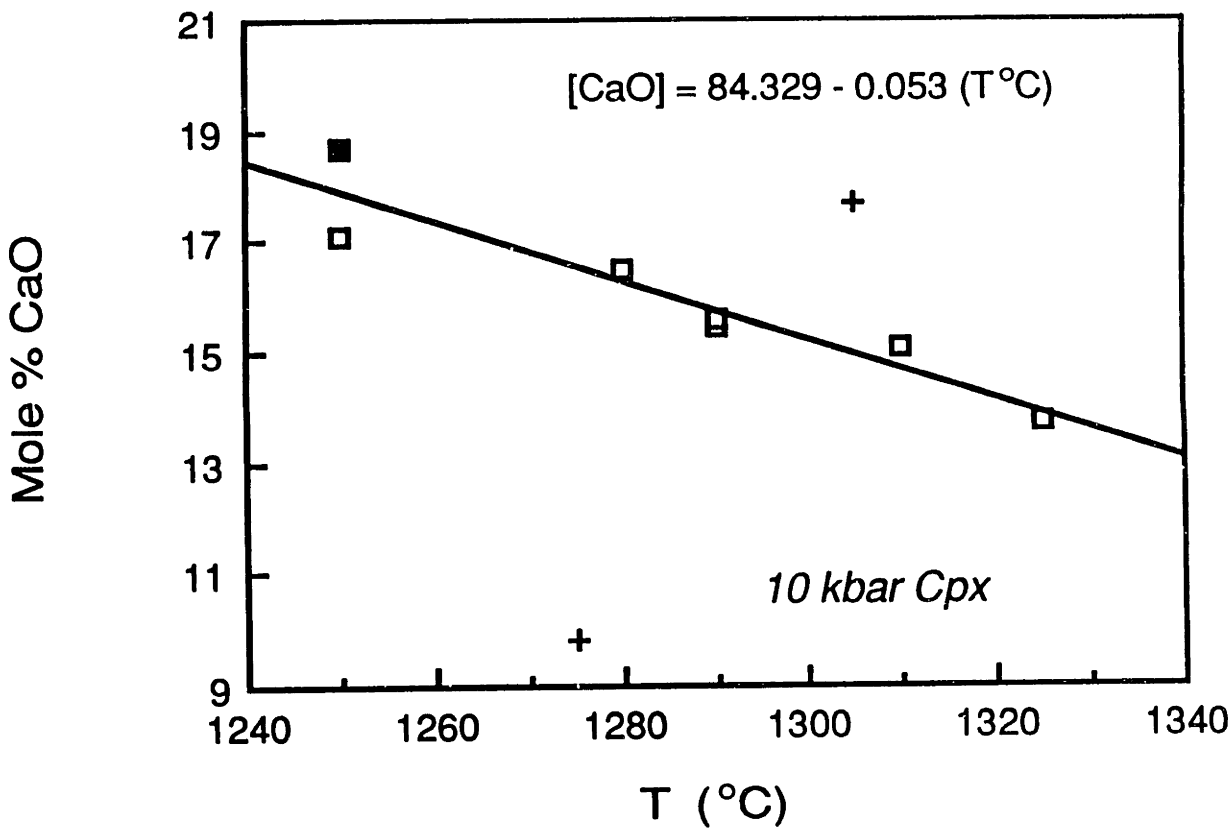
[CaO] = 84.329 - 0.053 (T°C)
10 kbar Cpx
Mole % CaO
T (°C)
21
19
17
15
13
11
9
1240
1260
1280
1300
1320
1340

Figure 4-4. Mole% MgO+FeO vs CaO in ~10 kbar clinopyroxenes; data from Table 4-4. Regression equation based on all data.

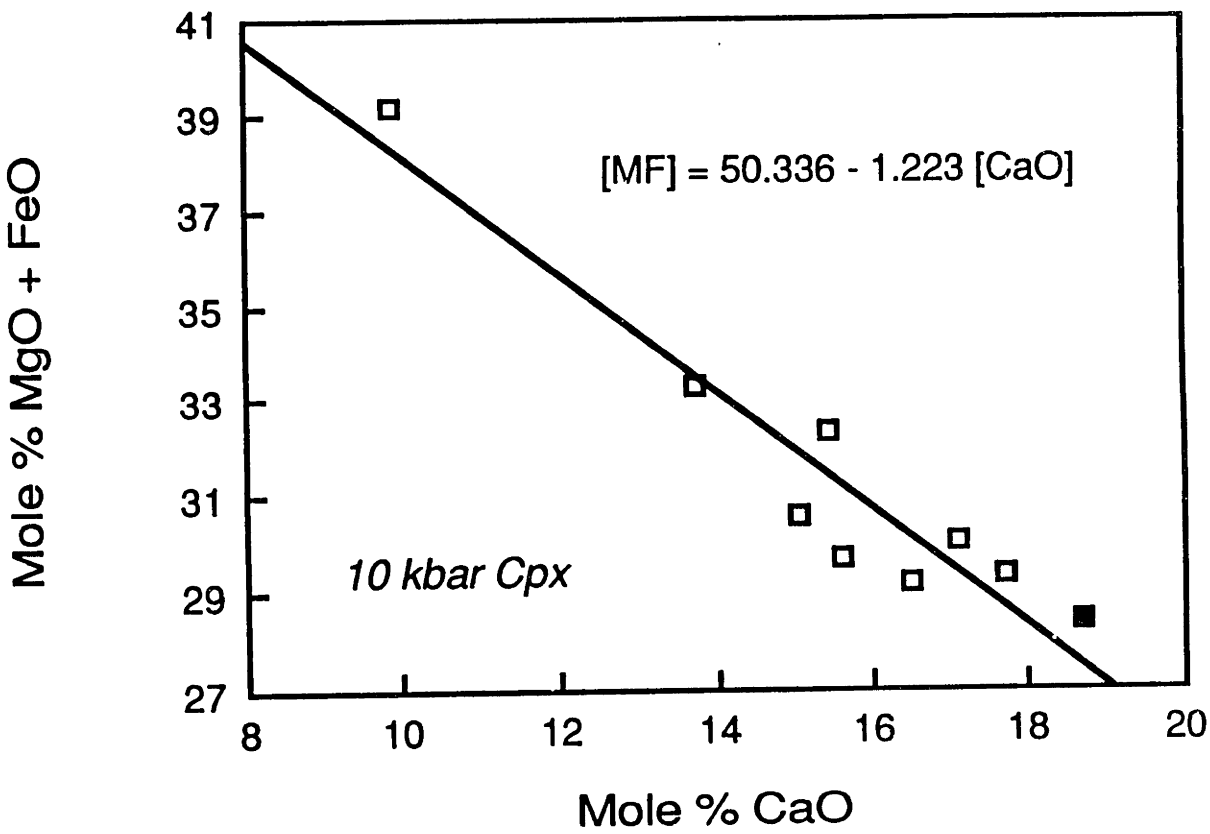
41
39
37
35
33
31
29
27
8
10
12
14
16
18
20
Mole % MgO + FeO
Mole % CaO
[MF] = 50.336 - 1.223 [CaO]
10 kbar Cpx

Figure 4-5. Al_2O_3 contents in spinels and orthopyroxenes calculated to be in equilibrium with basalts 1, 2, 4, 5 and 6. Field from San Carlos ultramafic inclusions, Frey and Prince (1978); field from abyssal and Alpine peridotites, Dick and Fischer (1985). Numbers by each symbol refer to the basalt used in the calculation.

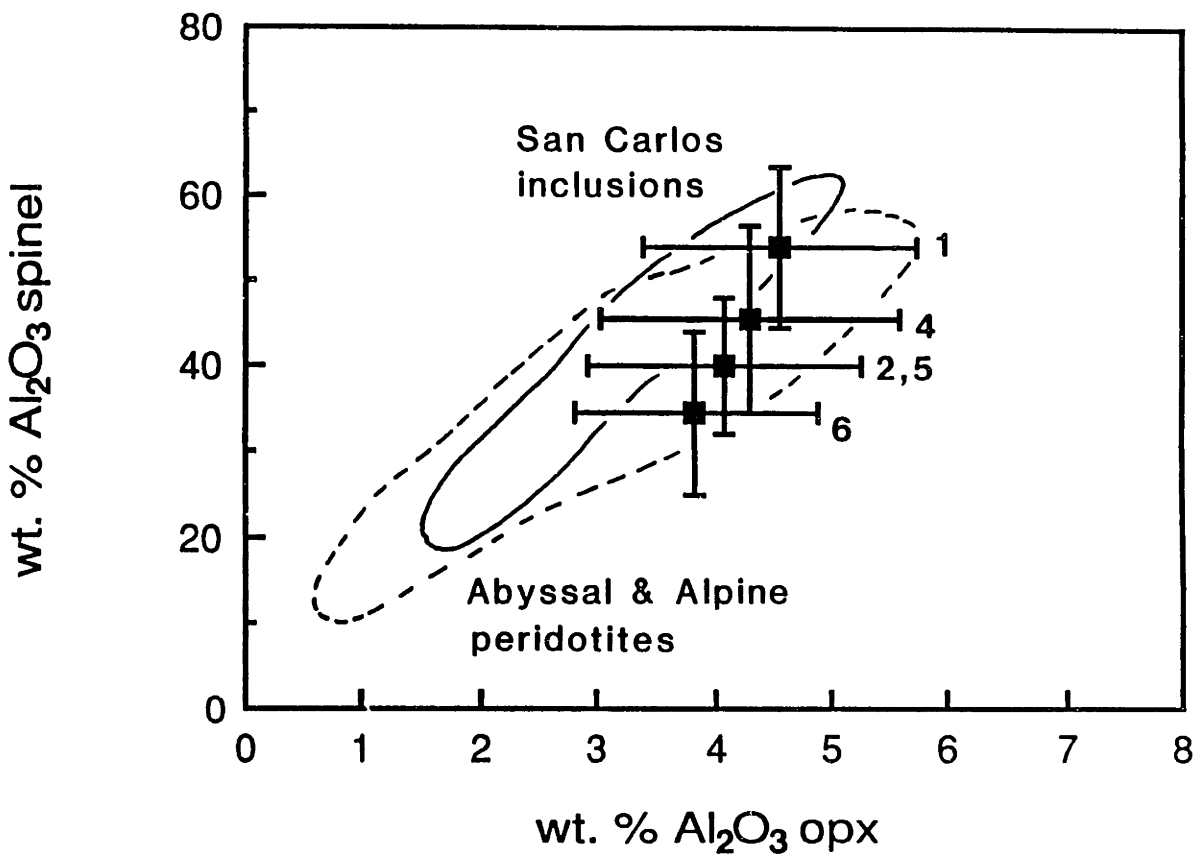
80
60
40
20
0
0
1
2
3
4
5
6
7
8
wt. % Al_2O_3 spinel
wt. % Al_2O_3 opx
San Carlos
inclusions
Abyssal & Alpine
peridotites
1
4
2,5
6

Figure 4-6. Cr/(Cr+Al) plotted against Mg/(Mg+Fe*), total Fe as FeO, for calculated equilibrium spinels in basalts 4 - 6. Uncertainties in the Mg# are based on the standard deviations for MgO and FeO in each spinel composition (Table 4-5). The errors in Cr/(Cr+Al) for each plotted spinel cover almost the entire field and are not shown. Abyssal peridotite field from Dick and Bullen (1984). Numbers beside each square refer to the basalt used in the calculation.

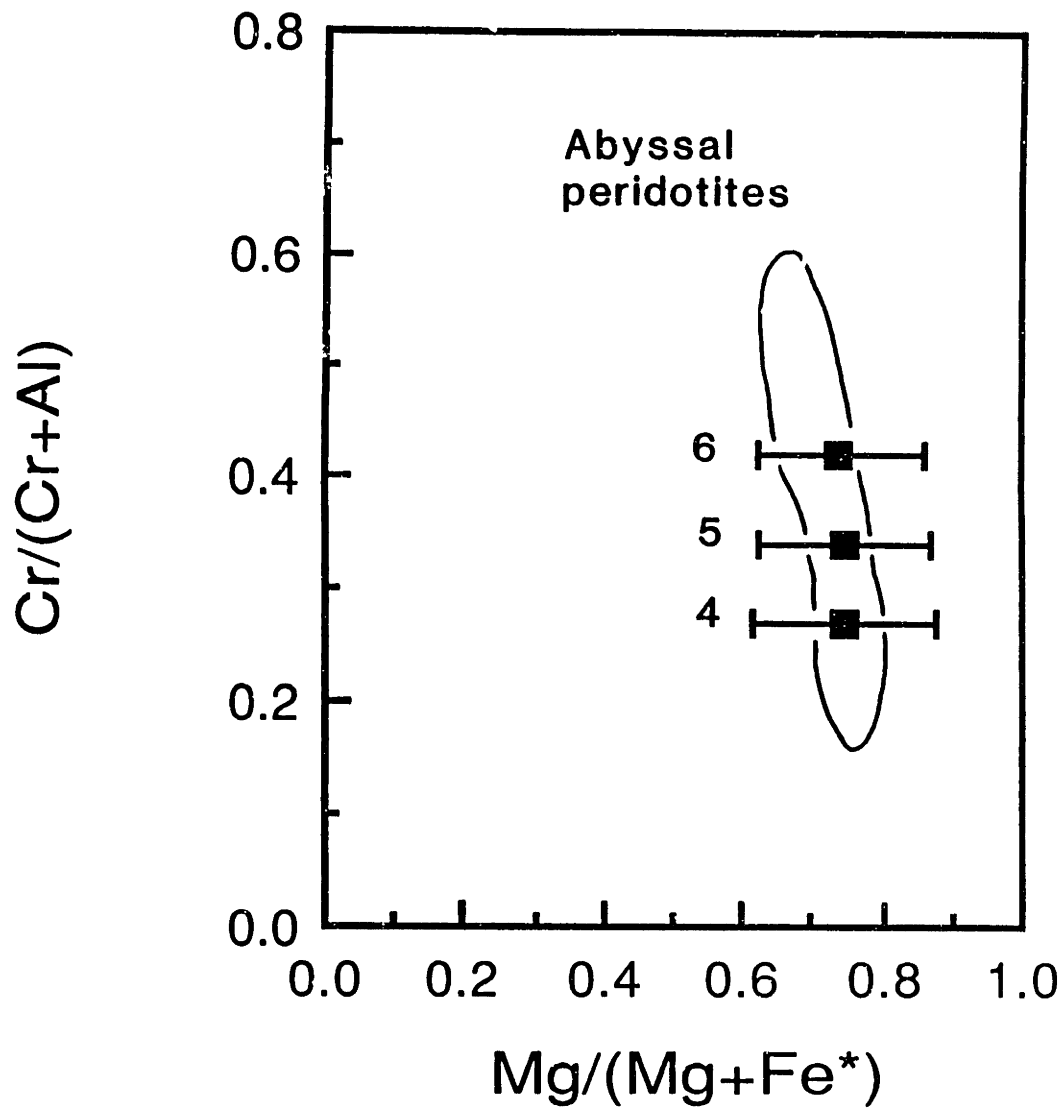
0.8
0.6
0.4
0.2
0.0
Cr/(Cr+Al)
Abyssal
peridotites
6
5
4
0.0
0.2
0.4
0.6
0.8
1.0
Mg/(Mg+Fe*)

Figure 4-7. Field of the percentage of melting neccessary to produce liquids with 11 to 13% MgO as a function of $CaO+Al_2O_3$ in the bulk mantle. Letters by each arrow show the calcium plus aluminum content in each mantle composition.

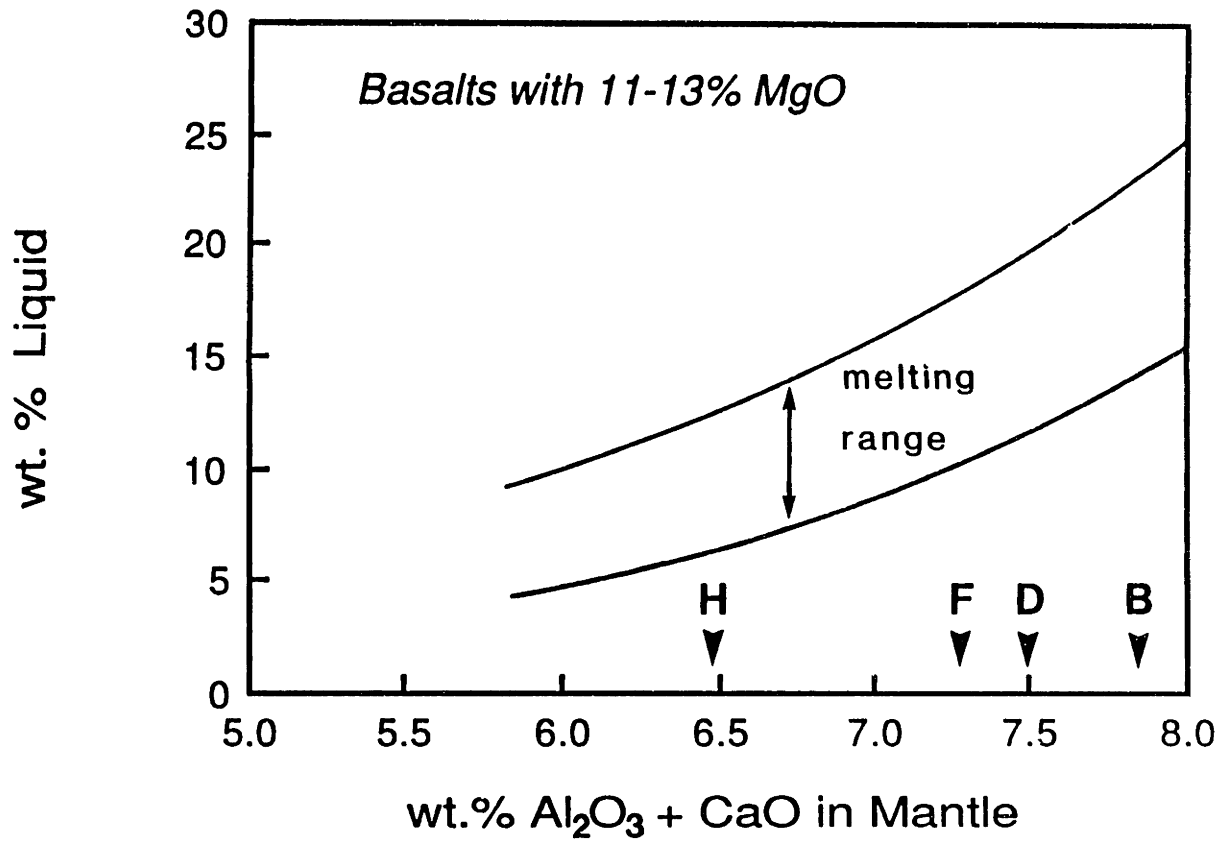
Basalts with 11-13% MgO
melting
range
H
F
D
B
30
25
20
15
10
5
0
5.0
5.5
6.0
6.5
7.0
7.5
8.0
wt. % Liquid
wt.% Al2O3 + CaO in Mantle

Figure 4-8. K_2O contents for basalts 1, 2, 3 ,5 and 6 calculated from the melting percentages (Tables 4-6 through 4-9), mantle potassium values (Table 4-2) and the batch melting equation. Bulk distribution coefficient for K_2O = 0.001 (Jochum et al., 1983). The band labelled primitive glasses represents the 1σ variation in K_2O in the 32 primitive mid-Atlantic glasses compiled by Presnall and Hoover (1987).

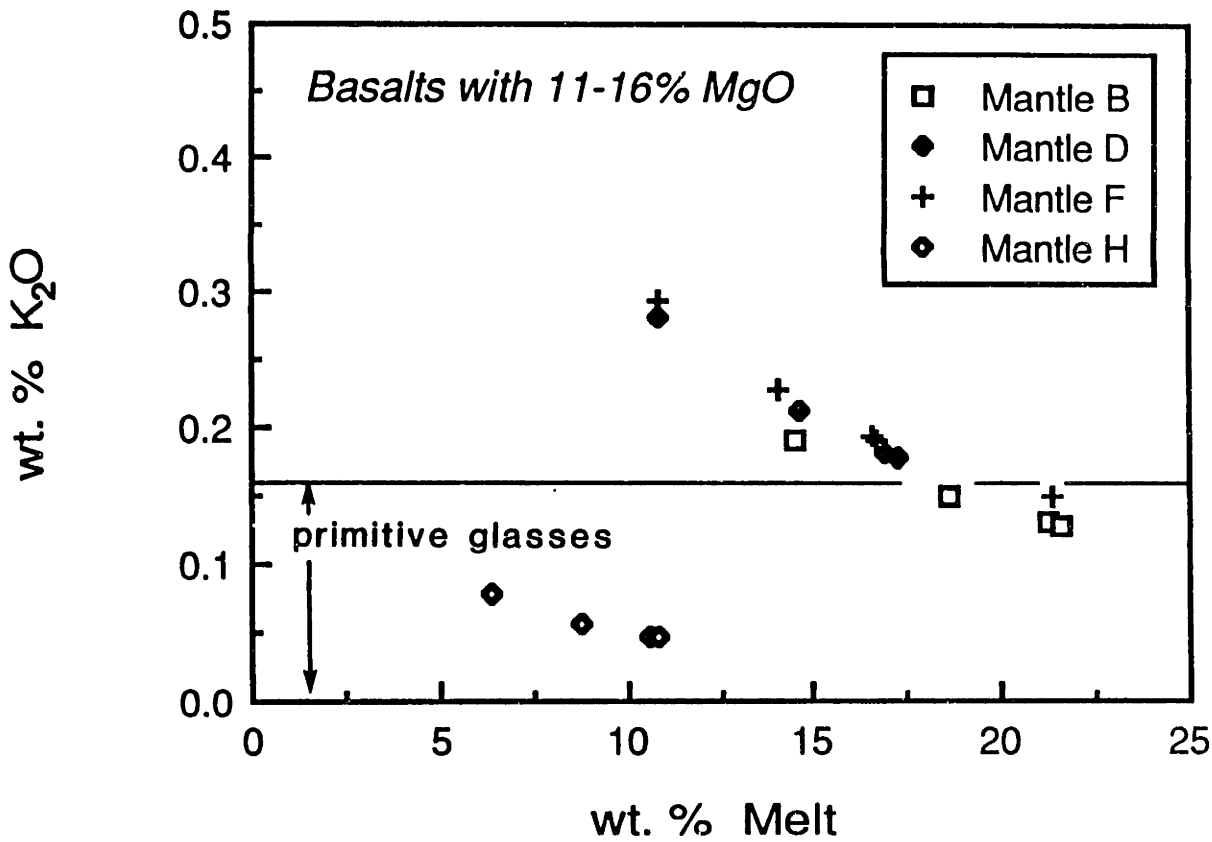
Basalts with 11-16% MgO
Mantle B
Mantle D
Mantle F
Mantle H
primitive glasses
wt. % K_2O
wt. % Melt
0.0
0.1
0.2
0.3
0.4
0.5
0
5
10
15
20
25

Table 4-1. Basalt compositions used in mass balance calculations

	1	2	3	4	5	6
SiO_2	49.1(1)[7]	49.3(1)	48.3(6)	49.9(8)	49.4(8)	49.0(8)
TiO_2	0.68(1)	0.63(1)	0.60(2)	0.79(11)	0.75(10)	0.71(10)
Al_2O_3	17.0(1)	15.4(1)	13.7(1)	16.8(8)	15.4(7)	14.7(7)
Cr_2O_3	0.08(1)	0.15(1)	0.15(1)	0.07(3)	0.10(4)	0.13(6)
FeO	7.00(8)	7.23(8)	7.9(1)	8.32(36)	8.46(37)	8.54(37)
MgO	11.1(1)	12.2(1)	16.7(2)	9.73(51)	11.5(6)	13.3(7)
CaO	12.0(1)	12.2(1)	10.9(2)	12.6(6)	12.0(5)	11.4(5)
Na_2O	2.29(6)	1.84(5)	1.65(7)	2.07(22)	1.97(21)	1.88(20)
Mg#[8]	73.9	75.0	79.0	67.6	70.8	73.5

[1] Glass #7; T=1275°C, P=10 kbars; Fujii and Scarfe (1985; Table 6); values in parentheses are estimated uncertainties for each oxide based on the standard deviations reported by Fujii and Scarfe (1985; Appendix). The reported standard deviations were converted into fraction errors (σ/mean), averaged and used to calculate the σ values for columns 1 and 2.

[2] Glass #8; T=1290°C, P=10 kbars; Fujii and Scarfe (1985; Table 6)

[3] Mix E, (Green et al., 1979; Table 1). Mix E equals 83% DSDP-18 + 17% olivine. Standard deviations calculated using fraction errors based on MORB glass analyses from Grove and Bryan (1983). Cr_2O_3 raised to a value comparable to chrome contents in lavas with similar MgO values (BVSP, 1981, Table 1.4.2.1).

[4] Average of 32 primitive Atlantic MORB glasses compiled in Presnall and Hoover (1987; Appendix 1). Values in parentheses represent 1 standard deviation about the mean.

[5] Glass #4 + 5 wt.% of the calculated equilibrium assemblage 0.98 olivine and 0.02 spinel.

[6] Glass #4 + 10 wt.% of the calculated equilibrium assemblage 0.98 olivine and 0.02 spinel.

[7] Parenthesized units represent one standard deviation in terms of the least units cited, i.e. 49.1(1) = 49.1±0.1.

[8] Mg# = 100 Mg/(Mg+Fe^*) where Fe^* = total Fe as Fe^{+2}.

Table 4-2. Primitive mantle estimates[1]

	A	B	C	D	E	F	G	H[2]	Error[3]
SiO_2	45.0	44.5	45.1	45.1	45.1	45.96	46.2	45.73	.013
TiO_2	0.09	0.22	0.2	0.22	0.22	0.18	0.23	0.14	.169
Al_2O_3	3.5	4.31	3.3	3.97	4.14	4.06	4.75	3.63	.050
Cr_2O_3	0.41	0.44	0.4	0.46	0.45	0.47	0.43	0.48	.059
FeO	8.0	8.36	8.0	7.82	7.82	7.55	7.70	7.56	.033
MgO	39.0	38.0	38.1	38.3	38.0	37.77	35.5	38.90	.029
CaO	3.25	3.50	3.1	3.50	3.54	3.21	4.36	2.82	.050
Na_2O	0.28	0.39	0.4	0.33	0.36	0.33	0.40	0.22	.111
K_2O	0.035	0.028	0.03	0.031	-	0.032	-	0.005	.083
Mg#[4]	89.7	89.0	89.5	89.7	89.6	89.9	89.2	90.2	
Ca/Al[5]	1.25	1.10	1.27	1.19	1.15	1.07	1.24	1.05	

[1] References: A - Hutchison (1974); B - Sun (1982); C - Ringwood (1979); D - Jagoutz et al. (1979); E - Wanke (1981); F,H - Hart and Zindler (1986); G - Palme and Nickel (1985).

[2] Composition F minus 4% melt. Melt composition: 51.4 SiO_2; 1.0 TiO_2; 13.2 Al_2O_3; 0.1 Cr_2O_3; 7.1 FeO; 10.8 MgO; 12.5 CaO; 3.0 Na_2O. SiO_2, Al_2O_3, MgO and CaO values from Hart and Zindler (1986; Table B-1); FeO calculated so that liquid would be in equilibrium with Fo_{90} olivine; TiO_2, Cr_2O_3 and Na_2O based on lowest temperature experimental glasses reported by Fujii and Scarfe (1985) and primitive liquids compiled in BVSP (1981; Table 1.4.2.1). K_2O from Jochum et al., (1983).

[3] Excepting Al_2O_3 and CaO, errors are fractional uncertainties based on the mean for each oxide in mantles A-G. Uncertainties for Al_2O_3 and CaO based on the standard deviations of these oxides for the mean C1 composition reported by Anders and Ebihara (1982).

[4] Mg# = 100 Mg/(Mg+Fe*) where Fe* equals total iron as Fe^{2+}.

[5] Ca/Al ratio calculated on a weight basis; chondritic value = 1.07 (Anders and Ebihara, 1982).

Dashes indicate that element was not reported.

Table 4-3. ~10 and 20 kbar orthopyroxene - liquid experimental data

10 kbar Opx Data[1]

Run#	[MF]	[CaO]	K_D	D_{Ti}	D_{Al}	D_{Cr}	D_{Na}	Co-existing ϕ	T(°C)	Ref[2]
35	46.52	2.68	.32	.23	.22	4.7	-	liq,ol,cpx	1275	1
13L1	47.13	2.46	.26	.15	.23	8.5	.05	liq,cpx	1290	2
D180	47.12	2.00	.27	-	-	-	-	liq,ol	1320	3
21	48.03	.80	.28	.17	.23	3.0	.04	liq,ol,cpx,sp	1325	4
519-12	48.18	.77	.27	.16	.23	2.2	.07	liq,ol	1350	5
519-10	47.94	.75	.24	.16	.22	6.0	.05	liq,ol	1350	5
Mean[3]	46.92	2.39	.27	.17	.23	6.4	.05			
Error[4]	.35	.35	.03	.03	.01	2.0	.01			

20 kbar Opx Data

43	46.35	1.94	.32	.11	.26	5.5	.04	liq,ol,cpx	1375	1
519-16	47.38	1.65	.30	.11	.33	2.0	.05	liq,ol	1450	5
Mean	46.86	1.63	.31	.16	.30	6.6	.05			
Error	.73	.54	.03	.04	.03	1.3	.01			

[1] Opx = orthopyroxene; [MF] = MgO+FeO in opx in oxide mole%, [CaO] = mole% of CaO in opx. Exchange (K_D) and distribution coefficients (D_i) calculated on an oxide mole% basis. $K_D = (Fe/Mg)^{opx}/(Fe/Mg)^{liq}$. Other abbreviations: liq = liquid, ol = olivine, cpx = clinopyroxene, sp = spinel.

[2] References: 1 - Takahashi and Kushiro (1983); 2 - Fujii and Bougault (1983); 3 - Tatsumi et al. (1983); 4 - Takahashi (1986); 5 - Stolper (1980).

[4] Mean, in general calculated from all of tha data in a given column; see text for exceptions.

[3] Errors generally represent 1σ about the mean; see discussion in text for exceptions. The 10kb MgO+FeO, CaO, D_{Ti}, D_{Cr} and D_{Na} parameters were included in the calculations of the 20kb means.

Dashes indicate that the data were not available to calculate the respective parameter.

Table 4-4. ~10 kbar clinopyroxene - liquid experimental data

	Cpx Composition[1]									
Run #	[MF]	[CaO]	K_D	D_{Ti}	D_{Al}	D_{Cr}	D_{Na}	Co-existing ϕ	T(°C)	Ref[2]
35	39.20	9.85	.32	.22	.17	2.7	.09	liq,ol,opx	1275	1
13L1	32.34	15.45	.29	.23	.31	10.5	.13	liq,opx	1290	2
5590	29.33	17.69	.29	-	-	-	-	liq	1305	3
5587	29.70	15.60	.32	-	-	-	-	liq,pl	1290	3
29	29.16	16.51	.35	.82	.54	-	.20	liq,ol	1280	4
24	30.56	15.07	.34	.44	.52	-	.20	liq	1310	4
21	33.34	13.75	.30	.23	.37	8.5	.19	liq,ol,opx,sp	1325	5
519-11	30.05	17.07	.21	.33	.43	-	.18	liq,ol,pl,sp	1250	6
116a	28.44	18.34	.23	.40	.42	-	.14	liq	1250	7
116b	28.01	18.65	.24	.34	.39	-	.15	liq	1250	7
116c	28.23	19.10	.23	.38	.36	-	.17	liq	1250	7
116d	28.54	18.71	.22	.38	.35	-	.17	liq	1250	7
Mean[3]	30.4	16.3	.27	.39	.41	10	.17			
Error[4]	1.3	1.0	.05	.17	.07	3	.02			

[1] [MF] = MgO+FeO in cpx (mole%); [CaO] = mole% CaO in cpx. All exchange and distribution coefficents calculated on an oxide mole% basis. Abbreviations as in Table 4-3.

[2] References: 1 - Takahashi and Kushiro (1983), 2 - Fujii and Bougault (1983), 3 - Green et al. (1979), 4 - Bender et al. (1978), 5 - Takahashi (1986), 6 - Stolper (1980), 7 - Dunn (1987).

[3] Mean for each column based on a subset of the data, see discussion in text.

[4] Error generally represents 1σ about the mean.

Table 4-5. Calculated mineral compositions[1]

	SiO_2	TiO_2	Al_2O_3	Cr_2O_3	FeO	MgO	CaO	Na_2O
Basalt 1								
Oliv	40.8(2)	-	-	-	10.0(8)	49.2(7)	-	-
Opx	54.1(6)	0.14(2)	4.6(2)	0.6(2)	5.5(6)	32.5(5)	2.5(34)	0.13(3)
Cpx	51.2(19)	0.3(1)	7.7(12)	0.9(3)	3.4(6)	19.9(10)	16.2(10)	0.43(5)
Sp	-	-	53.9(94)	17.0(99)	7.7(14)	21.5(18)	-	-
Basalt 2								
Oliv	40.9(1)	-	-	-	9.5(8)	46.6(6)	-	-
Opx	54.2(6)	0.12(2)	4.1(2)	1.1(4)	5.2(5)	32.6(5)	2.5(4)	0.11(2)
Cpx	51.5(17)	0.3(1)	6.9(12)	1.6(5)	3.2(5)	20.0(10)	16.2(10)	0.34(4)
Sp	-	-	40.0(79)	31.7(83)	9.3(15)	19.0(17)	-	-
Basalt 3								
Oliv	41.2(1)	-	-	-	8.2(6)	50.7(5)	-	-
Opx	54.7(11)	0.11(3)	4.6(4)	1.0(5)	4.8(4)	32.8(8)	1.8(5)	0.09(2)
Basalt 4								
Oliv	40.3(2)	-	-	-	12.8(13)	46.9(10)	-	-
Opx	54.0(6)	0.15(4)	4.30(27)	0.51(27)	7.2(8)	31.2(7)	2.5(4)	0.12(3)
Cpx	51.6(20)	0.33(15)	7.2(13)	0.75(40)	4.4(8)	19.1(11)	16.1(10)	0.38(6)
Sp	-	-	46.(11)	25.(12)	11.2(22)	18.3(25)	-	-
Basalt 5								
Oliv	40.6(2)	-	-	-	11.4(11)	48.1(9)	-	-
Opx	54.2(7)	0.15(4)	4.1(3)	0.7(4)	6.4(8)	31.9(6)	2.5(4)	0.11(2)
Cpx	51.7(19)	0.32(15)	6.9(12)	1.1(5)	3.9(8)	19.6(10)	16.3(10)	0.36(5)
Sp	-	-	40.(10)	31.(10)	10.8(20)	18.0(22)	-	-
Basalt 6								
Olix	40.8(2)	-	-	-	10.1(10)	49.1(8)	-	-
Opx	54.4(7)	0.14(3)	3.8(2)	0.9(5)	5.6(7)	32.4(6)	2.5(4)	0.11(2)
Cpx	52.0(19)	0.29(14)	6.4(10)	1.4(8)	3.4(6)	19.8(10)	16.2(10)	0.34(5)
Sp	-	-	34.5(95)	37.2(99)	10.8(19)	17.4(21)	-	-

[1] Numbers in parentheses represent 1σ uncertainties on each oxide in terms of the least units cited, e.g 10.8(19) is 10.8 ± 1.9.

Table 4-6. Mass balance calculations for basalts 1-3.[1]

	SiO_2	TiO_2	Al_2O_3	Cr_2O_3	FeO	MgO	CaO	Na_2O	Liq	Oliv	Opx	Cpx	Sp	(χ^2)	Q
Solutions to: Basalt 1 + Oliv + Opx + Cpx + Sp = Bulk Mantle[2]															
Mantle B	44.52	0.15	4.41	0.44	8.33	38.21	3.52	0.39	14.5(1.3)	60.2(3.4)	15.6(1.5)	8.6(1.5)	1.1(0.3)	4.43	0.35
Mantle D	45.13	0.14	4.07	0.46	7.86	38.27	3.52	0.32	10.9(1.2)	57.1(3.4)	20.4(3.8)	10.6(1.6)	1.0(0.3)	5.79	0.22
Mantle F	46.02	0.14	4.17	0.46	7.61	37.78	3.22	0.32	10.8(1.2)	51.6(3.4)	29.3(3.8)	7.5(1.5)	0.9(0.3)	3.16	0.53
Mantle H	45.86	0.12	3.71	0.48	7.62	38.89	2.83	0.22	6.4(0.9)	53.2(3.4)	31.3(3.7)	8.0(1.4)	1.1(0.3)	1.63	0.80
Solutions to: Basalt 2 + Oliv + Opx + Cpx + Sp = Bulk Mantle															
Mantle B	44.56	0.16	4.31	0.44	8.32	38.16	3.51	0.42	21.2(1.3)	61.4(3.3)	13.1(3.6)	4.7(1.4)	0.7(0.2)	3.17	0.53
Mantle D	45.22	0.15	3.96	0.46	7.84	38.24	3.52	0.35	16.9(1.2)	58.2(3.3)	18.2(3.7)	6.1(1.5)	0.4(0.2)	4.42	0.35
Mantle F	46.11	0.15	4.04	0.47	7.60	37.73	3.22	0.35	16.7(1.2)	52.6(3.2)	27.2(3.6)	3.0(1.4)	0.4(0.2)	1.69	0.79
Mantle H	46.07	0.12	3.52	0.49	7.58	38.84	2.84	0.25	10.9(1.0)	53.5(3.2)	30.5(3.6)	4.5(1.3)	0.6(0.3)	4.71	0.32
Solutions to: Basalt 3 + Oliv + Opx = Bulk Mantle															
Mantle B	45.29	0.18	4.45	0.43	8.00	38.27	3.28	0.44	26.0(1.0)	54.1(2.0)	19.9(2.2)			16.30	0.12E-1
Mantle D	45.68	0.17	4.18	0.45	7.63	38.53	3.14	0.39	22.8(1.1)	52.7(2.4)	24.5(2.8)			18.10	0.60E-2
Mantle F	46.28	0.16	4.19	0.46	7.41	38.23	3.03	0.37	21.4(1.2)	49.9(2.6)	28.7(3.1)			7.67	0.26
Mantle H	46.30	0.13	3.68	0.48	7.33	39.18	2.63	0.26	14.5(1.2)	48.8(2.8)	36.7(3.6)			14.52	0.24E-1

[1] Phase compositions given in Table 4-5. Calculated phase proportions in wt.%, units in parentheses represent standard errors, e.g. 14.5(1.3) = 14.5 ± 1.3. χ^2 is calculated from eqn (12). Q represents a statistical test of the fit, values ≥ 0.05 indicate an acceptable model, read 0.12E-1 as $.12 \times 10^{-1}$

[2] Bulk mantle compositions are calculated from the regressions, compare with compositions reported in Table 4-2.

Table 4-7. Mass balance calculations for basalt 4.[1]

	SiO_2	TiO_2	Al_2O_3	Cr_2O_3	FeO	MgO	CaO	Na_2O	Liq	Oliv	Opx	Cpx	Sp	(χ^2)	Q
Solutions to: Basalt 4 + Oliv + Opx = Bulk Mantle[2]															
Mantle B	45.90	0.20	4.30	0.42	8.63	35.85	3.26	0.40	18.5(1.0)	51.2(2.6)	30.2(2.7)			32.48	0.13E-4
Mantle D	46.29	0.19	4.04	0.44	8.11	36.06	3.16	0.35	16.2(1.1)	49.4(3.0)	34.4(3.1)			36.48	0.22E-5
Mantle F	46.86	0.17	4.06	0.45	7.84	35.79	3.03	0.34	14.6(1.2)	46.0(3.3)	39.3(3.5)			26.88	0.15E-3
Mantle H	46.86	0.14	3.58	0.47	7.84	36.82	2.64	0.24	10.4(1.1)	46.7(3.4)	42.9(3.7)			30.36	0.34E-4
Solutions to: Basalt 4 + Oliv + Opx + Cpx = Bulk Mantle															
Mantle B	45.79	0.19	4.11	0.41	8.60	35.97	3.53	0.38	15.0(1.4)	52.2(2.7)	26.6(3.0)	6.2(2.0)		27.81	0.40E-4
Mantle D	46.07	0.18	3.84	0.44	8.08	36.21	3.54	0.32	11.8(1.3)	51.1(3.0)	28.6(3.4)	8.6(2.0)		26.47	0.72E-4
Mantle F	46.76	0.17	3.93	0.45	7.83	35.85	3.22	0.32	12.1(1.4)	46.9(3.2)	35.9(3.5)	5.1(1.6)		22.82	0.36E-3
Mantle H	46.68	0.14	3.46	0.46	7.82	36.89	2.84	0.23	7.8(1.2)	48.2(3.2)	38.2(3.5)	5.8(1.6)		24.28	0.19E-3
Solutions to: Basalt 4 + Oliv + Opx + Cpx + Sp = Bulk Mantle															
Mantle B	44.43	0.18	4.29	0.44	8.62	36.63	3.51	0.38	15.9(1.7)	59.7(4.4)	16.5(4.6)	6.8(1.8)	1.1(0.3)	10.76	0.29E-1
Mantle D	45.00	0.17	3.97	0.46	8.09	36.74	3.51	0.32	12.2(1.5)	56.8(4.4)	21.0(4.7)	9.0(1.7)	1.0(0.3)	14.98	0.48E-2
Mantle F	45.89	0.16	4.06	0.47	7.84	36.25	3.21	0.31	11.8(1.5)	51.1(4.4)	30.2(4.7)	6.1(1.7)	0.9(0.3)	14.90	0.49E-2
Mantle H	45.74	0.13	3.63	0.48	7.83	37.32	2.82	0.22	7.2(1.2)	52.4(4.3)	32.4(4.6)	6.9(1.5)	1.2(0.4)	13.92	0.76E-2

[1] Phase compositions given in Table 4-5. Calculated phase proportions in wt %, units in parentheses represent standard errors, e.g. 18.5(1.0) = 18.5±1.0. χ^2 is calculated from eqn (12). Q is a statistical test of the fit, values ≥ 0.05 indicate acceptable models, read 0.13E-4 as 0.13×10^{-4}.

[2] Bulk mantle compositions are calculated from the regressions; compare with the compositions reported in Table 4-2.

Table 4-8. Mass balance calculations for basalt 5.[1]

	SiO_2	TiO_2	Al_2O_3	Cr_2O_3	FeO	MgO	CaO	Na_2O	Liq	Oliv	Opx	Cpx	Sp	(χ^2)	Q
Solutions to: Basalt 5 + Oliv + Opx = Bulk Mantle[2]															
Mantle B	45.71	0.20	4.29	0.42	8.54	36.55	3.30	0.41	20.9(1.1)	53.1(2.5)	26.0(2.6)			18.91	0.43E-2
Mantle D	46.11	0.19	4.04	0.45	8.04	36.76	3.19	0.36	18.5(1.2)	51.3(2.9)	30.2(3.1)			22.31	0.11E-2
Mantle F	46.71	0.18	4.04	0.46	7.78	36.48	3.06	0.35	16.8(1.2)	47.8(3.2)	35.4(3.5)			14.02	0.29E-1
Mantle H	46.73	0.15	3.56	0.47	7.76	37.53	2.67	0.25	12.3(1.2)	48.6(3.4)	39.1(3.8)			18.97	0.42E-2
Solutions to: Basalt 5 + Oliv + Opx + Cpx = Bulk Mantle															
Mantle B	45.61	0.19	4.12	0.42	8.51	36.69	3.54	0.39	17.8(1.4)	54.1(2.6)	22.8(2.9)	5.2(1.9)		15.15	0.97E-2
Mantle D	45.91	0.18	3.83	0.45	8.01	36.93	3.54	0.33	14.4(1.4)	53.1(3.0)	25.0(3.3)	7.5(1.8)		13.67	0.18E-1
Mantle F	46.61	0.17	3.92	0.46	7.76	36.56	3.23	0.33	14.4(1.4)	48.8(3.2)	32.5(3.5)	4.2(1.6)		10.83	0.55E-1
Mantle H	46.59	0.14	3.42	0.47	7.75	36.62	2.84	0.24	9.8(1.3)	50.0(3.3)	35.2(3.6)	5.0(1.6)		14.01	0.16E-1
Solutions to: Basalt 5 + Oliv + Opx + Cpx + Sp = Bulk Mantle															
Mantle B	44.57	0.19	4.25	0.44	8.54	37.17	3.51	0.40	18.6(1.7)	59.6(4.0)	15.4(4.4)	5.5(1.7)	0.9(0.3)	4.73	0.32
Mantle D	45.18	0.18	3.93	0.46	8.02	37.27	3.52	0.33	14.6(1.6)	56.6(4.0)	20.3(4.4)	7.8(1.7)	0.7(0.3)	7.49	0.11
Mantle F	46.07	0.17	4.01	0.47	7.77	36.79	3.22	0.33	14.0(1.5)	50.9(4.0)	29.5(4.3)	4.9(1.6)	0.7(0.3)	6.90	0.15
Mantle H	45.93	0.14	3.57	0.48	7.76	37.87	2.82	0.23	8.8(1.3)	52.1(3.9)	32.2(4.2)	5.9(1.5)	1.0(0.4)	7.43	0.11

[1] Phase compositions given in Table 4-5. Phase proportions in wt.%, units in parentheses represent standard errors, e.g. 20.9(1.1) = 20.9±1.1. χ^2 calculated from eqn (12). Q is a statistical test of the fit, values ≥ 0.05 indicate an acceptable fit, read 0.43E-2 as 0.43×10^{-2}.

[2] Bulk mantle compositions are calculated from the regressions, compare with the compositions reported in Table 4-2.

Table 4-9. Mass balance calculations for basalt 6.[1]

	SiO_2	TiO_2	Al_2O_3	Cr_2O_3	FeO	MgO	CaO	Na_2O	Liq	Oliv	Opx	Cpx	Sp	(χ^2)	Q
Solutions to: Basalt 6 + Oliv + Opx = Bulk Mantle[2]															
Mantle B	45.43	0.20	4.30	0.43	8.44	37.24	3.33	0.42	23.6(1.1)	55.2(2.4)	21.2(2.5)			10.52	0.10
Mantle D	45.85	0.20	4.04	0.45	7.96	37.43	3.22	0.37	21.2(1.2)	53.4(2.9)	25.4(3.2)			13.91	0.31E-1
Mantle F	46.52	0.18	4.03	0.47	7.70	37.12	3.08	0.36	19.2(1.3)	49.5(3.2)	31.3(3.6)			7.01	0.32
Mantle H	46.53	0.15	3.55	0.48	7.69	38.19	2.68	0.26	14.6(1.3)	50.8(3.5)	34.6(3.9)			13.70	0.33E-1
Solutions to: Basalt 6 + Oliv + Opx + Cpx = Bulk Mantle															
Mantle B	45.35	0.20	4.14	0.43	8.42	37.38	3.53	0.41	21.0(1.5)	56.4(2.6)	18.4(2.9)	4.3(1.8)		7.78	0.17
Mantle D	45.70	0.18	3.84	0.45	7.93	37.62	3.53	0.35	17.3(1.4)	55.2(3.0)	21.0(3.4)	6.5(1.7)		6.78	0.24
Mantle F	46.45	0.17	3.92	0.47	7.68	37.21	3.23	0.35	17.1(1.5)	50.4(3.2)	29.0(3.6)	3.5(1.6)		4.64	0.46
Mantle H	46.46	0.14	3.41	0.48	7.67	38.28	2.84	0.25	12.2(1.4)	51.8(3.4)	31.8(3.8)	4.1(1.5)		9.95	0.77E-1
Solutions to: Basalt 6 + Oliv + Opx + Cpx + Sp = Bulk Mantle															
Mantle B	44.63	0.20	4.24	0.44	8.45	37.68	3.51	0.41	21.6(1.7)	59.8(3.7)	13.6(4.1)	4.4(1.7)	0.6(0.2)	2.16	0.71
Mantle D	45.26	0.18	3.90	0.46	7.94	37.78	3.51	0.35	17.2(1.6)	56.9(3.7)	18.6(4.2)	6.7(1.6)	0.5(0.2)	4.01	0.40
Mantle F	46.16	0.17	3.97	0.47	7.69	37.29	3.22	0.34	16.5(1.6)	51.1(3.6)	27.9(4.1)	4.0(1.6)	0.5(0.3)	2.90	0.57
Mantle H	46.06	0.14	3.52	0.48	7.67	38.34	2.82	0.24	10.6(1.5)	51.9(3.6)	31.4(3.6)	5.1(1.5)	1.0(0.4)	5.70	0.22

1 Phase compositions reported in Table 4-5. Calculated phase proportions in wt. %, units in parentheses represent standard errors, 23.6(1.1) = 23.6 ± 1.1. χ^2 calculated from eqn (12). Q is a statistical test of the fit, values ≥ 0.05 indicate an acceptable model, read 0.31E-1 as 0.31×10^{-1}.

2 Bulk mantle compositions are calculated from the regression, compare with compositions reported in Table 4-2.